

NATIONAL CENTRE FOR NUCLEAR RESEARCH



Parton's energy loss in unstable
quark-gluon plasma

DOCTORAL THESIS

Author:
Katarzyna Deja

Supervisor:
prof. dr hab. Stanisław Mrówczyński

Warsaw 2015

Abstract

Motivated by the phenomenon of jet quenching observed in relativistic heavy-ion collisions, we compute the collisional energy loss of a test parton propagating through a quark-gluon plasma in which the momentum distribution is anisotropic. Consequently, the system, which is assumed to be weakly coupled, is unstable due to chromomagnetic plasma modes. To derive a spectrum of the collective modes, which is needed for the energy loss calculations, we have considered distributions with all degrees of deformation along the beam axis from extremely prolate - infinitely elongated, through isotropic to extremely oblate - infinitely squeezed in the beam direction. In every case we have calculated analytically or numerically the dispersion curves for the full spectrum. Unstable modes are shown to exist in all cases except that of isotropic plasma. We have derived the conditions on wave vectors for an existence of these instabilities. We have also discussed stable modes which are not limited to small domains of wave vectors and therefore have an important influence on the system's dynamics. The spectrum of the collective excitations is further used to calculate the energy loss of a high-energy parton scattering elastically. The approach, which is formulated as an initial value problem, is designed to study an unstable plasma, but it also reproduces the well known result in case of equilibrium plasma. As examples of unstable plasmas, the extremely prolate and oblate systems are considered, and two classes of initial conditions are discussed. When the initial chromodynamic field is uncorrelated with the colour state of the parton, the magnitude of the energy losses is comparable to that in an equilibrium plasma of the same density. When the initial chromodynamic field is induced by the test parton, it can be either accelerated or decelerated depending on the relative phase factor. With a correlated initial condition, the energy transfer grows exponentially in time and its magnitude can much exceed the absolute value of energy loss in equilibrium plasma. The energy loss is not only time dependent but it is also strongly directionally dependent. Consequences of our findings for the phenomenology of jet quenching in relativistic heavy-ion collisions are briefly considered.

This thesis is based on the following original publications:

1. M. E. Carrington, K. Deja, and S. Mrówczyński, *Plasmons in Anisotropic Quark-Gluon Plasma*, Phys. Rev. C **90**, 034914 (2014)
2. K. Deja and S. Mrówczyński, *Complete Plasmon Spectrum of Two-Stream System*, to appear in Acta Phys. Pol. B; arXiv 1503.08861
3. M. E. Carrington, K. Deja, and S. Mrówczyński, *Energy Loss in Unstable Quark-Gluon Plasma*, to appear in Phys. Rev. C; arXiv 1506.09082

Streszczenie

Aby dogłębnie zrozumieć zjawisko tłumienia dżetów obserwowane w zderzeniach ciężkich jonów, badaliśmy straty energii testowego wysokoenergetycznego partonu poruszającego się w plazmie kwarkowo-gluonowej, w której rozkład pędu cząstek plazmy jest anizotropowy. Na skutek anizotropii układ, który z założenia jest słabo sprzężony, jest niestabilny ze względu na plazmowe mody chromomagnetyczne. Aby uzyskać widmo wzbudzeń kolektywnych, które jest niezbędne do wyliczenia strat energii, rozważyliśmy rozkłady pędowe ze wszystkimi możliwymi jednowymiarowymi deformacjami wzdłuż osi wiązki od skrajnie „prolate” - nieskończenie wydłużonego, przez izotropowy, po skrajnie „oblate” - nieskończenie spłaszczony w kierunku wiązki. W każdym z rozważonych przypadków rozwiązaliśmy analitycznie bądź numerycznie równanie dyspersyjne, aby uzyskać pełne spektrum wzbudzeń. Pokazaliśmy, iż niestabilności występują w każdej konfiguracji z wyjątkiem systemu izotropowego. W przypadku, gdy w układzie istnieją mody niestabilne, wyprowadzony został warunek na wartość wektora falowego, kiedy pojawiają się niestabilności. Została przedstawiona również dyskusja modów stabilnych, które w przeciwieństwie do niestabilnych nie są ograniczone do pewnego zakresu wektora falowego i dlatego mają znaczący wpływ na dynamikę układu. Wyliczone widmo modów kolektywnych zostało użyte w dalszej części pracy do określenia zderzeniowych strat energii wysokoenergetycznego partonu. Podejście zaprezentowane w niniejszej rozprawie ma opisywać układy niestabilne, jednakże reprodukuje ono także dobrze znany wynik dla układu równowagowego. Obliczając straty energii, rozważyliśmy dwa przykłady układów niestabilnych - skrajnie „prolate” i „oblate”, oraz dwie klasy warunków początkowych. Jeśli początkowe pole chromodynamiczne jest nieskorelowane z kolorowym stanem partonu, wówczas wielkość strat energii jest porównywalna z przypadkiem izotropowym. W przypadku, gdy pole jest indukowane przez testowy parton, może on być przyśpieszany bądź spowalniany zależnie od wyboru warunku początkowego. Wartość przekazu energii w takim wypadku rośnie eksponencjalnie w czasie, a jej absolutna wartość może znacząco przewyższać wartość równowagową. Wykazaliśmy, iż straty energii przejawiają silną zależność od czasu i kierunku. Omówione zostały fenomenologiczne konsekwencje naszych spostrzeżeń. Podstawą rozprawy są następujące oryginalne publikacje:

1. M. E. Carrington, K. Deja, and S. Mrówczyński, *Plasmons in Anisotropic Quark-Gluon Plasma*, Phys. Rev. C **90**, 034914 (2014)
2. K. Deja and S. Mrówczyński, *Complete Plasmon Spectrum of Two-Stream System*, Acta Phys. Pol. B w druku; arXiv 1503.08861
3. M. E. Carrington, K. Deja, and S. Mrówczyński, *Energy Loss in Unstable Quark-Gluon Plasma*, Phys. Rev. C w druku; arXiv 1506.09082

Acknowledgements

The dissertation in its present form would not been possible without help and support from several people, to whom I would like to exprese my gratitude here.

First of all I would like to express my great gratitude to my supervisor prof. Stanisław Mrówczyński for his extensive advice and full support, as well as for his invaluable help both during my studies and in the time of preparing the thesis. He continuously supervised and encouraged me to get involved in the analysis, his thoughtful and well-informed suggestions led up my studies to the fruitful end.

Many thanks to our collaborator prof. Margaret Carrington whose suggestions and help never failed me. Her experience, knowledge and warmness were a great support for me - this work would never be possible without your help.

I would also like to thank all the members of the National Centre for Nuclear Research for their helpful hand, especially Andrzej Sandacz, Paweł Sznajder, Teresa Świerczyńska. I sincerely believe this group of people made one of the nicest environments to work.

Special thanks goes to my family for giving me a great deal of support and cheering me up all the time.

Contents

Acknowledgements vii

Contents ix

1	Introduction	1
1.1	Quark Gluon Plasma	1
1.2	Quantum Chromodynamics	3
1.3	Main experimental programmes	5
1.4	Important experimental results	8
1.5	Anisotropic plasma and role of instabilities	11
1.6	The aim of the thesis and its outline	13
2	Collective modes	15
2.1	Formulation of the problem	17
2.1.1	General dispersion equations	17
2.1.2	Decomposition of the Σ matrix	19
2.2	Isotropic plasma	22
2.3	Two stream system	25
2.3.1	Special cases	27
2.3.1.1	Special case: $\mathbf{k} \mathbf{u}$	27
2.3.1.2	Special case: $\mathbf{k} \perp \mathbf{u}$	28
2.3.1.3	Pure longitudinal electric field	30
2.3.2	General case	31
2.3.3	Special case: $\mathbf{u}^2 = 1$	36
2.4	Anisotropic plasma as deformed isotropic one	40
2.4.1	Momentum distributions	40
2.4.2	Coefficients $\alpha, \beta, \gamma, \delta$	42
2.5	Weakly anisotropic plasma	44
2.5.1	A -modes	45
2.5.2	B -modes	47
2.5.3	C -modes	47
2.5.4	Discussion	50
2.6	Finite anisotropy	52
2.7	Extremely prolate plasma	56
2.8	Extremely oblate plasma	61

2.8.1	Special case: $\mathbf{k} \parallel \mathbf{n}$	66
2.8.2	Special case: \mathbf{k} almost parallel to \mathbf{n}	68
2.8.3	Special case: $\mathbf{k} \perp \mathbf{n}$	69
2.9	Nyquist analysis	72
2.9.1	Isotropic plasma	75
2.9.2	Weakly anisotropic plasma	78
2.9.3	Extremely prolate plasma	80
2.9.4	Extremely oblate plasma	81
2.10	Summary and final remarks	84
3	Energy Loss	87
3.1	General formula	90
3.2	Equilibrium limit	94
3.3	Initial conditions	98
3.3.1	Uncorrelated initial conditions	98
3.3.2	Correlated initial conditions	100
3.4	Self-interactions	102
3.5	Unstable plasmas	104
3.5.1	Integrand	105
3.6	Extremely prolate and oblate plasmas	107
3.6.1	Extremely prolate plasma	108
3.6.2	Extremely oblate plasma	112
3.7	Important configurations	116
4	Conclusions and Outlook	119
A		123
A.1	Classical dispersion equation	123
A.2	Components of polarization tensor	124
A.3	Reality of energy loss	131
A.4	Temporal axial and Feynman-Lorentz gauges	132
	Bibliography	135

Dedicated to my mother

Chapter 1

Introduction

1.1 Quark Gluon Plasma

Over the past hundred years, our ideas about the ultimate constituents of matter have undergone a considerable evolution. In the early 1960's with the construction of proton accelerators with energies above the threshold for anti-proton production, a lot of new particles were discovered. There were doubts whether truly elementary constituents exist as all newly discovered hadrons were equally elementary or equally complex. In 1964 independently Murray Gell-Mann [1] and George Zweig [2] introduced the idea of quarks. According to Gell-Mann, it was mostly a mathematical concept which was based on the notification that particles of similar mass sharing the same quantum numbers (baryon number, spin, parity) follow the symmetry of the SU(3) group and the quarks constituted its fundamental representation. For Zweig quarks were rather physical objects which form hadrons. These ideas successfully explained the systematics of observed hadrons and also led to the prediction of new particles. The quark model assumed 3 elementary quarks (up, down, strange) with spin $\frac{1}{2}$ and fractional electrical charge $-\frac{1}{3}$ or $\frac{2}{3}$ of the elementary charge e . To explain an existence of the new baryon Ω^- of spin $\frac{3}{2}$, which consists of three strange quarks (because its strangeness equals 3), a new degree of freedom (colour) was introduced by Greenberg [3], to allow 3 identical quarks to occupy the same momentum and spin state. In 1970 Glashow and Bjorken [4] added the fourth charm quark to explain a suppression of certain channels in weak decays of strange-particles. The quark model evolved into a complex theory with 6 elementary quarks and gluons. Table 1.1 gives the additive quantum numbers for the three generations of quarks.

At the same time, thanks to theoretical efforts by Feynman [5] and Bjorken [6], the quark-like structure of proton was found in the experiment [7], where the deep inelastic scattering of electrons on protons (DIS) was studied. Meanwhile the theory of strong

	d	u	s	c	b	t
Q - electric charge	$-\frac{1}{3}$	$\frac{2}{3}$	$-\frac{1}{3}$	$\frac{2}{3}$	$-\frac{1}{3}$	$\frac{2}{3}$
S - strangeness	0	0	-1	0	0	0
C- charm	0	0	0	+1	0	0
B - bottomness	0	0	0	0	-1	0
T - topness	0	0	0	0	0	+1

TABLE 1.1: Additive quantum numbers of quarks.

interactions, known nowadays as QCD, was developing. The theory was formulated as a non-Abelian gauge field theory introduced by Yang and Mills [8]. The Quantum ChromoDynamics (QCD) was finalized soon after the discovery of asymptotic freedom by Gross, Wilczek [9] and Politzer [10], in the early 1970's.

In 1975 Collins and Perry [11] suggested an existence of a new phase of nuclear matter composed of quarks and gluons, which was soon later termed by Shuryak [12] *quark-gluon plasma* (QGP). In 1978 Shuryak found that at high temperature T the colour charge is screened, indicating that the system was then weakly interacting. When we consider different states of matter, it is common to use a phase diagram. Such a diagram for nuclear matter is presented in Fig. 1.1, where different states are shown in a plane of baryochemical potential and temperature. At low temperatures and/or baryochemical potential, there is a hadron gas which changes into the quark-gluon plasma when the temperature or/and baryochemical potentials is sufficiently high.

It was realized in the 1970's that it is possible to obtain a drop of superdense nuclear matter in a terrestrial laboratory by colliding of relativistic heavy ions [13, 14]. It initiated a rapid progress in experimental heavy-ion physics which is briefly described in Sec. 1.3. In February 2000 leaders of the experimental CERN's heavy ion programme presented "the compelling evidence for the existence of a new state of matter in which quarks, instead of being bound up into more complex particles such as protons and neutrons, are liberated to roam freely. . ." [15]. The new state of matter - quark-gluon plasma was discovered.

In the today's cold Universe, we do not observe free quarks - they are confined in nucleons. Maybe there are some deconfined quarks in the dense cores of neutron stars, but it is still uncertain. However, the early Universe was extremely hot [16]. Its temperature exceeded 150 MeV (about $2 \cdot 10^{12}$ K) until about 10 ms after the Big Bang. QCD predicts that such conditions are sufficient for the quark-gluon plasma to exist. Understanding of the evolution of our Universe thus requires knowledge of the structure and dynamics of QGP governed by Quantum Chromodynamics.

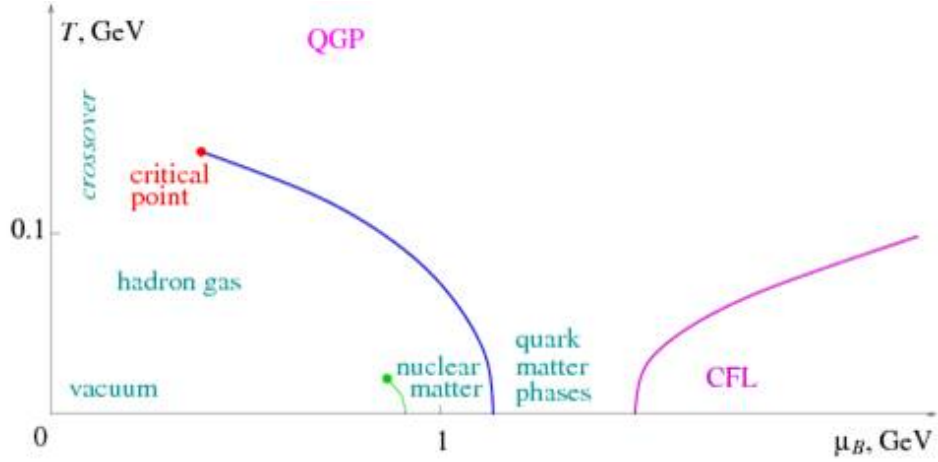


FIGURE 1.1: Phase diagram of nuclear matter. Figure taken from [17].

1.2 Quantum Chromodynamics

QCD is defined by the Lagrangian which encodes the dynamics in a fundamental way. The strong forces come from the requirement of local SU(3) gauge symmetry of the Lagrangian. Quarks interact by the exchange of massless spin-one gluons which due to the non-Abelian nature of the theory carry themselves the colour charge, and consequently interact with each other. The Lagrangian of the interacting quarks and gluons is:

$$\mathcal{L}_{QCD} = \sum_f \bar{\psi}_f \gamma^\mu (i\partial_\mu - gA_\mu^a \tau^a) \psi_f + \sum_{f=1}^{N_f} m_f \bar{\psi}_f \psi_f - \frac{1}{4} F_{\mu\nu}^a F_a^{\mu\nu}, \quad (1.2.1)$$

where ψ_f denotes the quark spinor field of flavour $f = u, d, s, \dots$, γ^μ are the Dirac matrices, g is dimensionless coupling constant, τ^a are the generators of the fundamental representation of the SU(3) group, a ($a=1, 2, \dots, 8$), m_f is the mass of a quark of flavour f , N_f is the number of quark flavours, f^{abc} are the antisymmetric structure constants of SU(3) group, A_ν^a and $F_{\mu\nu}^a$ denote the gluon potential and field strength tensor of colour a , respectively, related to each other as

$$F_{\mu\nu}^a = \partial_\mu A_\nu^a - \partial_\nu A_\mu^a - g_s f^{abc} A_\mu^b A_\nu^c. \quad (1.2.2)$$

The third term in (1.2.2) is responsible for gluon self-interactions which appears when we construct the gauge-invariant Lagrangian. The square of $F_{\mu\nu}^a$ in (1.2.2) gives rise to both cubic and quartic gluon terms corresponding to 3 and 4 gluon couplings.

The two most significant features of QCD are the asymptotic freedom and colour confinement.

- Asymptotic freedom

The asymptotic freedom (discovered by Gross, Wilczek and Politzer [9, 10]) implies that with increasing momentum transfer Q or with decreasing distance $\frac{1}{Q}$, the interaction between quarks becomes weaker and weaker, that is the coupling constant decreases with Q^2 as:

$$\alpha_s(Q) = \frac{g^2}{4\pi} = \frac{12\pi}{(33 - 2N_f) \log \left[\frac{Q^2}{\Lambda_{QCD}^2} \right]}, \quad (1.2.3)$$

where $\Lambda_{QCD} \approx 200\text{MeV}$ is the QCD scale parameter.

Equation (1.2.3) shows that $\alpha_s(Q) \rightarrow 0$ as $Q^2 \rightarrow \infty$. In the limit of large momentum transfer, the interactions can be treated in a perturbative way, which requires a small value of the strong coupling constant. The perturbative QCD is very successful theory in describing hard processes ($Q^2 \gg \Lambda_{QCD}^2$) such as production of jets. The coupling constant also decreases logarithmically with growing temperature of QGP, but just above the deconfinement $\alpha_s(Q) = 0.2 - 0.5$ and the perturbative approach is not easily applicable. Fig. 1.2 presents the value of the running coupling constant, α_s , as a function of the energy scale Q . The curve that slopes downwards (negative beta function) is a prediction of the asymptomatic freedom of QCD and, as can be seen, agrees very well with the measurements.

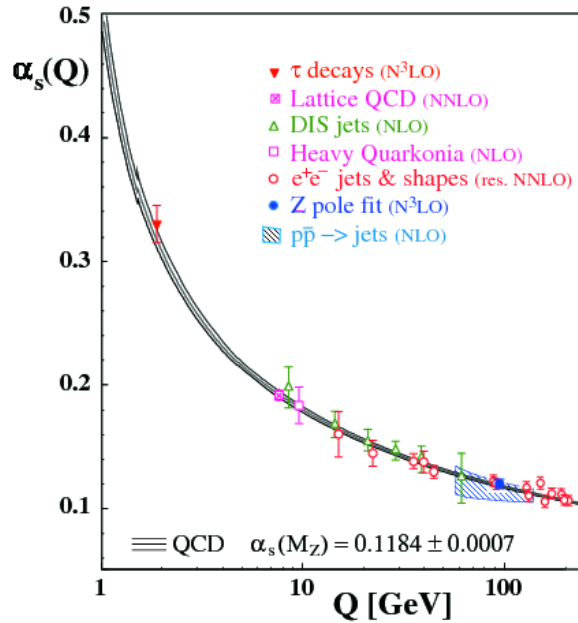


FIGURE 1.2: The running coupling constant α_s , as a function of momentum transfer Q . Figure taken from [18].

- Colour confinement

The confinement property implies that any isolated object of Nature must be colour neutral or, technically, a singlet of the $SU(3)$ colour group. This means that the colours of the quarks, antiquarks, gluons which form a hadron must combine to give a net colourless object. The confinement of colours does not, obviously, exclude an existence of QGP. However it requires that the plasma as a whole has no colour charge. While the asymptotic freedom is well understood, an explanation of the confinement remains a theoretical challenge.

1.3 Main experimental programmes

Heavy-ion collisions provide a unique opportunity to study the hadronic matter in a laboratory. The systematical experimental research program with relativistic heavy-ions started with experiments at the Bevelack at Berkeley in the 1980s. The first, truly relativistic ion beam of medium mass ions was obtained at European Center for Nuclear Research (CERN) at the Super Proton Synchrotron (SPS) in 1986. The beginning of the XXI century started with the operation of the Relativistic Heavy Ion Collider (RHIC) at BNL. Ten years later in 2010 at CERN, the largest experimental facility - the Large Hadron Collider (LHC) was completed. In this chapter we will briefly review the experimental programs at AGS, SPS, RHIC and LHC.

- The Alternating Gradient Synchrotron at BNL

The AGS synchrotron was built in 1957 and accelerated the high intensity proton beam to the energy of 33 GeV. The AGS synchrotron was also used to accelerate Si ions at energies of 14 GeV per nucleon, and heavier ions like Au up to 11 GeV per nucleon. Several fixed target heavy-ion experiments were performed, like E866, E877, E891, E895, E896, E910, E917 to study the hadronic matter at high temperature. However it is not clear whether the AGS could produce the deconfined matter since the initial energy density is presumably below $1 \text{ GeV}/\text{fm}^3$.

- The Super Proton Synchrotron at CERN

In 1976 the Super Proton Synchrotron was built, allowing the acceleration of protons up to 500 GeV. Initially the SPS was a proton accelerator but later on SPS became a proton - antiproton collider. In 1981 the first proton - antiproton collisions at a center of mass energy of 520 GeV took place. In 1986 the SPS started the ion program, the

ions of ^{16}O and ^{32}S were accelerated to the energy 200 GeV. Several ion experiments contributed to the SPS heavy ion physics programme: WA80, WA93, WA98, WA85, WA94, WA97, NA57, Helios-2, NA44, CERES, Helios-3, NA35, NA49, NA36, NA52, NA38, NA50, NA60, and NA61. The names WA and NA came from the experimental fixed-target halls in the west area (WA) in Switzerland and north area (NA) in France. Some interesting physical phenomena have been discovered at SPS like strangeness, dilepton enhancements, and the J/ψ suppression. These experimental facts indicate that the deconfined state of strongly interacting matter is produced in heavy-ion collision.

- The Relativistic Heavy Ion Collider at BNL

RHIC was the first ever built machine dedicated to study collisions of relativistic heavy ions. The primary goal of RHIC was the experimental investigation of the QCD phase transition. RHIC started regular beam operations in the summer of year 2000 producing head-on collisions of two beams of fully stripped Au ions with the center-of-mass energy 130 GeV per nucleon-nucleon collision. Above mentioned AGS is the injector of the RHIC, the beams are accelerated in two different rings in the opposite directions to the energy 9 GeV and then the beams are delivered to RHIC. RHIC collider allows also to study collisions of polarised protons at 500 GeV, and collisions of d-Au, Cu-Cu, Au-Au and U-U in the energy range 20 – 200 GeV per nucleon pair. The impressive number of the experimental results, which are summarized in [19–22], have been obtained by four major experiments at RHIC: PHENIX, STAR, PHOBOS and BRAHMS.

The Solenoidal Tracker at RHIC (STAR) is one of two largest RHIC experiments. STAR is the only one RHIC detector with the full azimuthal coverage in particle detection and identification. The STAR detector is designed for a very broad physical program. It is well suited for otherwise difficult measurements like non-statistical fluctuations of event multiplicity or high- p_T jets. Its experimental setup has also been used for strangeness measurements by detection of particle's decays.

PHENIX (Pioneering High Energy Nuclear Interaction eXperiment) has been designed for good identification of electromagnetic and hard signals as well as the high- p_T jets and particle correlations.

PHOBOS, which was a much smaller experiment than the two presented above, was used for precise measurements of charged particle multiplicity in a wide range of rapidity together with their azimuthal distribution.

BRAHMS (Broad RAnge Hadron Magnetic Spectrometers) was designed to measure event multiplicity and inclusive rapidity distribution in a wide rapidity range.

These four experiments have developed a high quality physics program, producing a huge amount of experimental results. Today only the two major experiments: PHENIX and STAR are still active and taking data.

- The Large Hadron Collider at CERN

LHC is designed to collide two counter rotating beams of protons or heavy ions. Upgraded SPS is used as an injector for LHC. It generates a Pb ion beam of 177 GeV per nucleon. In the November 2010 the first lead-lead collision with the energy of 2.76 TeV per pair of colliding nucleons was observed. After the long shutdown in 2013/2014 the nominal energy 5.5 TeV per nucleon pair was reached. Three of the four LHC experiments participate in the heavy ion program: ALICE, ATLAS and CMS. They have already obtained many interesting results [23–27].

ALICE (A Large Ion Collider Experiment) is the only LHC experiment fully devoted to study QGP. The physics of ALICE program is very rich, it includes the following main topics: the thermalization of QGP, the mechanisms of energy loss and the dissociation of quarkonium states.

LHC experiments not only confirm all results, which were obtained at RHIC, at much higher energy, but they also provide a lot of new information. The heavy-ion programs at RHIC and LHC promise fascinating and exciting results in the next decade.

1.4 Important experimental results

As already mentioned, a primary goal of experimental analysis of heavy-ion collisions is to understand and characterize a dynamics of dense partonic medium. It occurs that measurements of azimuthal distribution of particles produced in heavy ion collisions have provided crucial information about quark-gluon plasma. In this chapter we will briefly present two main physical results from the RHIC and LHC heavy ion programmes: the collective flow and jet quenching. These two phenomena motivate our studies.

- Collective flow

The experimental observable, which is sensitive to the dynamics of the early stages of heavy-ion collisions, is angular distribution with respect to the reaction plane defined by beam axis and the impact parameter. When we consider non-central collisions of heavy nuclei, then the initial matter distribution is anisotropic in coordinate space. This initial spatial anisotropy of the overlapping zone of colliding nuclei is converted *via* the action of azimuthally anisotropic pressure gradients into the momentum space anisotropy of particle distribution, see Fig. 1.3. This anisotropy influences the azimuthal distribution of produced particles which is expressed as a Fourier series

$$\frac{dN(p_T, \phi)}{dp_T d\phi} = \frac{dN(p_T)}{dp_T} \left(1 + 2 \sum_{n=0}^{\infty} v_n(p_T) \cos(n\phi) \right), \quad (1.4.1)$$

where v_n are the flow coefficients, p_T is the transverse momentum and ϕ is the azimuthal angle. The distribution averaged over events is azimuthally symmetric, then only the radial flow (v_0), survives. The first, second and third Fourier components of the azimuthal distribution of the final state hadrons present in the equation (1.4.1) are known as the directed (v_1), elliptic (v_2), and triangular (v_3) flow, respectively.

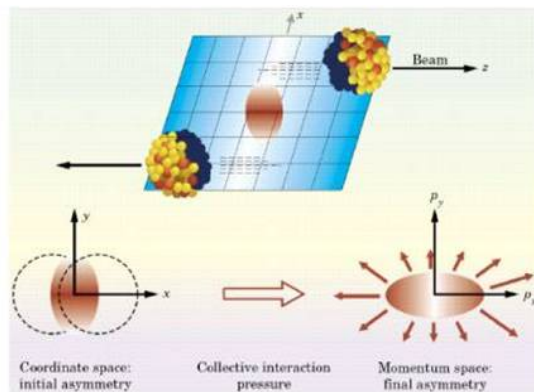


FIGURE 1.3: Almond-shaped interaction volume after a non-central collision of two nuclei and generation of elliptic flow. Figure taken from [28].

The largest of the anisotropic flows is the elliptic flow which has been extensively studied at RHIC and LHC. The observed large value of the elliptic flow suggests that the strongly interacting matter equilibrates at the early stage of the collision, and then it evolves following the laws of hydrodynamics. QGP also behaves like an almost perfect fluid. Fig. 1.4 presents the elliptic flow for various identified particles, as obtained by PHENIX and STAR in the low p_T region. Figure shows the reasonable agreement between experimental results and ideal hydro calculations for p_T up to 2 GeV/ c .

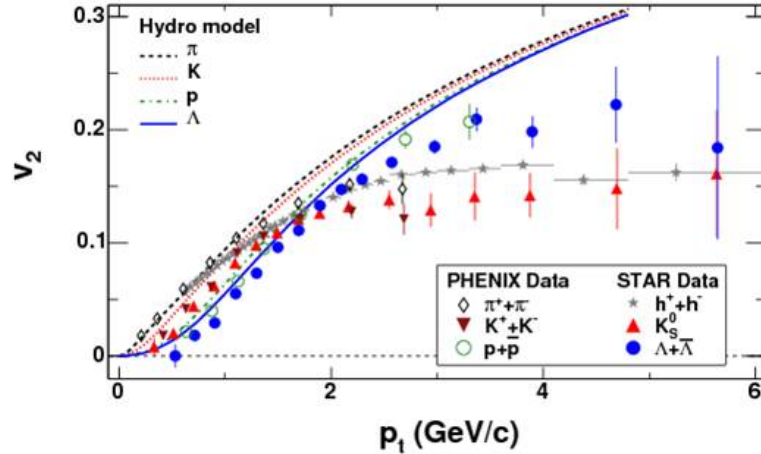


FIGURE 1.4: The elliptic flow as a function of the transverse momentum measured by PHENIX and STAR. Figure taken from [29].

To apply hydrodynamic models, one has to assume that the plasma system is at least approximately in a local thermal equilibrium. It is needed because an equilibrium equation of state (EOS) is used to close the system of equations, and because the structure of the energy-momentum tensor requires an isotropy of the system. The success of ideal hydrodynamic models in describing the measured elliptic flow implies that the equilibration time of the system is as short as 1 fm/ c [30]. Therefore one asks what is a mechanism of such a fast thermalization.

- Jet quenching

At the early stage of nuclear collisions two energetic partons are sometimes created back to back in a hard scattering process. Bjorken suggested that such an energetic parton can lose a large fraction of its energy flying across the deconfined medium [31]. This effect is called the jet quenching. The STAR collaboration proposed a simple method to observe the phenomenon. In the center of mass of colliding nuclei, one looks of the high p_T particle emitted perpendicularly to the beam axis. Then, one should observe an associated particle on the opposite side at 180°.

Fig. 1.5 compares the data for gold-gold central collisions, where the hot medium is expected to be formed, with the proton-proton and deuterium-gold collisions. The expected correlation is clearly visible for p-p and d-Au data - two peaks separated by 180° . For Au-Au collisions we see only the peak at zero degree (near side peak). Vanishing of the away-side peak at 180° gives a hint that a coloured partonic medium was created which quenched the jet.

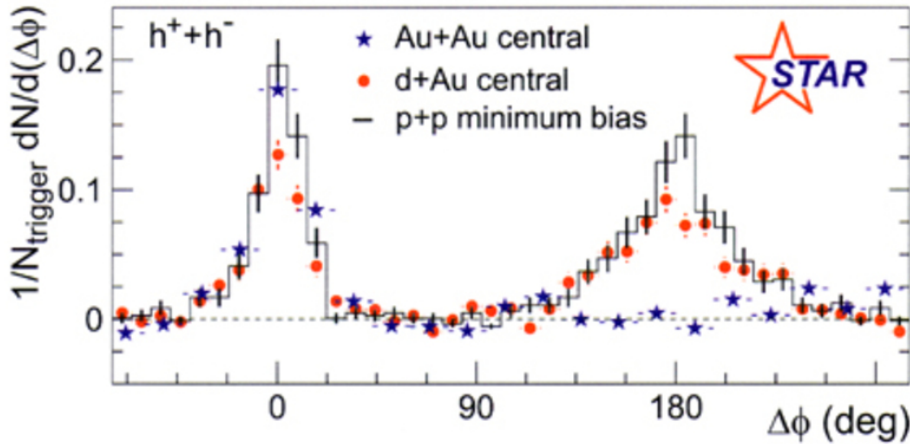


FIGURE 1.5: Dihadron angular correlation in Au-Au, d-Au, and p-p collisions at $\sqrt{s_{NN}} = 200$ GeV. Figure taken from [32].

In a more quantitative investigation of the jet quenching, one considers the nuclear modification factor (R_{AA}), which measures the yield of hadrons relative to the expected yield from proton-proton reactions and it is expressed by the equation:

$$R_{AA}(y, p_T) = \frac{1}{\langle N_{coll} \rangle} \frac{\frac{d^2 N_{AA}}{dp_T dy}}{\frac{d^2 N_{pp}}{dp_T dy}}, \quad (1.4.2)$$

where $\frac{d^2 N_{AA}}{dp_T dy}$ and $\frac{d^2 N_{pp}}{dp_T dy}$ are the single particle inclusive distributions in A-A and p-p collisions, respectively, y is a given rapidity and p_T is a transverse momentum, and $\langle N_{coll} \rangle$ is the average number of binary collisions in the heavy ion medium. R_{AA} is a nice quantity to work with, as it displays the effect of nuclear collisions: $R_{AA} = 1$ means no modification when compared to the trivially scaled p-p collisions, $R_{AA} > 1$ means an enhancement, and $R_{AA} < 1$ means a suppression. High transverse momentum hadrons, such as π^0 and η mesons are suppressed in central Au-Au collisions when compared to measurements in p-p collisions. The first evidence of parton energy loss was found at RHIC. Similar results have been obtained at LHC at much broader p_T range. The evolution of the nuclear modification factor with center-of-mass energy, from the SPS to RHIC and then to the LHC, is presented in Fig. 1.6.

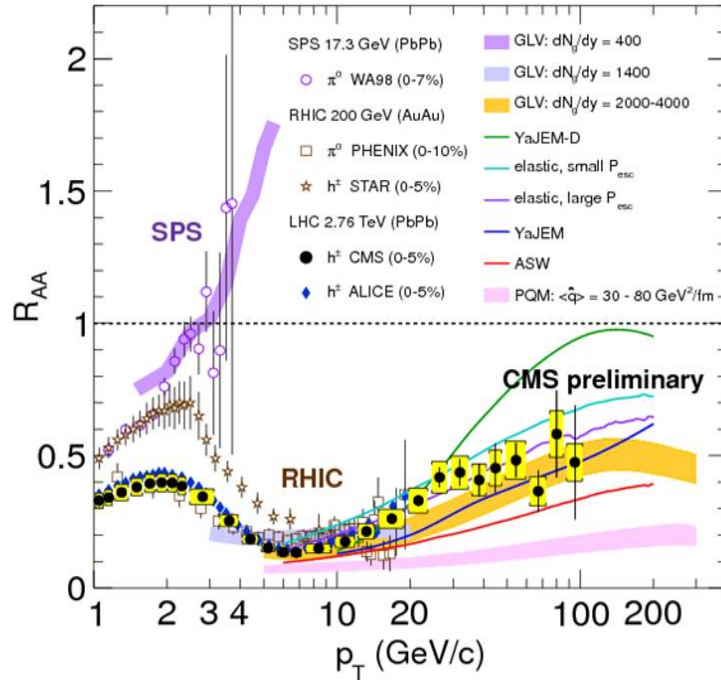


FIGURE 1.6: The nuclear modification factor R_{AA} in central heavy-ion collisions at three different center-of-mass energies, as a function of p_T , for neutral pions and charged hadrons, compared to several theoretical predictions. Figure taken from [33].

In the range $p_T = 5\text{--}10$ GeV/ c , the suppression at LHC is stronger than that observed at RHIC. Beyond 10 GeV/ c , R_{AA} shows a rising trend, but at p_T as large as 100 GeV the nuclear suppression factor is still 0.5–0.6.

1.5 Anisotropic plasma and role of instabilities

The quark-gluon plasma occurs as a transient state in relativistic heavy-ion collisions, see *e.g.* [34]. At the early stage of the collisions, the momenta of produced partons are mostly along the beam, which means that the characteristic longitudinal momentum is much bigger than the transverse one. The momentum distribution is thus strongly elongated along the beam - it is prolate. The distribution evolves - mostly due to the free streaming - and, as discussed in *e.g.* [35], it becomes squeezed along the beam or oblate with the characteristic transverse momentum bigger than typical longitudinal momenta. The system moves towards an isotropic local equilibrium state but does not actually reach it because of viscous effects [36, 37].

Using theoretical methods known from the electron-ion plasma extended to the quark-gluon plasma transport theory, one can study chromodynamic collective modes in anisotropic

QGP [38]. Then, one proofs, assuming that the quark-gluon plasma is weakly coupled, an existence of the instability analogous to the so-called Weibel or filamentation instability. Weibel showed [39] that the unstable transverse mode exists in electrodynamic plasma with the two-stream momentum distribution and he derived its growth rate in linear response theory. The instability generates strong magnetic field which was confirmed experimentally [39]. As shown in Chapter 2 the filamentation mode exists not only in the two-stream plasma but even an infinitesimally small anisotropy is sufficient to cause the instability.

The growth rate of the unstable transverse mode is parametrically gT for a sufficiently anisotropic momentum distribution [40–45]. The parameter T is here not the temperature but rather a typical momentum of plasma constituents which in the equilibrium plasma coincides with the temperature. Let us note that the characteristic rate of binary parton-parton collisions varies from g^4T to g^2T depending whether the collision is *hard* or *soft* with the typical momentum transfer of order T or gT [46]. Therefore, the growth of unstable modes is much faster than the parton-parton collisions if $g \ll 1$. This fact has two important consequences. First of all, it guarantees a very existence of the unstable modes - if the collisions are faster than the mode growth, the collisions actually prevent the mode growth. The fact that the instabilities are faster than the collisions also makes the instabilities important in the process of system's equilibration.

As mentioned in the Chapter 1.4, a hydrodynamic description of relativistic heavy-ion collisions requires a local thermal equilibrium and experimental data on the particle spectra and elliptic flow suggest that the matter produced in heavy-ion collision reaches the thermal equilibrium in a very short time, as short as 1 fm/c [30]. Fast equilibration is naturally explained by the assumption that the quark-gluon plasma is strongly coupled [47], as the relaxation time, which is proportional to g^n with $n = 2 \div 4$, is then very short. But one rather expects that, due to extremely high energy density at the collision early stage, the asymptotic freedom regime of QCD is then reached. In this case, the quark-gluon plasma is weakly coupled. So, one asks whether the weakly interacting plasma may equilibrate within 1 fm/c.

To thermalize a system, a few hard collisions of momentum transfer of order T are needed or many collisions of smaller momentum transfer. The calculations performed within the 'bottom-up' thermalization scenario [48], where not only binary collisions but also the particle production and absorption ($2 \leftrightarrow 3$) are taken into account [49], give an equilibration time of at least 2.6 fm/c [50] which is rather too long. However, the instabilities, which are generated in anisotropic plasma, speed-up the equilibration of the quark-gluon plasma. They help to isotropize the momentum distribution due to the Lorentz force, which acts on the plasma constituents, and due to the momentum carried

directly by the unstable modes. The instabilities thus play a crucial role in the early stage nonequilibrium plasma.

1.6 The aim of the thesis and its outline

The aim of this thesis is to consider a behaviour of high-energy parton which flies across an anisotropic unstable plasma, and calculate an energy transfer between the parton and the medium. We want to know whether the energy, which is lost in a short transient phase of non-equilibrium unstable plasma, can give a sizeable contribution to the total energy loss of high-energy parton in relativistic heavy-ion collisions. The problem of the energy loss is formulated here as an initial value problem and it crucially depends on a spectrum of collective excitations in the plasma. Therefore, after a general introduction to the physics of quark gluon plasma, we submit in Chapter 2 a systematic analysis of collective modes in anisotropic plasma.

We start with a definition of the general dispersion equation of plasmons - gluon collective modes which is discussed and solved later on. Our analysis of the collective modes begins with the isotropic plasma in Sec. 2.2 which provides a reference for all other cases. Section 2.3 is devoted to the two-stream system where spectrum of plasmons is found in a closed analytic form for any orientation of the wave vector. In Sec. 2.4 we discuss the anisotropic momentum distributions which is obtained by deforming the isotropic one. Section 2.5 is dedicated to the weakly anisotropic plasma where the spectrum of collective modes changes qualitatively when compared to the isotropic plasma. In particular, instabilities occur. However, the calculations are almost completely analytical when the anisotropy is weak, which makes this situation important and interesting. In Sec. 2.6 we present numerically obtained dispersion relations for finite anisotropy. The next two Secs. 2.7 and 2.8 deal with the extremely prolate - infinitely elongated in one direction, and extremely oblate - infinitely squeezed in one direction, respectively, which again can be treated analytically to some extent.

The results which are given in Chapter 2 are used in Chapter 3, where we first derive the general energy loss formula of a relativistic classical parton in an unstable QCD plasma which depends on the initial conditions, see Section 3.1. Our analysis of energy loss starts with the equilibrium limit which is discussed in Sec. 3.2. The dependence on initial conditions drops out, and our expression reduces to the familiar equilibrium result. In Sec. 3.3 we introduce two classes of initial conditions that we will apply later on to unstable plasmas. In Sec. 3.4 we study the effect of self-interaction which needs to be subtracted from the energy loss formula. We develop further our formalism in Sec. 3.6, where we also apply it to the extremely prolate and oblate systems. In Sec. 3.4 we present our numerical results on the energy loss in unstable plasma. Our findings are

summarized and the outlook is presented in Chapter 4.

In Appendix [A.1](#) we remind the reader how the dispersion equation of plasma waves is derived in classical electrodynamics. Appendix [A.2](#) presents some useful results for the components of the anisotropic polarisation tensor. Appendix [A.3](#) shows that according to our formula the energy loss is real as it should be. The temporal axial gauge is compared to the Feynman-Lorentz gauge in Appendix [A.4](#).

Chapter 2

Collective modes

In this part of the thesis, based on our original papers [51, 52], we analyze collective modes of quark-gluon plasma which will play the crucial role in the computation of energy loss presented in Chapter 3.

A spectrum of collective excitations of quark-gluon plasma is very rich. There are collective modes that correspond to plasma particles, that is, quarks and (transverse) gluons, and there are also collective excitations which are genuine many-body phenomena like longitudinal gluon modes (longitudinal plasmons) and phonons. We focus here on longitudinal and transverse gluon collective modes which we all call *plasmons*. A mode is called longitudinal when the electric field is parallel to the wave vector \mathbf{k} ($\mathbf{E} \parallel \mathbf{k}$), while in the second case the field is perpendicular to \mathbf{k} ($\mathbf{E} \perp \mathbf{k}$), and the mode is called transverse. Since the electric field plays a key role in the generation of longitudinal modes, they are also called electric modes, while the transverse modes are called magnetic modes.

Classically plasmons correspond to plasma oscillations or plasma waves. A system, which is on average spatially homogeneous and neutral, fluctuates causing an appearance of local charges and currents generating electric and magnetic fields. The fields in turn interact with charged plasma particles and the plasma experiences a collective motion.

In the early stage of heavy-ion collision the parton momentum distribution is elongated in the beam direction $\langle |p_L| \rangle \gg \langle p_T \rangle$ but due to rapid longitudinal expansion the plasma cools faster in the longitudinal direction leading to $\langle |p_L| \rangle \ll \langle p_T \rangle$. Such a momentum anisotropy leads to collective modes having characteristic behaviour very distinct from what happens in isotropic plasma which has been extensively studied, see *e.g.* the handbook [53], and which we analyze here as a reference point.

In the weakly-coupled quark-gluon plasma a presence of momentum anisotropy induces unstable plasma modes, the amplitudes of which exponentially grow in time. When

the instability occurs, a kinetic energy of plasma particles is converted to an energy of chromodynamic field. This process speeds up an equilibration of the system and therefore it plays an important role in the dynamical evolution of a quark-gluon plasma, as mentioned in Sec. 1.5.

We start the discussion of anisotropic systems with a momentum distribution with more than one maximum - the two-stream system. Such a distribution is common in the electron-ion plasma, but in relativistic heavy-ion collisions the momentum distribution is expected to be decreasing in every direction and the two-stream distribution is rather inappropriate. However, it can be treated as a toy model of unstable QGP.

Further on, we study a quark-gluon plasma with the momentum distribution introduced by Romatschke and Strickland [43, 54] who parameterized an anisotropic momentum distribution by deforming an isotropic one. This distribution, which is appropriate for partons produced in relativistic heavy-ion collisions, has been used to study various aspects of quark-gluon plasma, see *e.g.* [55–59]. We will use the Romatschke-Strickland momentum distribution to compute the energy loss of a highly energetic parton traversing an unstable QGP, which, as will be seen, depends crucially on the spectrum of collective excitations. Therefore, a complete information about the collective modes is important for the energy-loss calculations.

Our analysis of plasmons is methodologically very close to the study by Romatschke and Strickland [43, 54], but they mostly focused on unstable modes, and did not pay much attention to the stable excitations. The stable modes manifest an interesting property of *mode coupling* which is well known in the electron plasma, however it was not discussed in the context of QGP. It should also be noted that the stable modes, in contrast to the unstable modes, are not limited to small domains of wave vectors. So their influence on the system's dynamics may be very important.

There is a small number of configurations when a complete and exact spectrum of collective modes can be obtained analytically. So, we often use numerical methods to obtain the dispersion relations. If the dispersion equation has to be solved numerically we also solve it analytically by looking at certain special cases such as large or small anisotropy, small wave vector, or the wave vector (almost) parallel or perpendicular to the anisotropy direction to check our numerical result.

2.1 Formulation of the problem

In this section we present the general dispersion equation which depends on the momentum distribution of plasma constituent. It will be solved in the subsequent sections for different plasma momentum distributions.

A dispersion equation for plasma collective excitations can be obtained in two ways which are rather different at first glance. These equations are the conditions for existence of solutions of a homogeneous equation of motion. In the case of QGP the equations of motion are the Yang-Mills equations of the chromodynamic field. In kinetic theory, the equations of motion depend on the chromodynamic permeability, or chromodielectric tensor, which contains an effect of the plasma medium. In a quantum field theory, dynamical information about the medium is contained in the polarization tensor which enters the gluon propagator, and the dispersion equation is just the equation that determines poles of the gluon propagator. A character of the approach - whether it is classical or quantum mechanical - depends on how the polarization tensor or chromodynamic permeability are calculated. When using kinetic theory, one typically applies a linear response analysis of classical (or semiclassical) transport equations. Within the quantum field theory formulation, the standard calculation use a perturbative method within the hard loop approximation. These two approaches are fully equivalent (the latter is essentially classical in spite of its quantum-field-theory formulation) and the chromodielectric tensor can be expressed directly in terms of the polarization tensor and *vice versa*. The only quantum effects that are taken into account are those that are due to the quantum statistics of the plasma constituents. The equivalence of the two approaches was first discovered for the case of equilibrium plasma, see the reviews [60, 61], and the result was later generalized to non-equilibrium systems [62, 63].

2.1.1 General dispersion equations

In Appendix A.1 we give a derivation of plasmon dispersion equation in terms of classical electrodynamics. A dispersion equation for gluon collective excitations in the hard-loop approximation is fully analogous:

$$\det[\Sigma(\omega, \mathbf{k})] = 0, \quad (2.1.1)$$

where matrix $\Sigma(\omega, \mathbf{k})$ is defined as:

$$\Sigma^{ij}(\omega, \mathbf{k}) \equiv -\mathbf{k}^2 \delta^{ij} + k^i k^j + \omega^2 \epsilon^{ij}(\omega, \mathbf{k}), \quad (2.1.2)$$

here ω is the frequency, \mathbf{k} denotes the wave vector and $\varepsilon^{ij}(\omega, \mathbf{k})$ is the chromodielectric tensor. For a locally colourless anisotropic plasma in the collisionless limit the dielectric tensor equals

$$\varepsilon^{ij}(\omega, \mathbf{k}) = \delta^{ij} + \frac{g^2}{2\omega} \int \frac{d^3p}{(2\pi)^3} \frac{v^i}{\omega - \mathbf{v} \cdot \mathbf{k} + i0^+} \left(\left(1 - \frac{\mathbf{k} \cdot \mathbf{v}}{\omega}\right) \delta^{jk} + \frac{v^j k^k}{\omega} \right) \nabla_p^k f(\mathbf{p}), \quad (2.1.3)$$

where \mathbf{p} and $\mathbf{v} \equiv \mathbf{p}/|\mathbf{p}|$ are the momentum and velocity of a *massless* parton, and $f(\mathbf{p})$ is the effective parton distribution function. For the $SU(N_c)$ gauge group $f(\mathbf{p}) = n(\mathbf{p}) + \bar{n}(\mathbf{p}) + 2N_c n_g(\mathbf{p})$, where $n(\mathbf{p})$, $\bar{n}(\mathbf{p})$, $n_g(\mathbf{p})$ are the distribution functions of quarks, antiquarks and gluons of a single colour component. We note that the chromodielectric tensor does not carry any colour indices, as the state corresponding to the momentum distribution $f(\mathbf{p})$ is assumed to be colourless. The $i0^+$ prescription makes the Fourier transformed dielectric tensor $\varepsilon^{ij}(t, \mathbf{r})$ vanish for $t < 0$, which is required by causality. In kinetic theory, the infinitesimal quantity $i0^+$ can be treated as a remnant of interparticle collisions. After performing the partial integration, the chromodielectric tensor (2.1.3) can be rewritten as

$$\varepsilon^{ij}(\omega, \mathbf{k}) = \delta^{ij} - \frac{g^2}{2\omega^2} \int \frac{d^3p}{(2\pi)^3} \frac{f(\mathbf{p})}{|\mathbf{p}|} \left[\delta^{ij} + \frac{k^i v^j + v^i k^j}{\omega - \mathbf{v} \cdot \mathbf{k} + i0^+} + \frac{(\mathbf{k}^2 - \omega^2) v^i v^j}{(\omega - \mathbf{v} \cdot \mathbf{k} + i0^+)^2} \right], \quad (2.1.4)$$

which is often more convenient than the expression (2.1.3).

In the field theory formulation, where collective modes are determined by a location of a poles of the propagator, the matrix $\Sigma^{ij}(\omega, \mathbf{k})$ defined by Eq. (2.1.2) equals the inverse *retarded* gluon propagator in the temporal axial gauge ($A^0 = 0$). The dielectric tensor $\varepsilon^{ij}(\omega, \mathbf{k})$ is related to the retarded gluon polarization tensor $\Pi^{ij}(\omega, \mathbf{k})$ as

$$\varepsilon^{ij}(\omega, \mathbf{k}) = \delta^{ij} - \frac{1}{\omega^2} \Pi^{ij}(\omega, \mathbf{k}). \quad (2.1.5)$$

The polarization tensor carries Lorentz indices ($\mu, \nu = 0, 1, 2, 3$) which label coordinates in Minkowski space (and not Cartesian indices ($i, j = 1, 2, 3$)). The components of the polarization tensor, which are not determined by Eq. (2.1.5), can be reconstructed from the transversality condition $k_\mu \Pi^{\mu\nu}(k) = 0$ with $k^\mu = (\omega, \mathbf{k})$, which is required by gauge invariance.

The solutions $\omega(\mathbf{k})$ of Eq. (2.1.1), which represent plasmons, are, in general, complex but the wave vector \mathbf{k} is assumed to be real. As it was mentioned on the beginning of this Chapter, we can distinguish the *transverse* and *longitudinal* plasmons. The transverse modes correspond to oscillations of current, and the longitudinal ones to oscillations of charge density. A mode is called *unstable* if $\Im\omega(\mathbf{k}) > 0$, because the amplitude $e^{\Im\omega(\mathbf{k})t}$ grows exponentially in time. When $\Im\omega(\mathbf{k}) \leq 0$, the mode is stable and it is damped

if $\Im\omega(\mathbf{k}) < 0$, as its amplitude decays exponentially in time. The mode is called overdamped, when additionally it is pure imaginary.

Using kinetic theory in the linear response regime, or equivalently working in the hard loop approximation, the dielectric and polarization tensors have the same form for chromodynamic and electrodynamic plasmas of massless constituents, see *e.g.* [38]. The spectrum of plasmons is also qualitatively the same in chromodynamic and electrodynamic plasmas. Therefore, we often use the more familiar electromagnetic terminology to discuss our results.

2.1.2 Decomposition of the Σ matrix

To solve the general dispersion equation (2.1.1), one must either find zeros of the determinant of the matrix Σ (2.1.2), or invert Σ and find the poles of the inverted matrix. We will follow the second strategy.

The first step is to decompose the matrix using a complete set of projection operators for an anisotropic system in which there is only one preferred direction given by the vector \mathbf{n} . In the two-stream system, the vector \mathbf{n} is identified with the stream velocity \mathbf{u} . Consequently $\mathbf{u}^2 \leq 1$. In case of momentum distribution obtained by deforming the isotropic one, $\mathbf{n} = 1$. We know that in isotropic plasmas, an arbitrary tensor depends only on the wave vector \mathbf{k} , and can be decomposed into two components, which are transverse and longitudinal with respect to \mathbf{k} . An arbitrary symmetric tensor, which depends on two vectors, can be decomposed in terms of four projection operators. Following [43, 64], we introduce the vector \mathbf{n}_T transverse to \mathbf{k} , which equals

$$n_T^i = \left(\delta^{ij} - \frac{k^i k^j}{\mathbf{k}^2} \right) n^j, \quad (2.1.6)$$

and define four projectors

$$\begin{aligned} A^{ij}(\mathbf{k}) &= \delta^{ij} - \frac{k^i k^j}{\mathbf{k}^2}, & B^{ij}(\mathbf{k}) &= \frac{k^i k^j}{\mathbf{k}^2}, \\ C^{ij}(\mathbf{k}, \mathbf{n}) &= \frac{n_T^i n_T^j}{\mathbf{n}_T^2}, & D^{ij}(\mathbf{k}, \mathbf{n}) &= k^i n_T^j + k^j n_T^i, \end{aligned}$$

which obey the following relations

$$\begin{aligned}
 AA &= A, & AB &= 0, & AC &= C, & (AD)^{ij} &= n_T^i k^j, \\
 BA &= 0, & BB &= B, & BC &= 0, & (BD)^{ij} &= k^i n_T^j, \\
 CA &= C, & CB &= 0, & CC &= C, & (CD)^{ij} &= n_T^i k^j, \\
 (DA)^{ij} &= k^i n_T^j, & (DB)^{ij} &= n_T^i k^j, & (DC)^{ij} &= k^i n_T^j, & DD &= n_T^2 \mathbf{k}^2 (B + C).
 \end{aligned} \tag{2.1.7}$$

Using this projector basis, the inverse propagator can be decomposed as

$$\Sigma^{ij} = a A^{ij} + b B^{ij} + c C^{ij} + d D^{ij}, \tag{2.1.8}$$

and the coefficients a , b , c and d can be found from the equations

$$\begin{aligned}
 k^i \Sigma^{ij} k^j &= \mathbf{k}^2 b, & n_T^i \Sigma^{ij} n_T^j &= \mathbf{n}_T^2 (a + c), \\
 n_T^i \Sigma^{ij} k^j &= \mathbf{n}_T^2 \mathbf{k}^2 d, & \text{Tr} \Sigma &= 2a + b + c.
 \end{aligned} \tag{2.1.9}$$

With the help of the relations (2.1.7), we invert the matrix (2.1.8) and obtain

$$(\Sigma^{-1})^{ij} = \frac{1}{a} A^{ij} + \frac{-a(a+c) B^{ij} + (-d^2 \mathbf{k}^2 \mathbf{n}_T^2 + bc) C^{ij} + ad D^{ij}}{a(d^2 \mathbf{k}^2 \mathbf{n}_T^2 - b(a+c))}. \tag{2.1.10}$$

The inverse propagator can be written in terms of the polarization tensor as

$$(\Delta^{-1})^{ij}(\omega, \mathbf{k}) = \Sigma^{ij}(\omega, \mathbf{k}) = \delta^{ij}(\omega^2 - \mathbf{k}^2) + k^i k^j - \Pi^{ij}(\omega, \mathbf{k}), \tag{2.1.11}$$

and the polarization tensor is decomposed as

$$\Pi^{ij}(\omega, \mathbf{k}) = \alpha(\omega, \mathbf{k}) A^{ij} + \beta(\omega, \mathbf{k}) B^{ij} + \gamma(\omega, \mathbf{k}) C^{ij} + \delta(\omega, \mathbf{k}) D^{ij}. \tag{2.1.12}$$

The coefficients $\alpha, \beta, \gamma, \delta$ are related to the functions a, b, c, d from Eq. (2.1.8) as

$$a(\omega, \mathbf{k}) = \omega^2 - \mathbf{k}^2 - \alpha(\omega, \mathbf{k}), \tag{2.1.13}$$

$$b(\omega, \mathbf{k}) = \omega^2 - \beta(\omega, \mathbf{k}), \tag{2.1.14}$$

$$c(\omega, \mathbf{k}) = -\gamma(\omega, \mathbf{k}), \tag{2.1.15}$$

$$d(\omega, \mathbf{k}) = -\delta(\omega, \mathbf{k}). \tag{2.1.16}$$

Inverting the matrix (2.1.11), the propagator is written

$$\Delta^{ij} = (A^{ij} - C^{ij}) \Delta_A + ((\omega^2 - \mathbf{k}^2 - \alpha - \gamma) B^{ij} - (\beta - \omega^2) C^{ij} + \delta D^{ij}) \Delta_G. \tag{2.1.17}$$

The dispersion equations, which are obtained from the poles of the propagator (2.1.10) or (2.1.17), are

$$\Delta_A^{-1}(\omega, \mathbf{k}) = a(\omega, \mathbf{k}) = \omega^2 - \mathbf{k}^2 - \alpha(\omega, \mathbf{k}) = 0, \quad (2.1.18)$$

$$\frac{1}{\omega^2} \Delta_G^{-1}(\omega, \mathbf{k}) = 0, \quad (2.1.19)$$

where

$$\begin{aligned} \Delta_G^{-1}(\omega, \mathbf{k}) &= b(\omega, \mathbf{k})(a(\omega, \mathbf{k}) + c(\omega, \mathbf{k})) - \mathbf{k}^2 \mathbf{n}_T^2 d^2(\omega, \mathbf{k}) \\ &= (\omega^2 - \beta(\omega, \mathbf{k}))(\omega^2 - \mathbf{k}^2 - \alpha(\omega, \mathbf{k}) - \gamma(\omega, \mathbf{k})) - \mathbf{k}^2 \mathbf{n}_T^2 \delta^2(\omega, \mathbf{k}). \end{aligned} \quad (2.1.20)$$

The factor ω^{-2} is introduced in Eq. (2.1.19) to remove the trivial $\omega = 0$ solutions.

2.2 Isotropic plasma

In this section we discuss the dispersion relations of a plasma system which is isotropic but not necessarily in equilibrium. Plasmons in isotropic plasmas are discussed in textbooks, see *e.g.* [53, 65], and we include the discussion for the sake of completeness, and as a reference for our analysis of anisotropic plasmas.

In isotropic plasmas, the vector \mathbf{n} drops out, and the propagator and its inverse can be written in terms of the two projection operators A and B

$$\Sigma^{ij} = a A^{ij} + b B^{ij}, \quad (\Sigma^{-1})^{ij} = \Delta^{ij} = \frac{1}{a} A^{ij} + \frac{1}{b} B^{ij}. \quad (2.2.1)$$

The dispersion relations are $a(\omega, \mathbf{k}) = 0$ and $\omega^{-2}b(\omega, \mathbf{k}) = 0$, where, we have introduced the factor ω^{-2} to remove trivial zero solutions.

Using the decomposition (2.2.1), one derives the coefficients α_{iso} and β_{iso} which have the form

$$\alpha_{\text{iso}}(\omega, \mathbf{k}) = \frac{m^2 \omega^2}{2k^2} \left[1 - \left(\frac{\omega}{2k} - \frac{k}{2\omega} \right) \ln \left(\frac{\omega + k + i0^+}{\omega - k + i0^+} \right) \right], \quad (2.2.2)$$

$$\beta_{\text{iso}}(\omega, \mathbf{k}) = -\frac{m^2 \omega^2}{k^2} \left[1 - \frac{\omega}{2k} \ln \left(\frac{\omega + k + i0^+}{\omega - k + i0^+} \right) \right], \quad (2.2.3)$$

where m is the Debye mass defined as

$$m^2 = \frac{g^2}{2\pi^2} \int_0^\infty dp p f^{\text{iso}}(p). \quad (2.2.4)$$

If one uses the general decomposition (2.1.12), one simply finds the same result for α_{iso} and β_{iso} , and $\gamma_{\text{iso}} = \delta_{\text{iso}} = 0$. The $i0^+$ prescription is needed only if $\omega, k \in \mathbb{R}$ and $\omega^2 \leq k^2$. When ω and k are both real, the coefficients can be written as

$$\alpha_{\text{iso}}(\omega, \mathbf{k}) = \frac{m^2 \omega^2}{2k^2} \left[1 - \left(\frac{\omega}{2k} - \frac{k}{2\omega} \right) \left(\ln \left| \frac{k + \omega}{k - \omega} \right| - i\pi \Theta(k - \omega) \right) \right], \quad (2.2.5)$$

$$\beta_{\text{iso}}(\omega, \mathbf{k}) = -\frac{m^2 \omega^2}{k^2} \left[1 - \frac{\omega}{2k} \left(\ln \left| \frac{k + \omega}{k - \omega} \right| - i\pi \Theta(k - \omega) \right) \right]. \quad (2.2.6)$$

For $k^2 \ll \omega^2$, the logarithm in Eqs. (2.2.2), (2.2.3) can be expanded in powers of k/ω and the functions $\alpha_{\text{iso}}(\omega, \mathbf{k})$ and $\beta_{\text{iso}}(\omega, \mathbf{k})$ are approximated as

$$\alpha_{\text{iso}}(\omega, \mathbf{k}) = \frac{m^2}{3} \left[1 + \frac{k^2}{5\omega^2} + \mathcal{O}\left(\frac{k^4}{\omega^4}\right) \right], \quad (2.2.7)$$

$$\beta_{\text{iso}}(\omega, \mathbf{k}) = \frac{m^2}{3} \left[1 + \frac{3k^2}{5\omega^2} + \mathcal{O}\left(\frac{k^4}{\omega^4}\right) \right]. \quad (2.2.8)$$

The dispersion equations for isotropic plasma are given by Eqs. (2.1.18), (2.1.19) together with the formulae (2.2.2), (2.2.3) and read

$$\omega^2 - \mathbf{k}^2 - \alpha_{\text{iso}}(\omega, \mathbf{k}) = 0, \quad (2.2.9)$$

$$\frac{1}{\omega^2} (\omega^2 - \beta_{\text{iso}}(\omega, \mathbf{k})) = 0. \quad (2.2.10)$$

These equations describe transverse and longitudinal plasmons, respectively. Expressing the coefficients α_{iso} , β_{iso} through the transverse and longitudinal components of the dielectric tensor as

$$\alpha_{\text{iso}}(\omega, \mathbf{k}) = \omega^2(1 - \varepsilon_T(\omega, \mathbf{k})), \quad \beta_{\text{iso}}(\omega, \mathbf{k}) = \omega^2(1 - \varepsilon_L(\omega, \mathbf{k})), \quad (2.2.11)$$

the dispersion equations (2.2.9), (2.2.10) can be written in the form

$$\omega^2 \varepsilon_T(\omega, \mathbf{k}) - \mathbf{k}^2 = 0, \quad \varepsilon_L(\omega, \mathbf{k}) = 0, \quad (2.2.12)$$

which is well known in classical electrodynamics. We note that in the vacuum, where $\varepsilon_{T,L} = 1$, Eqs. (2.2.12) give two transverse modes $\omega = \pm|\mathbf{k}|$ and no longitudinal one. We also note that not having the multiplier $1/\omega^2$ in dispersion equation (2.1.19), the equation of longitudinal modes, which is $\omega^2 \varepsilon_L(\omega, \mathbf{k}) = 0$, has two trivial solutions $\omega = 0$ even in the vacuum.

We note that when counting the number of solutions, one should be careful to specify the form of the dispersion equation under consideration. If one looks at the determinant of the inverse propagator, as in Eq. (2.1.1), the number of solutions is 8 and not 4. This happens because there are two trivial $\omega = 0$ solutions and there are two possible orientations of the chromoelectric vector $\mathbf{E}(\omega, \mathbf{k})$ which are transverse to \mathbf{k} . Therefore, the transverse mode appears twice. For an isotropic system one can see this directly from the matrix $\Sigma(\omega, \mathbf{k})$. Choosing $\mathbf{k} = (k, 0, 0)$ we have

$$\Sigma(\omega, \mathbf{k}) = \begin{bmatrix} \omega^2 - \beta_{\text{iso}}(\omega, \mathbf{k}) & 0 & 0 \\ 0 & \omega^2 - k^2 - \alpha_{\text{iso}}(\omega, \mathbf{k}) & 0 \\ 0 & 0 & \omega^2 - k^2 - \alpha_{\text{iso}}(\omega, \mathbf{k}) \end{bmatrix}. \quad (2.2.13)$$

To clarify a physical character of the solutions, one should remember that the dispersion equation (2.1.1) comes from the equation of motion $\Sigma^{ij}(\omega, \mathbf{k})E^j(\omega, \mathbf{k}) = 0$. Therefore, the component $\Sigma^{xx} = \omega^2 - \beta_{\text{iso}}$ acts on E^x and thus the solution of Eq. (2.2.10) represents, as expected, the longitudinal mode. The components Σ^{yy} , Σ^{zz} act on E^y , E^z , respectively, and thus the solutions of Eq. (2.2.9) correspond to two transverse modes.

Using the approximations (2.2.7), (2.2.8), the dispersion equations can be solved analytically in the long wavelength limit ($\omega^2 \gg k^2$) and one obtains

$$\omega_T^2(\mathbf{k}) = \frac{m^2}{3} + \frac{6}{5}k^2 + \mathcal{O}\left(\frac{k^4}{m^2}\right), \quad (2.2.14)$$

$$\omega_L^2(\mathbf{k}) = \frac{m^2}{3} + \frac{3}{5}k^2 + \mathcal{O}\left(\frac{k^4}{m^2}\right). \quad (2.2.15)$$

The frequency at $k = 0$ is the lowest possible frequency of the plasma wave and is known as the *plasma frequency* (usually denoted as ω_p). For both transverse and longitudinal modes in isotropic plasma, we have $\omega_p = m/\sqrt{3}$. The equality of the frequency for transverse and longitudinal modes results from the fact that no direction can be distinguished in an isotropic medium when $\mathbf{k} = 0$.

The dispersion equations can also be solved analytically in the short wavelength limit ($k^2 \gg m^2$) and the dispersion relations are

$$\omega_T^2(\mathbf{k}) \approx \frac{m^2}{2} + k^2, \quad (2.2.16)$$

$$\omega_L^2(\mathbf{k}) \approx k^2 \left(1 + 4e^{-\frac{2k^2}{m^2} - 2}\right). \quad (2.2.17)$$

Thus, with increasing momentum the transverse branch becomes that of the relativistic particle with an effective mass $m_\infty = m/\sqrt{2}$. The longitudinal branch approaches the light cone exponentially.

Numerical results for the transverse and longitudinal dispersion relations for arbitrary k are shown in Fig. 2.1. The curves stay above the light cone and consequently there is no Landau damping, as the phase velocity of the plasma waves exceeds the speed of light. The longitudinal mode approaches the light cone as $k \rightarrow \infty$ in agreement with the formula (2.2.17).

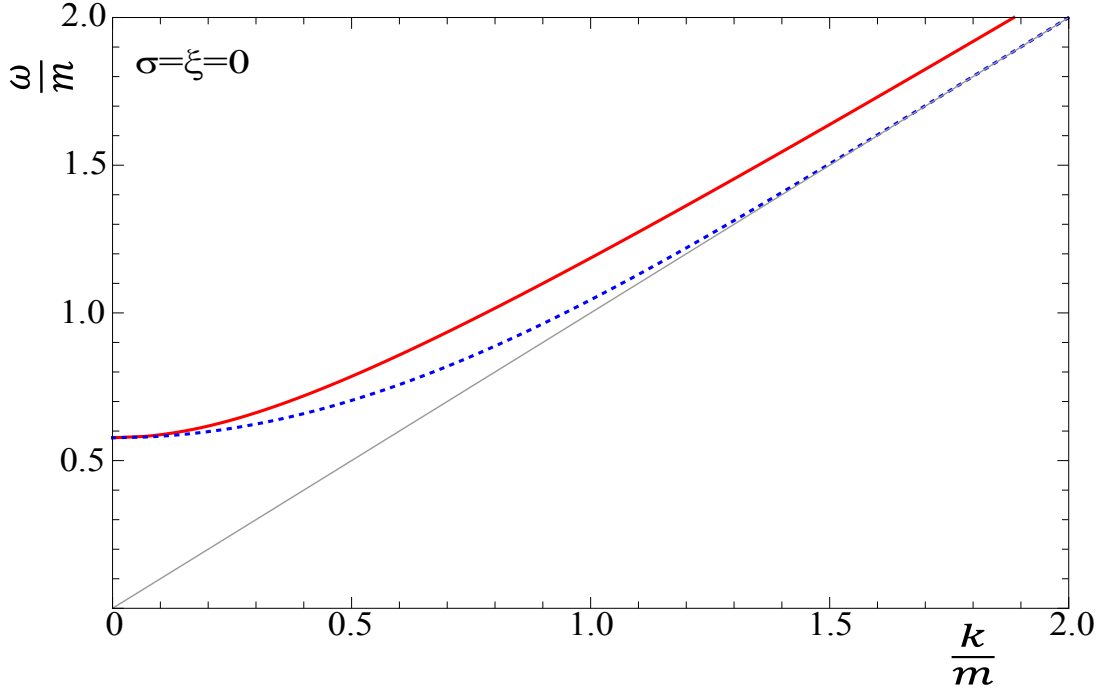


FIGURE 2.1: Dispersion curves of transverse (solid red) and longitudinal (dotted blue) plasmons in isotropic plasma.

2.3 Two stream system

The dielectric tensor given by Eq. (2.1.3) or (2.1.4) is fully determined by the momentum distribution of plasma constituents. The distribution function of the two-stream system is assumed to be:

$$f(\mathbf{p}) = (2\pi)^3 n \left[\delta^{(3)}(\mathbf{p} - \mathbf{q}) + \delta^{(3)}(\mathbf{p} + \mathbf{q}) \right], \quad (2.3.1)$$

where n is the effective parton density in a single stream. The distribution (2.3.1) should be treated as an idealization of the two-peak distribution where the particles have momenta close to \mathbf{q} or $-\mathbf{q}$ but it is not required that the momenta are exactly \mathbf{q} or $-\mathbf{q}$.

Further one we use the same procedure of the inversion of the Σ matrix presented in Sec. 2.1.2, however we replace the vector \mathbf{n} , which determines the plasma anisotropy, by the vector \mathbf{u} which is the stream velocity. But there is one important difference: the vector \mathbf{u} , which is analogous to the vector \mathbf{n} , is not of unit length but $\mathbf{u}^2 \leq 1$.

The distribution function (2.3.1) substituted into Eq. (2.1.4) provides the dielectric tensor in the form

$$\begin{aligned} \varepsilon^{ij}(\omega, \mathbf{k}) = & \delta^{ij} \left(1 - \frac{\mu^2}{\omega^2} \right) + u^i u^j \frac{\mu^2}{\omega^2} \frac{(\omega^2 - \mathbf{k}^2)(\omega^2 + (\mathbf{k} \cdot \mathbf{u})^2)}{(\omega^2 - (\mathbf{k} \cdot \mathbf{u})^2)^2} \\ & - (k^i u^j + u^i k^j) \frac{\mu^2}{\omega^2} \frac{(\mathbf{k} \cdot \mathbf{u})}{\omega^2 - (\mathbf{k} \cdot \mathbf{u})^2}, \end{aligned} \quad (2.3.2)$$

where $\mu^2 \equiv g^2 n / E_{\mathbf{q}}$ is a parameter analogous to the Debye mass squared, and $\mathbf{u} \equiv \mathbf{q} / E_{\mathbf{q}}$ is the stream velocity. Since we consider the system of massless constituents the $E_{\mathbf{q}} = |\mathbf{q}|$ and $\mathbf{u}^2 = 1$. However, when the distribution (2.3.1) is treated as an approximation of the two-peak structure and partons have non-vanishing momenta perpendicular to the stream velocity, $E_{\mathbf{q}} \geq |\mathbf{q}|$ and $\mathbf{u}^2 \leq 1$. In the subsequent section where the special cases $(\mathbf{k} \cdot \mathbf{u}) = 0$ and $(\mathbf{k} \cdot \mathbf{u}) = \mathbf{k}^2 \mathbf{u}^2$ are discussed, we assume that $\mathbf{u}^2 \leq 1$.

Substituting the dielectric tensor expressed by Eq. (2.3.2) into the matrix sigma formula (2.1.2), we get the result:

$$\begin{aligned} \Sigma^{ij}(\omega, \mathbf{k}) \equiv & (\omega^2 - \mathbf{k}^2 - \mu^2) \delta^{ij} + k^i k^j - \frac{\mu^2 (\mathbf{k} \cdot \mathbf{u})}{\omega^2 - (\mathbf{k} \cdot \mathbf{u})^2} (k^i u^j + u^i k^j) \\ & - \frac{\mu^2 (\omega^2 + (\mathbf{k} \cdot \mathbf{u})^2) (\mathbf{k}^2 - \omega^2)}{(\omega^2 - (\mathbf{k} \cdot \mathbf{u})^2)^2} u^i u^j. \end{aligned} \quad (2.3.3)$$

Applying the decomposition (2.1.8) and solving the set of equations analogous to (2.1.9), one finds the coefficients a , b , c , d for two-stream system:

$$a(\omega, \mathbf{k}) = \omega^2 - \mu^2 - \mathbf{k}^2, \quad (2.3.4)$$

$$b(\omega, \mathbf{k}) = \omega^2 - \mu^2 - \frac{2\mu^2 (\mathbf{k} \cdot \mathbf{u})^2}{\omega^2 - (\mathbf{k} \cdot \mathbf{u})^2} - \frac{\mu^2 (\omega^2 + (\mathbf{k} \cdot \mathbf{u})^2) (\mathbf{k}^2 - \omega^2)}{(\omega^2 - (\mathbf{k} \cdot \mathbf{u})^2)^2} \frac{(\mathbf{k} \cdot \mathbf{u})^2}{\mathbf{k}^2}, \quad (2.3.5)$$

$$c(\omega, \mathbf{k}) = -\frac{\mu^2 (\omega^2 + (\mathbf{k} \cdot \mathbf{u})^2) (\mathbf{k}^2 - \omega^2)}{(\omega^2 - (\mathbf{k} \cdot \mathbf{u})^2)^2} \left(\mathbf{u}^2 - \frac{(\mathbf{k} \cdot \mathbf{u})^2}{\mathbf{k}^2} \right), \quad (2.3.6)$$

$$d(\omega, \mathbf{k}) = -\frac{\mu^2 (\mathbf{k} \cdot \mathbf{u})}{\omega^2 - (\mathbf{k} \cdot \mathbf{u})^2} - \frac{\mu^2 (\omega^2 + (\mathbf{k} \cdot \mathbf{u})^2) (\mathbf{k}^2 - \omega^2) (\mathbf{k} \cdot \mathbf{u})}{\mathbf{k}^2 (\omega^2 - (\mathbf{k} \cdot \mathbf{u})^2)^2}. \quad (2.3.7)$$

2.3.1 Special cases

We first consider two special limits which are quite simple to solve analytically. We analyze configuration when $\mathbf{k} \parallel \mathbf{u}$ ($\theta = 0^\circ$), then we discuss the limit $\mathbf{k} \perp \mathbf{u}$ ($\theta = 90^\circ$). This analysis is useful to make a bridge with our next investigations.

2.3.1.1 Special case: $\mathbf{k} \parallel \mathbf{u}$

When the decomposition (2.1.8) is used to invert the matrix Σ , the case $(\mathbf{k} \cdot \mathbf{u})^2 = \mathbf{k}^2 \mathbf{u}^2$ needs some care as then $\mathbf{u}_T = 0$. The fact that the vectors \mathbf{k} and \mathbf{u} are parallel to each other means that the matrix Σ actually depends on one vector only. Consequently, one needs only the matrices A and B to fully decompose Σ *i.e.*

$$\Sigma = a A + b B, \quad (2.3.8)$$

where the coefficients $a(\omega, \mathbf{k})$ and $b(\omega, \mathbf{k})$ are found from the equations

$$k^i \Sigma^{ij} k^j = \mathbf{k}^2 b, \quad \text{Tr} \Sigma = 2a + b.$$

The inverse matrix equals

$$\Sigma^{-1} = \frac{1}{a} A + \frac{1}{b} B. \quad (2.3.9)$$

For $(\mathbf{k} \cdot \mathbf{u})^2 = \mathbf{k}^2 \mathbf{u}^2$, the matrix Σ (2.1.2) equals

$$\Sigma^{ij}(\omega, \mathbf{k}) = (\omega^2 - \mu^2 - \mathbf{k}^2) \delta^{ij} + \left(1 - \frac{2\mu^2 \mathbf{u}^2}{\omega^2 - \mathbf{k}^2 \mathbf{u}^2} - \frac{\mu^2 \mathbf{u}^2 (\omega^2 + \mathbf{k}^2 \mathbf{u}^2) (\mathbf{k}^2 - \omega^2)}{\mathbf{k}^2 (\omega^2 - \mathbf{k}^2 \mathbf{u}^2)^2} \right) k^i k^j,$$

and the coefficients $a(\omega, \mathbf{k})$ and $b(\omega, \mathbf{k})$ are found to be

$$a(\omega, \mathbf{k}) = \omega^2 - \mu^2 - \mathbf{k}^2, \quad (2.3.10)$$

$$b(\omega, \mathbf{k}) = \omega^2 - \mu^2 - \frac{2\mu^2 \mathbf{k}^2 \mathbf{u}^2}{\omega^2 - \mathbf{k}^2 \mathbf{u}^2} - \frac{\mu^2 \mathbf{u}^2 (\omega^2 + \mathbf{k}^2 \mathbf{u}^2) (\mathbf{k}^2 - \omega^2)}{(\omega^2 - \mathbf{k}^2 \mathbf{u}^2)^2}. \quad (2.3.11)$$

The dispersion equation (2.1.18) $a(\omega, \mathbf{k}) = 0$ gives a quite simple solution which represents the transverse plasmon:

$$\omega_\alpha^2(k) = \mu^2 + k^2. \quad (2.3.12)$$

Instead of the second dispersion equation (2.1.20), we have the equation $b(\omega, \mathbf{k}) = 0$, which gives the longitudinal modes. With the coefficient $b(\omega, \mathbf{k})$ given by the formula

(2.3.11), the second dispersion equation is:

$$\omega^2 \left(\omega^4 - (2k^2u^2 + \mu^2(1 - u^2))\omega^2 + k^4u^4 - \mu^2k^2u^2(1 - u^2) \right) = 0, \quad (2.3.13)$$

which has two solutions:

$$\omega_{\pm}^2(k) = k^2u^2 + \frac{\lambda^2}{2} \pm \frac{\lambda}{2} \sqrt{8k^2u^2 + \lambda^2}, \quad (2.3.14)$$

where $\lambda \equiv \mu\sqrt{1 - u^2}$. As seen, $\omega_{+}^2(k)$ is always positive but $\omega_{-}^2(k)$ is negative for $k^2 < \frac{\lambda^2}{u^2}$. Then, we have the instability which is well known in plasma physics as the two-stream electrostatic instability. When $\mathbf{u}^2 \rightarrow 1$, the mode $\omega_{-}^2(k)$ becomes stable and $\omega_{-}^2(k) = \omega_{+}^2(k) = k^2$.

The solution (2.3.12) and (2.3.14) can be also easily found directly from the matrix Σ . Choosing $\mathbf{u} = (0, 0, u)$ and $\mathbf{k} = (0, 0, k)$ the matrix Σ is

$$\Sigma(\omega, \mathbf{k}) = \begin{bmatrix} \omega^2 - \mu^2 - k^2 & 0 & 0 \\ 0 & \omega^2 - \mu^2 - k^2 & 0 \\ 0 & 0 & \omega^2 - \mu^2 - \frac{2\mu^2k^2u^2}{\omega^2 - k^2u^2} - \frac{\mu^2(\omega^2 + k^2u^2)(k^2 - \omega^2)u^2}{(\omega^2 - k^2u^2)^2} \end{bmatrix}. \quad (2.3.15)$$

The equation $\det \Sigma = 0$ gives, as expected, the solutions (2.3.12) and (2.3.14) and the first one is doubled.

2.3.1.2 Special case: $\mathbf{k} \perp \mathbf{u}$

Let us now consider a situation when the angle between \mathbf{k} and \mathbf{u} - the θ angle - equals 90° . In the case $\mathbf{k} \cdot \mathbf{u} = 0$, we obtain the dispersion relation from the general dispersion equations (2.1.18), (2.1.19) with the coefficients (2.3.4)-(2.3.7), which are simplified to

$$a(\omega, \mathbf{k}) = \omega^2 - \mu^2 - k^2, \quad (2.3.16)$$

$$b(\omega, \mathbf{k}) = \omega^2 - \mu^2, \quad (2.3.17)$$

$$c(\omega, \mathbf{k}) = \frac{m^2(\omega^2 - k^2)u^2}{\omega^2}, \quad (2.3.18)$$

$$d(\omega, \mathbf{k}) = 0. \quad (2.3.19)$$

Then, the equation $a(\omega, \mathbf{k}) = 0$ gives

$$\omega_\alpha^2(k) = \mu^2 + k^2, \quad (2.3.20)$$

but the dispersion equation (2.1.19) reads

$$(\omega^2 - \mu^2)(\omega^2 - \mu^2 - k^2 + \frac{\mu^2(\omega^2 - k^2)u^2}{\omega^2}) = 0, \quad (2.3.21)$$

and it provides three solutions

$$\omega_0^2(k) = \mu^2, \quad \omega_\pm^2(k) = \frac{1}{2}(\lambda + k^2 \pm \sqrt{(\lambda + k^2)^2 + 4\mu^2 u^2 k^2}), \quad (2.3.22)$$

where, as previously, $\lambda \equiv \mu\sqrt{1 - u^2}$. So, there are three pairs of modes of the opposite sign.

To clarify a physical character of the solutions (2.3.20) and (2.3.22), we explicitly compute the matrix Σ assuming that $\mathbf{u} = (0, 0, u)$ and $\mathbf{k} = (k, 0, 0)$. Then, one finds

$$\Sigma(\omega, \mathbf{k}) = \begin{bmatrix} \omega^2 - \mu^2 & 0 & 0 \\ 0 & \omega^2 - \mu^2 - k^2 & 0 \\ 0 & 0 & \omega^2 - \mu^2 - k^2 + \frac{\mu^2(\omega^2 - k^2)u^2}{\omega^2} \end{bmatrix}, \quad (2.3.23)$$

and its determinant equals

$$\det[\Sigma(\omega, \mathbf{k})] = (\omega^2 - \mu^2)(\omega^2 - \mu^2 - k^2) \left(\omega^2 - \mu^2 - k^2 + \frac{\mu^2(\omega^2 - k^2)u^2}{\omega^2} \right). \quad (2.3.24)$$

The general dispersion equation (2.1.1), that is $\det\Sigma = 0$, gives, as expected, the solutions (2.3.22) and (2.3.20). The structure of the matrix (2.3.23) clearly shows that the mode $\omega_0(k)$ is longitudinal (the electric field is along the wave vector) and the remaining modes $\omega_\alpha(k), \omega_\pm(k)$ are transverse (the electric field is perpendicular to the wave vector). The solutions $\omega_\alpha^2(k), \omega_0^2(k)$ and $\omega_+^2(k)$, which are all positive, correspond to stable real modes while the solution $\omega_-^2(k)$, which is negative, represents two imaginary modes - the Weibel or filamentation unstable and overdamped modes. Let us also note that the solutions $\omega_0^2(k)$ and $\omega_+^2(k)$ cross each other at $k = \mu u / \sqrt{1 + u^2}$.

2.3.1.3 Pure longitudinal electric field

In the two-stream system, which has unstable longitudinal electric modes, the chromodynamic field can be dominated after a sufficiently long time by the longitudinal chromoelectric. That is why in this subsection we consider the case when $\mathbf{B}(\omega, \mathbf{k}) = 0$ and $\mathbf{E}(\omega, \mathbf{k}) = \mathbf{k}(\mathbf{k} \cdot \mathbf{E}(\omega, \mathbf{k}))/\mathbf{k}^2$, that is the electric field is purely longitudinal.

Then, the dispersion equation for purely longitudinal electric field is

$$\varepsilon_L(\omega, \mathbf{k}) = 0, \quad (2.3.25)$$

where the longitudinal chromoelectric field is defined as:

$$\varepsilon_L(\omega, \mathbf{k}) \equiv \varepsilon^{ij}(\omega, \mathbf{k}) \frac{k^i k^j}{\mathbf{k}^2}. \quad (2.3.26)$$

The next step is to calculate $\varepsilon_L(\omega, \mathbf{k})$ and solve the dispersion equation. The four roots of the dispersion equation (2.3.25) are

$$\begin{aligned} \omega_{\pm}^2(\mathbf{k}) = & \frac{1}{\mathbf{k}^2} \left[\mathbf{k}^2(\mathbf{k} \cdot \mathbf{u})^2 + 2\mu^2(\mathbf{k}^2 - (\mathbf{k} \cdot \mathbf{u})^2) \right. \\ & \left. \pm \mu \sqrt{2(\mathbf{k}^2 - (\mathbf{k} \cdot \mathbf{u})^2)(4\mathbf{k}^2(\mathbf{k} \cdot \mathbf{u})^2 + 4\mu^2(\mathbf{k}^2 - (\mathbf{k} \cdot \mathbf{u})^2))} \right]. \end{aligned} \quad (2.3.27)$$

It is easy to see that $0 < \omega_+(\mathbf{k}) \in \mathbb{R}$ for any \mathbf{k} . For $\mathbf{k}^2(\mathbf{k} \cdot \mathbf{u})^2 \geq 4\mu^2(\mathbf{k}^2 - (\mathbf{k} \cdot \mathbf{u})^2)$, the minus mode is also stable, $0 < \omega_-(\mathbf{k}) \in \mathbb{R}$, but for $\mathbf{k} \cdot \mathbf{u} \neq 0$ and $\mathbf{k}^2(\mathbf{k} \cdot \mathbf{u})^2 < 4\mu^2(\mathbf{k}^2 - (\mathbf{k} \cdot \mathbf{u})^2)$, one finds that $\omega_-(\mathbf{k})$ is imaginary which is the well-known two-stream electric instability.

2.3.2 General case

The dispersion equation for the A -modes (2.1.18) with the coefficient $a(\omega, \mathbf{k})$ given by Eq. (2.3.4) has the simple solution

$$\omega_\alpha^2(k) = \mu^2 + k^2. \quad (2.3.28)$$

Further on we discuss in full generality the dispersion equation (2.1.19), with the coefficients a, b, c, d given by the Eqs. (2.3.4)-(2.3.7). A crucial finding is that the ratio $\omega^2/(\omega^2 - (\mathbf{k} \cdot \mathbf{u})^2)^2$ factors out from the right hand side of Eq. (2.1.19). Consequently, we obtain a cubic dispersion equation

$$R_3 x^3 + R_2 x^2 + R_1 x + R_0 = 0, \quad (2.3.29)$$

where $x \equiv \omega^2$ and the coefficients R_0, R_1, R_2, R_3 are real numbers equal to

$$\begin{aligned} R_0 &= -((\mathbf{k} \cdot \mathbf{u})^2 + \mu^2 \mathbf{u}^2)(\mu^2(\mathbf{k} \cdot \mathbf{u})^2 + \mathbf{k}^2((\mathbf{k} \cdot \mathbf{u})^2 - \mu^2)), \\ R_1 &= (\mathbf{k} \cdot \mathbf{u})^2((\mathbf{k} \cdot \mathbf{u})^2 + 2\mathbf{k}^2 + \mu^2(1 + \mathbf{u}^2)) + \mu^2(1 - \mathbf{u}^2)(\mathbf{k}^2 + \mu^2), \\ R_2 &= -\mathbf{k}^2 - 2(\mathbf{k} \cdot \mathbf{u})^2 + \mu^2(-2 + \mathbf{u}^2), \\ R_3 &= 1. \end{aligned} \quad (2.3.30)$$

As well known, see *e.g.* [66], all three roots of a cubic equation can be found algebraically. Since the coefficients R_0, R_1, R_2, R_3 are real, the nature of roots is determined by the discriminant in the form:

$$\Delta = 18R_0R_1R_2R_3 - 4R_2^3R_0 + R_1^2R_2^2 - 4R_3R_1^3 - 27R_0^2R_3^2. \quad (2.3.31)$$

One distinguishes three cases:

- if $\Delta > 0$, the equation has three real roots;
- if $\Delta = 0$, there exist at least two roots which coincide, and they are all real;
- if $\Delta < 0$, the equation has one real root and two complex roots.

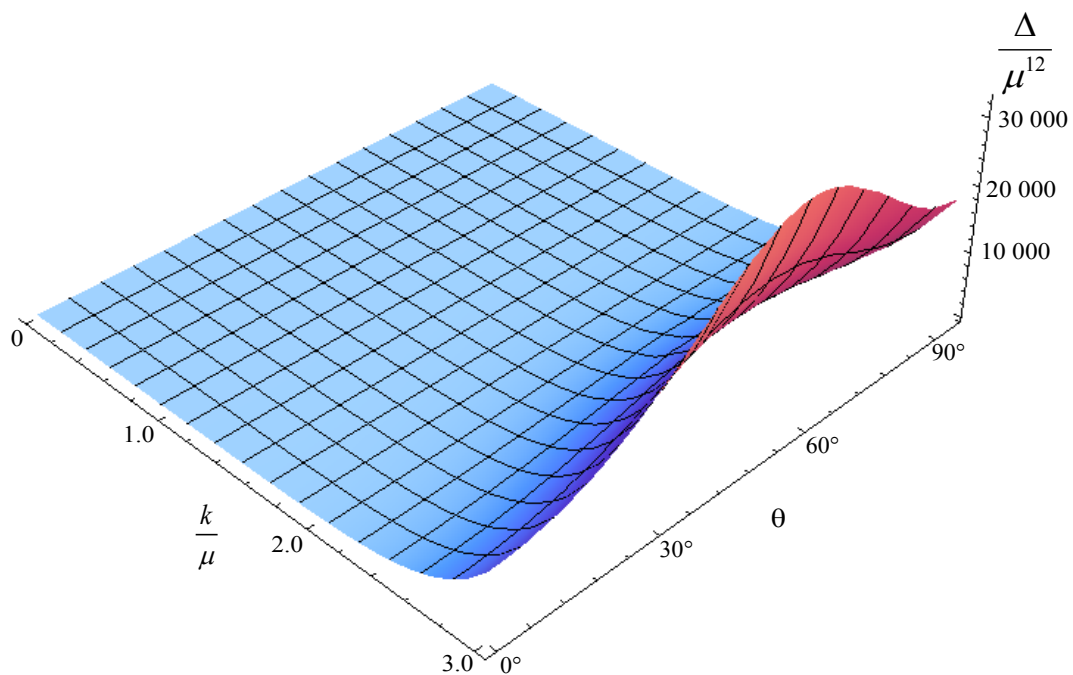


FIGURE 2.2: The discriminant Δ as function of \mathbf{k} and θ for $\mathbf{u}^2 = \frac{1}{2}$.

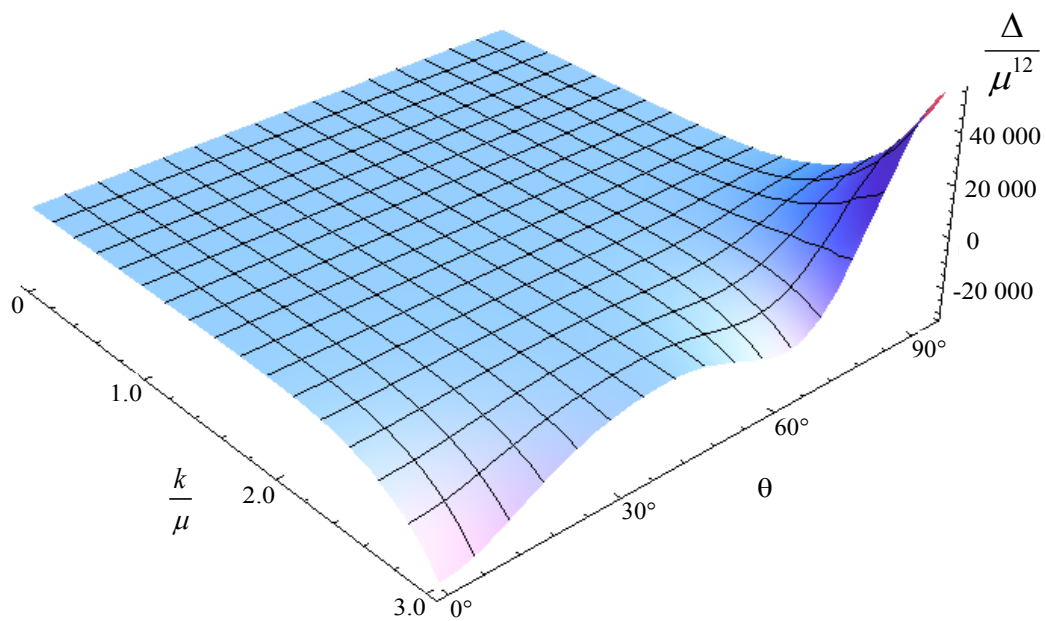


FIGURE 2.3: The discriminant Δ as function of \mathbf{k} and θ for $\mathbf{u}^2 = \frac{3}{2}$.

One shows that the discriminant (2.3.31) computed with the coefficients (2.3.30) is nonnegative for any \mathbf{k} , if $0 \leq \mathbf{u}^2 \leq 1$ but there is a domain of \mathbf{k} where Δ is negative for $\mathbf{u}^2 > 1$. This is demonstrated in Figs. 2.2-2.3 where the discriminant is plotted as a function of k and θ for $\mathbf{u}^2 = \frac{1}{2}$ (Fig. 2.2) and $\mathbf{u}^2 = \frac{3}{2}$ (Fig. 2.3). Since the stream velocity is limited by the speed of light, we always have three real solutions of the dispersion equation (2.3.29).

The real solutions of the cubic equation can be written down in the Viete's trigonometric form [66]

$$\omega_n^2 = 2\sqrt{\frac{-p}{3}} \cos \left[\frac{1}{3} \arccos \left[\frac{3\sqrt{3}q}{2p^{\frac{3}{2}}} \right] - \frac{2\pi n}{3} \right] - \frac{R_2}{3R_3}, \quad (2.3.32)$$

where $n = 1, 2, 3$ and

$$p \equiv \frac{3R_3R_1 - R_2^2}{3R_3^2}, \quad q \equiv \frac{2R_2^3 - 9R_3R_2R_1 + 27R_3^2R_0}{27R_3^3}. \quad (2.3.33)$$

These formulae assume that $p < 0$ and that the argument of the arccosine belongs to $[-1, 1]$. These conditions are guaranteed as long as $\Delta = -R_3^4(4p^3 + 27q^2) > 0$ which is the case under consideration.

The complete set of dispersion curves of plasmons predicted by the formulae (2.3.28) and (2.3.32) is shown in Figs. 2.4-2.7 for $\mathbf{u}^2 = \frac{3}{4}$ and four different orientations of the wave vector \mathbf{k} . θ is the angle between \mathbf{k} and \mathbf{n} . The red (solid) lines are for $\omega_\alpha^2(\mathbf{k})$, the green (dashed) for $\omega_1^2(\mathbf{k})$, the blue (dotted) for $\omega_2^2(\mathbf{k})$, and the orange (dashed-dotted) for $\omega_3^2(\mathbf{k})$. The light cone is presented as a light grey line.

As seen, the solution $\omega_3^2(\mathbf{k})$ corresponds to the unstable and overdamped modes. We also observe in the figures that the green (dashed) line representing $\omega_1^2(\mathbf{k})$ approaches the blue (dotted) line which refers to $\omega_2^2(\mathbf{k})$. At $\theta = 90^\circ$ the lines hit each other but they do not cross. This is the phenomenon of *mode coupling* which is nicely explained in the §64 of the textbook [65].

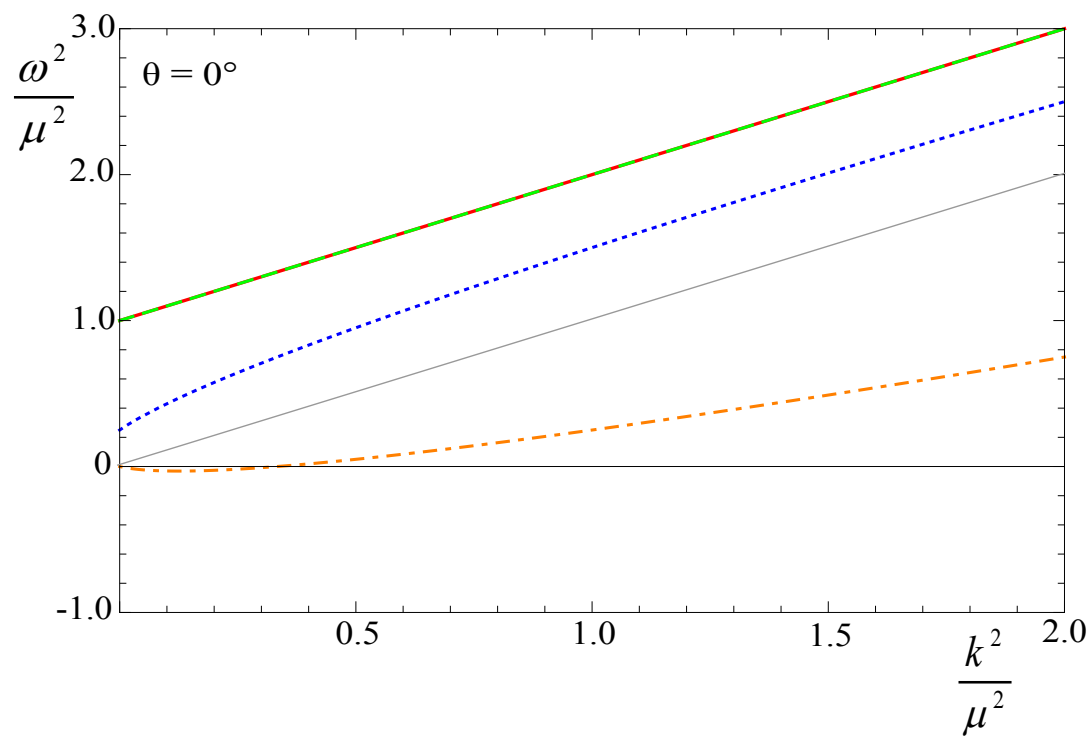


FIGURE 2.4: Dispersion curves $\omega^2(\mathbf{k})$ vs. \mathbf{k}^2 at $\mathbf{u}^2 = \frac{3}{4}$ for $\theta = 0^\circ$.

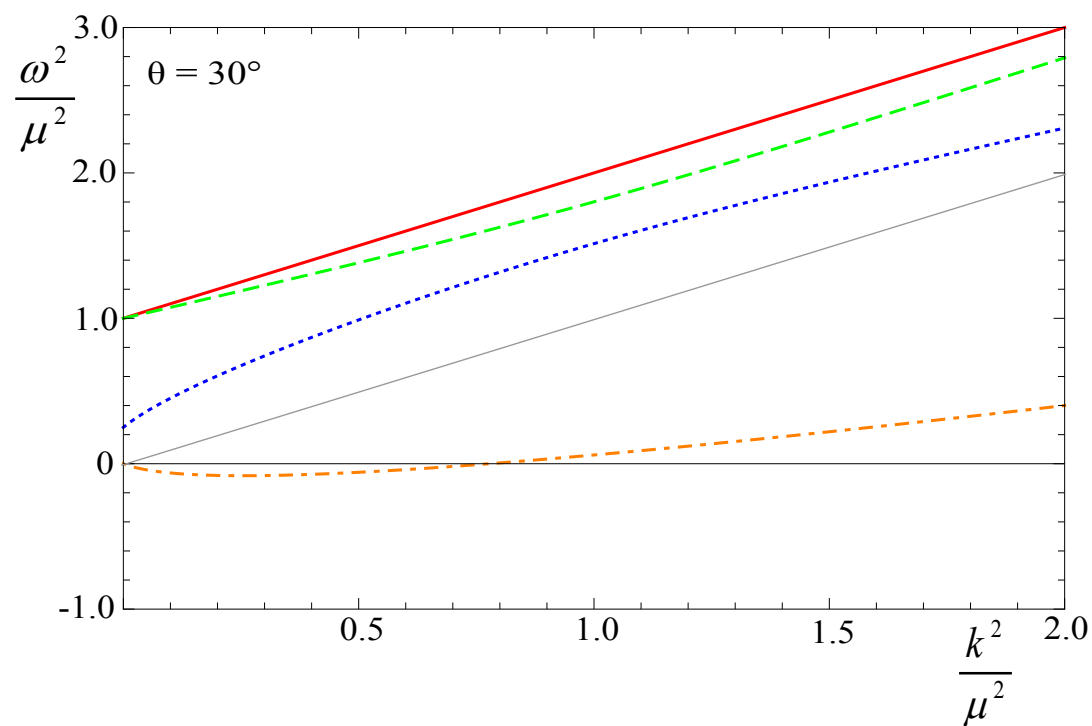


FIGURE 2.5: Dispersion curves $\omega^2(\mathbf{k})$ vs. \mathbf{k}^2 at $\mathbf{u}^2 = \frac{3}{4}$ for $\theta = 30^\circ$.

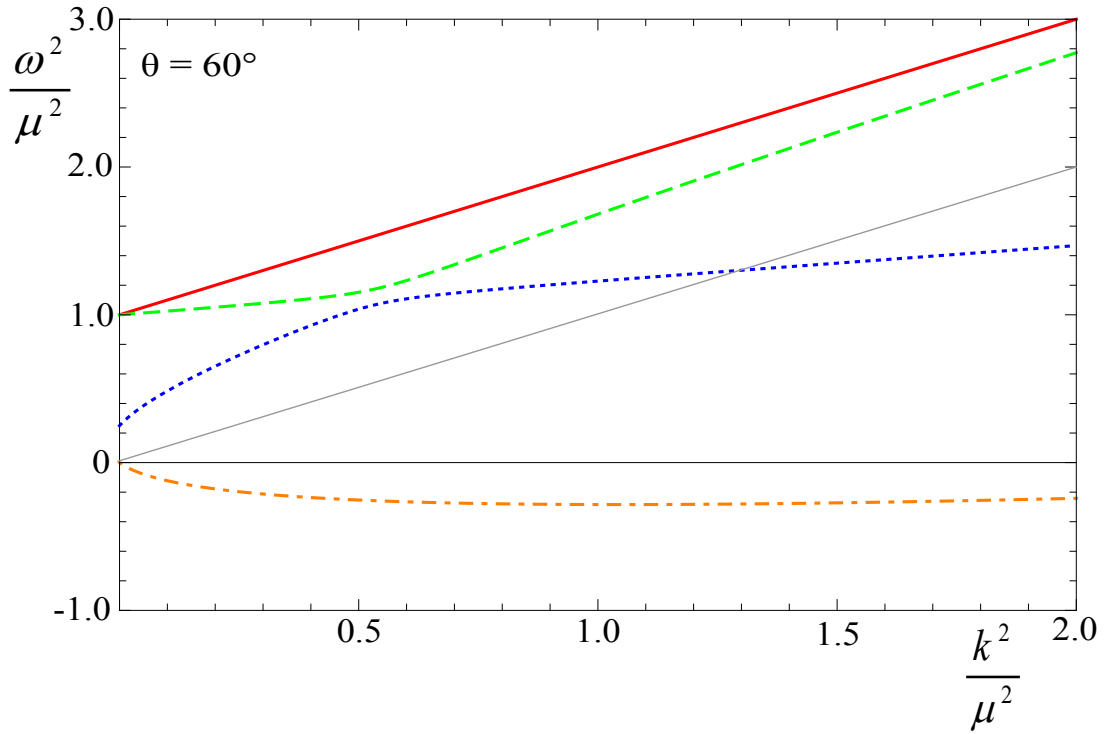


FIGURE 2.6: Dispersion curves $\omega^2(\mathbf{k})$ vs. \mathbf{k}^2 at $\mathbf{u}^2 = \frac{3}{4}$ for $\theta = 60^\circ$.

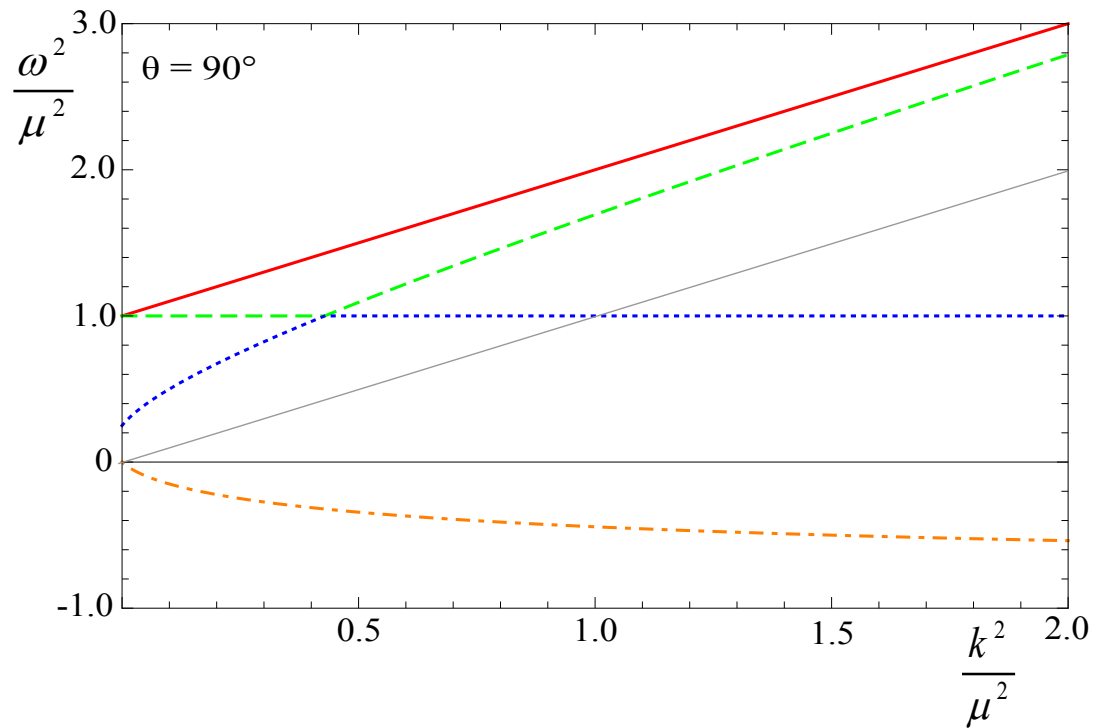


FIGURE 2.7: Dispersion curves $\omega^2(\mathbf{k})$ vs. \mathbf{k}^2 at $\mathbf{u}^2 = \frac{3}{4}$ for $\theta = 90^\circ$.

How the general solutions (2.3.32) are related to those found in Sec. 2.3.1.1 - 2.3.1.2 for $\mathbf{k}||\mathbf{u}$ and $\mathbf{k}\perp\mathbf{u}$? In the former case, we have the relations:

$$\omega_1^2(k) = \begin{cases} \omega_0^2(k) & \text{for } k < \frac{\mu u}{\sqrt{1+u^2}}, \\ \omega_+^2(k) & \text{for } k \geq \frac{\mu u}{\sqrt{1+u^2}}, \end{cases} \quad (2.3.34)$$

$$\omega_2^2(k) = \begin{cases} \omega_+^2(k) & \text{for } k < \frac{\mu u}{\sqrt{1+u^2}}, \\ \omega_0^2(k) & \text{for } k \geq \frac{\mu u}{\sqrt{1+u^2}}, \end{cases} \quad (2.3.35)$$

and $\omega_3^2(\mathbf{k}) = \omega_-^2(\mathbf{k})$. The crossing of the solutions $\omega_0^2(\mathbf{k})$ and $\omega_+^2(\mathbf{k})$ derived in the previous section actually comes from the limit $(\mathbf{k} \cdot \mathbf{u}) \rightarrow 0$. The general solutions shown in Figs. 2.4-2.7 do not cross each other.

The special solution for $\mathbf{k}||\mathbf{u}$ are related to the general solution as: $\omega_1^2(\mathbf{k}) = \omega_\alpha^2(\mathbf{k})$, $\omega_2^2(\mathbf{k}) = \omega_+^2(\mathbf{k})$ and $\omega_3^2(\mathbf{k}) = \omega_-^2(\mathbf{k})$.

2.3.3 Special case: $\mathbf{u}^2 = 1$

We consider here the case when the stream velocity \mathbf{u} equals the speed of light. This case is interesting both from physical and mathematical points of view. The dielectric tensor of the two-stream system with $\mathbf{u}^2 = 1$ exactly coincides (under the replacement $\mathbf{u} \rightarrow \mathbf{n}$) with that of the plasma with an extremely prolate (infinitely elongated in one direction) momentum distribution discussed in Sec. 2.7. Therefore, the plasmon spectra are obviously the same. Nevertheless, when the spectrum is found as a limit $\mathbf{u} \rightarrow 1$, the mode crossing observed in the extremely prolate plasma gets a different physical meaning. As explained below, instead of mode crossing we rather have the extreme mode coupling mentioned in the previous section. The dispersion equation (2.3.29) for $\mathbf{u}^2 = 1$ is also interesting mathematically. The form of the solutions (2.3.32) with the trigonometric and inverse trigonometric functions is required, if we deal with the so-called *casus irreducibilis*, when three real and distinct roots of a cubic equation cannot be expressed in terms of real radicals. However, a cubic equation, which has three real and distinct roots, can be sometimes reduced to a quadratic equation by means of the *rational root test*. Then, all three real roots of the cubic equation are expressed by real radicals and the Viète's trigonometric form is an unnecessary complication.

Since the coefficient R_3 in Eq. (2.3.29) equals unity, see Eq. (2.3.30), the rational root test suggests to look for a root of the equation among the factors of R_0 given by the formula (2.3.31). When $\mathbf{u}^2 = 1$, there is a factor $\mu^2 + (\mathbf{k} \cdot \mathbf{u})^2$ which is indeed the root of

the equation. Consequently, the cubic equation (2.3.29) is reduced to a quadratic one, which is easily solved, and the three solutions read

$$\omega_0^2(k) = \mu^2 + (\mathbf{k} \cdot \mathbf{u})^2, \quad (2.3.36)$$

$$\begin{aligned} \omega_{\pm}^2(k) &= \frac{1}{2}(\mathbf{k}^2 + (\mathbf{k} \cdot \mathbf{u})^2) \\ &\pm \sqrt{\mathbf{k}^4 + (\mathbf{k} \cdot \mathbf{u})^4 + 4\mu^2 k^2 - 4\mu^2 (\mathbf{k} \cdot \mathbf{u})^2 - 2k^2 (\mathbf{k} \cdot \mathbf{u})^2}. \end{aligned} \quad (2.3.37)$$

The solutions $\omega_0^2(\mathbf{k})$ and $\omega_+^2(\mathbf{k})$ are positive for any \mathbf{k} and consequently they represent real modes. The modes $\omega_0^2(\mathbf{k})$ and $\omega_+^2(\mathbf{k})$ cross each other at $k = \frac{\mu}{\sqrt{2} \sin \theta}$. The solution $\omega_-^2(\mathbf{k})$ is negative for $k < \mu |\tan \theta|$ and positive otherwise. It represents the Weibel unstable mode and its overdamped partner for sufficiently small wave vectors. When $\mathbf{k} \perp \mathbf{n}$ or $\theta = 90^\circ$, the unstable mode exists for all values of k . When $\mathbf{k} \parallel \mathbf{n}$ or $\theta = 0^\circ$ the configuration is cylindrically symmetric and there is no instability.

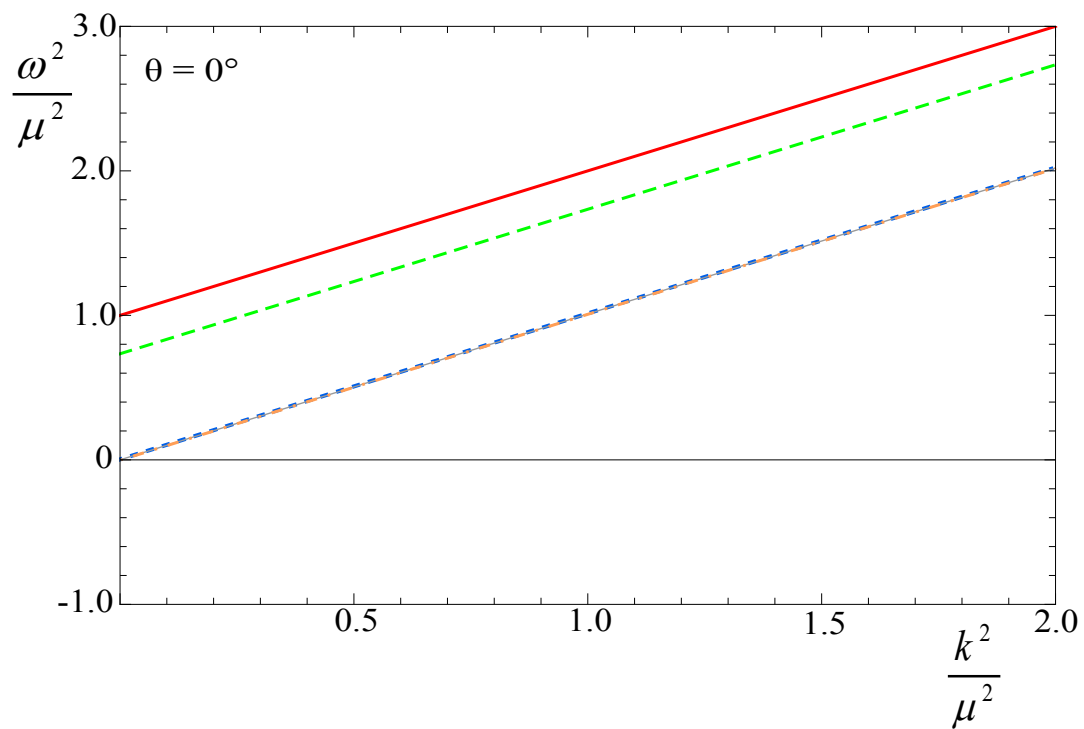
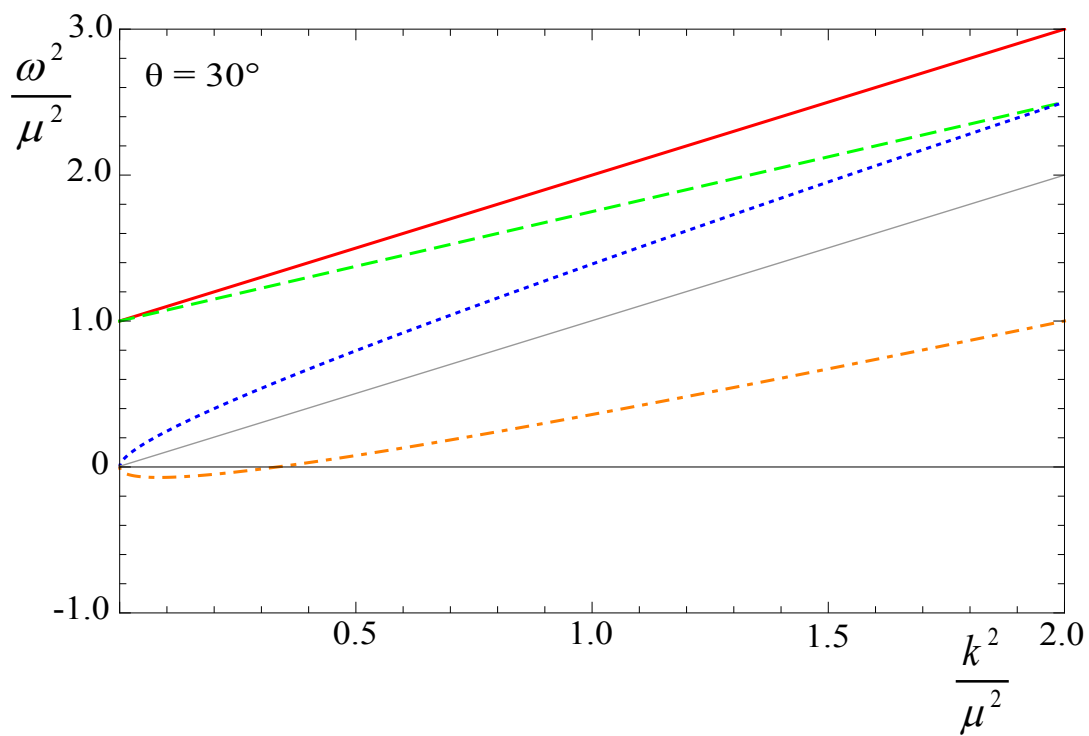
Comparing the solutions (2.3.36) and (2.3.37) to the general ones given by the formula (2.3.32), one realizes that

$$\omega_1^2(k) = \begin{cases} \omega_0^2(k) & \text{for } k < \frac{\mu}{\sqrt{2} \sin \theta}, \\ \omega_+^2(k) & \text{for } k \geq \frac{\mu}{\sqrt{2} \sin \theta}, \end{cases} \quad (2.3.38)$$

$$\omega_2^2(k) = \begin{cases} \omega_+^2(k) & \text{for } k < \frac{\mu}{\sqrt{2} \sin \theta}, \\ \omega_0^2(k) & \text{for } k \geq \frac{\mu}{\sqrt{2} \sin \theta}, \end{cases} \quad (2.3.39)$$

and $\omega_3^2(\mathbf{k}) = \omega_-^2(\mathbf{k})$. The crossing of the solutions $\omega_0^2(\mathbf{k})$ and $\omega_+^2(\mathbf{k})$ is actually an artifact of the limit $\mathbf{u}^2 \rightarrow 1$. The physical solutions are the combination of Eqs. (2.3.38) and (2.3.39).

The complete spectrum of plasmons, which includes $\omega_1^2(\mathbf{k})$, $\omega_2^2(\mathbf{k})$, $\omega_3^2(\mathbf{k})$ and $\omega_\alpha^2(\mathbf{k})$, is shown in Figs. 2.8-2.11 for four different orientations of the wave vector \mathbf{k} . The red (solid) lines are for $\omega_\alpha^2(\mathbf{k})$, the green (dashed) for $\omega_1^2(\mathbf{k})$, the blue (dotted) for $\omega_2^2(\mathbf{k})$, and the orange (dashed-dotted) for $\omega_3^2(\mathbf{k})$. The light cone is represented as a light grey line. The qualitative difference, when compared to the case $\mathbf{u}^2 < 1$, occurs when $\theta \rightarrow 0$. Then, the solutions $\omega_2^2(\mathbf{k})$ and $\omega_3^2(\mathbf{k})$ merge into one double solution $\omega_2^2(\mathbf{k}) = \omega_3^2(\mathbf{k}) = \mathbf{k}^2$.

FIGURE 2.8: Dispersion curves $\omega^2(\mathbf{k})$ vs. \mathbf{k}^2 at $\mathbf{u}^2 = 1$ for $\theta = 0^\circ$.FIGURE 2.9: Dispersion curves $\omega^2(\mathbf{k})$ vs. \mathbf{k}^2 at $\mathbf{u}^2 = 1$ for $\theta = 30^\circ$

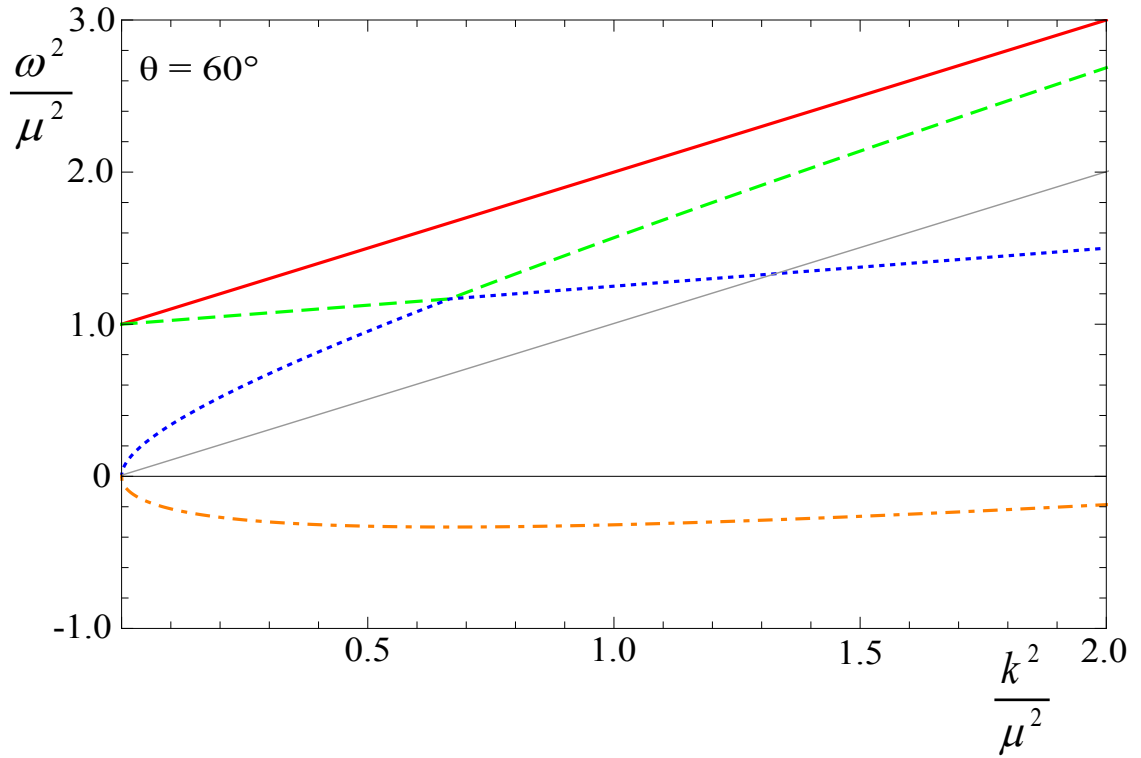


FIGURE 2.10: Dispersion curves $\omega^2(\mathbf{k})$ vs. \mathbf{k}^2 at $\mathbf{u}^2 = 1$ for $\theta = 60^\circ$.

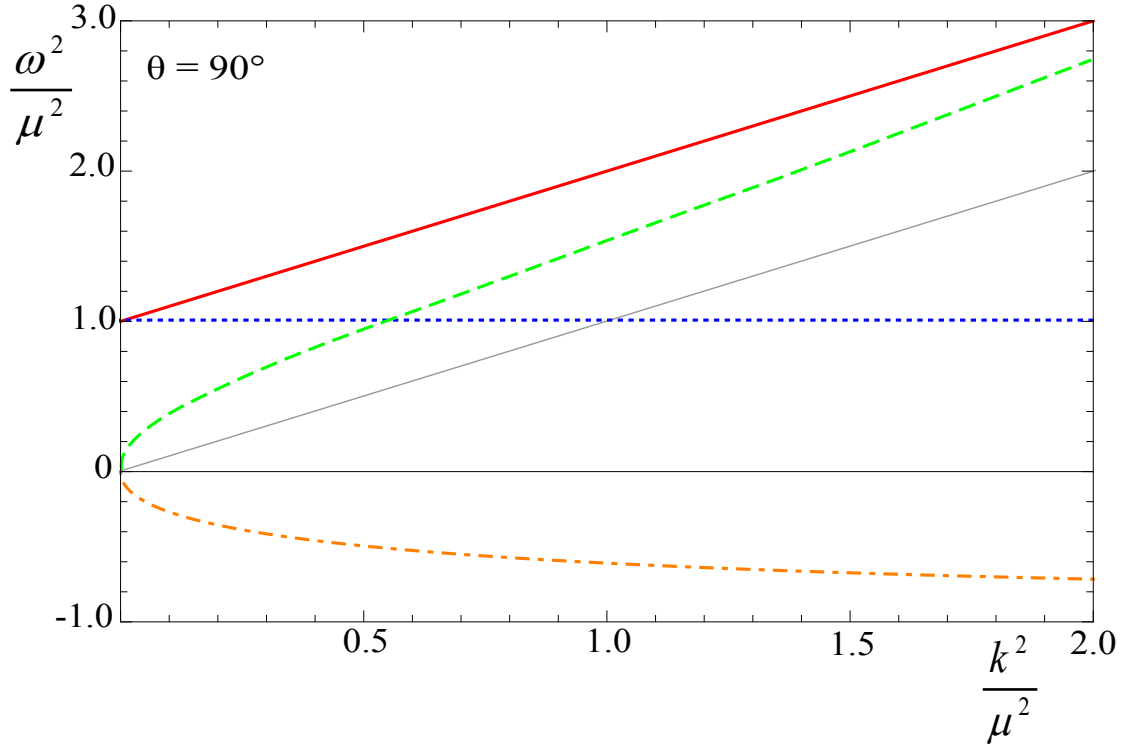


FIGURE 2.11: Dispersion curves $\omega^2(\mathbf{k})$ vs. \mathbf{k}^2 at $\mathbf{u}^2 = 1$ for $\theta = 90^\circ$.

2.4 Anisotropic plasma as deformed isotropic one

2.4.1 Momentum distributions

The dielectric tensor given by Eq. (2.1.3) or (2.1.4) is fully determined by the momentum distribution of plasma constituents. Romatschke and Strickland [43] introduced an Ansatz to model anisotropic distributions by deforming isotropic ones. They considered a momentum distribution of the form

$$f_\xi(\mathbf{p}) = C_\xi f_{\text{iso}}(\sqrt{\mathbf{p}^2 + \xi(\mathbf{p} \cdot \mathbf{n})^2}), \quad (2.4.1)$$

where $f_{\text{iso}}(|\mathbf{p}|)$ is an isotropic distribution, C_ξ is a normalization constant, \mathbf{n} is a unit vector, and the parameter $\xi \in (-1, \infty)$ controls the shape of the distribution. When $\xi = 0$ the distribution is isotropic. The vector \mathbf{n} is usually chosen along the beam direction, so that $p_L \equiv \mathbf{p} \cdot \mathbf{n}$ and $p_T \equiv |\mathbf{p} - (\mathbf{p} \cdot \mathbf{n})\mathbf{n}|$. For $-1 < \xi < 0$ the distribution is elongated in the direction of \mathbf{n} - it is *prolate*. For $\xi > 0$ the distribution is squeezed in the direction of the vector \mathbf{n} - it is *oblate* - becoming more and more oblate as the parameter ξ increases.

There is some freedom in choosing the normalization constant C_ξ of the distribution (2.4.1). Initially Romatschke and Strickland put $C_\xi = 1$ [43] but in a later publication [54] they used $C_\xi = \sqrt{1 + \xi}$, which is equivalent to normalizing the anisotropic distribution to the isotropic one, so that

$$\int \frac{d^3p}{(2\pi)^3} f_\xi(\mathbf{p}) = \int \frac{d^3p}{(2\pi)^3} f_{\text{iso}}(|\mathbf{p}|). \quad (2.4.2)$$

We adopt a different normalization. In case of massless partons, the whole spectrum of collective excitations depends on a single mass parameter which is usually chosen to be

$$m^2 \equiv g^2 \int \frac{d^3p}{(2\pi)^3} \frac{f_\xi(\mathbf{p})}{|\mathbf{p}|}. \quad (2.4.3)$$

When $\xi = 0$ (the momentum distribution is isotropic), the parameter m reduces to the usual Debye mass (2.2.4). To compare collective modes at different anisotropies, it is natural to use a mass parameter that is independent of ξ . To accomplish this we require the momentum distribution (2.4.1) to be normalized so that

$$\int \frac{d^3p}{(2\pi)^3} \frac{f_\xi(\mathbf{p})}{|\mathbf{p}|} = \int \frac{d^3p}{(2\pi)^3} \frac{f_{\text{iso}}(|\mathbf{p}|)}{|\mathbf{p}|}, \quad (2.4.4)$$

which determines the normalization constant as

$$C_\xi = \begin{cases} \frac{\sqrt{|\xi|}}{\operatorname{Arctanh}\sqrt{|\xi|}} & \text{for } -1 \leq \xi < 0, \\ \frac{\sqrt{\xi}}{\operatorname{Arctan}\sqrt{\xi}} & \text{for } 0 \leq \xi. \end{cases} \quad (2.4.5)$$

In addition to Eq. (2.4.1), which we refer to as the ξ -distribution, we also consider a distribution of the form

$$f_\sigma(\mathbf{p}) \equiv C_\sigma f_{\text{iso}}(\sqrt{(\sigma+1)\mathbf{p}^2 - \sigma(\mathbf{p} \cdot \mathbf{n})^2}), \quad (2.4.6)$$

where $\sigma \geq -1$, which we will call the σ -distribution. For $0 > \sigma \geq -1$ the distribution (2.4.6) is oblate, for $\sigma = 0$ it is isotropic, for $\sigma > 0$ it is prolate, increasing in prolateness as the parameter σ grows. If the normalization constant C_σ is determined by requiring that the distributions $f_\sigma(\mathbf{p})$ and $f_{\text{iso}}(|\mathbf{p}|)$ satisfy the condition analogous to Eq. (2.4.2), one finds $C_\sigma = \sigma + 1$. We will require the condition analogous to (2.4.4), so that the mass parameter (2.4.3) is independent of σ , which gives

$$C_\sigma = \begin{cases} \frac{\sqrt{|\sigma(\sigma+1)|}}{\operatorname{Arctan}\sqrt{|\frac{\sigma}{\sigma+1}|}} & \text{for } -1 \leq \sigma < 0, \\ \frac{\sqrt{\sigma(\sigma+1)}}{\operatorname{Arctanh}\sqrt{\frac{\sigma}{\sigma+1}}} & \text{for } 0 \leq \sigma. \end{cases} \quad (2.4.7)$$

We are particularly interested in two special cases which are easier to deal with analytically: the extremely prolate and extremely oblate distributions. The latter is proportional to $\delta(\mathbf{n} \cdot \mathbf{p}) = \delta(p_L)$ and can be obtained from the ξ -distribution (2.4.1) by taking the limit $\xi \rightarrow \infty$ (it does not correspond to the limit $\sigma \rightarrow -1$ of the σ -distribution (2.4.6)). The extremely prolate distribution is proportional to $\delta(\mathbf{p}^2 - (\mathbf{n} \cdot \mathbf{p})^2) \sim \delta(p_T)$ and corresponds to the limit $\sigma \rightarrow \infty$ of the σ -distribution (but not the limit $\xi \rightarrow -1$ of the ξ -distribution).

In practice, the simplest way to obtain the extremely oblate and extremely prolate distributions is not to take the limits described above, but to start from the forms

$$f_{\xi=\infty}(\mathbf{p}) = \delta(p_L) h(p_T), \quad (2.4.8)$$

$$f_{\sigma=\infty}(\mathbf{p}) = \delta(p_T) \frac{|p_L|}{p_T} g(p_L), \quad (2.4.9)$$

where, as previously, $p_L \equiv \mathbf{p} \cdot \mathbf{n}$ and $p_T \equiv |\mathbf{p} - (\mathbf{p} \cdot \mathbf{n})\mathbf{n}|$, and determine the functions $h(p_T)$ and $g(p_L)$ from the normalization condition analogous to Eq. (2.4.4):

$$m^2 = \frac{g^2}{4\pi^2} \int_0^\infty dp_T h(p_T) = \frac{g^2}{4\pi^2} \int_{-\infty}^\infty dp_L g(p_L). \quad (2.4.10)$$

Using any one of the momentum distributions (2.4.1), (2.4.6), (2.4.8), or (2.4.9), the dielectric tensor (2.1.3) or (2.1.4) is uniquely defined and the mass (2.4.3) is the only dimensional parameter which enters the problem. We define our system of units by rescaling all dimensional quantities by the appropriate power of the mass m , which is numerically equivalent to setting $m = 1$.

2.4.2 Coefficients α , β , γ , δ

Starting with the decomposition (2.1.12) and solving the set of equations analogous to (2.1.9), one finds the coefficients α , β , γ , δ :

$$\alpha(\omega, \mathbf{k}) = \frac{g^2}{2} \int \frac{d^3p}{(2\pi)^3} \frac{f(\mathbf{p})}{|\mathbf{p}|} \left[1 + \frac{\mathbf{k}^2 - \omega^2}{(\omega - \mathbf{k} \cdot \mathbf{v} + i0^+)^2} \left(1 - \frac{(\mathbf{n}_T \cdot \mathbf{v})^2}{\mathbf{n}_T^2} - \frac{(\mathbf{k} \cdot \mathbf{v})^2}{\mathbf{k}^2} \right) \right], \quad (2.4.11)$$

$$\beta(\omega, \mathbf{k}) = \frac{g^2}{2} \int \frac{d^3p}{(2\pi)^3} \frac{f(\mathbf{p})}{|\mathbf{p}|} \left[1 + \frac{2(\mathbf{k} \cdot \mathbf{v})}{\omega - \mathbf{k} \cdot \mathbf{v} + i0^+} + \frac{(\mathbf{k}^2 - \omega^2)(\mathbf{k} \cdot \mathbf{v})^2}{\mathbf{k}^2(\omega - \mathbf{k} \cdot \mathbf{v} + i0^+)^2} \right], \quad (2.4.12)$$

$$\gamma(\omega, \mathbf{k}) = \frac{g^2}{2} \int \frac{d^3p}{(2\pi)^3} \frac{f(\mathbf{p})}{|\mathbf{p}|} \left[\frac{\mathbf{k}^2 - \omega^2}{(\omega - \mathbf{k} \cdot \mathbf{v} + i0^+)^2} \left(-1 + 2 \frac{(\mathbf{n}_T \cdot \mathbf{v})^2}{\mathbf{n}_T^2} + \frac{(\mathbf{k} \cdot \mathbf{v})^2}{\mathbf{k}^2} \right) \right], \quad (2.4.13)$$

$$\delta(\omega, \mathbf{k}) = \frac{g^2}{2} \int \frac{d^3p}{(2\pi)^3} \frac{f(\mathbf{p})}{|\mathbf{p}|} \left[\frac{1}{\omega - \mathbf{k} \cdot \mathbf{v} + i0^+} \frac{\mathbf{n}_T \cdot \mathbf{v}}{\mathbf{n}_T^2} + \frac{\mathbf{k}^2 - \omega^2}{(\omega - \mathbf{k} \cdot \mathbf{v} + i0^+)^2} \frac{(\mathbf{n}_T \cdot \mathbf{v})(\mathbf{k} \cdot \mathbf{v})}{\mathbf{n}_T^2 \mathbf{k}^2} \right]. \quad (2.4.14)$$

An important advantage of a momentum distribution in the form (2.4.1) or (2.4.6) is that, for massless plasma constituents, the integral over the magnitude of the momentum and the angular integrals factorize. The momentum distributions can be written as

$$f_\xi(\mathbf{p}) = C_\xi f_{\text{iso}}(M_\xi |\mathbf{p}|), \quad M_\xi \equiv \sqrt{1 + \xi(\mathbf{n} \cdot \mathbf{v})^2}, \quad (2.4.15)$$

$$f_\sigma(\mathbf{p}) = C_\sigma f_{\text{iso}}(M_\sigma |\mathbf{p}|), \quad M_\sigma \equiv \sqrt{1 + \sigma + \sigma(\mathbf{n} \cdot \mathbf{v})^2}, \quad (2.4.16)$$

and the functions M_ξ and M_σ depend only on the angles θ and ϕ . Introducing the variable $\tilde{p} = M_{\xi/\sigma} |\mathbf{p}|$ and taking the integrals over \tilde{p} , which produces the factors m^2 , the formulae (2.4.11), (2.4.12), (2.4.13) and (2.4.14) get the form

$$X_{\xi/\sigma} = \frac{m^2}{2} \int \frac{d\Omega}{4\pi} \frac{F_X(\theta, \phi)}{M_{\xi/\sigma}^2}, \quad (2.4.17)$$

where X stands for α, β, γ or δ and the functions F_X , which equal the expressions in the square brackets in Eqs. (2.4.11)-(2.4.14), depend on the angles.

The azimuthal integrals can be done analytically in a straightforward manner. The polar integration can also be done analytically, but the resulting expressions are complicated and not very enlightening. In Appendix A.2 we present analytic expressions for the coefficients $\alpha, \beta, \gamma, \delta$ for the ξ -distribution (2.4.1) and σ -distribution (2.4.6) in which only the azimuthal integration has been done. In the same appendix, we also show some numerical results for the four components of the polarization tensor, after the azimuthal integration is done. In the sections below, we give analytic expressions (after performing both angular integrations) for $\alpha, \beta, \gamma, \delta$ for some special cases where the results are relatively simple.

The analytic structure of the coefficients α and β for finite ξ or σ is the same as in the isotropic case. For real valued ω all four coefficients are complex for $\omega^2 < k^2$ and real for $\omega^2 > k^2$, and for imaginary valued ω all four coefficients are real. This can be understood as follows. From the formulae (2.4.11)-(2.4.14) we see that for real ω , an imaginary contribution to any component of the polarization tensor comes from the denominators $\omega - \mathbf{k} \cdot \mathbf{v} + i0^+$ or $(\omega - \mathbf{k} \cdot \mathbf{v} + i0^+)^2$ where the Landau infinitesimal elements $i0^+$ are needed to define the integrands when $\omega = \mathbf{k} \cdot \mathbf{v}$. If $\omega^2 > k^2$, the denominators are always positive and the polarization tensor is pure real. If $\omega^2 < k^2$, the denominators produce an imaginary part due to the $i0^+$ prescription. When ω is imaginary, it is easy to see that the complex conjugate of every integrand in the formulae (2.4.11)-(2.4.14) equals the original integrand with the change $\mathbf{p} \rightarrow -\mathbf{p}$. Changing the sign of the integration variable and using the fact that the momentum distributions under consideration are even functions of \mathbf{p} , one finds that the polarization tensor is pure real for imaginary ω . We summarize this information as

$$\begin{aligned}
 \omega \in \mathbb{R} \quad \&\& \quad \omega^2 > k^2 \quad \Rightarrow \quad \{\alpha, \beta, \gamma, \delta\} \in \mathbb{R}, \\
 \omega \in \mathbb{R} \quad \&\& \quad \omega^2 < k^2 \quad \Rightarrow \quad \{\alpha, \beta, \gamma, \delta\} \in \mathbb{C}, \\
 \omega = i\gamma \quad \&\& \quad \gamma \in \mathbb{R} \quad \Rightarrow \quad \{\alpha, \beta, \gamma, \delta\} \in \mathbb{R}.
 \end{aligned} \tag{2.4.18}$$

2.5 Weakly anisotropic plasma

This section shows that the spectrum of plasmons changes qualitatively when an infinitesimal anisotropy is introduced. As we will demonstrate in Sec. 2.6, all qualitative features of the weakly anisotropic plasma survive in case of strong anisotropy. Since a weakly anisotropic system can be treated analytically to a large extent, this case deserves particularly careful analysis.

To derive the spectrum of collective modes in a weakly anisotropic plasma, we use the ξ -distribution (2.4.1) with the assumption $\xi \ll 1$ which gives

$$f_\xi(\mathbf{p}) = \left(1 + \frac{\xi}{3}\right) f_{\text{iso}}(p) + \frac{\xi}{2} \frac{df_{\text{iso}}(p)}{dp} p (\mathbf{v} \cdot \mathbf{n})^2, \quad (2.5.1)$$

where we have taken into account that the normalization constant (2.4.5) equals

$$C_\xi = 1 + \frac{\xi}{3} + \mathcal{O}(\xi^2). \quad (2.5.2)$$

The distribution (2.5.1) is weakly prolate for $\xi < 0$ and weakly oblate for $\xi > 0$.

Using the formula (2.5.1), the coefficients α , β , γ , δ given by Eqs. (2.4.11)-(2.4.14) can be computed analytically. For α and β there are contributions of order ξ^0 which are just the isotropic results of the previous section. All four functions α , β , γ , δ have contributions of order ξ . Since the coefficient $\delta(\omega, \mathbf{k})$ enters the dispersion equation (2.1.19) quadratically, it does not contribute to linear order in ξ and it can be neglected and the second dispersion equation (2.1.19) factors into two simpler equations which are

$$\frac{1}{\omega^2} \Delta_B^{-1}(\omega, \mathbf{k}) = 0, \quad \Delta_B^{-1}(\omega, \mathbf{k}) = b(\omega, \mathbf{k}) = \omega^2 - \beta(\omega, \mathbf{k}), \quad (2.5.3)$$

$$\Delta_C^{-1}(\omega, \mathbf{k}) = a(\omega, \mathbf{k}) + c(\omega, \mathbf{k}) = \omega^2 - \mathbf{k}^2 - \alpha(\omega, \mathbf{k}) - \gamma(\omega, \mathbf{k}) = 0. \quad (2.5.4)$$

We will refer to the solutions of these equations as B -modes and C -modes, respectively. In the B -mode equation we have again removed two zero solutions. So that we have the three dispersion equations of A -modes (2.1.18), B -modes (2.5.3) and C -modes (2.5.4).

The coefficients α , β , γ are computed as

$$\begin{aligned} \alpha(\omega, \mathbf{k}) = & \left(1 + \frac{\xi}{3}\right) \alpha_{\text{iso}}(\omega, \mathbf{k}) - \xi \frac{m^2}{8} \left\{ \frac{8}{3} \cos^2 \theta + \frac{2}{3} (5 - 19 \cos^2 \theta) \frac{\omega^2}{k^2} - 2(1 - 5 \cos^2 \theta) \frac{\omega^4}{k^4} \right. \\ & \left. + \left[1 - 3 \cos^2 \theta - (2 - 8 \cos^2 \theta) \frac{\omega^2}{k^2} + (1 - 5 \cos^2 \theta) \frac{\omega^4}{k^4} \right] \frac{\omega}{k} \ln \left(\frac{\omega + k}{\omega - k} \right) \right\}, \end{aligned} \quad (2.5.5)$$

$$\begin{aligned} \beta(\omega, \mathbf{k}) = & \left(1 + \frac{\xi}{3}\right) \beta_{\text{iso}}(\omega, \mathbf{k}) - \xi m^2 \left\{ \left(-\frac{2}{3} + \cos^2 \theta \right) \frac{\omega^2}{k^2} + (1 - 3 \cos^2 \theta) \frac{\omega^4}{k^4} \right. \\ & \left. + \frac{1}{2} \left[(1 - 2 \cos^2 \theta) \frac{\omega^2}{k^2} - (1 - 3 \cos^2 \theta) \frac{\omega^4}{k^4} \right] \frac{\omega}{k} \ln \left(\frac{\omega + k}{\omega - k} \right) \right\}, \end{aligned} \quad (2.5.6)$$

$$\gamma(\omega, \mathbf{k}) = -\xi \frac{m^2}{4} \sin^2 \theta \left[-\frac{4}{3} + \frac{10}{3} \frac{\omega^2}{k^2} - 2 \frac{\omega^4}{k^4} + \left(1 - 2 \frac{\omega^2}{k^2} + \frac{\omega^4}{k^4} \right) \frac{\omega}{k} \ln \left(\frac{\omega + k}{\omega - k} \right) \right], \quad (2.5.7)$$

where α_{iso} , β_{iso} are given by Eqs. (2.2.2), (2.2.3).

As in the case for the isotropic plasma, the dispersion relations cannot be solved analytically for arbitrary k . When $k^2 \ll \omega^2$, the functions $\alpha(\omega, \mathbf{k})$, $\beta(\omega, \mathbf{k})$, $\gamma(\omega, \mathbf{k})$ are approximated as

$$\alpha(\omega, \mathbf{k}) = m^2 \left\{ \frac{1}{3} \left(1 - \frac{\xi}{15} \right) + \frac{1}{5} \left[\frac{1}{3} + \frac{\xi}{7} \left(\frac{1}{9} + \cos^2 \theta \right) \right] \frac{k^2}{\omega^2} + \mathcal{O} \left(\frac{k^4}{\omega^4} \right) \right\}, \quad (2.5.8)$$

$$\begin{aligned} \beta(\omega, \mathbf{k}) = & m^2 \left\{ \frac{1}{3} \left[1 + \frac{\xi}{5} \left(-\frac{1}{3} + \cos^2 \theta \right) \right] \right. \\ & \left. + \frac{1}{5} \left[1 + \frac{\xi}{7} \left(\frac{1}{3} - \cos^2 \theta \right) \right] \frac{k^2}{\omega^2} + \mathcal{O} \left(\frac{k^4}{\omega^4} \right) \right\}, \end{aligned} \quad (2.5.9)$$

$$\gamma(\omega, \mathbf{k}) = \xi m^2 \sin^2 \theta \left[\frac{1}{15} - \frac{4k^2}{105\omega^2} + \mathcal{O} \left(\frac{k^4}{\omega^4} \right) \right]. \quad (2.5.10)$$

In the next three subsections we discuss solutions of the dispersion equations (2.1.18), (2.1.20), and (2.5.4) using the coefficients (2.5.5)-(2.5.7) or (2.5.8)-(2.5.10).

2.5.1 *A*-modes

As we show in Sec. 2.9, where the Nyquist analysis is performed, the *A*-mode dispersion equation (2.1.18) has four solutions when

$$k^2 - \xi \frac{m^2}{3} \cos^2 \theta < 0 \quad (2.5.11)$$

and two solutions otherwise. The condition (2.5.11) is never fulfilled for the prolate plasma ($\xi < 0$) and it is fulfilled for any oblate momentum distribution ($\xi > 0$) when

$$k < k_A \equiv \sqrt{\frac{\xi}{3}} m |\cos \theta|. \quad (2.5.12)$$

We solve here the A -mode dispersion equation analytically, by looking at certain simplifying limits, and show that the results agree with the those of the Nyquist analysis performed in Sec. 2.9. We first look for real A -modes which satisfy $\omega^2 \gg k^2$. In this limit $\alpha(\omega, \mathbf{k})$ is approximated by the formula (2.5.8) and Eq. (2.1.18) is solved by

$$\omega^2(\mathbf{k}) = \frac{m^2}{3} \left(1 - \frac{\xi}{15}\right) + \frac{6}{5} \left[1 + \frac{\xi}{14} \left(\frac{4}{15} + \cos^2 \theta\right)\right] k^2 + \mathcal{O}\left(\frac{k^4}{m^2}\right), \quad (2.5.13)$$

which reduces to the well-known result for the transverse plasmon (2.2.14) when $\xi = 0$. The plasmon mass, which is given by the first term on the right side of Eq. (2.5.13), depends on the anisotropy parameter ξ but is independent on the orientation of the wave vector \mathbf{k} . When compared to isotropic plasma, the plasmon mass is smaller for oblate momentum distributions ($\xi > 0$) and bigger for prolate ones ($\xi < 0$).

We can also look for pure imaginary solutions by substituting $\omega = i\gamma$ with $\gamma \in \mathbb{R}$ and assuming $\gamma^2 \ll k^2$. Using the approximate formula

$$\frac{\omega + k}{\omega - k} = \frac{\gamma^2 - k^2}{\gamma^2 + k^2} - i \frac{2\gamma k}{\gamma^2 + k^2} \stackrel{\gamma^2 \ll k^2}{\approx} \exp\left(-i\pi \frac{\gamma}{|\gamma|}\right), \quad (2.5.14)$$

the coefficient $\alpha(\omega, \mathbf{k})$ becomes

$$\alpha(\omega, \mathbf{k}) = -\frac{1}{3} \xi m^2 \cos^2 \theta + \frac{\pi}{4} \left[1 - \frac{\xi}{2} \left(\frac{1}{3} - 3 \cos^2 \theta\right)\right] m^2 \frac{|\gamma|}{k} + \mathcal{O}\left(\frac{\gamma^2}{k^2}\right), \quad (2.5.15)$$

and the dispersion equation (2.1.18) is written in the form

$$\gamma^2 + \frac{\lambda}{k} |\gamma| - k_A^2 + k^2 = 0, \quad (2.5.16)$$

where k_A is defined by the formula (2.5.12) and

$$\lambda \equiv \frac{\pi}{4} \left[1 - \frac{\xi}{2} \left(\frac{1}{3} - 3 \cos^2 \theta\right)\right] m^2. \quad (2.5.17)$$

Eq. (2.5.16) has no roots for an isotropic or prolate system, since $k_A^2 \leq 0$ when $\xi \leq 0$. For oblate systems, ξ and k_A^2 are positive and there are two solutions which read

$$\gamma(\mathbf{k}) = \pm \frac{1}{2} \left(\sqrt{\frac{\lambda^2}{k^2} + 4(k_A^2 - k^2)} - \frac{\lambda}{k} \right). \quad (2.5.18)$$

Equations (2.5.12), (2.5.17) show that in the limit of weak anisotropy $\lambda \gg k_A^2$, and therefore the expression (2.5.18) can be approximated as

$$\gamma(\mathbf{k}) \approx \pm \frac{1}{\lambda} k(k_A^2 - k^2). \quad (2.5.19)$$

The solutions (2.5.18) or (2.5.19) represent the unstable and overdamped transverse modes which exist only for oblate plasmas ($\xi > 0$) provided the condition (2.5.12) is satisfied.

2.5.2 *B*-modes

The *B*-mode dispersion equation (2.5.3) describes the longitudinal modes. We consider the limit $\omega^2 \gg k^2$ and find two analytical solutions. The coefficient $\beta(\omega, \mathbf{k})$ is approximated by the formula (2.5.9) and the dispersion equation (2.5.3) is solved by

$$\omega^2(\mathbf{k}) = \frac{m^2}{3} \left[1 + \frac{\xi}{5} \left(-\frac{1}{3} + \cos^2 \theta \right) \right] + \frac{3}{5} \left[1 + \frac{4\xi}{35} (1 - 3 \cos^2 \theta) \right] k^2 + \mathcal{O}\left(\frac{k^4}{m^2}\right), \quad (2.5.20)$$

which reduces to the well-known result for the longitudinal plasmon (2.2.15) when $\xi = 0$. The first term on the right side gives the plasmon mass which depends on the anisotropy parameter ξ and the orientation of wave vector \mathbf{k} . The formula analogous to (2.2.17) shows that the longitudinal mode approaches the light cone as $k \rightarrow \infty$.

2.5.3 *C*-modes

The *C*-mode dispersion equation (2.5.4) has the richest structure. In Sec. 2.9.2 we show that the *C*-mode dispersion equation has four solutions when

$$k^2 + \xi \frac{m^2}{3} (1 - 2 \cos^2 \theta) < 0, \quad (2.5.21)$$

and two solutions otherwise. The condition (2.5.21) can be fulfilled for oblate plasma ($\xi > 0$) when $1/2 < \cos^2 \theta$ and for prolate plasma ($\xi < 0$) when $1/2 > \cos^2 \theta$. In both cases the wave vector must satisfy

$$k < k_C \equiv m \Re \sqrt{\frac{\xi}{3} (2 \cos^2 \theta - 1)}. \quad (2.5.22)$$

When the argument of the square root is negative, the real part of the root is zero and the critical wave vector k_C vanishes.

In the rest of this subsection we look at specific limits and solve the *C*-mode dispersion equation analytically. The results agree with those of the Nyquist analysis performed in

Sec. 2.9. We first look for real solutions in the long wavelength limit ($\omega^2 \gg k^2$) when the coefficients $\alpha(\omega, \mathbf{k})$ and $\gamma(\omega, \mathbf{k})$ are approximated by the formulae (2.5.8), (2.5.10). The dispersion equation (2.5.4) is solved by

$$\omega^2(\mathbf{k}) = \frac{m^2}{3} \left[1 + \frac{\xi}{5} \left(\frac{2}{3} - \cos^2 \theta \right) \right] + \frac{6}{5} \left[1 - \frac{\xi}{5} \left(\frac{23}{42} - \cos^2 \theta \right) \right] k^2 + \mathcal{O}\left(\frac{k^4}{m^2}\right), \quad (2.5.23)$$

which reduces to the well-known transverse plasmon (2.2.14) when $\xi = 0$. The plasmon mass, which is given by the first term on the right side, depends on the anisotropy parameter ξ and on the orientation of \mathbf{k} .

One also finds pure imaginary solutions by substituting $\omega = i\gamma$ with $\gamma \in \mathbb{R}$ and assuming $\gamma^2 \ll k^2$. The dispersion equation and its solutions have the same form as in the previous section, see Eqs. (2.5.16), (2.5.18), and (2.5.19), but the coefficient λ is now defined as

$$\lambda \equiv \frac{\pi}{4} \left[1 - \frac{\xi}{2} \left(\frac{7}{3} - 5 \cos^2 \theta \right) \right] m^2, \quad (2.5.24)$$

and k_A is replaced by k_C given in Eq. (2.5.22).

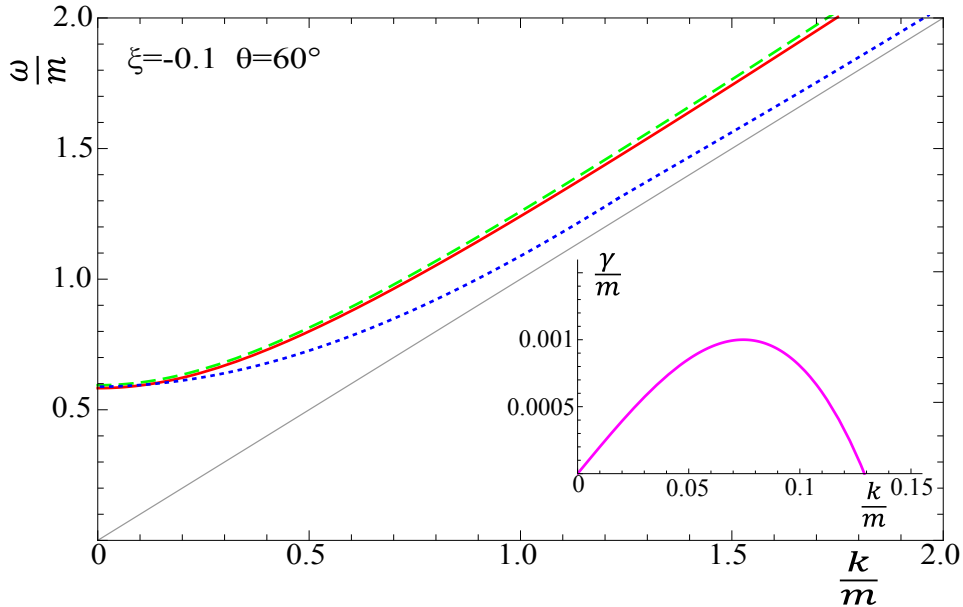


FIGURE 2.12: Dispersion curves of plasmons in weakly prolate plasma with $\xi = -0.1$ for $\theta = 60^\circ$.

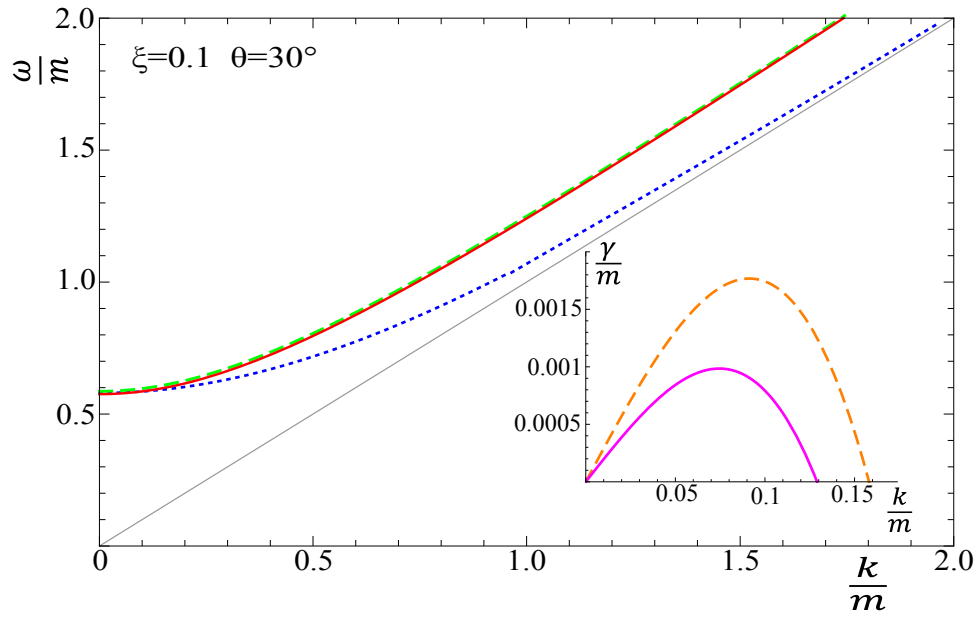


FIGURE 2.13: Dispersion curves of plasmons in weakly oblate plasma with $\xi = 0.1$ for $\theta = 30^\circ$.

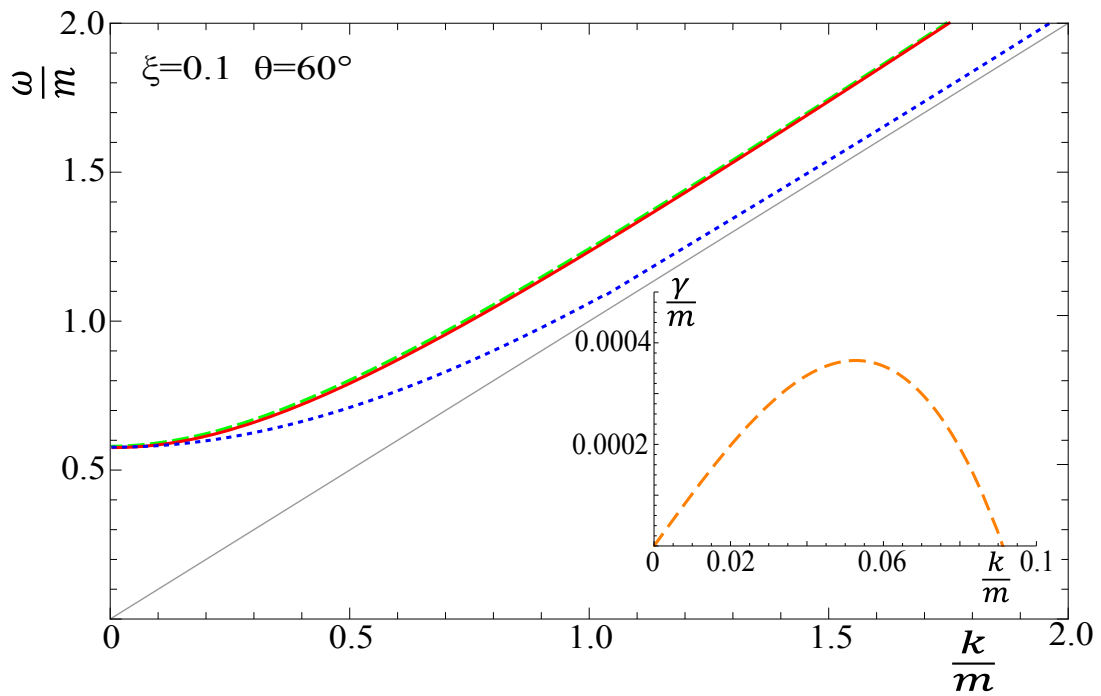


FIGURE 2.14: Dispersion curves of plasmons in weakly oblate plasma with $\xi = 0.1$ for $\theta = 60^\circ$.

2.5.4 Discussion

We have found a complete spectrum of plasmons in weakly anisotropic QGP solving numerically the dispersion equations (2.1.18), (2.5.3), and (2.5.4). The numerical solutions agree very well with the approximated analytical ones (2.5.20), (2.5.13), (2.5.18) and (2.5.23) in the domains of their applicability. Fig. 2.12 shows the spectrum for weakly prolate plasma ($\xi = -0.1$) at $\theta = 60^\circ$. Figs. 2.13 and 2.14 demonstrate the spectra for weakly oblate plasma ($\xi = 0.1$) at $\theta = 30^\circ$ and $\theta = 60^\circ$. The main part of each figure shows the dispersion curves of the positive real modes and the inserts present the positive imaginary solutions.

In Figs. 2.12-2.14 and through the whole chapter when we plot real solutions we show only the positive partner, and for imaginary solutions we show the positive imaginary part of the frequency. The light cone is always represented as a thin light grey dotted line. We also use the following notation for the dispersion curves:

- red (solid) - real A -modes denoted ω_α ,
- green (dashed) - real G -modes, which stay above the light cone, denoted ω_+ ,
- blue (dotted) - real G -modes, which cross the light cone, denoted ω_- ,
- orange (dotted) - imaginary A -modes denoted $\omega_{\alpha i} = i\gamma_\alpha$,
- pink (solid) - imaginary G -modes denoted $\omega_{-i} = i\gamma_-$.

For weakly prolate and oblate systems, real A -, B - and C -modes exist for all wave vectors and depend only weakly on the angle. The real A - and C -modes look very much like the isotropic transverse real modes. The real B -mode looks like the isotropic longitudinal real mode.

In addition to the real modes, for weakly prolate plasma there is an imaginary C -mode, seen in Fig. 2.12, which exists for $k < k_C$. The critical wave vector k_C is maximal for $\theta = 90^\circ$. When θ decreases, k_C also decreases until it reaches zero at $\theta = 45^\circ$ and the imaginary C -mode disappears. In a weakly oblate system there are two imaginary modes seen in Fig. 2.14 when $k < k_C < k_A$. Both k_A and k_C are maximal when $\theta = 0^\circ$. As θ increases from 0° , k_A and k_C decrease. At $\theta = 45^\circ$, k_C goes to zero and the imaginary C -mode disappears. The regime of the imaginary A -mode shrinks to zero at $\theta = 90^\circ$.

In comparison with the spectra of an isotropic system, the weakly anisotropic plasma exhibits the following important differences.

- The transverse mode, which is doubled in the isotropic case, is now split into two slightly different modes, the *A*-mode and the *C*-mode, which are given in Eqs. (2.5.13), or (2.5.23). In Figs. 2.12-2.14 the curves that correspond to these modes are represented by the red and green curves which lie almost on top of each other.
- In isotropic plasma longitudinal and transverse plasmons have the same plasma frequency $\omega_p = m/\sqrt{3}$, but in anisotropic plasma there are three different minimal frequencies for the three real modes.
- In isotropic plasma there are no imaginary solutions. In anisotropic plasma the number of imaginary solutions depends on the magnitude and orientation of the wave vector \mathbf{k} . In prolate plasma the number of imaginary solutions is zero or two (one pair) and in oblate plasma there are zero, two (one pair) or four (two pairs) imaginary modes.

Using the formulae (2.5.12), (2.5.22), the number of modes can be written as

$$A - \text{modes: } \begin{cases} 2 + 2\Theta(k_A - k) & \text{for oblate plasma,} \\ 2 & \text{for prolate plasma,} \end{cases} \quad (2.5.25)$$

$$B - \text{modes: } 2, \quad (2.5.26)$$

$$C - \text{modes: } 2 + 2\Theta(k_C - k), \quad (2.5.27)$$

which show that there is a maximum of 8 solutions for prolate plasma and 10 for oblate plasma.

The analysis presented in this section could equally well have been done using the σ -distribution (2.4.6) in the limit $|\sigma| \ll 1$. This would reproduce the results expressed by Eqs. (2.5.11), (2.5.21) with $\xi \rightarrow -\sigma$. Since the weakly prolate and weakly oblate systems correspond to $\sigma > 0$ and $\sigma < 0$, respectively, the number of modes in Eqs. (2.5.25)-(2.5.27) is obviously reproduced.

There is no anisotropy threshold for an existence of unstable modes, and even an infinitesimal anisotropy produces an instability. However, when $\xi \rightarrow 0$ (or $\sigma \rightarrow 0$) the growth rate of instability (γ) decreases and the domain of wave vectors, for which unstable modes exist (bounded by k_A or k_C), shrinks. In this sense, the system becomes less and less unstable, as it tends to isotropy. When the effect of inter-parton collisions is taken into account [67], the growth rates of unstable modes are reduced and systems of small anisotropy are effectively stabilized.

2.6 Finite anisotropy

When the anisotropy parameter is not small, the coefficients α , β , γ , δ of the decomposition (2.1.12) and the solutions of the dispersion equations must be computed numerically. However, the spectrum of plasmons has the same structure as in the case of the weakly anisotropic plasma discussed in the previous section - the number of modes is the same and the behavior of the dispersion curves is very similar.

We consider both the ξ -distribution (2.4.1) and the σ -distribution (2.4.6), which together describe deformations of an isotropic distribution with arbitrary prolateness and oblateness. In Appendix A.2 we give analytic expressions for the components α , β , γ , δ of the polarization tensor with the polar integrals unevaluated, and show some graphs of the results after the polar integrals are done. For finite ξ or σ , the analytic structure of the coefficients α, β is the same as in the isotropic case. For real valued ω all coefficients are complex for $\omega^2 < k^2$ and real for $\omega^2 > k^2$, and for imaginary valued ω all four coefficients are real, see Eq. (2.4.18).

If the anisotropy parameter is not assumed small, the coefficient δ cannot be neglected, which means that the dispersion equation for the G -modes (2.1.19) does not factorize into equations (2.5.3), (2.5.4). However it can be factorized as

$$\Delta_G^{-1} = (\omega^2 - \Omega_+^2(\omega, k))(\omega^2 - \Omega_-^2(\omega, k)) = 0, \quad (2.6.1)$$

where

$$\Omega_{\pm}^2(\omega, k) \equiv \frac{1}{2} \left(\alpha + \beta + \gamma + k^2 \pm \sqrt{(\alpha - \beta + \gamma + k)^2 + 4k^2 n_T^2 \delta^2} \right). \quad (2.6.2)$$

The square root in Eq. (2.6.2) is undefined if its argument is pure real and negative. When all coefficients of the polarization tensor are real, the argument of the root is positive definite. When these coefficients are complex, the root argument is also complex. Therefore, there is no case for which the argument of the root is real and negative, which means that one can find the dispersion relations by solving the equations $\omega = \pm(\Omega_{\pm}(\omega, k))$ self-consistently.

Characteristic examples of the complete spectra of plasmons in prolate and oblate plasmas, computed with the ξ - and σ -distribution, respectively, are shown in Figs. 2.15-2.16 and 2.17-2.18 for fixed values of θ . For both prolate and oblate cases, there are six (three pairs) of real modes for all \mathbf{k} which change slowly with θ . For prolate plasmas, there is at most one pair of imaginary modes. For small angles these modes are absent. As the angle increases, the imaginary modes appear at small k , and extend to larger and larger k as the angle increases. In oblate systems, there are at most two pairs of imaginary

modes. They are both absent at $\theta = 90^\circ$. When the angle decreases, the A -modes shows up first, and both pairs extend to larger and larger k as θ continues to decrease. All of these features are the same as for the weakly anisotropic plasma discussed in Sec. 2.5.

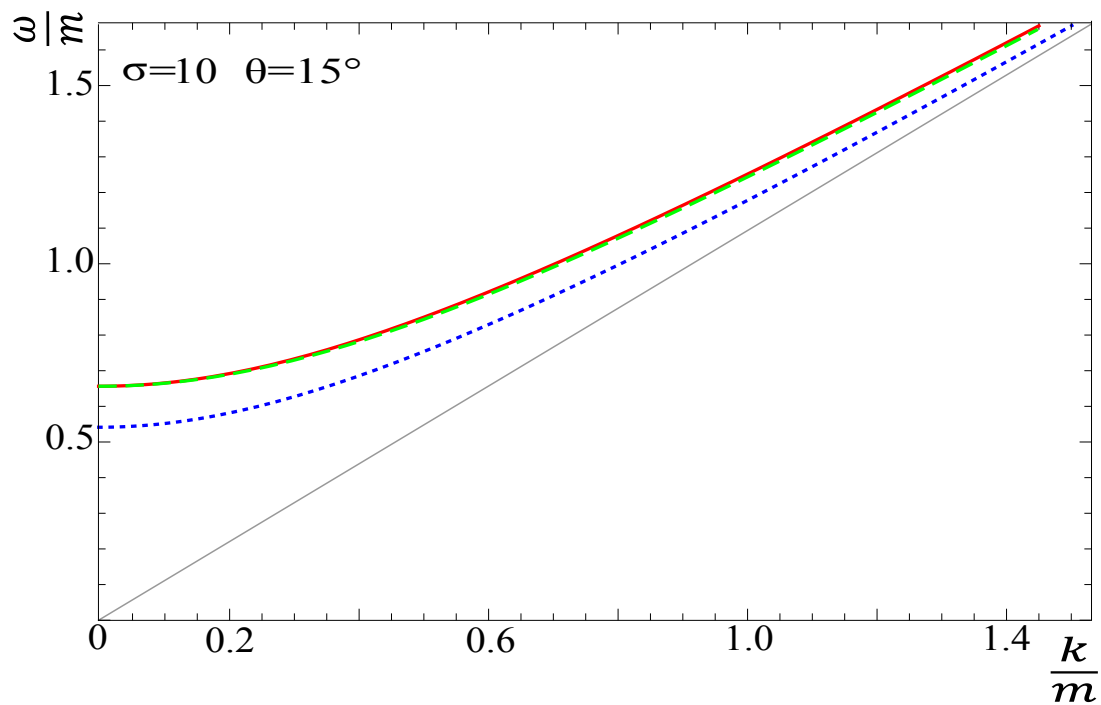


FIGURE 2.15: Dispersion curves of plasmons in prolate plasma with $\sigma = 10$ for $\theta = 15^\circ$. Here is a green curve that is almost completely covered by the red curve.

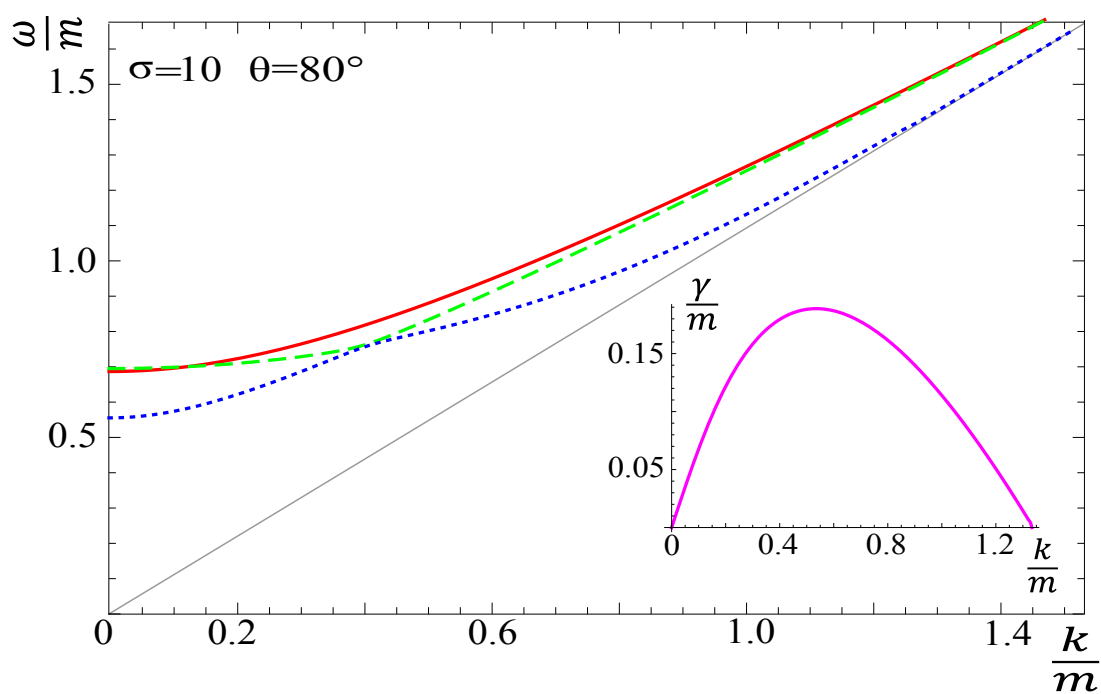


FIGURE 2.16: Dispersion curves of plasmons in prolate plasma with $\sigma = 10$ for $\theta = 80^\circ$.

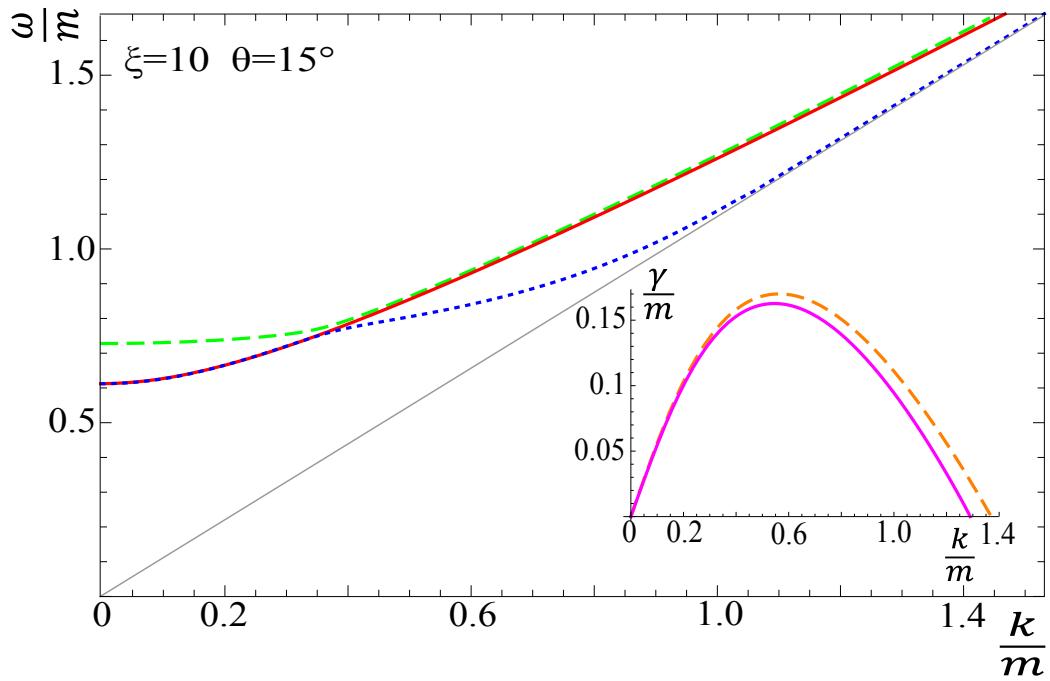


FIGURE 2.17: Dispersion curves of plasmons in oblate plasma with $\xi = 10$ for $\theta = 15^\circ$.

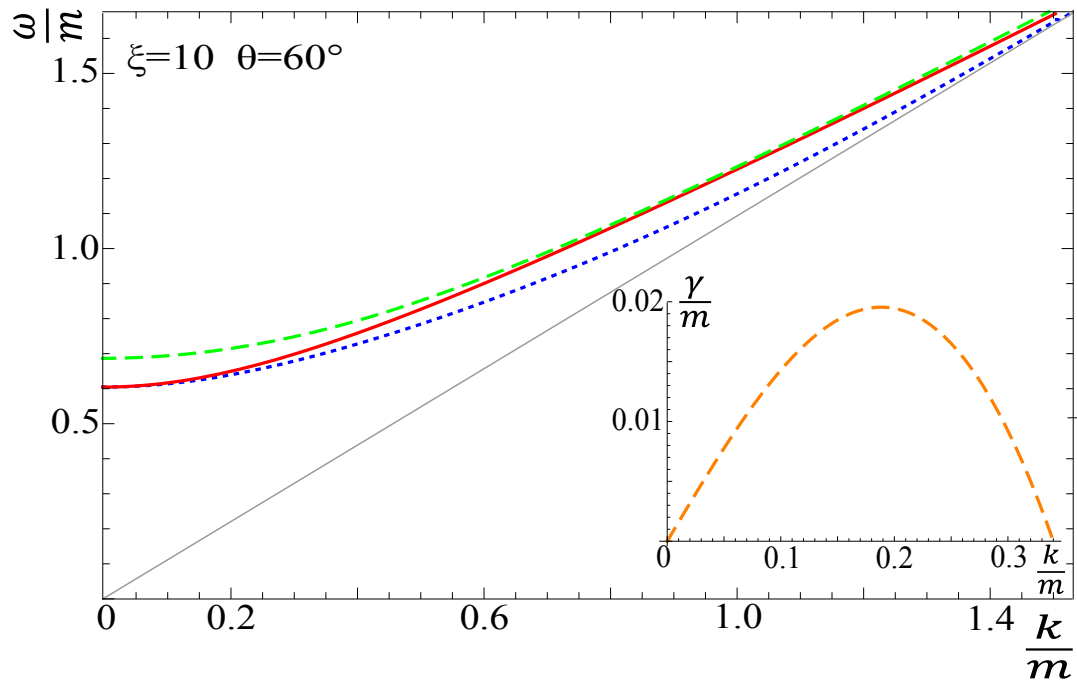


FIGURE 2.18: Dispersion curves of plasmons in oblate plasma with $\xi = 10$ for $\theta = 60^\circ$.

2.7 Extremely prolate plasma

The extremely prolate system with the momentum distribution (2.4.9) is the easiest case of all to study analytically. It was analysed in [44] using a different method. The coefficients α , β , γ , δ and the inverse propagator Σ defined by Eq. (2.1.2) can be computed analytically not even specifying the coordinate system. Since the velocity \mathbf{v} of a massless parton is $\mathbf{v} = \mathbf{n}$ for $\mathbf{p} \cdot \mathbf{n} > 0$ and $\mathbf{v} = -\mathbf{n}$ for $\mathbf{p} \cdot \mathbf{n} < 0$, the matrix Σ is found to be

$$\begin{aligned} \Sigma^{ij}(\omega, \mathbf{k}) = & (\omega^2 - \frac{m^2}{2} - \mathbf{k}^2)\delta^{ij} + k^i k^j - \frac{m^2 \mathbf{k} \cdot \mathbf{n}}{2(\omega^2 - (\mathbf{k} \cdot \mathbf{n})^2)}(k^i n^j + n^i k^j) \\ & - \frac{m^2(\omega^2 + (\mathbf{k} \cdot \mathbf{n})^2)(\mathbf{k}^2 - \omega^2)}{2(\omega^2 - (\mathbf{k} \cdot \mathbf{n})^2)^2} n^i n^j, \end{aligned} \quad (2.7.1)$$

and the coefficients α , β , γ , δ are

$$\alpha(\omega, \mathbf{k}) = \frac{m^2}{2}, \quad (2.7.2)$$

$$\beta(\omega, \mathbf{k}) = \frac{m^2}{2} + \frac{m^2(\mathbf{k} \cdot \mathbf{n})^2}{\omega^2 - (\mathbf{k} \cdot \mathbf{n})^2} + \frac{m^2(\omega^2 + (\mathbf{k} \cdot \mathbf{n})^2)(\mathbf{k}^2 - \omega^2)}{2(\omega^2 - (\mathbf{k} \cdot \mathbf{n})^2)^2} \frac{(\mathbf{k} \cdot \mathbf{n})^2}{\mathbf{k}^2}, \quad (2.7.3)$$

$$\gamma(\omega, \mathbf{k}) = \frac{m^2(\omega^2 + (\mathbf{k} \cdot \mathbf{n})^2)(\mathbf{k}^2 - \omega^2)}{2(\omega^2 - (\mathbf{k} \cdot \mathbf{n})^2)^2} \left(1 - \frac{(\mathbf{k} \cdot \mathbf{n})^2}{\mathbf{k}^2}\right), \quad (2.7.4)$$

$$\delta(\omega, \mathbf{k}) = \frac{m^2(\mathbf{k} \cdot \mathbf{n})}{2(\omega^2 - (\mathbf{k} \cdot \mathbf{n})^2)} + \frac{m^2(\omega^2 + (\mathbf{k} \cdot \mathbf{n})^2)(\mathbf{k}^2 - \omega^2)}{2(\omega^2 - (\mathbf{k} \cdot \mathbf{n})^2)^2} \frac{(\mathbf{k} \cdot \mathbf{n})}{\mathbf{k}^2}. \quad (2.7.5)$$

The dispersion equation for the A -modes (2.1.18) has the simple solution

$$\omega_\alpha^2(\mathbf{k}) = \frac{m^2}{2} + \mathbf{k}^2. \quad (2.7.6)$$

Although the dispersion equation for the G -modes (2.1.19) is rather complicated, it also has three relatively simple solutions

$$\omega_2^2(\mathbf{k}) = \frac{m^2}{2} + (\mathbf{k} \cdot \mathbf{n})^2, \quad (2.7.7)$$

$$\begin{aligned} \omega_\pm^2(\mathbf{k}) = & \frac{1}{2} \left(\mathbf{k}^2 + (\mathbf{k} \cdot \mathbf{n})^2 \right. \\ & \left. \pm \sqrt{\mathbf{k}^4 + (\mathbf{k} \cdot \mathbf{n})^4 + 2m^2 \mathbf{k}^2 - 2m^2 (\mathbf{k} \cdot \mathbf{n})^2 - 2\mathbf{k}^2 (\mathbf{k} \cdot \mathbf{n})^2} \right). \end{aligned} \quad (2.7.8)$$

The modes ω_α , ω_2 and ω_+ are real and exist for any \mathbf{k} . The solutions ω_α and ω_+ lie always above the light cone. The mode ω_2 lies above the light cone for $k < \frac{m}{\sqrt{2} \sin \theta}$ and below for $k > \frac{m}{\sqrt{2} \sin \theta}$. The modes ω_+ and ω_2 cross each other at $k = \frac{m}{2 \sin \theta}$.

The solution ω_- can be either pure real or pure imaginary. It is imaginary for

$$k < k_{\text{pG}} \equiv \frac{m}{\sqrt{2}} |\tan \theta|, \quad (2.7.9)$$

and real for $k > k_{\text{pG}}$. The solution $i\gamma$, where $\gamma \equiv |\omega_-|$, is the Weibel unstable mode, and $-i\gamma$ is its overdamped partner. When $\mathbf{k} \perp \mathbf{n}$ or $\theta = 90^\circ$, the unstable mode exists for all values of k , as k_{pG} given by Eq. (2.7.9) goes to infinity. When $\mathbf{k} \parallel \mathbf{n}$ or $\theta = 0^\circ$ the configuration is cylindrically symmetric and there is no instability, since $k_{\text{pG}} \rightarrow 0$. The real modes are $\omega_\alpha^2(\mathbf{k}) = \omega_2^2(\mathbf{k}) = m^2/2 + k^2$ and $\omega_+^2(\mathbf{k}) = \omega_-^2(\mathbf{k}) = k^2$ in this limit. The behaviour of the unstable G -mode is shown in Fig. 2.19.

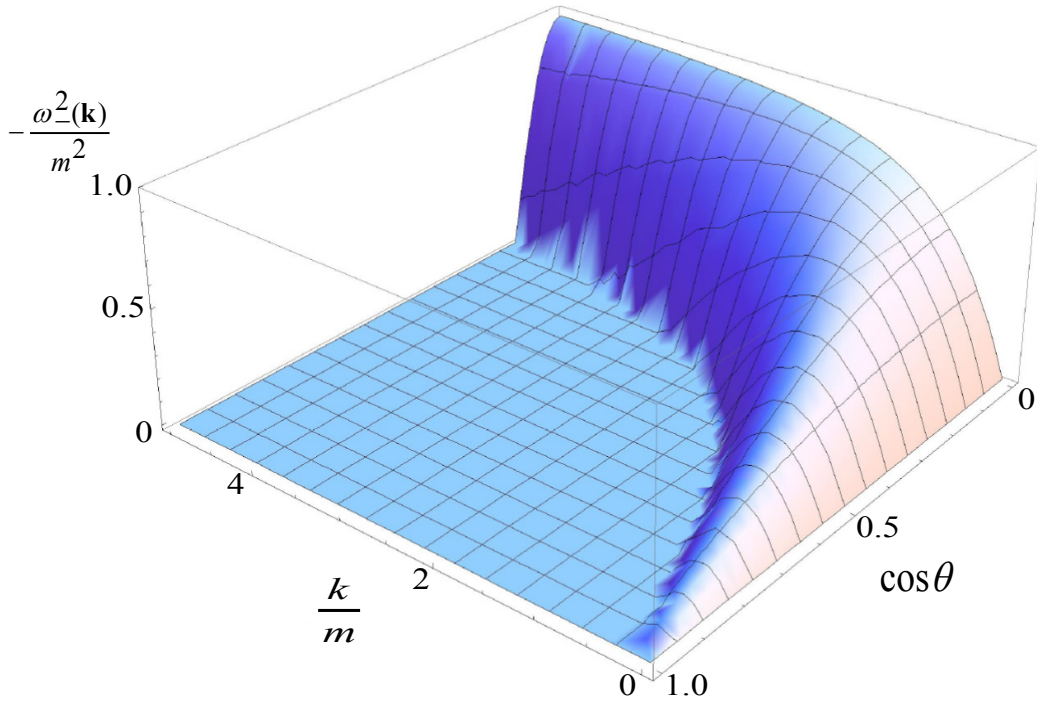


FIGURE 2.19: Unstable mode for the extremely prolate plasma: $-\omega_-^2(\mathbf{k})$ as a function of k and $\cos \theta$ in the domain where $\omega_-^2(\mathbf{k}) < 0$. The angle θ is between the vectors \mathbf{k} and \mathbf{n} .

The spectra of plasmons in an extremely prolate plasma are shown in Figs. 2.20-2.23 for different orientations of the wave vector \mathbf{k} . The imaginary mode emerges at finite θ and it extends to infinite k at $\theta = 90^\circ$. The mode $\omega_\alpha(\mathbf{k})$ is independent of θ , and $\omega_2(\mathbf{k})$ changes qualitatively when θ grows from 0° to 90° . The mode $\omega_+(\mathbf{k})$ is massless, that is $\omega_+(0) = 0$, and its dispersion curve is everywhere concave, in contrast to other real dispersion curves which are usually convex.

There is a qualitative difference between the plasmon spectra of the extremely prolate system, which is discussed here, and that of a system with prolateness characterized by the parameter $\sigma \gg 1$. In extremely prolate plasma, the mode ω_- given by the formula

(2.7.8) exists for any wave vector \mathbf{k} : it is real for $k > k_{\text{pG}}$ and imaginary for $k < k_{\text{pG}}$. For a very large but finite σ , only the imaginary piece at $k < k_{\text{pG}}$ is found. One could suspect that a solution has been missed in the numerical calculation, but the Nyquist analysis, which is presented in Sec. 2.9.3, proves that this is not the case. The key point is that when $\sigma \rightarrow \infty$ there is a change in the analytic properties of the left-hand-side of the G -mode dispersion equation (2.1.19) as a function of ω . The cut singularity at $\omega \in [-k, k]$ is replaced by double poles at $\omega = \pm \mathbf{k} \cdot \mathbf{n}$ and the number of modes in extremely prolate plasma equals 8 for any \mathbf{k} .

Another important point is that the limit of extreme prolateness is approached very slowly as $\sigma \rightarrow \infty$. To illustrate this point we consider, as an example, the coefficient $\alpha(\omega, \mathbf{k} = 0)$ which is the mass of A -mode. When computed with the σ -distribution (2.4.6) we obtain

$$\alpha_\sigma(\omega, \mathbf{k} = 0) = \frac{m^2 C_\sigma}{8 \sigma} \left[\left(\sqrt{\frac{\sigma}{\sigma+1}} + \sqrt{\frac{\sigma+1}{\sigma}} \right) \ln \left(\frac{\sqrt{\sigma+1} + \sqrt{\sigma}}{\sqrt{\sigma+1} - \sqrt{\sigma}} \right) - 2 \right], \quad (2.7.10)$$

and for $\sigma \gg 1$ we have

$$\alpha_\sigma(\omega, \mathbf{k} = 0) \approx \frac{m^2}{2} \left(1 - \frac{1}{\ln 4\sigma} \right). \quad (2.7.11)$$

From this expression we find that even for σ as large as 10^4 , the coefficient differs from its extremely prolate value at $\sigma \rightarrow \infty$ by 10%. As will be shown in the subsequent section, when $\xi \rightarrow \infty$ the parameter $\alpha_\xi(\omega, \mathbf{k} = 0)$ approaches the extremely oblate value much more quickly.

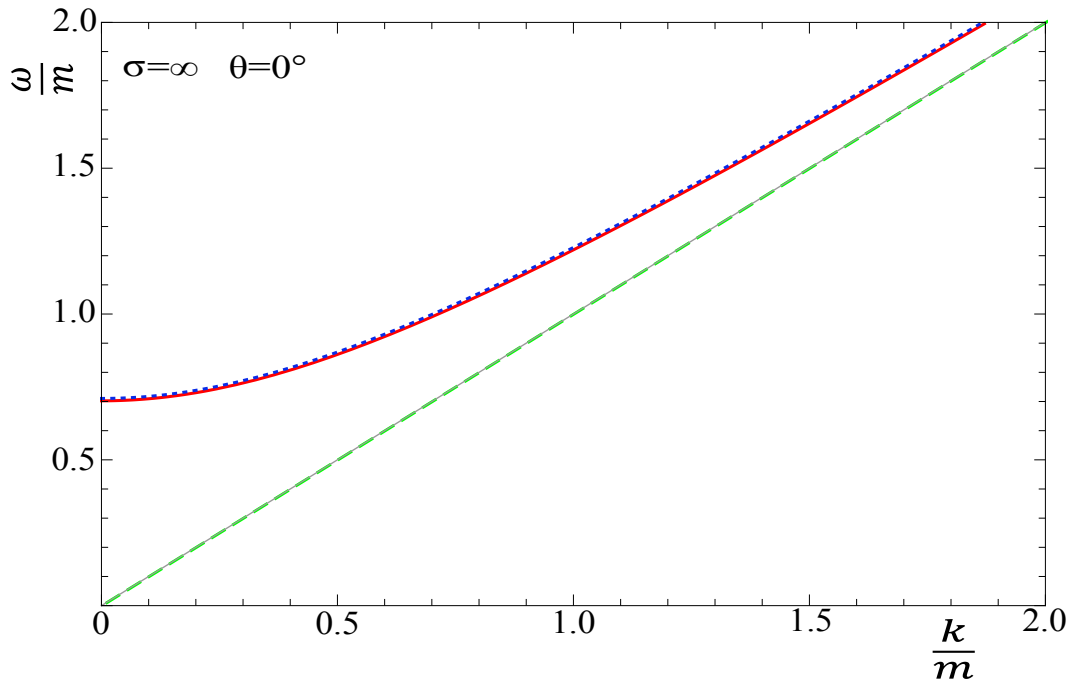


FIGURE 2.20: Dispersion curves of plasmons in extremely prolate plasma for $\theta = 0^\circ$.

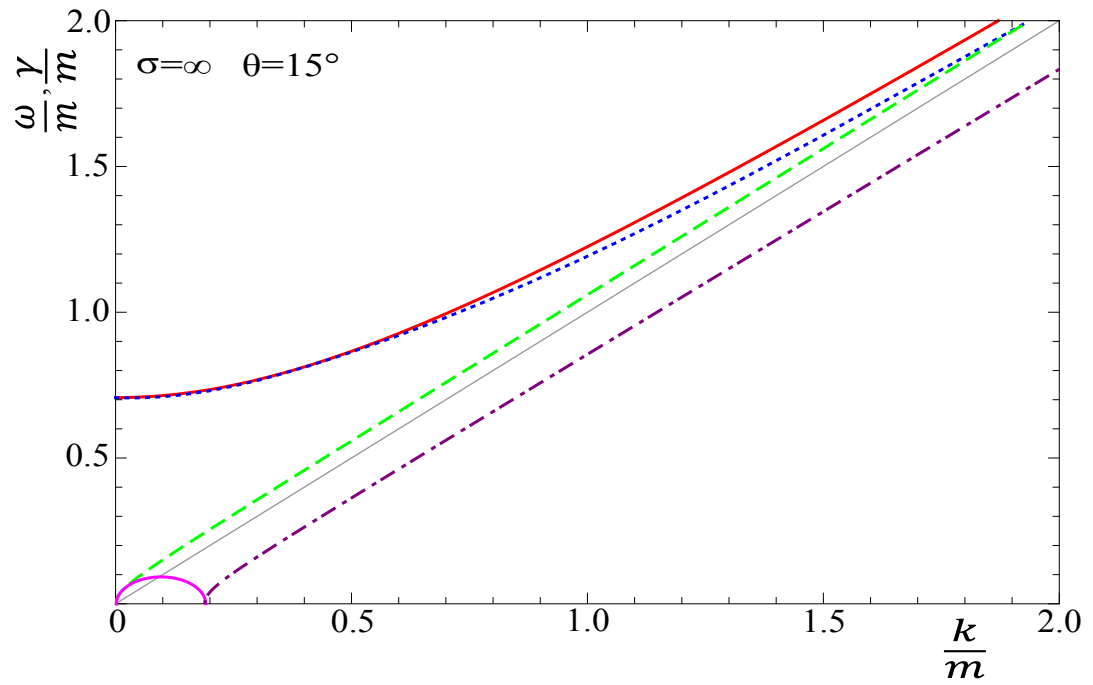


FIGURE 2.21: Dispersion curves of plasmons in extremely prolate plasma for $\theta = 15^\circ$.

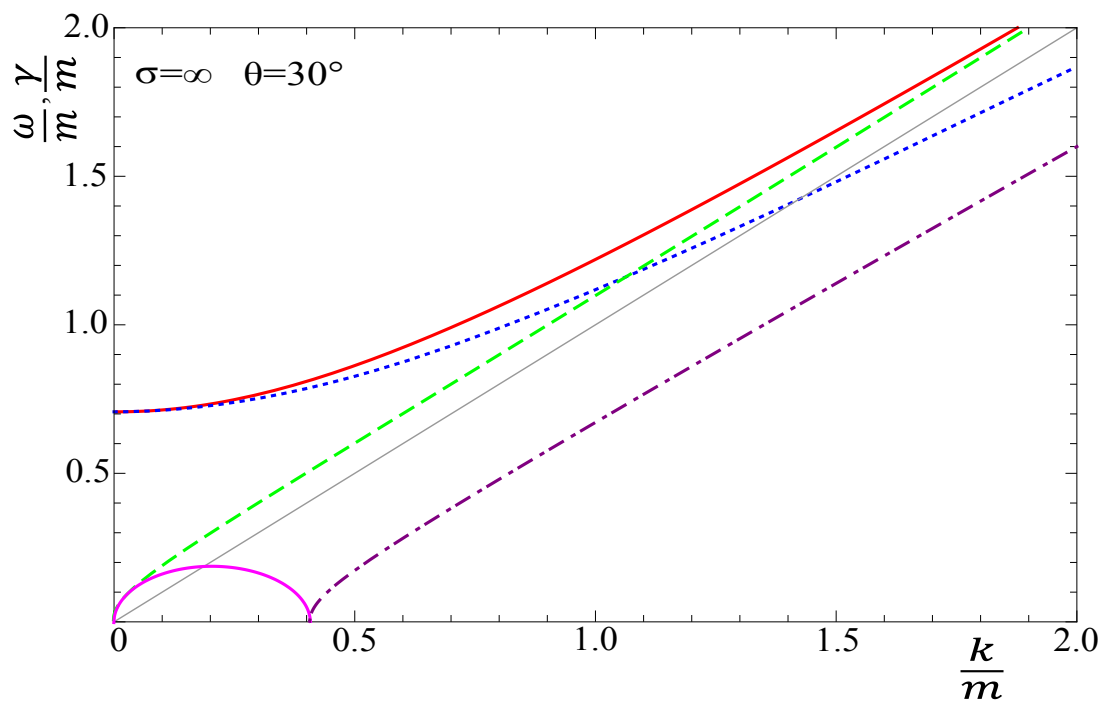


FIGURE 2.22: Dispersion curves of plasmons in extremely prolate plasma for $\theta = 30^\circ$.

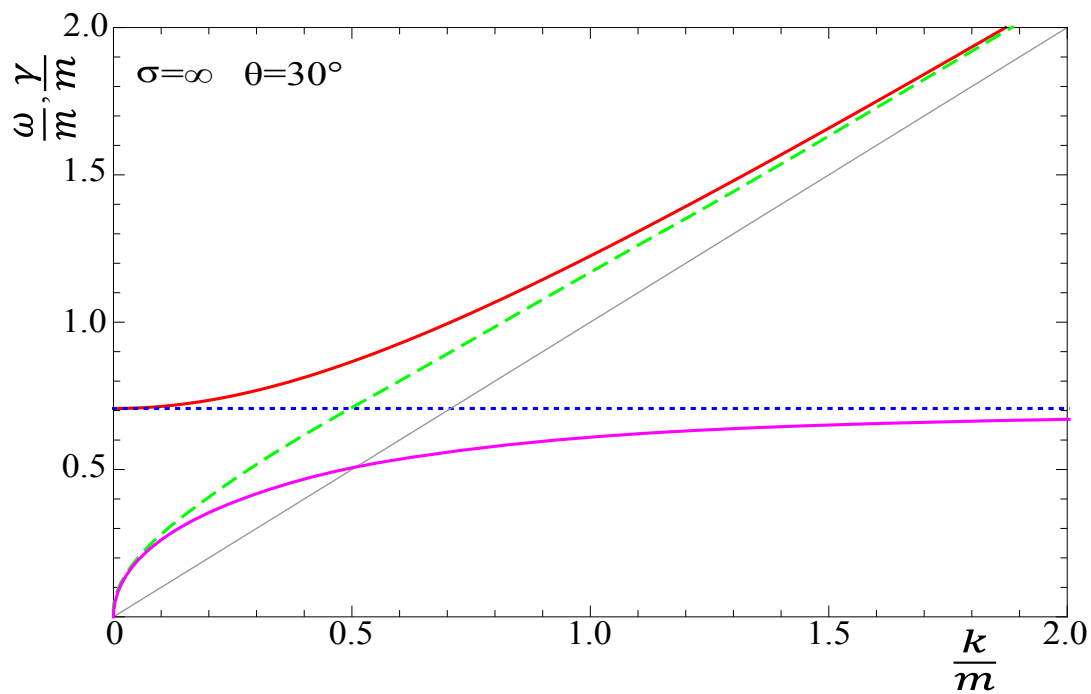


FIGURE 2.23: Dispersion curves of plasmons in extremely prolate plasma for $\theta = 90^\circ$.

2.8 Extremely oblate plasma

In this section we consider the second limiting case - the extremely oblate plasma with the momentum distribution given by Eq. (2.4.8). The coefficients α , β , γ , δ , which have a much more complicated structure than for the extremely prolate plasma, equal

$$\alpha(\omega, \mathbf{k}) = \frac{m^2}{2(1-x^2)} \left[\hat{\omega}^2 - x^2 + \frac{\hat{\omega}(1-\hat{\omega}^2)}{r_+ r_-} \right], \quad (2.8.1)$$

$$\beta(\omega, \mathbf{k}) = \frac{m^2 \hat{\omega}^2}{2} \left[-1 + \frac{\hat{\omega}(2x^2 + \hat{\omega}^2 - 1)}{r_+^3 r_-^3} \right], \quad (2.8.2)$$

$$\gamma(\omega, \mathbf{k}) = \frac{m^2(\hat{\omega}^2 - 1)}{2(1-x^2)} \left[\frac{\hat{\omega}(2x^4 + (x^2 + 1)\hat{\omega}^2 - x^2 - 1)}{r_+^3 r_-^3} - x^2 - 1 \right], \quad (2.8.3)$$

$$k\delta(\omega, \mathbf{k}) = \frac{m^2 \hat{\omega} x}{2(1-x^2)} \left[\frac{-2(x^2 - 1)\hat{\omega}^2 + x^2 - \hat{\omega}^4 - 1}{r_+^3 r_-^3} + \hat{\omega} \right], \quad (2.8.4)$$

where $\hat{\omega} \equiv \omega/k$, $x \equiv \cos \theta$ and

$$r_+ r_- \equiv \left(\hat{\omega} + \sqrt{1-x^2} + i0^+ \right)^{1/2} \left(\hat{\omega} - \sqrt{1-x^2} + i0^+ \right)^{1/2}. \quad (2.8.5)$$

The dispersion equations (2.1.18), (2.1.19) with the coefficients (2.8.1)-(2.8.4) cannot be solved analytically. We have found numerically that there are no complex solutions, only pure real and pure imaginary ones. Using a Nyquist analysis we have verified that all solutions have been found by our numerical method. Details are given in Sec. 2.9.4. The A -mode dispersion equation (2.1.18) has a pair of real solutions for all \mathbf{k} and a pair of imaginary solutions if the wave vector obeys

$$k < k_{oA} \equiv \frac{m}{\sqrt{2}} |\cot \theta|. \quad (2.8.6)$$

The G -mode dispersion equation (2.1.19) has two pairs of real solutions for all \mathbf{k} and a pair of imaginary solutions when the wave vector satisfies the condition

$$k < k_{oG} \equiv \frac{m}{2} \Re \sqrt{\frac{|\cos \theta| \sqrt{\cos^2 \theta + 4} + \cos^2 \theta - 2}{\sin^2 \theta}}. \quad (2.8.7)$$

When $\cos^2 \theta < 1/2$ (that is $90^\circ > \theta > 45^\circ$), the argument of the square root is negative, the real part of the root is zero, and the critical wave vector k_{oG} vanishes. One observes that k_{oA} is obtained from k_{pG} by changing the tangent function into a cotangent. As explained in Sec. 2.9.4, the critical values (2.8.6), (2.8.7) are the values of k for which the inverse propagators Δ_A^{-1} and Δ_G^{-1} , given by Eqs. (2.1.18)-(2.1.19), vanish at $\omega = 0$.

The unstable A - and G -modes for the extremely oblate system are shown in Figs. 2.24-2.25.

The total number of modes is 6, 8 or 10 exactly as in the weakly oblate case (2.5.25)-(2.5.27). The above results can be written in a compact form as

$$A - \text{modes} : 2 + 2\Theta(k_{oA} - k), \quad (2.8.8)$$

$$G - \text{modes} : 4 + 2\Theta(k_{oG} - k). \quad (2.8.9)$$

In Fig. 2.26-2.29 we show the dispersion curves obtained numerically from Eqs. (2.1.18), and (2.1.19) for the angle θ equal 0° , 15° , 60° and 90° . When $\theta = 0^\circ$ the real solutions ω_- and ω_+ exhibit sharp corners at the same value of k . The ω_α solution lies on top of the ω_- solution at small k and on top of ω_+ at large k . The two imaginary solutions extend through all values of k and lie on top of each other, which is consistent with the observation that k_{oA} and k_{oG} both go to infinity at $\theta = 0$. At $\theta = 15^\circ$ we see that increasing the angle softens the corner in the real modes and causes the imaginary modes to retreat. The inset shows a blow-up of the region where the real modes approach each other. When θ has increased to 60° , the imaginary G -mode has dropped out, and at 90° both imaginary modes are gone.

The structure of the plasmon spectrum in Figs. 2.26-2.29 is rather complicated. To understand it better, we consider three special limits which can be treated analytically. We start with $\mathbf{k} \parallel \mathbf{n}$ ($\theta = 0^\circ$), then we discuss the situation when \mathbf{k} is almost parallel to \mathbf{n} ($|\sin\theta| \ll 1$), and finally we analyze the limit $\mathbf{k} \perp \mathbf{n}$ ($\theta = 90^\circ$).

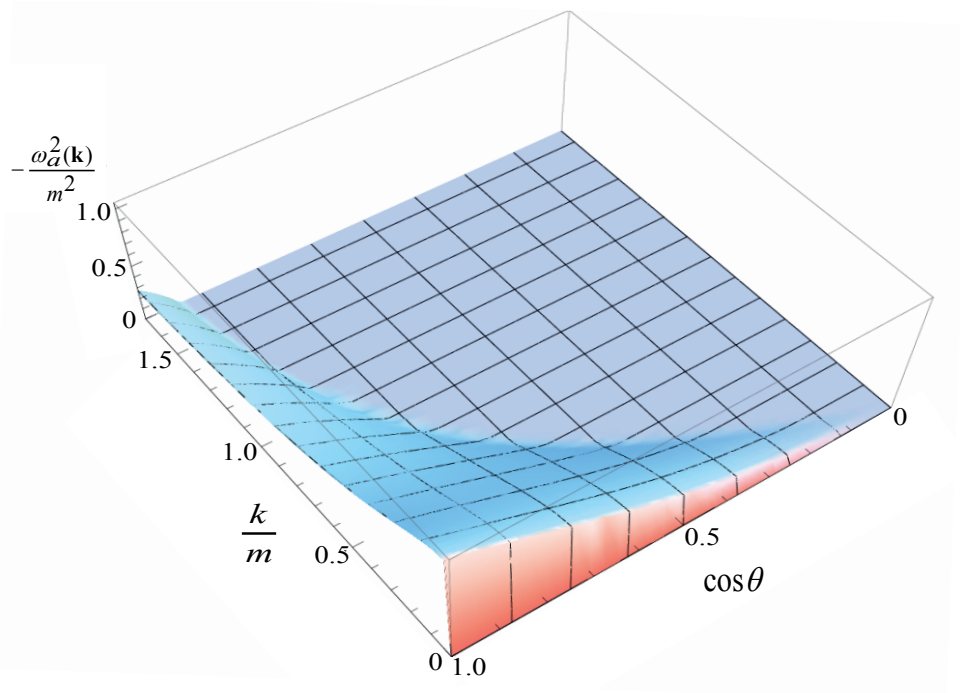


FIGURE 2.24: Unstable A -mode for the extremely oblate plasma: $-\omega_a^2$ as functions of k and $\cos\theta$ in the domain where the mode exists. The angle θ is between the vectors \mathbf{k} and \mathbf{n}

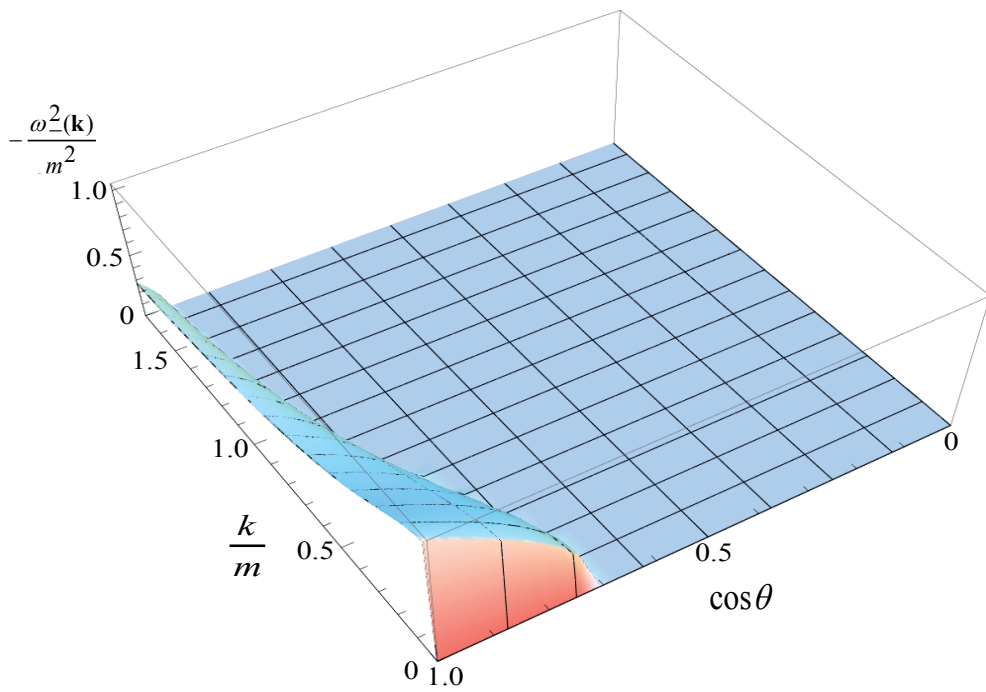


FIGURE 2.25: Unstable G -modes for the extremely oblate plasma: ω_-^2 as functions of k and $\cos\theta$ in the domain where the mode exists. The angle θ is between the vectors \mathbf{k} and \mathbf{n} .

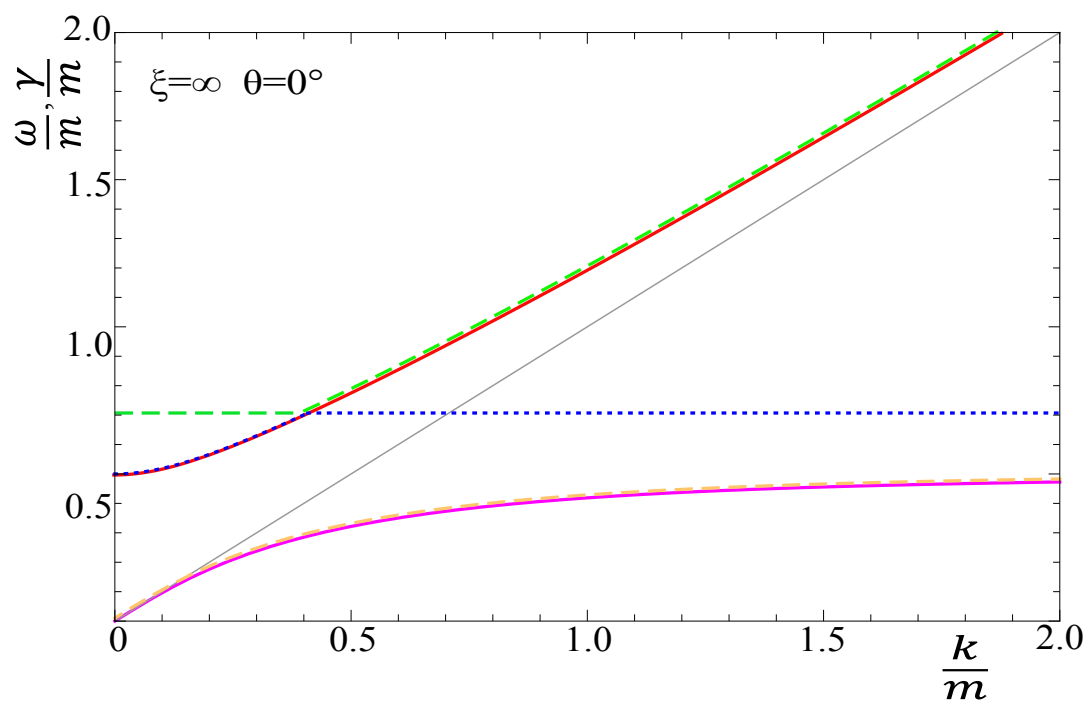


FIGURE 2.26: Dispersion curves of plasmons in extremely oblate plasma for $\theta = 0^\circ$.

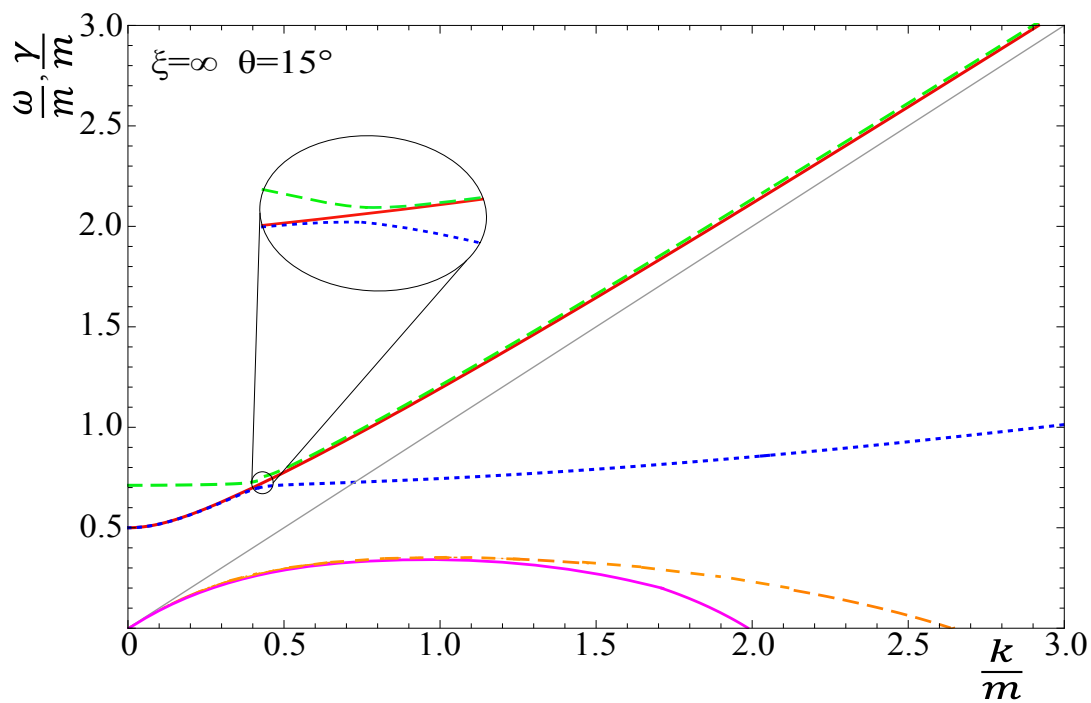


FIGURE 2.27: Dispersion curves of plasmons in extremely oblate plasma for $\theta = 15^\circ$.

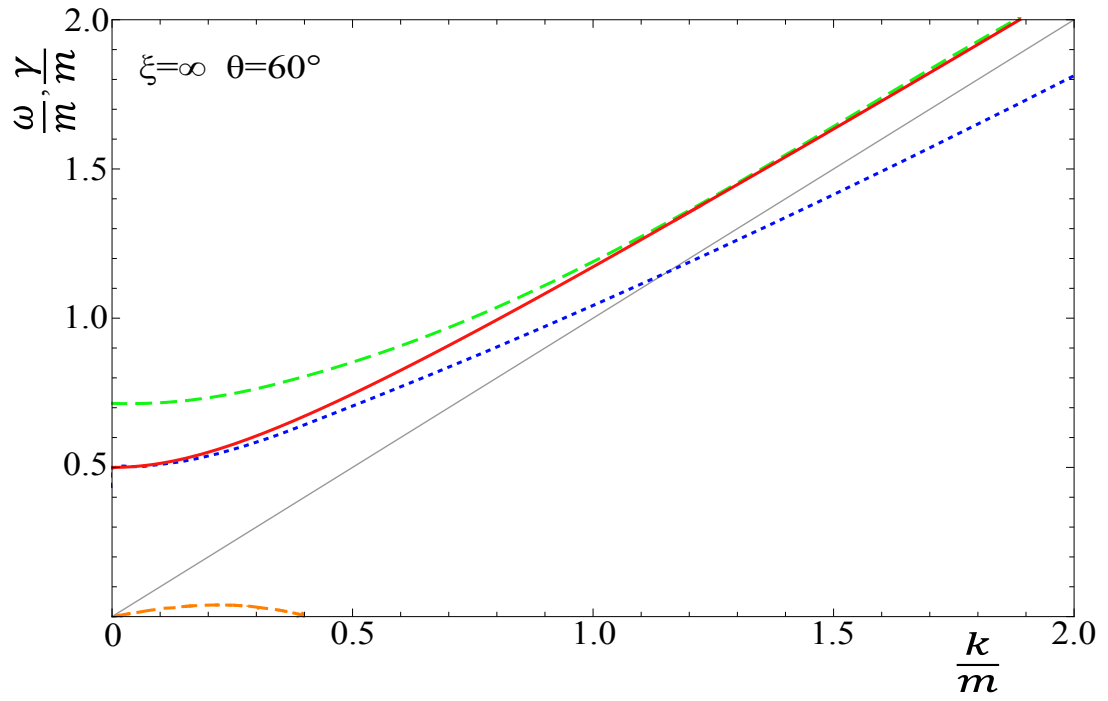


FIGURE 2.28: Dispersion curves of plasmons in extremely oblate plasma for $\theta = 60^\circ$.

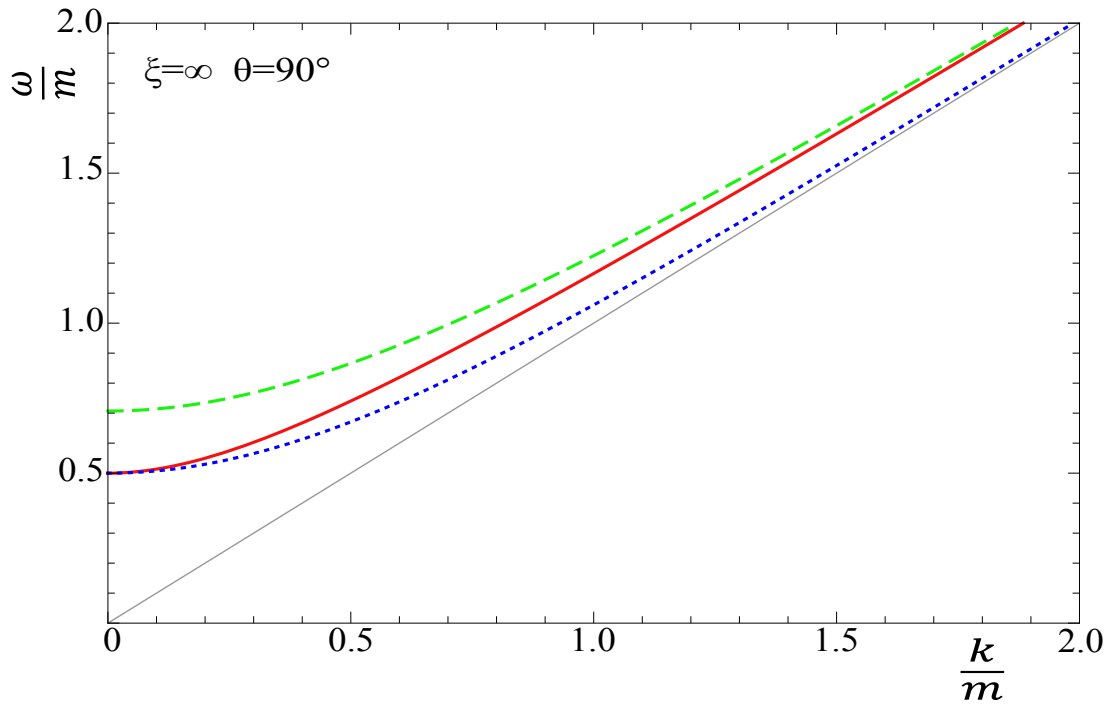


FIGURE 2.29: Dispersion curves of plasmons in extremely oblate plasma for $\theta = 90^\circ$.

2.8.1 Special case: $\mathbf{k} \parallel \mathbf{n}$

We consider $\mathbf{k} = (0, 0, k)$ parallel to $\mathbf{n} = (0, 0, 1)$. In this case, the vector \mathbf{n}_T , which is defined by Eq. (2.1.6), vanishes. The decomposition using the basis A, B, C, D , which is introduced in Sec. 2.1.2, is therefore singular. However, since there is only one independent vector in this case, one can decompose the inverse propagator or dielectric tensor using the same basis as in the isotropic case (2.3.8). One finds easily

$$\alpha(\omega, \mathbf{k}) = \frac{m^2}{2} - \frac{m^2(\omega^2 - k^2)}{4\omega^2}, \quad (2.8.10)$$

$$\beta(\omega, \mathbf{k}) = \frac{m^2}{2}. \quad (2.8.11)$$

Alternatively, one can obtain these results in a straightforward way from the dielectric tensor (2.1.4) which can be easily computed. For the extremely oblate distribution, $\mathbf{v} \perp \mathbf{k}$ and the denominators of the second and third terms in the integrand in Eq. (2.1.4) are ω and ω^2 , respectively. Observing further that the second term of the integral vanishes due to azimuthal symmetry, the dielectric tensor is diagonal. It is easy to show that the matrix Σ equals

$$\Sigma(\omega, \mathbf{k}) = \begin{bmatrix} \omega^2 - k^2 - \alpha(\omega, \mathbf{k}) & 0 & 0 \\ 0 & \omega^2 - k^2 - \alpha(\omega, \mathbf{k}) & 0 \\ 0 & 0 & \omega^2 - \beta(\omega, \mathbf{k}) \end{bmatrix}. \quad (2.8.12)$$

The structure of the matrix Σ given by Eq. (2.8.12) is similar to the isotropic case (2.2.13), except that the matrix components 11 and 33 are interchanged because the wave vector was chosen as $\mathbf{k} = (k, 0, 0)$ in Sec. 2.2. The conclusion is therefore the same as for isotropic plasma: the solutions of the dispersion equation $\omega^2 - k^2 - \alpha(\omega, \mathbf{k}) = 0$ are transverse modes, which appear twice, and the solutions to $\omega^2 - \beta(\omega, \mathbf{k}) = 0$ are longitudinal modes. Using Eq. (2.8.10) it is easy to find the dispersion relations which are

$$\begin{aligned} \omega_\alpha^2(k) &= \frac{1}{2} \left(\frac{1}{4} m^2 + k^2 + \sqrt{\left(\frac{1}{4} m^2 + k^2 \right)^2 + m^2 k^2} \right) \\ &\approx \begin{cases} \frac{1}{4} m^2 + 2k^2 & \text{for } m^2 \gg k^2, \\ k^2 & \text{for } m^2 \ll k^2, \end{cases} \end{aligned} \quad (2.8.13)$$

$$\omega_{\alpha i}^2(k) = \frac{1}{2} \left(\frac{1}{4} m^2 + k^2 - \sqrt{\left(\frac{1}{4} m^2 + k^2 \right)^2 + m^2 k^2} \right)$$

$$\approx \begin{cases} -k^2 & \text{for } m^2 \gg k^2, \\ -\frac{1}{4} m^2 & \text{for } m^2 \ll k^2, \end{cases} \quad (2.8.14)$$

$$\omega_{\beta}^2(k) = \frac{1}{2} m^2. \quad (2.8.15)$$

Both ω_{α} and ω_{β} are real solutions which exist for all k , and $\omega_{\alpha i} = i\gamma$ is an imaginary solution which also exists for all k . The maximum of the imaginary frequency is $\gamma_{\max} = m/2$.

From Eqs. (2.8.8) and (2.8.9) the maximal number of solutions in extremely oblate plasma is 10. When $\mathbf{k} \parallel \mathbf{n}$, we have $\theta = 0^\circ$ which means k_{oA} and k_{oG} both approach infinity. Therefore, our analysis of the special case $\mathbf{k} \parallel \mathbf{n}$ should produce the maximal number of solutions. Remembering that the transverse (α) modes are doubled, Eqs. (2.8.13)-(2.8.15) correspond to 10 solutions.

The solutions ω_{α}^2 and ω_{β}^2 cross each other at

$$k^2 = k_c^2 \equiv \frac{m^2}{6}. \quad (2.8.16)$$

Let us define two combinations of the real solutions:

$$\omega_{-}^2(k) = \begin{cases} \omega_{\alpha}^2(k) & \text{for } k < k_c, \\ \omega_{\beta}^2(k) & \text{for } k > k_c, \end{cases} \quad (2.8.17)$$

$$\omega_{+}^2(k) = \begin{cases} \omega_{\beta}^2(k) & \text{for } k < k_c, \\ \omega_{\alpha}^2(k) & \text{for } k > k_c. \end{cases} \quad (2.8.18)$$

The dispersion curves are shown on the Fig. 2.26. The modes denoted ω_{-} and ω_{+} are represented, respectively, by the blue (dotted) and green (dashed) lines. As will be explained in the next section, the modes ω_{+} and ω_{-} are physical in the sense that one can obtain them by taking the limit $\theta \rightarrow 0^\circ$ of the solutions with the same names which were found at $\theta > 0^\circ$.

2.8.2 Special case: \mathbf{k} almost parallel to \mathbf{n}

When the wave vector is not exactly along the z -axis but is slightly tilted, the spectrum of collective modes is changed qualitatively. To discuss this case we assume that the wave vector has a small x component $k_x = k \sin \theta \approx k\theta$. The matrix Σ , which for $\theta = 0^\circ$ is given by Eq. (2.8.12), now contains small off-diagonal components $\sim k^2\theta$ and is given by

$$\Sigma(\omega, \mathbf{k}) = \begin{bmatrix} -k^2 + \omega^2 - \frac{m^2}{2} + \frac{m^2(\omega^2 - k^2)}{4\omega^2} & 0 & k^2\theta \\ 0 & -k^2 + \omega^2 - \frac{m^2}{2} + \frac{m^2(\omega^2 - k^2)}{4\omega^2} & 0 \\ k^2\theta & 0 & \omega^2 - \frac{m^2}{2} \end{bmatrix}. \quad (2.8.19)$$

Computing the determinant of Σ , one finds two dispersion equations. The first reproduces the α modes in Eq. (2.8.13), and the solutions are doubled as was the case for \mathbf{k} parallel to \mathbf{n} . The second dispersion equation can be written as

$$\frac{1}{\omega^2} (\omega^2 - \omega_\alpha^2(k)) (\omega^2 - \omega_{\alpha i}^2(k)) (\omega^2 - \omega_\beta^2(k)) = k^4\theta^2. \quad (2.8.20)$$

When $\theta = 0^\circ$ we clearly recover the solutions of the previous section. Since the mode $\omega_{\alpha i}^2$ does not cross either ω_α^2 or ω_β^2 , we express it as $\omega_{\alpha i}^2 = -\gamma^2$ and rewrite Eq. (2.8.20) in the form

$$(\omega^2 - \omega_\alpha^2(k)) (\omega^2 - \omega_\beta^2(k)) = \epsilon, \quad (2.8.21)$$

where $\epsilon \equiv \frac{\omega^2 k^4 \theta^2}{\omega^2 + \gamma^2}$. We want to look at the modes ω_α and ω_β in the vicinity of the point where they cross. To lowest order in deviations from the solutions with $\theta = 0^\circ$, we take ϵ as constant and solve the quadratic equation to obtain

$$\omega_-^2 = \frac{1}{2} \left(\omega_\alpha^2 + \omega_\beta^2 - \sqrt{(\omega_\alpha^2 - \omega_\beta^2)^2 + 4\epsilon} \right), \quad (2.8.22)$$

$$\omega_+^2 = \frac{1}{2} \left(\omega_\alpha^2 + \omega_\beta^2 + \sqrt{(\omega_\alpha^2 - \omega_\beta^2)^2 + 4\epsilon} \right). \quad (2.8.23)$$

From these expressions, it is clear that the small parameter ϵ plays a role only in the vicinity of the crossing point where $\omega_\alpha = \omega_\beta$. We note that $\epsilon \geq 0$ as both ω_α^2 and ω_β^2 are positive. Assuming that $(\omega_\alpha^2 - \omega_\beta^2)^2 \gg \epsilon$, we expand the square roots in the formulae

(2.8.22) and (2.8.23) to obtain

$$\omega_-^2(k) = \begin{cases} \omega_\alpha^2(k) - \frac{\epsilon}{|\omega_\alpha^2 - \omega_\beta^2|} & \text{for } k < k_c, \\ \omega_\beta^2(k) - \frac{\epsilon}{|\omega_\alpha^2 - \omega_\beta^2|} & \text{for } k > k_c, \end{cases} \quad (2.8.24)$$

$$\omega_+^2(k) = \begin{cases} \omega_\beta^2(k) + \frac{\epsilon}{|\omega_\alpha^2 - \omega_\beta^2|} & \text{for } k < k_c, \\ \omega_\alpha^2(k) + \frac{\epsilon}{|\omega_\alpha^2 - \omega_\beta^2|} & \text{for } k > k_c. \end{cases} \quad (2.8.25)$$

This result shows that the modes ω_-^2 and ω_+^2 approach each other at $k = k_c$ but do not cross. This is phenomenon of mode coupling already encountered in Sec. 2.3.2. One can also show that the double imaginary mode $\omega_{\alpha i}$ splits into two different modes when θ is finite.

The complete spectrum is presented on the Fig. 2.27 for $\theta = 15^\circ$. As shown in the inset, the ω_+ and ω_- modes approach each other at $k = k_c$ but do not cross. The number of modes is the same as for the extremely oblate distribution with arbitrary values of θ .

2.8.3 Special case: $\mathbf{k} \perp \mathbf{n}$

When $\mathbf{k} \perp \mathbf{n}$, the wave vector can be written as $\mathbf{k} = k(\cos \phi, \sin \phi, 0)$ and therefore the system can be treated as effectively two-dimensional *isotropic* in the $x-y$ plane. From Eqs. (2.8.6)-(2.8.7) we see that both of the critical wave vectors k_{oA} and k_{oG} go to zero in the limit $\theta \rightarrow 90^\circ$ and therefore the two imaginary modes disappear, as expected for an isotropic system. There should be two real solutions (one pair) from the A -mode dispersion equation (2.1.18) and four real solutions (two pairs) from the G -mode equation (2.1.19).

When $x \equiv \cos \theta = 0$, the coefficients (2.8.1), (2.8.2), (2.8.3), and (2.8.4) simplify to

$$\alpha(\omega, \mathbf{k}) = \frac{m^2 \omega^2}{2 k^2} \left[1 - \frac{\sqrt{\omega^2 - k^2}}{\omega} \right], \quad (2.8.26)$$

$$\beta(\omega, \mathbf{k}) = \frac{m^2 \omega^2}{2 k^2} \left[\frac{\omega}{\sqrt{\omega^2 - k^2}} - 1 \right], \quad (2.8.27)$$

$$\gamma(\omega, \mathbf{k}) = \frac{m^2 \omega^2 - k^2}{2 k^2} \left[\frac{\omega}{\sqrt{\omega^2 - k^2}} - 1 \right], \quad (2.8.28)$$

$$\delta(\omega, \mathbf{k}) = 0, \quad (2.8.29)$$

where $\omega \in \mathbb{R}$ and $\omega^2 > k^2$.

Since $\delta(\omega, \mathbf{k}) = 0$, the second dispersion equation factors into two equations, as in the case of the weakly anisotropic plasma discussed in Sec. 2.5, and we solve the dispersion equations for A -modes, B -modes, and C -modes (2.1.18), (2.5.3) and (2.5.4). The A -mode dispersion equation (2.1.18) has the form

$$(\omega^2 - k^2)k^2 + \frac{m^2}{2} \left[\omega \sqrt{\omega^2 - k^2} - \omega^2 \right] = 0, \quad (2.8.30)$$

which is quadratic in ω^2 and can be solved analytically. The solution is

$$\begin{aligned} \omega_\alpha^2(k) &= \frac{m^4 + 4m^2k^2 - 8k^4 + m^3\sqrt{m^2 + 8k^2}}{8(m^2 - k^2)} \\ &\approx \begin{cases} \frac{1}{4}m^2 + \frac{5}{4}k^2 & \text{for } m^2 \gg k^2, \\ k^2 & \text{for } m^2 \ll k^2. \end{cases} \end{aligned} \quad (2.8.31)$$

The B -mode dispersion equation (2.5.3) simplifies to

$$k^2 + \frac{m^2}{2} \left[1 - \frac{\omega}{\sqrt{\omega^2 - k^2}} \right] = 0, \quad (2.8.32)$$

and the solution gives the longitudinal mode

$$\omega_\beta^2(k) = \frac{\left(\frac{m^2}{2} + k^2\right)^2}{m^2 + k^2} \approx \begin{cases} \frac{1}{4}m^2 + \frac{3}{4}k^2 & \text{for } m^2 \gg k^2, \\ k^2 & \text{for } m^2 \ll k^2. \end{cases} \quad (2.8.33)$$

Finally, the C -mode dispersion equation (2.5.4) becomes

$$\omega^2 - k^2 - \frac{m^2}{2} = 0, \quad (2.8.34)$$

which produces the solution

$$\omega_{\alpha\gamma}^2(k) = \frac{1}{2}m^2 + k^2. \quad (2.8.35)$$

These real solutions are the limits $\theta \rightarrow 90^\circ$ of those found for arbitrary angles by solving numerically the G -mode dispersion equation (2.1.19). The solution $\omega_{\alpha\gamma}$ is the larger of the two real G -modes (which we call ω_+) and ω_β is the smaller G -mode (called ω_-) which stays above the light cone for all k when $\theta = 90^\circ$. The dispersion curves for $\mathbf{k} \perp \mathbf{n}$ are shown on the Fig. 2.29.

The spectrum of the extremely oblate system coincides with that of large but finite ξ . We also note that the limit $\xi \rightarrow \infty$ is approached much more quickly than the limit $\sigma \rightarrow \infty$, which was discussed at the end of Sec. 2.7. In order to compare the two limits, we consider the same example: the coefficient $\alpha(\omega, \mathbf{k} = 0)$ which is the mass of A -mode.

Using the ξ -distribution (2.4.1) we find

$$\alpha_\xi(\omega, \mathbf{k} = 0) = \frac{m^2}{4} \frac{C_\xi}{\sqrt{\xi}} \left[\left(1 - \frac{1}{\xi}\right) \text{Arctan} \sqrt{\xi} + \frac{1}{\sqrt{\xi}} \right], \quad (2.8.36)$$

and for $\xi \gg 1$ we have

$$\alpha_\xi(\omega, \mathbf{k} = 0) \approx \frac{m^2}{4} \left(1 + \frac{2}{\pi\sqrt{\xi}}\right). \quad (2.8.37)$$

From this expression we find that for $\xi = 10^4$ the coefficient $\alpha_\xi(\omega, \mathbf{k} = 0)$ differs from the extremely oblate limit ($\xi \rightarrow \infty$) by only 0.6%. In comparison, $\alpha_\sigma(\omega, \mathbf{k} = 0)$ differs from the extremely prolate limit by 10% (see Eq. (2.7.11)).

2.9 Nyquist analysis

A Nyquist analysis allows one to determine the number of solutions of a given equation without solving the equation. Knowing the number of solutions is very important for our analysis of plasmons, because in all cases except that of the two-stream and extremely prolate distribution, it is not possible to obtain general exact analytic solutions of the dispersion equations. In some cases we have used analytic approximations, and in others we have found solutions numerically. When an approximation is used, there is a danger to find solutions that are artifacts of the approximation. When numerical methods are used, a solution that is outside the range of the search can be missed.

To explain the idea of a Nyquist analysis, we discuss a generic equation of the form

$$f(\omega) = 0, \quad (2.9.1)$$

and we define the function

$$F(\omega) \equiv \frac{f'(\omega)}{f(\omega)} = \frac{d}{d\omega} \ln f(\omega). \quad (2.9.2)$$

We consider the contour integral

$$\oint_C \frac{d\omega}{2\pi i} F(\omega), \quad (2.9.3)$$

where the contour is a positively (anticlockwise) oriented closed loop, which is chosen so that $F(\omega)$ is analytic inside the loop except at isolated points. The integral is equal to the sum of the residues. It is straightforward to show that the residue of $F(\omega)$ at a zero of $f(\omega)$ of order l is l , and the residue of $F(\omega)$ at a pole of $f(\omega)$ of order l is $-l$. Thus, we have

$$\oint_C \frac{d\omega}{2\pi i} F(\omega) = n_Z - n_P, \quad (2.9.4)$$

where n_Z and n_P are the numbers of zeros and poles of $f(\omega)$ inside the contour C , taking into account the fact that each zero and pole of order l is counted l times. Our aim is to determine n_Z . The first step in the Nyquist analysis is to choose the contour C . If $f(\omega)$ has only isolated singular points, then C can be chosen as the big circle which includes the entire plane of complex ω . If $f(\omega)$ has cuts, then the contour must be chosen to exclude these cuts. For example, for isotropic plasma, which is discussed in Sec. 2.9.1, $f(\omega)$ has a cut for $\omega \in [-k, k]$ and consequently the contour C is chosen as in Fig. 2.30.

For all of the momentum distributions, except the two-stream and extremely prolate cases, we have considered in this chapter, the dispersion equation has a cut along the real axis. The contours we will use in the Nyquist analysis of all dispersion equations are all

similar to Fig. 2.30, but the length of the cut depends on the particular distribution. The integrals along the lines connecting the circular contour C_∞ to C_{cut} always compensate each other and therefore the contour integral (2.9.4) equals

$$\oint_{C_\infty} \frac{d\omega}{2\pi i} F(\omega) + \oint_{C_{\text{cut}}} \frac{d\omega}{2\pi i} F(\omega) = n_Z - n_P. \quad (2.9.5)$$

The contribution from the big circle is easy to calculate by writing $\omega = |\omega|e^{i\phi}$ and taking $|\omega| \rightarrow \infty$. Using $d\omega = i\omega d\phi$, we have

$$\oint_{C_\infty} \frac{d\omega}{2\pi i} F(\omega) = \lim_{|\omega| \rightarrow \infty} \omega F(\omega) \equiv n_\infty. \quad (2.9.6)$$

The integral along the cut can be calculated using the fact that $F(\omega)$, defined by Eq. (2.9.2), is the logarithmic derivative of $f(\omega)$. Consequently

$$\oint_{C_{\text{cut}}} \frac{d\omega}{2\pi i} F(\omega) = \frac{1}{2\pi i} \oint_{C_{\text{cut}}} \frac{d}{d\omega} \ln f(\omega) = \frac{1}{2\pi i} \left(\ln f(\omega_e) - \ln f(\omega_s) \right) \equiv n_W, \quad (2.9.7)$$

where ω_s is the (arbitrarily chosen) starting point of the contour which encloses the cut, and ω_e is the end point. The points ω_s and ω_e have the same modulus, but their phases differ by 2π . The value of the right-hand-side of Eq. (2.9.7) can be found by mapping the closed contour C_{cut} in the plane of complex ω onto a path in the plane of complex $f(\omega)$. Since the logarithm of f has a cut, which runs along the real axis from $f = -\infty$ to $f = 0$, the value of the integral (2.9.7) is a *winding number* (denoted n_W) which equals the number of times that the curve in the plane of complex f , which starts at $f(\omega_s)$ and ends at $f(\omega_e)$, travels counterclockwise around the point $f = 0$.

Combining the results (2.9.6) and (2.9.7), we rewrite Eq. (2.9.5) as

$$n_Z = n_P + n_\infty + n_W, \quad (2.9.8)$$

which tells us that the number of zeros of the function $f(\omega)$ inside the contour C equals the number of poles of $f(\omega)$ inside this contour, plus n_∞ given by the limit (2.9.6), plus the winding number (2.9.7). In the following subsections we show how to evaluate the numbers n_P , n_∞ and n_W for the dispersion equations under study. In each case, the only difficult piece is the calculation of n_W , for which we will need to determine the signs of the real and imaginary parts of the function $f(\omega)$ along the contour C_{cut} .

To illustrate the procedure, we will produce graphs of $f(\omega)$ using the following conventions. We plot $f(\omega)$ as a function of ω along the cut for various choices of the angle θ . The real part of $f(\omega)$ is the same whether ω has a positive or negative infinitesimal imaginary part, and is represented as a red (solid) line. The imaginary part with positive

infinitesimal imaginary part (values of ω along the top of the cut) is a blue (dotted) line, and for negative infinitesimal imaginary part (on the bottom of the cut) it is a green (dashed) line.

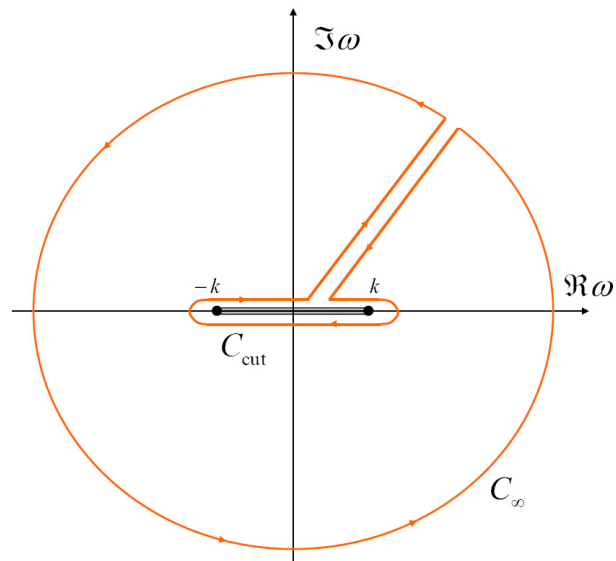


FIGURE 2.30: The contour C in the plane of complex ω which is used to compute the number of solutions of some dispersion equations.

2.9.1 Isotropic plasma

We start with the familiar case of isotropic plasma. It is instructive to see how the Nyquist analysis works in this case for which the answer is known. The function $f(\omega)$ for (transverse) A -modes and (longitudinal) B -modes is given by equations (2.2.9) and (2.2.10), respectively. The coefficients $\alpha_{\text{iso}}(\omega, \mathbf{k})$ and $\beta_{\text{iso}}(\omega, \mathbf{k})$ (given by Eqs. (2.2.2), (2.2.3)) have cuts for $\omega \in [-k, k]$, which means that the contour C should be chosen as in Fig. 2.30. In both cases, $f(\omega)$ does not have any poles inside the contour, and therefore $n_P = 0$. Using Eq. (2.9.6) it is straightforward to show that $n_\infty = 2$ for A -modes and $n_\infty = 0$ for B -modes.

The winding number n_W is calculated from Eq. (2.9.7) by mapping the contour C_{cut} in the plane of complex ω onto the plane of complex $f(\omega)$. In Fig. 2.33, and 2.34 we show the real and imaginary parts of $f(\omega)$ as functions of ω , considering only values of ω which lie infinitesimally above and below the cut. The structure of the graph reflects the well known symmetry properties of the dielectric functions (2.2.11)

$$\Re \varepsilon_{L,T}(-\omega, \mathbf{k}) = \Re \varepsilon_{L,T}(\omega, \mathbf{k}), \quad \Im \varepsilon_{L,T}(-\omega, \mathbf{k}) = -\Im \varepsilon_{L,T}(\omega, \mathbf{k}). \quad (2.9.9)$$

We move around the cut shown in Fig. 2.30 in the counter-clockwise direction, using the data presented in Fig. 2.33, and 2.34. We describe the process of mapping for A -modes. Let us start, for example, at the top left corner of the cut where $\omega = -k + i0^+$. The red (solid) line in Fig. 2.33 tells us that the real part of the dispersion equation at this value of ω is negative, and the blue (dotted) curve tells us that the imaginary part is also negative. Combining these results, $f(\omega = -k + i0^+)$ is found to be in the third quadrant of its complex plane, as shown in the bottom left corner of Fig. 2.31. Continuing in the same fashion, one produces the map shown in Fig. 2.31 where the point $f = 0$ is circumnavigated zero times. Equivalently, the cut of the function $\ln f$ is crossed twice in each direction, so that $\ln f$ remains on the same Riemann sheet, and consequently the integral (2.9.7) vanishes. The conclusion is that the winding number n_W equals zero. The equivalent mapping for B -modes is shown in Fig. 2.32. In this case, the circular trajectory is shifted to the right so that the origin is enclosed within the loop. The mapping circumnavigates the origin twice, and the winding number is therefore $n_W = 2$.

Combining the results derived above, Eq. (2.9.8) gives

$$\begin{aligned} A - \text{modes} : \quad n_Z &= 0 + 2 + 0 = 2, \\ B - \text{modes} : \quad n_Z &= 0 + 0 + 2 = 2, \end{aligned} \quad (2.9.10)$$

which agrees with the known result that the dispersion equations for (transverse) A -modes and (longitudinal) B -modes both have two solutions (one pair of positive and negative real solutions).

We note that for B -modes, the non-zero winding number is obtained because the circular trajectory in Fig. 2.32 is shifted to the right so that the origin is inside the loop, or equivalently, because the real part of $f(\omega = 0)$ is positive. In the following sections we will see that for anisotropic plasmas (except in the case of the extremely prolate distribution) there are cases for which $f(\omega = 0) > 0$, $n_W \neq 0$, and extra solutions to the dispersion equations appear, when a specific condition on the wave vector \mathbf{k} is satisfied. These extra solutions are imaginary modes, which do not exist in isotropic plasmas. We comment that the Nyquist analysis itself can only tell us the number of solutions of a given equation but gives no information about the nature (real, imaginary or complex) of these solutions.

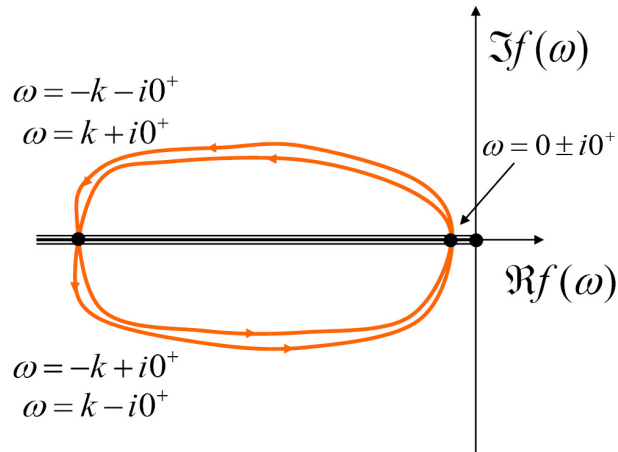


FIGURE 2.31: The mapping of the contour C_{cut} onto the path in complex $f(\omega)$ for isotropic plasma. Plot shows the mapping for the A -mode dispersion equation.

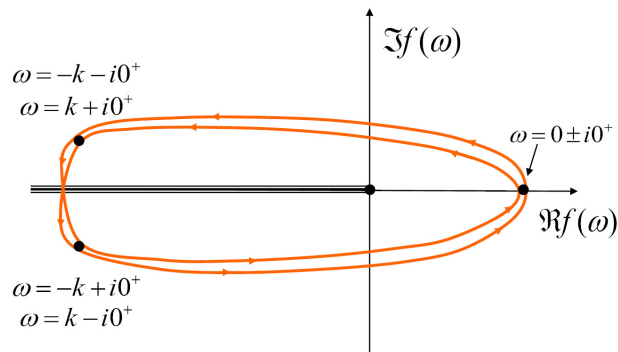


FIGURE 2.32: The mapping of the contour C_{cut} onto the path in complex $f(\omega)$ for isotropic plasma. Plot shows the mapping for the B -mode dispersion equation.

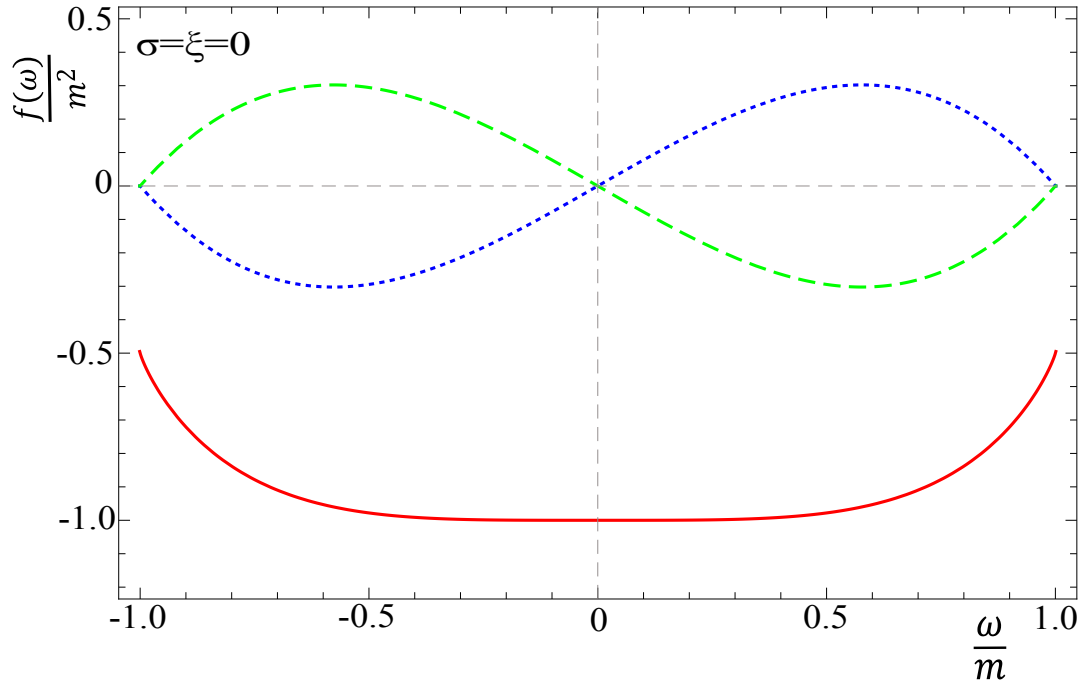


FIGURE 2.33: The real and imaginary parts of $f(\omega)$ for A-modes in isotropic plasma for $k/m = 1$ and ω along the cut.

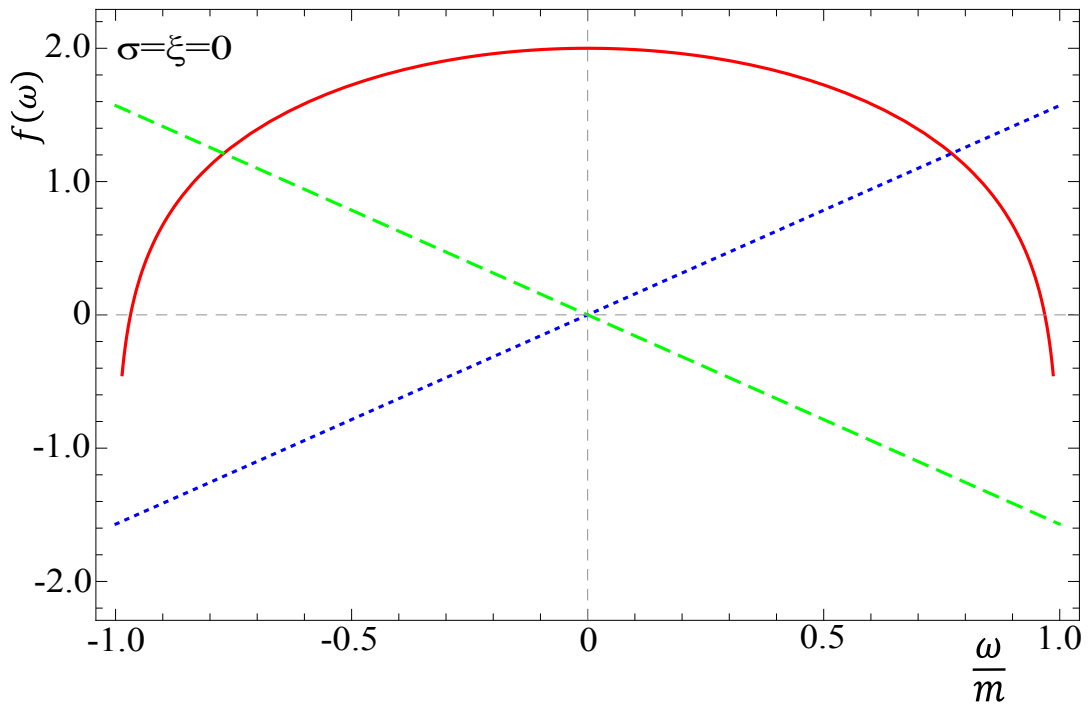


FIGURE 2.34: The real and imaginary parts of $f(\omega)$ for B-modes in isotropic plasma for $k/m = 1$ and ω along the cut.

2.9.2 Weakly anisotropic plasma

In the case of a weakly anisotropic plasma, there are three dispersion equations (2.1.18), (2.5.3), and (2.5.4) whose solutions give A -, B - and C -modes. The components α , β , γ of the polarization tensor are given in Sec. 2.5. We first note that the analytic structure of $f(\omega)$ in all three cases is the same as for isotropic plasma, and therefore we can use the contour shown in Fig. 2.30. For all three equations there are no poles inside the contour, which means $n_P = 0$.

We start by considering Eq. (2.5.3) which produces B -modes. It is easy to show that $n_\infty = 0$, as for the isotropic case. The mapping of the cut into the complex plane of $f(\omega)$ also looks like the mapping for the isotropic case (Fig. 2.32), and therefore $n_W = 2$, also as for the isotropic case. The conclusion is that there are 2 solutions - the same as for longitudinal modes in isotropic plasmas.

Now we consider A -modes and C -modes. Equation (2.9.6) gives $n_\infty = 2$ in both cases, and therefore equation (2.9.8) tells us that the number of solutions is $n_Z = 2 + n_W$. For isotropic A -modes we showed in the previous section that $f(\omega = 0) \leq 0$ for any \mathbf{k} , $n_W = 0$, and the number of solutions is always 2. We will show below that for anisotropic plasmas with arbitrarily small ξ , for both A -modes and C -modes, there are wave vectors for which $f(\omega = 0) > 0$, $n_W > 0$, and additional solutions appear.

For the A -mode and C -mode dispersion equations, $f(\omega = 0)$ can be either negative or positive depending on the length and orientation of the wave vector \mathbf{k} . Two examples are shown in Fig. 2.35, and 2.36 for A -modes. When $f(\omega = 0) \leq 0$, as in Fig. 2.35, the mapping of the contour C_{cut} in the plane of complex ω onto the plane of complex $f(\omega)$ looks qualitatively like in Fig. 2.31 and we have $n_W = 0$. When $f(\omega = 0) > 0$, as shown in Fig. 2.36, the mapping looks like Fig. 2.32, and $n_W = 2$. The corresponding analysis of C -modes is qualitatively similar.

We can find analytically the condition that distinguishes the case of $n_W = 0$ from that of $n_W = 2$. Using Eqs. (2.2.2), (2.5.5), (2.5.7), one obtains

$$A - \text{modes} : \quad f(\omega = 0) = -k^2 + \xi \frac{m^2}{3} \cos^2 \theta, \quad (2.9.11)$$

$$C - \text{modes} : \quad f(\omega = 0) = -k^2 - \xi \frac{m^2}{3} (1 - 2 \cos^2 \theta). \quad (2.9.12)$$

From these expressions we can derive a critical value of the magnitude of the wave vector (as a function of θ) at which $f(\omega = 0)$ becomes positive and the winding number changes from 0 to 2. These critical values are denoted k_A and k_C and given in Eqs. (2.5.12), (2.5.22). The number of solutions of the A -mode dispersion equation is either 2

or 4, depending on whether k is smaller or greater than k_A , and the C -mode dispersion equation has either 2 or 4 solutions, depending on whether k is smaller or greater than k_C . These results agree with Eqs. (2.5.25), (2.5.27).

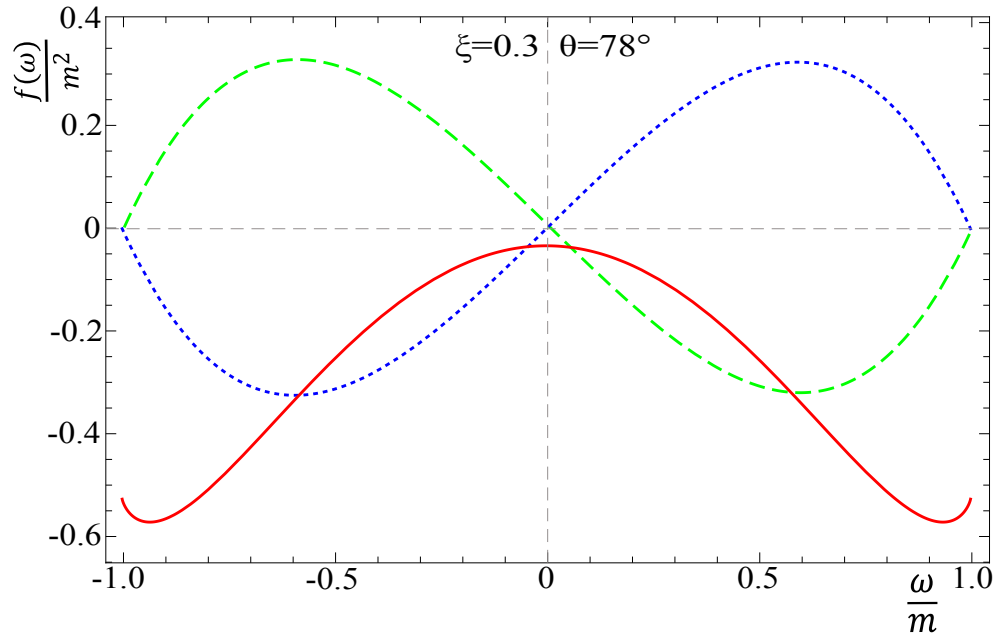


FIGURE 2.35: The real and imaginary parts of $f(\omega)$ for A -modes in weakly anisotropic plasma with $\xi = 0.3$ for ω along the cut where $k/m = 0.2$ and $\theta = 78^\circ$.

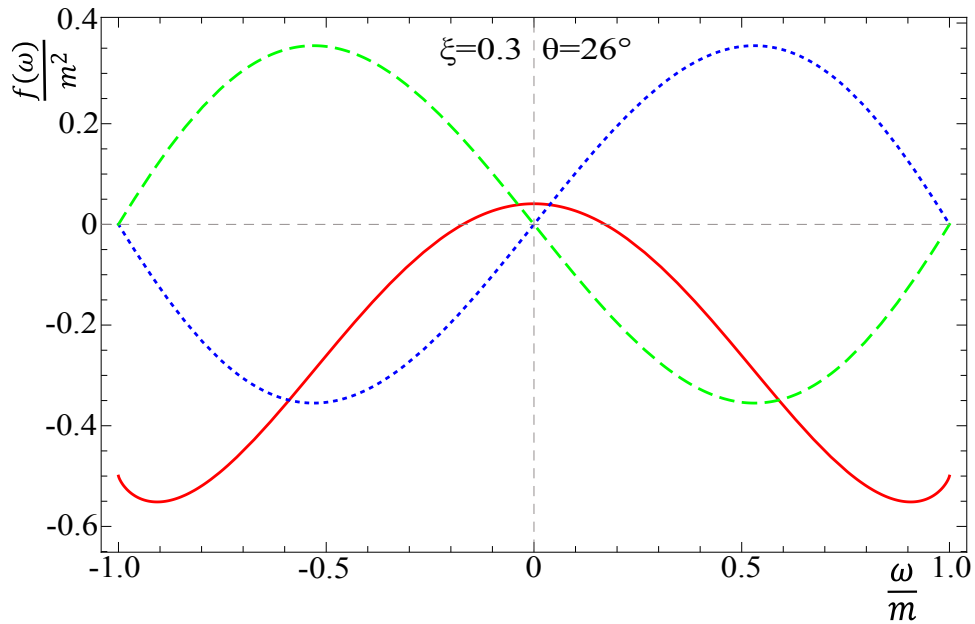


FIGURE 2.36: The real and imaginary parts of $f(\omega)$ for A -modes in weakly anisotropic plasma with $\xi = 0.3$ for ω along the cut where $k/m = 0.2$ and $\theta = 26^\circ$.

2.9.3 Extremely prolate plasma

A Nyquist analysis is not necessary for the extremely prolate system, because one can find exact analytic solutions (2.7.6), (2.7.7), and (2.7.8) to the dispersion equations (2.1.18), (2.1.19), and therefore there is no possibility that solutions have been missed. The extremely prolate distribution is interesting for a different reason however. There is a qualitative difference between the numerical solutions found using the σ -distribution (2.4.6) with very large values of σ and the solutions obtained from the extremely prolate distribution, which corresponds to $\sigma \rightarrow \infty$. The analogous statement is not true for the ξ -distribution. In order to understand this point, we have done a Nyquist analysis of the extremely prolate case.

The analysis of the A -mode dispersion equation (2.1.18) is completely trivial. The function $f(\omega)$ has no poles and no cuts, and therefore we choose the contour as a big circle that includes the whole complex plane. Equation (2.1.18) has two solutions, $n_Z = n_\infty = 2$. In the case of the G -mode dispersion equation (2.1.19), there are no cuts, the contour is chosen as the same big circle, and the winding number is zero. The function $f(\omega)$ has two double poles at $\omega = \pm \mathbf{k} \cdot \mathbf{n}$ and thus $n_P = 2 \times 2 = 4$. From the definition (2.9.6) one obtains $n_\infty = 2$. Combining these results, Eq. (2.9.8) gives $n_Z = 6$. Adding the A -modes and G -modes together we reproduce the result from Sec. 2.7, that the extremely prolate system has a total of 8 solutions at all wave vectors, in contrast to the system with very large prolate anisotropy, which has 8 solutions only for certain wave vectors.

The important point is that the analytic properties of the left-hand-side of the G -mode dispersion equation (2.1.19) as a function of ω change when $\sigma \rightarrow \infty$. In this limit, the cut singularity at $\omega \in [-k, k]$ changes into double poles at $\omega = \pm \mathbf{k} \cdot \mathbf{n}$. For σ very large but finite, there is a contribution to n_Z from $n_W = 2$ for $k < k_{pG}$ (see Eq. (2.7.9)). When $\sigma \rightarrow \infty$, the cut, and therefore also the winding number, disappears, but n_Z acquires a contribution from n_P which exists for all k . Therefore the limit $\sigma \rightarrow \infty$ produces the same number of solutions as the $k < k_{pG}$ region of the large σ distribution, but not the $k > k_{pG}$ region. There are always 8 solutions of the dispersion equations in case of extremely prolate plasma, and there are 8 or 6 solutions for large σ depending whether or not the condition $k < k_{pG}$ is satisfied.

2.9.4 Extremely oblate plasma

The A -modes are obtained from the dispersion equation (2.1.18) with the coefficient $\alpha(\omega, \mathbf{k})$ given by Eq. (2.8.1). The function $\Delta_A^{-1}(\omega, \mathbf{k}) \equiv \omega^2 - \mathbf{k}^2 - \alpha(\omega, \mathbf{k})$ equals

$$\Delta_A^{-1}(\omega, \mathbf{k}) = \omega^2 - k^2 - \frac{m^2}{2(1 - \cos^2 \theta)k^2} \left[\omega^2 - k^2 \cos^2 \theta - \frac{\omega(\omega^2 - k^2)}{k\sqrt{\omega + k\sqrt{1 - \cos^2 \theta}} \sqrt{\omega - k\sqrt{1 - \cos^2 \theta}}} \right]. \quad (2.9.13)$$

This function has a cut due to the square root, and we choose the contour C as in Fig. 2.30, but with the cut extending from $-k\sqrt{1 - \cos^2 \theta}$ to $k\sqrt{1 - \cos^2 \theta}$ instead of $[-k, k]$, as in the isotropic and weakly anisotropic cases. The mapping of the path along the cut to the plane of complex $f(\omega)$ is discontinuous, because of the fact that $\Im f(\omega)$ is infinite at $\omega = \pm k\sqrt{1 - \cos^2 \theta}$. To avoid this problem, we analyze the function

$$f(\omega) \equiv \sqrt{\omega + k\sqrt{1 - \cos^2 \theta}} \sqrt{\omega - k\sqrt{1 - \cos^2 \theta}} \Delta_A^{-1}(\omega, \mathbf{k}), \quad (2.9.14)$$

which has the same cut and the same number of zeros as the original function of the A -mode dispersion equation (2.9.13). The function $f(\omega)$ has no singularity inside the contour and thus $n_P = 0$. Equation (2.9.6) gives $n_\infty = 3$ and thus the number of zeros of $f(\omega)$ is $n_Z = 3 + n_W$. To map the path around the cut to the plane of complex $f(\omega)$, we use Fig. 2.37, and 2.38 where the real and imaginary parts of $f(\omega)$ along the cut are shown for two different values of $\cos \theta$ for $k/m = 1$. For the case shown in Fig. 2.37, where $\Im f(\omega = i0^+) < 0$, the point $f = 0$ is encircled once in the negative (clockwise) direction which gives $n_W = -1$. In the case corresponding to Fig. 2.38, where $\Im f(\omega = i0^+) > 0$, the point $f = 0$ is encircled once in the positive (anticlockwise) direction and $n_W = 1$. The winding number is therefore determined by the sign of $\Im f(\omega = i0^+)$. The number of solutions thus equals $2 + 2\theta(\Im f(\omega = i0^+)) = 2 + 2\Theta(k_{oA} - k)$ which gives Eq. (2.8.8).

The G -modes are obtained from the dispersion equation (2.1.19) with the coefficients $\alpha, \beta, \gamma, \delta$ given by Eqs. (2.8.1)-(2.8.4). In this case it is easier to work with the function defined as

$$f(\omega) = \frac{k^2}{\omega^2} \left(\omega + k\sqrt{1 - \cos^2 \theta} \right)^{3/2} \left(\omega - k\sqrt{1 - \cos^2 \theta} \right)^{3/2} \Delta_G^{-1}(\omega, \mathbf{k}). \quad (2.9.15)$$

Since this function has a cut for $\omega \in [-k\sqrt{1 - \cos^2 \theta}, k\sqrt{1 - \cos^2 \theta}]$, we choose the same contour as for the analysis of the A -modes described above. The function $f(\omega)$ has no singularities inside the contour and therefore $n_P = 0$. Eq. (2.9.6) gives $n_\infty = 5$, and consequently, the number of zeros of $f(\omega)$ inside the contour equals $n_Z = 5 + n_W$. The winding number is calculated from the graphs shown in Fig. 2.39 and 2.40.

In Fig. 2.39 $n_W = -1$ and Fig. 2.40 $n_W = 1$. The number of solutions of the dispersion equation (2.1.19) is therefore either 4 or 6, depending on the sign of $\Im f(\omega = i0^+)$. The result can be written as in Eq. (2.8.9) with the critical value of wave vector defined by Eq. (2.8.7).

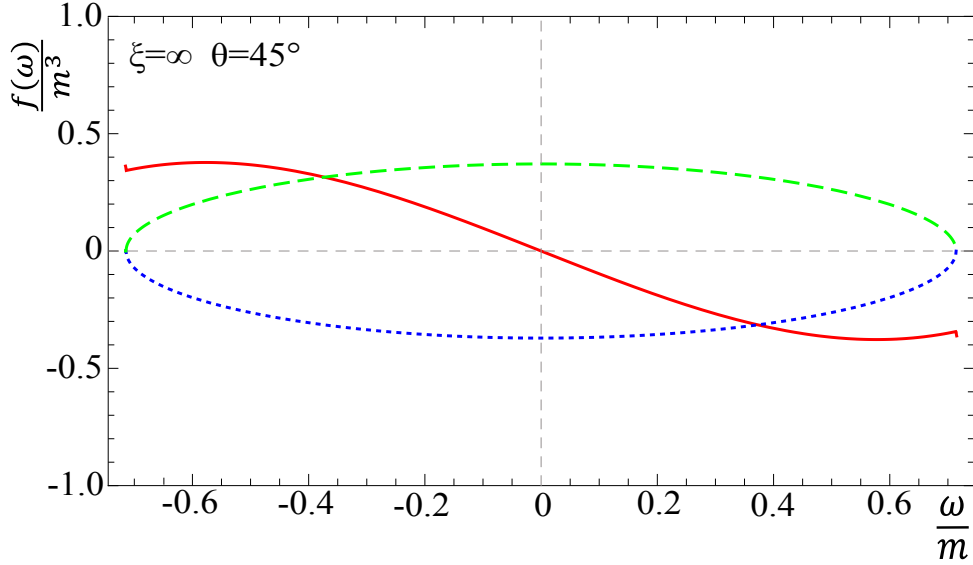


FIGURE 2.37: The real and imaginary parts of $f(\omega)$ for A -modes in extremely oblate plasma for ω along the cut and $k/m = 1$. For $\theta = 45^\circ$ which corresponds to $k > k_{oA}$ and gives $n_W = -1$.

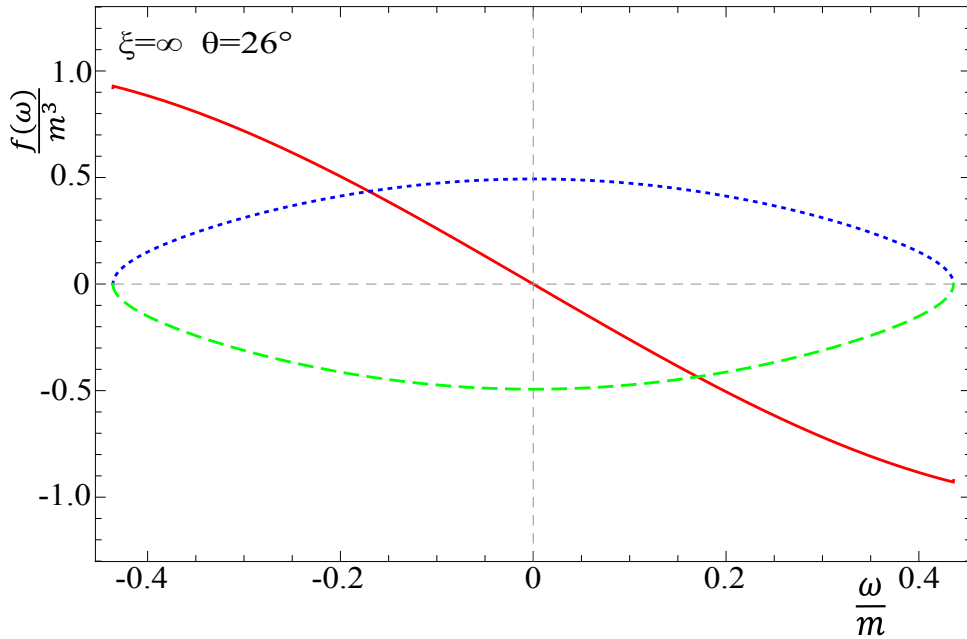


FIGURE 2.38: The real and imaginary parts of $f(\omega)$ for A -modes in extremely oblate plasma for ω along the cut and $k/m = 1$. For $\theta = 26^\circ$ which gives $k < k_{oA}$ and $n_W = 1$.

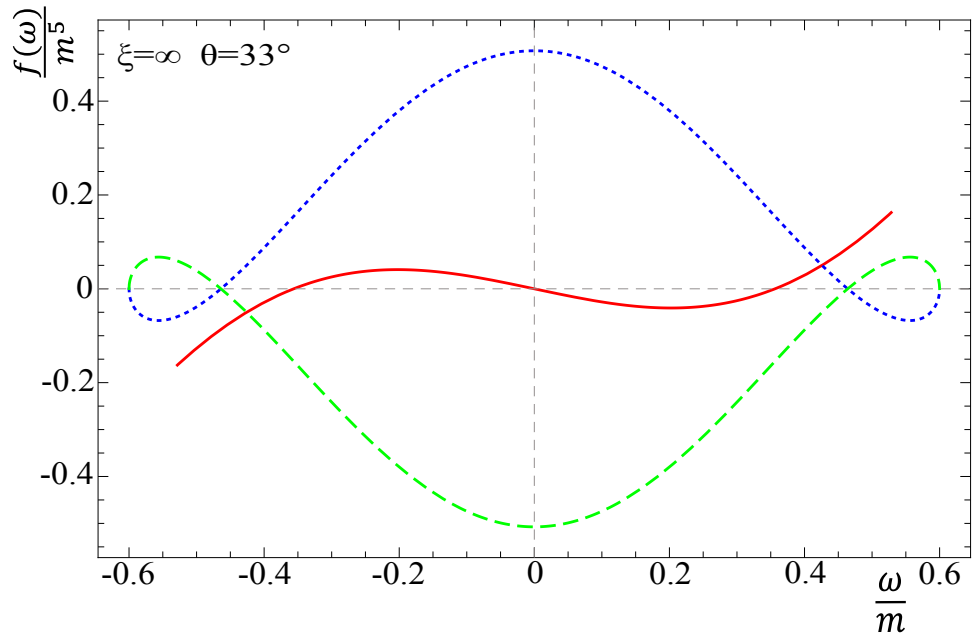


FIGURE 2.39: The real and imaginary parts of $f(\omega)$ for G -modes in extremely oblate plasma for ω along the cut and $k/m = 1$. For $\theta = 33^\circ$ which corresponds to $k > k_{oG}$ and gives $n_W = -1$.

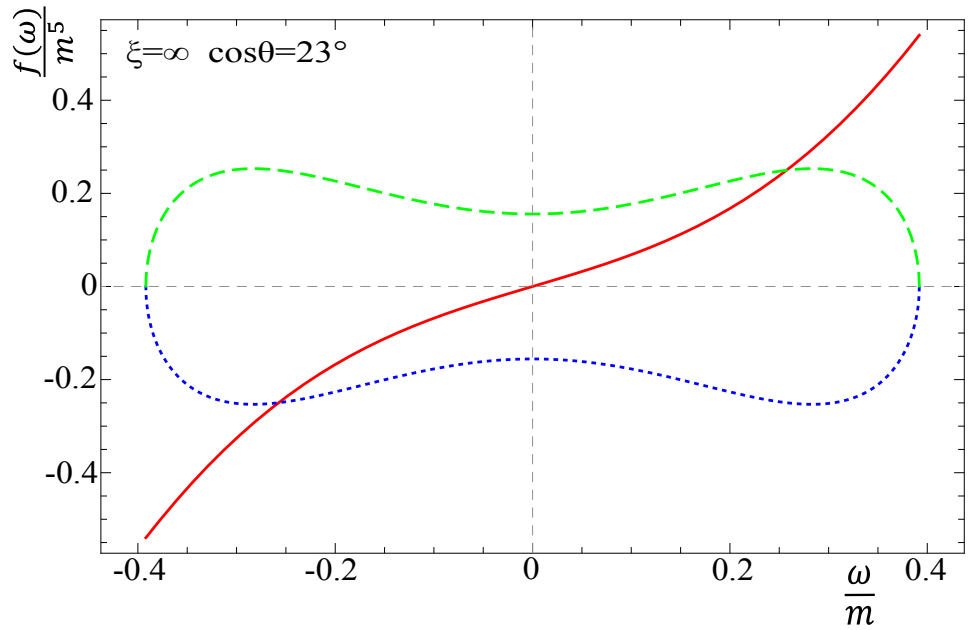


FIGURE 2.40: The real and imaginary parts of $f(\omega)$ for G -modes in extremely oblate plasma for ω along the cut and $k/m = 1$. For $\theta = 23^\circ$ which gives $k < k_{oG}$ and $n_W = 1$.

2.10 Summary and final remarks

In this chapter we performed a systematic analyses of the collective modes for anisotropic plasma. In every case which is presented in this thesis we have calculated the dispersion curves for the full spectrum, in some cases numerically and in some cases analytically. As we proved there are no complex solutions. The plasmons are either pure real or pure imaginary, and always show up with a partner with opposite sign. In all systems which are considered in this chapter there are unstable modes which are limited to the certain domain of the wave vector, except the isotropic system where the unstable mode does not exist. The number of modes for each system obtained by deforming the isotropic one is summarized in Table 2.1.

To complete our analyses it is interesting to look at these critical wave vectors as functions of θ . In Fig. 2.41 we show the behaviour of the critical vectors k_A , k_{oA} , k_C , k_{oG} and k_{pG} as a function of angle ($0^\circ < \theta < 90^\circ$) for different values of the anisotropy parameters.

The prolate critical wave vector has a maximum at $\theta = 90^\circ$, which goes to infinity in the extreme prolate case, and the oblate critical vectors have maximum at $\theta = 0^\circ$ which approaches infinity in the extreme oblate case. The prolate plasma system produces the strongest instability when the wave vector \mathbf{k} is exactly transverse to the anisotropy vector \mathbf{n} . For the oblate system the situation is exactly reversed, and the strongest instability occurs when the wave vector and anisotropy vector are parallel to each other.

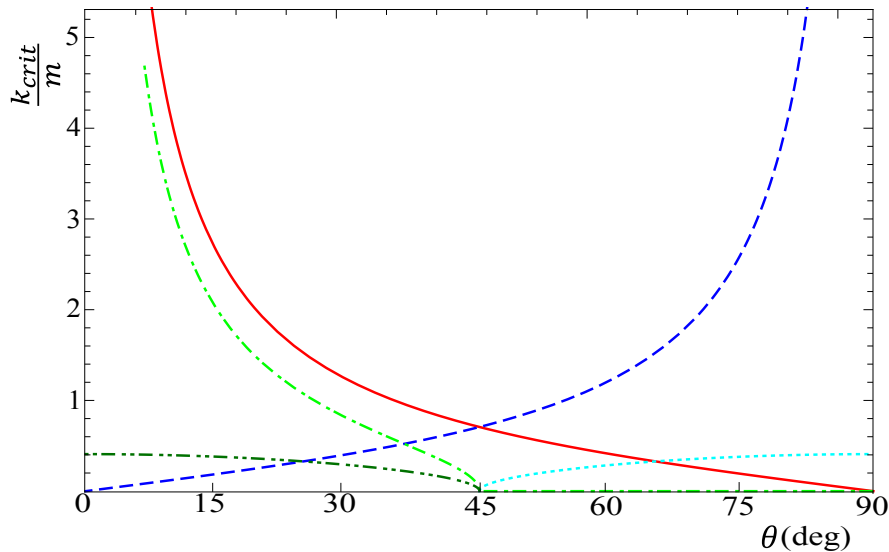


FIGURE 2.41: The critical wave vectors as a function of θ . The red (solid) line represents k_{oA} , blue (dashed) curve is k_{pG} , cyan (dotted) is k_C with $\sigma = -\xi = 0.5$, green (dot-dash) is k_{oG} , and finally the dark green (dot-dot-dash) line is k_C with $\xi = -\sigma = 0.5$.

TABLE 2.1: Number of modes in deformed isotropic plasma.

Momentum distribution	Number of real modes	Number of imaginary modes	Total number of modes	Maximal number of modes
extremely prolate	$6 + 2\Theta(k - k_p)$	$2\Theta(k_p - k)$	8	8
weakly prolate	6	$2\Theta(k_C - k)$	$6 + 2\Theta(k_C - k)$	8
isotropic	6	0	6	6
weakly oblate	6	$2\Theta(k_A - k) + 2\Theta(k_C - k)$	$6 + 2\Theta(k_A - k) + 2\Theta(k_C - k)$	10
extremely oblate	6	$2\Theta(k_{oA} - k) + 2\Theta(k_{oG} - k)$	$6 + 2\Theta(k_{oA} - k) + 2\Theta(k_{oG} - k)$	10

Chapter 3

Energy Loss

In this chapter, which is based on our paper [68], we will use the spectra of collective excitations obtained in Chapter 2 to calculate the energy loss of a test parton in QCD plasma which is in a non-equilibrium unstable state.

The energy loss of charged particles passing through matter is a standard problem in nuclear physics, actively studied both theoretically and experimentally for decades (Jackson, 1975), but the problem is, in general, very complex and it is still far from being completely solved [69, 70].

The total energy loss of a parton traversing a quark-gluon medium is the sum of collisional and radiative contributions: $\Delta E = \Delta E_{coll} + \Delta E_{rad}$. The first one is caused by elastic collisions with QGP constituents and in the second case a parton traversing the plasma loses energy by medium-induced multiple gluon emission. The collisional energy loss was originally estimated by Bjorken (1982) [31], Gyulassy and Thoma [71] and Mrówczyński [72] and then systematically derived by Braaten and Thoma [73, 74]. Later on it was improved by various authors [75, 76]. The energy loss due to multiple gluon radiation (“gluonstrahlung”) was estimated and shown to be the dominant process when the test parton is a light quark or gluon [77–81]. For heavy quarks the collisional energy loss is expected to give the dominant contribution because the radiation phase space is restricted by the “dead-cone effect” [82]. For a review on the energy loss see *e.g.* Ref. [69].

In the following we will focus on the collisional energy loss in anisotropic plasma using the formalism of classical kinetic theory. Although the anisotropic phase of QGP is very short lived, it might have a significant effect on the energy loss of a test parton because the weakly interacting anisotropic QGP is populated with large chromodynamic fields which act back onto the test parton leading to a sizable change of its energy. The collisional energy loss in anisotropic QGP was studied in [83] but the unstable plasma

was treated as a static medium and the interaction of the test parton with exponentially growing chromodynamic fields was missed.

We derive the energy loss in unstable plasma as a solution of the initial value problem. The test parton is treated as a classical particle with $SU(N_c)$ color charge. A motion of such a particle in an external colour field is described by the Wong equations [84], which we combine with the classical Yang-Mills equations. This approach is equivalent to using QCD within the hard-loop (HL) approximation [61]. In the equilibrium limit the time dependence of the energy loss disappears and we reproduce the soft part of the collisional energy loss [31, 71, 72, 74], where the momentum transfer is of the order of the Debye mass.

Our crucial finding is that depending on the initial conditions the test parton can either lose or gain energy when it is traversing the unstable QGP. In an equilibrium plasma the parton loses energy and the energy change per unit length dE/dx is negative. If the parton gains energy from the plasma fields, dE/dx is positive. Although the energy transfer can be either negative or positive, depending on the situation, we use the term ‘energy loss’ generically to describe both situations. Our results show that the magnitude of the energy loss increases exponentially, which indicates that the unstable modes play an important role. The energy loss, which is found, is strongly time dependent and the dependence is much stronger than the switching-on effect studied in [85, 86]. It is also strongly directionally dependent. At late enough times, the energy loss can be much bigger than in equilibrium plasmas. In contrast, the energy loss computed in the framework of AdS/CFT duality in the strong coupling regime is rather similar in equilibrium and in far-from-equilibrium plasma at the same energy density [87].

The acceleration of a test particle in a plasma system might seem rather exotic, but the phenomenon is well known in the physics of electromagnetic plasmas. It is caused by the electric field associated with plasma waves in the system. Charged particles are carried forward on the electrostatic wave with a motion like surfing with speed equal to the phase velocity of the wave, and can therefore be boosted to very high energies. This picture motivates the idea to use a plasma excited by a laser or particle beam as a particle accelerator. A mechanism was proposed in 1979 by Tajima and Dawson [88], and was experimentally verified soon afterwards [89]. Since plasmas can sustain accelerating fields orders of magnitude larger than those in the radio-frequency modules of standard accelerators, small plasma devices can be extremely efficient. In the experiment in Ref. [90], electrons were accelerated to an energy as high as 1 GeV over a distance of 3.3 cm, demonstrating immense promise for affordable and compact plasma accelerators for various applications.

Our treatment is fully classical, and we assume that the momenta of the collective modes are much less than the momenta of the plasma constituents. Our results are ultraviolet sensitive, which is expected since the approach is classical. In case of equilibrium (stable) plasma, the energy loss due to soft interactions diverges logarithmically with the upper limit of the collective mode momentum, which we call k_{\max} . In our anisotropic calculations, we also find an approximately logarithmic dependence on k_{\max} . This divergence signals the necessity to combine the classical contribution to the energy loss at small wave vectors with the quantum contribution at higher ones. A quantum approach to parton energy loss in unstable plasma needs to be developed, but it goes beyond the scope of the thesis.

3.1 General formula

Our formalism is based on the HL QCD effective action. It can be shown that the Wong equations [84] and the linearised Yang-Mills (Maxwell) equations can be obtained directly from this action [61]. The Wong equations describe the motion of a classical parton moving in the fields of a plasma. The motion of the parton changes the field configuration, which is self-consistently taken into account through the linearised Yang-Mills equations relating the chromodynamic fields to the parton charge and current. We emphasize that even though the Yang-Mills equations are linearised by the HL approximation, HL QCD is *not* equivalent to HL QED (up to an overall factor), because the gluons contribute to the color charge density and current in these equations.

The Wong equations, which describe the motion of a parton in a chromodynamic field, are usually written in the Lorentz covariant form [84]

$$\frac{dx^\mu(\tau)}{d\tau} = u^\mu(\tau), \quad (3.1.1)$$

$$\frac{dp^\mu(\tau)}{d\tau} = gQ^a(\tau) F_a^{\mu\nu}(x(\tau)) u_\nu(\tau), \quad (3.1.2)$$

$$\frac{dQ_a(\tau)}{d\tau} = -gf^{abc} u_\mu(\tau) A_b^\mu(x(\tau)) Q_c(\tau), \quad (3.1.3)$$

where τ , $x^\mu(\tau)$, $u^\mu(\tau)$ and $p^\mu(\tau)$ are, respectively, the parton's proper time, trajectory, four-velocity and four-momentum; $F_a^{\mu\nu}$ and A_a^μ denote, respectively, the chromodynamic field strength tensor and four-potential in the adjoint representation of the $SU(N_c)$ gauge group with the color index $a = 1, 2, \dots, N_c^2 - 1$; g is the coupling constant, which is assumed to be small, and finally Q^a is the classical color charge of the parton.

The Wong equations (3.1.1), (3.1.2), and (3.1.3) are supplemented by the linearised Yang-Mills equations describing the self-consistent generation of the chromodynamic field. We write the linearised Yang-Mills equations in a non-covariant three-vector notation where they have the familiar form of Maxwell equations in a medium. In Heaviside-Lorentz electromagnetic units, which are usually used in quantum field theory, we have

$$\nabla \cdot \mathbf{D}_a(t, \mathbf{r}) = \rho_a(t, \mathbf{r}), \quad \nabla \cdot \mathbf{B}_a(t, \mathbf{r}) = 0, \quad (3.1.4)$$

$$\nabla \times \mathbf{E}_a(t, \mathbf{r}) = -\frac{\partial \mathbf{B}_a(t, \mathbf{r})}{\partial t}, \quad \nabla \times \mathbf{B}_a(t, \mathbf{r}) = \mathbf{j}_a(t, \mathbf{r}) + \frac{\partial \mathbf{D}_a(t, \mathbf{r})}{\partial t}, \quad (3.1.5)$$

where \mathbf{E}_a , \mathbf{D}_a , \mathbf{B}_a are the chromoelectric field, chromoelectric induction and chromomagnetic field; and ρ_a and \mathbf{j}_a are the density and current of the test parton, respectively. To close the system of Maxwell equations (3.1.4) and (3.1.5), the chromoelectric induction

is expressed through the chromoelectric field

$$D_a^i(t, \mathbf{r}) = \int dt' d^3r' \varepsilon^{ij}(t-t', \mathbf{r}-\mathbf{r}') E_a^j(t', \mathbf{r}'), \quad (3.1.6)$$

where $\varepsilon^{ij}(t, \mathbf{r})$ is the chromodielectric permeability, see Eq. (2.1.3).

To solve the Wong equations (3.1.1), (3.1.2), and (3.1.3) we adopt two simplifying assumptions. The first is that we choose the gauge condition

$$u_\mu(\tau) A_a^\mu(x(\tau)) = 0, \quad (3.1.7)$$

which requires that the potential vanishes along the parton's trajectory. Using this gauge, the third Wong equation (3.1.3) simply states that the parton's charge is a constant of motion, or that Q_a is independent of τ . The second important simplification comes from the fact that we consider a highly energetic parton and assume that its velocity \mathbf{v} is constant and $\mathbf{v}^2 = 1$. In an equilibrium plasma the characteristic momentum transfer $|\Delta\mathbf{p}|$ is of order gT and the parton's momentum $|\mathbf{p}| \gg T$, where T is the temperature. The hard loop approach requires $gT \ll T$, and therefore $|\Delta\mathbf{v}| \sim |\Delta\mathbf{p}|/|\mathbf{p}| \ll 1$. When we consider anisotropic systems, we assume the same hierarchy of scales which gives $|\Delta\mathbf{v}| \ll 1$. The physical picture is that due to interaction with the chromodynamic field the parton's energy and momentum evolve in time without changing the magnitude of its velocity.

Replacing the proper time τ by the time $t = \gamma\tau$ and writing $x^i(t) = r^i(t)$ and $u^i(t) = \gamma v^i$, the first Wong equation (3.1.1) gives $\mathbf{r}(t) = \mathbf{v}t$. Using this result, we obtain from the second Wong equation (3.1.2) with $\mu = 0$

$$\frac{dE(t)}{dt} = gQ^a \mathbf{E}_a(t, \mathbf{r}(t)) \cdot \mathbf{v}. \quad (3.1.8)$$

Since the current generated by the moving parton equals

$$\mathbf{j}_a(t, \mathbf{r}) = gQ^a \mathbf{v} \delta^{(3)}(\mathbf{r} - \mathbf{v}t), \quad (3.1.9)$$

we rewrite Eq. (3.1.8) as

$$\frac{dE(t)}{dt} = \int d^3r \mathbf{E}_a(t, \mathbf{r}) \cdot \mathbf{j}_a(t, \mathbf{r}). \quad (3.1.10)$$

To obtain the energy loss we must solve equations (3.1.4) and (3.1.5) for the electric field and substitute into equation (3.1.10).

The electric field that appears in equations (3.1.8) and (3.1.10) is the total electric field, which is the sum of the external field generated directly by the moving test parton

and the induced electric field produced by the charge distributions and currents that are induced by the parton in the plasma medium. The external electric field gives the parton's self-interaction and does not contribute to the energy loss. The energy loss comes physically from the motion of the parton into the opposing induced electric field. We derive below an expression for the total electric field from Maxwell's equations. At the end of the procedure, we must either show that the self-interaction does not contribute to the energy loss, or we must subtract it.

It seems clear from Eq. (3.1.10) that if the parton moves into an electric field of opposite orientation to its current, the change in the energy will be negative and we have energy loss. We will show, however, that is not always the case. If the calculation is done as an initial value problem, then the sign of the energy transfer crucially depends on the choice of initial conditions.

To solve Maxwell's equations we use the usual method which is to Fourier transform the differential equations to change them into algebraic equations which can be easily solved. However, we do not use a standard (two-sided) Fourier transform. Our problem is to track the evolution of a parton starting from some arbitrary initial time (which we take to be $t = 0$) and calculate its behaviour at future times. The non-equilibrated plasma is not time-translation invariant, and the energy loss formula should depend on the initial conditions, which means that we need to formulate the calculation as an initial value problem. In order to do this, we use a one-sided Fourier transformation defined as

$$f(\omega, \mathbf{k}) = \int_0^\infty dt \int d^3r e^{i(\omega t - \mathbf{k} \cdot \mathbf{r})} f(t, \mathbf{r}), \quad (3.1.11)$$

$$f(t, \mathbf{r}) = \int_{-\infty + i\sigma}^{\infty + i\sigma} \frac{d\omega}{2\pi} \int \frac{d^3k}{(2\pi)^3} e^{-i(\omega t - \mathbf{k} \cdot \mathbf{r})} f(\omega, \mathbf{k}). \quad (3.1.12)$$

The inverse transformation (3.1.12) involves the real parameter $\sigma > 0$ which is chosen so that the integral over ω is taken along a straight line in the complex ω -plane, parallel to the real axis and above all singularities of $f(\omega, \mathbf{k})$.

The one-sided Fourier transform of the current (3.1.9) is obtained from Eq. (3.1.11) where the time integral is defined through the limit

$$\lim_{\epsilon \rightarrow 0^+} \int_0^\infty dt e^{i(\omega - \mathbf{k} \cdot \mathbf{v} + i0^+)t} = \frac{i}{\omega - \mathbf{k} \cdot \mathbf{v} + i0^+}, \quad (3.1.13)$$

which gives

$$\mathbf{j}_a(\omega, \mathbf{k}) = \frac{igQ^a \mathbf{v}}{\omega - \mathbf{k} \cdot \mathbf{v} + i0^+}. \quad (3.1.14)$$

This procedure is mathematically equivalent to multiplying the current in equation (3.1.9) by a factor e^{-0^+t} , which can be interpreted physically as imposing the boundary condition that the current goes to zero as the time approaches infinity.

The one-sided Fourier transform of the relation (3.1.6) provides

$$D_a^i(\omega, \mathbf{k}) = \varepsilon^{ij}(\omega, \mathbf{k}) E_a^j(\omega, \mathbf{k}). \quad (3.1.15)$$

Applying the one-sided Fourier transform to the Maxwell equations (3.1.4) and (3.1.5) and using the relation (3.1.15) gives

$$ik^i \varepsilon^{ij}(\omega, \mathbf{k}) E_a^j(\omega, \mathbf{k}) = \rho_a(\omega, \mathbf{k}), \quad (3.1.16)$$

$$ik^i B_a^i(\omega, \mathbf{k}) = 0, \quad (3.1.17)$$

$$i\varepsilon^{ijk} k^j E_a^k(\omega, \mathbf{k}) = i\omega B_a^i(\omega, \mathbf{k}) + B_{0a}^i(\mathbf{k}), \quad (3.1.18)$$

$$i\varepsilon^{ijk} k^j B_a^k(\omega, \mathbf{k}) = j_a^i(\omega, \mathbf{k}) - i\omega \varepsilon^{ij}(\omega, \mathbf{k}) E_a^j(\omega, \mathbf{k}) - D_{0a}^i(\mathbf{k}), \quad (3.1.19)$$

where we have written $B_{0a}^i(\mathbf{k}) \equiv B_a^i(t=0, \mathbf{k})$ and similarly for $D_{0a}^i(\mathbf{k})$. These initial values come from the time integrals of the time derivatives of fields after performing an integration by parts. The algebraic equations (3.1.16)-(3.1.19) are solved for the field $E_a^i(\omega, \mathbf{k})$

$$E_a^i(\omega, \mathbf{k}) = -i(\Sigma^{-1})^{ij}(\omega, \mathbf{k}) \left[\omega j_a^j(\omega, \mathbf{k}) + \varepsilon^{jkl} k^k B_{0a}^l(\mathbf{k}) - \omega D_{0a}^j(\mathbf{k}) \right], \quad (3.1.20)$$

where the $\Sigma^{ij}(\omega, \mathbf{k})$ matrix is defined by Eq. (2.1.2).

The energy loss in equation (3.1.10) can now be written in terms of the Fourier transformed field and current. Performing the inverse transformation (3.1.12), we have

$$\frac{dE(t)}{dt} = \int_{-\infty+i\sigma}^{\infty+i\sigma} \frac{d\omega}{2\pi} \int_{-\infty+i\sigma'}^{\infty+i\sigma'} \frac{d\omega'}{2\pi} \int \frac{d^3k}{(2\pi)^3} e^{-i(\omega+\omega')t} \mathbf{E}_a(\omega, \mathbf{k}) \cdot \mathbf{j}_a(\omega', -\mathbf{k}), \quad (3.1.21)$$

and substituting the formulae (3.1.14) and (3.1.20) into Eq. (3.1.21), one obtains

$$\begin{aligned} \frac{dE(t)}{dt} = & -i \int_{-\infty+i\sigma}^{\infty+i\sigma} \frac{d\omega}{2\pi} \int_{-\infty+i\sigma'}^{\infty+i\sigma'} \frac{d\omega'}{2\pi} \int \frac{d^3k}{(2\pi)^3} e^{-i(\omega+\omega')t} \\ & \times \frac{igQ^a v^i}{\omega' + \mathbf{k} \cdot \mathbf{v}} (\Sigma^{-1})^{ij}(\omega, \mathbf{k}) \left[\frac{i\omega gQ^a v^j}{\omega - \mathbf{k} \cdot \mathbf{v}} + \varepsilon^{jkl} k^k B_{0a}^l(\mathbf{k}) - \omega D_{0a}^j(\mathbf{k}) \right]. \end{aligned} \quad (3.1.22)$$

The integral over ω' can be done easily since the integrand has only one pole at $\omega' = -\bar{\omega} \equiv -\mathbf{k} \cdot \mathbf{v}$. The result of integration over ω' is

$$\begin{aligned} \frac{dE(t)}{dt} = & gQ^a v^i \int \frac{d^3k}{(2\pi)^3} \int_{-\infty+i\sigma}^{\infty+i\sigma} \frac{d\omega}{2\pi i} e^{-i(\omega-\bar{\omega})t} (\Sigma^{-1})^{ij}(\omega, \mathbf{k}) \\ & \times \left[\frac{i\omega gQ^a v^j}{\omega - \bar{\omega}} + \epsilon^{jkl} k^k B_{0a}^l(\mathbf{k}) - \omega D_{0a}^j(\mathbf{k}) \right], \end{aligned} \quad (3.1.23)$$

which is the main result of this section. In Appendix A.3 we prove that the energy loss given by Eq.(3.1.23) is real.

Equation (3.1.23) gives the change of energy of the parton as a function of time, and the expression depends on the initial conditions. The integral over ω is controlled by the poles of the matrix $\Sigma^{-1}(\omega, \mathbf{k})$ (or equivalently the gluon propagator) which determine the gluon collective modes in the system. These modes are found as solutions of the dispersion equation. This problem is discussed in Chapter 2, where the equation (2.1.2) is solved for different distribution functions. Physically that means, that the test parton does not interact with plasma constituents but rather with the plasma collective modes.

In Sec. 3.3 we discuss how to choose the initial conditions which enter the energy loss formula (3.1.23). In the next section, however, we show that in the equilibrium limit, Eq. (3.1.23) reduces to the familiar result which is independent of the initial conditions.

3.2 Equilibrium limit

When the plasma is in equilibrium all collective modes are damped and all poles of the propagator $\Delta^{ij}(\omega, \mathbf{k}) \equiv (\Sigma^{-1})^{ij}(\omega, \mathbf{k})$ are located in the lower half-plane of complex ω . The corresponding contributions to the energy loss (3.1.23) exponentially decay in time, and the only stationary contribution is given by the pole $\omega = \bar{\omega} = \mathbf{k} \cdot \mathbf{v}$ which comes from the current of the test parton. This means that the terms in Eq. (3.1.23) which include the initial values of the fields can be neglected. It is mathematically equivalent to use a two-sided Fourier transform from the beginning of the calculation, which means that the initial conditions do not appear in the Maxwell equations (3.1.16), and the Fourier transform of the current (3.1.9) is just proportional to $\delta(\omega - \mathbf{k} \cdot \mathbf{v})$. The result is that, once again, the only contribution to the integral over ω comes from $\omega = \bar{\omega} \equiv \mathbf{k} \cdot \mathbf{v}$. In both approaches the result is that the energy loss of a high-energy parton traversing an equilibrium plasma is given by the time independent expression

$$\frac{dE}{dt} = -ig^2 Q^a Q^a v^i v^j \int \frac{d^3k}{(2\pi)^3} \bar{\omega} (\Sigma^{-1})^{ij}(\bar{\omega}, \mathbf{k}). \quad (3.2.1)$$

Since the parton's color charge is not an observable quantity because of its gauge dependence, the energy loss (3.2.1) has to be averaged over the parton's color state. This is achieved by means of the relations

$$\int dQ Q_a = 0, \quad (3.2.2)$$

and

$$\int dQ Q_a Q_a = C_2, \quad (3.2.3)$$

which are derived in [61]; $C_2 = 1/2$ for a quark in the fundamental representation of the $SU(N_c)$ gauge group and $C_2 = N_c$ for a gluon in the adjoint representation. Using the relation (3.2.3), the color averaged energy loss is

$$\frac{d\bar{E}}{dt} = -ig^2 C_R v^i v^j \int \frac{d^3k}{(2\pi)^3} \bar{\omega} (\Sigma^{-1})^{ij}(\bar{\omega}, \mathbf{k}), \quad (3.2.4)$$

where the color factor C_R is given as

$$C_R \equiv \begin{cases} \frac{C_2(N_c^2-1)}{N_c} = \frac{N_c^2-1}{2N_c} & \text{for quark,} \\ C_2 = N_c & \text{for gluon.} \end{cases}$$

It is easy to see that the result in equation (3.2.4) is real. Since the electric field and electric induction are both real in coordinate space, it follows from Eq. (3.1.6) that the dielectric tensor obeys the relations

$$\Re \varepsilon^{ij}(-\omega, -\mathbf{k}) = \Re \varepsilon^{ij}(\omega, \mathbf{k}), \quad \Im \varepsilon^{ij}(-\omega, -\mathbf{k}) = -\Im \varepsilon^{ij}(\omega, \mathbf{k}). \quad (3.2.5)$$

Since the analogous relations hold for the matrix (propagator) $\Sigma^{-1}(\omega, \mathbf{k})$, the real and imaginary contributions to the integrand in Eq. (3.2.4) are, respectively, odd and even as functions of \mathbf{k} . Therefore, only the imaginary part of $\Sigma^{-1}(\omega, \mathbf{k})$, which is responsible for dissipative phenomena, contributes to the integral (3.2.4), and the energy loss is real as it should be.

In an isotropic plasma the dielectric tensor can be decomposed into longitudinal and transverse components

$$\varepsilon^{ij}(\omega, \mathbf{k}) = \varepsilon_L(\omega, \mathbf{k}) \frac{k^i k^j}{\mathbf{k}^2} + \varepsilon_T(\omega, \mathbf{k}) \left(\delta^{ij} - \frac{k^i k^j}{\mathbf{k}^2} \right), \quad (3.2.6)$$

and the matrix $\Sigma^{ij}(\omega, \mathbf{k})$ can be inverted to obtain the propagator as

$$(\Sigma^{-1})^{ij}(\omega, \mathbf{k}) = \frac{1}{\omega^2 \varepsilon_L(\omega, \mathbf{k})} \frac{k^i k^j}{\mathbf{k}^2} + \frac{1}{\omega^2 \varepsilon_T(\omega, \mathbf{k}) - \mathbf{k}^2} \left(\delta^{ij} - \frac{k^i k^j}{\mathbf{k}^2} \right). \quad (3.2.7)$$

Substituting this expression into Eq. (3.2.4), the energy loss is written

$$\frac{d\bar{E}}{dt} = -ig^2 C_R \int \frac{d^3k}{(2\pi)^3} \frac{\bar{\omega}}{\mathbf{k}^2} \left[\frac{1}{\varepsilon_L(\bar{\omega}, \mathbf{k})} + \frac{\mathbf{k}^2 \mathbf{v}^2 - \bar{\omega}^2}{\bar{\omega}^2 \varepsilon_T(\bar{\omega}, \mathbf{k}) - \mathbf{k}^2} \right]. \quad (3.2.8)$$

Using the symmetry relations (3.2.5) for $\varepsilon_{L,T}(\omega, \mathbf{k})$, Eq. (3.2.4) becomes

$$\frac{d\bar{E}}{dt} = -g^2 C_R \int \frac{d^3k}{(2\pi)^3} \frac{\bar{\omega}}{\mathbf{k}^2} \left[\frac{\text{Im} \varepsilon_L(\bar{\omega}, \mathbf{k})}{|\varepsilon_L(\bar{\omega}, \mathbf{k})|^2} + \frac{\bar{\omega}^2 (\mathbf{k}^2 \mathbf{v}^2 - \bar{\omega}^2) \text{Im} \varepsilon_T(\bar{\omega}, \mathbf{k})}{|\bar{\omega}^2 \varepsilon_T(\bar{\omega}, \mathbf{k}) - \mathbf{k}^2|^2} \right]. \quad (3.2.9)$$

As discussed under equation (3.1.10), the energy loss formula (3.1.10), and consequently the formula (3.1.23), includes the self-interaction of the test parton with the electric field generated by the parton's current (3.1.9). The parton's self-interaction should not contribute to the energy loss (3.2.8), and therefore we need to calculate this contribution separately and, if it is not zero, we need to subtract it from the energy loss obtained from Eq. (3.2.8). Since the effect of self-interaction is the same in a vacuum and in a medium, we derive it substituting into Eq. (3.2.8) the dielectric functions of the vacuum, which are

$$\varepsilon_L(\omega, \mathbf{k}) = \varepsilon_T(\omega, \mathbf{k}) = 1. \quad (3.2.10)$$

Using Eq. (3.2.10) the formula (3.2.8) gives

$$\begin{aligned} \left. \frac{d\bar{E}}{dt} \right|_{\text{vacuum}} &= ig^2 C_R (1 - v^2) \int \frac{d^3k}{(2\pi)^3} \frac{\bar{\omega}}{\bar{\omega}^2 - \mathbf{k}^2} \\ &= -i \frac{g^2 C_R}{(2\pi)^2} (1 - v^2) \int_0^\infty dk k \int_{-1}^{+1} \frac{d(\cos \theta) \cos \theta}{1 - v^2 \cos^2 \theta} = 0, \end{aligned} \quad (3.2.11)$$

where we have chosen the axis z along the vector \mathbf{v} and written $\bar{\omega} = \mathbf{k} \cdot \mathbf{v} = k \cos \theta$. Although the momentum integral is quadratically divergent, the angular integral vanishes and the three-dimensional integral is zero. The zero result is also expected from Eq. (3.2.9) because the vacuum dielectric functions (3.2.10) are purely real. Thus we see that the parton's self-interaction does not contribute to the equilibrium energy loss formula (3.2.8) or (3.2.9). In Sec. 3.4 we will show that this is not the case when the energy loss calculation is formulated as an initial value problem.

The result (3.2.8) or (3.2.9) agrees with the expression obtained in [72] using kinetic theory, and with the result for the energy loss due to soft collisions calculated in the HTL approximation [74], see also the textbook [53]. However, this is not the complete energy loss but rather the soft contribution to it when the wave vector \mathbf{k} is of the order of the Debye mass. Physically it corresponds to an interaction of the test parton with soft collective excitations of the plasma medium.

The incompleteness of the formula (3.2.8) or (3.2.9) is signaled by the logarithmic divergence as $|\mathbf{k}| \rightarrow \infty$. To obtain the complete collisional energy loss, the formula (3.2.8) should be combined with the hard contribution describing elastic collisions of the test parton with plasma constituents with momentum transfer much exceeding the Debye mass. The hard contribution is not ultraviolet divergent, as the maximal momentum transfer is constrained by the collision kinematics. The soft contribution to the energy loss depends logarithmically on the upper cut-off k_{\max} divided by the Debye mass m , while the hard contribution has a logarithmic dependence on the energy of the parton E divided by the same cut-off k_{\max} . The energy loss thus equals

$$\frac{d\bar{E}}{dt} = X \ln\left(\frac{k_{\max}}{m}\right) + Y \ln\left(\frac{E}{k_{\max}}\right). \quad (3.2.12)$$

It can be shown [53, 74] that the coefficients X, Y are equal to each other and therefore

$$\frac{d\bar{E}}{dt} = X \ln\left(\frac{E}{m}\right). \quad (3.2.13)$$

The result is that the cut-offs cancel and one obtains a good approximation to the energy loss from the soft contribution with the parton energy used as an upper cut-off.

As was mentioned on the beginning of this chapter, the energy loss in anisotropic QGP was computed previously by Romatschke and Strickland [83]. Their result can be obtained from our formula (3.2.4) by using an anisotropic propagator for $\Sigma^{-1}(\omega, \mathbf{k})$ and including only the contribution from the pole $\omega = \bar{\omega}$. Clearly this procedure produces a result for the energy loss that is completely time independent. As we will see in the subsequent sections, the energy loss in anisotropic plasma is actually strongly time dependent because of the unstable modes.

In order to compare our results for the energy loss in an unstable plasma to the corresponding equilibrium result, we have computed numerically the integral (3.2.8) in spherical coordinates. As already mentioned, the integral is logarithmically divergent at large $k \equiv |\mathbf{k}|$, so we introduce a cutoff $k \leq k_{\max}$. When studying plasmas with massless constituents, the mass m given by the Eq. (2.4.3) can be chosen as the only dimensionful parameter, and we therefore use a system of units where all dimensionful quantities are rescaled by the appropriate powers of m .

In Fig. 3.1 we show the energy loss in isotropic QGP divided by $g^2 m^2$ as a function of $\frac{k_{\max}}{m}$ computed for $C_R = N_c = 3$ which corresponds to a gluon. Since the energy loss is divided by $g^2 m^2$ we do not need to specify the value of g . The numbers from this figure will serve as a reference for our results on the energy loss in unstable plasmas.

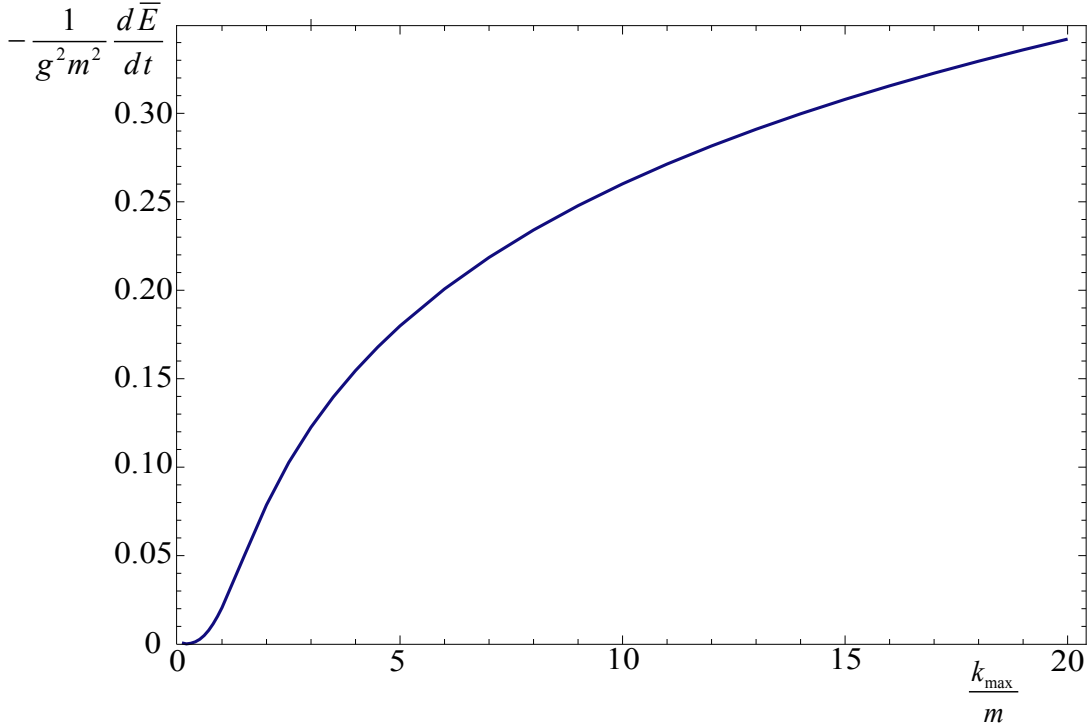


FIGURE 3.1: The parton energy loss per unit time in equilibrium plasma as a function of k_{\max} .

3.3 Initial conditions

When the plasma is anisotropic, the propagator $\Delta(\omega, \mathbf{k}) = \Sigma^{-1}(\omega, \mathbf{k})$ has poles in the upper half-plane of complex ω which correspond to instabilities, and the contributions to the energy loss from these poles grow exponentially in time. This means that the terms in Eq. (3.1.23) which contain the initial values of fields \mathbf{D}_0 and \mathbf{B}_0 are amplified by an exponential factor and, in contrast to the equilibrium situation, they cannot, in general, be neglected.

3.3.1 Uncorrelated initial conditions

The simplest choice of the initial condition is $\mathbf{D}_0 = \mathbf{B}_0 = 0$, which means that the energy loss formula (3.1.10) becomes

$$\frac{d\bar{E}(t)}{dt} = ig^2 C_R v^i v^j \int \frac{d^3 k}{(2\pi)^3} \int_{-\infty+i\sigma}^{\infty+i\sigma} \frac{d\omega}{2\pi i} e^{-i(\omega-\bar{\omega})t} \frac{\omega}{\omega-\bar{\omega}} (\Sigma^{-1})^{ij}(\omega, \mathbf{k}), \quad (3.3.1)$$

where we have used the relation (3.2.3) to average over colors. In fact, the formula (3.3.1) holds for a whole class of initial conditions whenever \mathbf{D}_0 and \mathbf{B}_0 are *independent* of the test parton's current. In this case, the contributions to the energy loss (3.1.23) which

contain \mathbf{D}_0 and \mathbf{B}_0 are linear in the parton's color charge Q_a , and consequently they vanish when color averaging is performed using the relation (3.2.2).

Physically this result can be understood as follows. Let us consider an electron moving in an external electromagnetic field which is independent of the current generated by the electron. The energy loss formula is given by the electromagnetic analog of the formula (3.1.8) where $\mathbf{E}(t, \mathbf{r}(t))$ is the external electric field along the electron's trajectory. The electromagnetic analog of averaging over the parton's color is the averaging over the possible charges of a hypothetical electron which could carry either negative or positive charge, or the averaging over the charges of an electron and a positron. If an electron's energy increases by ΔE in the time interval Δt , a positron's energy would decrease by $-\Delta E$ in the same field configuration and time interval. Therefore, after averaging over charges, the net change in the energy is zero.

It is important to remember that the contribution to the energy loss from the first term in (3.1.23), which is proportional to the current and not the initial fields, is non zero, even when uncorrelated initial conditions are used. Mathematically, this happens because this term is proportional to the square of the charge. In an electromagnetic plasma, e^2 is strictly positive, and in a QCD plasma the factor $Q^a Q^a$ does not give zero when averaged (see equation (3.2.3)). Physically we see that the energy losses of the electron and positron have same sign because they are not interacting with external fields which are independent of their currents, but instead with the electric fields which they have induced in the medium. We also note that the procedure of averaging over electric charges looks similar to that of averaging over colors but the physical situation is quite different. A color charge is gauge dependent and consequently it is not a physical observable. Therefore, the averaging over colors must be performed in order for the energy loss to have a physical meaning.

It is interesting to note that we can obtain the same energy loss formula (3.3.1) in a different way. If we multiply the current in equation (3.1.9) by a step function $\Theta(t)$ and then repeat the whole calculation using the usual two-sided Fourier transformation, the identical result is found. The initial fields \mathbf{D}_0 and \mathbf{B}_0 do not appear in the two-sided Fourier transformed Maxwell equations, and the two-sided Fourier transform of the current with the additional step function is the same as the one-sided Fourier transform of original current. Although the same result can be obtained in two different ways, the physical interpretation of the two procedures is somewhat different. Using the two-sided transformation with the current multiplied by a step function, we assume that the plasma system exists for all times but the test parton appears in the plasma at $t = 0$. This was the problem studied in the papers [85, 86]. When the one-sided Fourier transformation is used, it is understood that we observe the whole system, which includes the plasma

and the test parton, starting only at $t = 0$. The initial values of the fields \mathbf{D}_0 and \mathbf{B}_0 can be chosen to be independent of the parton's color state, but they could also be specified differently. In the next section we consider a class of nontrivial initial conditions for which the fields \mathbf{D}_0 and \mathbf{B}_0 are strongly correlated with the current generated by the test parton.

3.3.2 Correlated initial conditions

We have shown in the previous section that if the initial conditions are chosen in any way that is independent of the parton's current, they will not contribute to the energy loss. In this section we will consider another kind of initial conditions. First we note that although initial conditions are always required to solve differential equations, they are usually determined by physical arguments which go beyond the differential equations under consideration. We argue below that in the energy loss calculation, a kind of correlated initial conditions might be the most physical. We imagine that a process which is responsible for the occurrence of a test parton in a plasma system at the time $t = 0$, also polarizes the medium producing a chromodynamic field which is then correlated with the parton's color state. We would like to see if the energy loss is sensitive to this kind of *correlated* initial condition. To derive an upper limit on the effect, we assume that the parton enters the system in the remote past at $t = -\infty$, observing that the parton's current (3.1.9) can be extended to the time interval from $-\infty$ to ∞ . Flying across the plasma, the parton polarizes the medium and induces a chromodynamic field. The initial fields \mathbf{D}_0 and \mathbf{B}_0 are identified with the induced fields at $t = 0$.

To determine the fields \mathbf{D}_0 and \mathbf{B}_0 we solve the Maxwell equations (3.1.4) and (3.1.5) using a normal (two-sided) Fourier transform with the time integral from $-\infty$ to ∞ . We use tildes to indicate that a two-sided Fourier transform was taken, which means that, for example, $D(\omega, \mathbf{k})$ and $\tilde{D}(\omega, \mathbf{k})$ are different functions of ω but the same function of \mathbf{k} . However, we note that $\tilde{\varepsilon}(\omega, \mathbf{k}) = \varepsilon(\omega, \mathbf{k})$ and $\tilde{\Sigma}^{-1}(\omega, \mathbf{k}) = \Sigma^{-1}(\omega, \mathbf{k})$ because these functions obey the retarded initial condition and therefore $\varepsilon(t, \mathbf{r}) = \Sigma^{-1}(t, \mathbf{r}) = 0$ for $t < 0$. Solving the equations (3.1.4) and (3.1.5) using a two-sided Fourier transform produces the result in equation (3.1.20) with E_a^i and j_a^j tilded and $B_{0a}^l = D_{0a}^j = 0$, since the initial fields in Eq. (3.1.20) come from the $t = 0$ lower limit in the one-sided Fourier transform. Using the tilded version of the material relation (3.1.15), the electric induction is

$$\tilde{D}_a^i(\omega, \mathbf{k}) = -i\omega \varepsilon^{ij}(\omega, \mathbf{k})(\Sigma^{-1})^{jk}(\omega, \mathbf{k})\tilde{j}_a^k(\omega, \mathbf{k}), \quad (3.3.2)$$

where the two-sided Fourier transform of the current in equation (3.1.9) is

$$\tilde{\mathbf{j}}_a(\omega, \mathbf{k}) = gQ^a \mathbf{v} 2\pi \delta(\omega - \bar{\omega}). \quad (3.3.3)$$

Taking the inverse two-sided Fourier transform of the result (3.3.2), we obtain

$$D_a^i(t, \mathbf{k}) = \int_{-\infty}^{\infty} \frac{d\omega}{2\pi} e^{-i\omega t} \tilde{D}_a^i(\omega, \mathbf{k}) = -ie^{-i\bar{\omega}t} gQ^a \bar{\omega} \varepsilon^{ij}(\bar{\omega}, \mathbf{k}) (\Sigma^{-1})^{jk}(\bar{\omega}, \mathbf{k}) v^k, \quad (3.3.4)$$

and setting $t = 0$, we arrive at

$$D_{0a}^i(\mathbf{k}) = -igQ^a \bar{\omega} \varepsilon^{ij}(\bar{\omega}, \mathbf{k}) (\Sigma^{-1})^{jk}(\bar{\omega}, \mathbf{k}) v^k. \quad (3.3.5)$$

Using the same method we obtain the initial value of the chromomagnetic field

$$B_{0a}^i(\mathbf{k}) = -igQ^a \varepsilon^{ijk} k^j (\Sigma^{-1})^{kl}(\bar{\omega}, \mathbf{k}) v^l. \quad (3.3.6)$$

The formulae (3.3.5) and (3.3.6) provide maximally correlated initial conditions. In order to consider initial conditions with differing degrees of correlation, we will multiply the initial fields (3.3.5) and (3.3.6) by a phase factor $\cos \alpha \in [-1, 1]$. The choices $\cos \alpha = \pm 1$ correspond to maximally correlated and anticorrelated initial fields. These two extreme cases provide limits on the possible effects of correlated initial conditions. We substitute the initial fields \mathbf{D}_0 and \mathbf{B}_0 given by Eqs. (3.3.5) and (3.3.6) into the energy loss formula (3.1.23) and insert the phase factor $\cos \alpha$ as described above. After averaging over the parton's color we obtain

$$\begin{aligned} \frac{d\bar{E}(t)}{dt} &= ig^2 C_R v^i v^l \int \frac{d^3k}{(2\pi)^3} \int_{-\infty+i\sigma}^{\infty+i\sigma} \frac{d\omega}{2\pi i} e^{-i(\omega-\bar{\omega})t} (\Sigma^{-1})^{ij}(\omega, \mathbf{k}) \\ &\times \left\{ \frac{\omega \delta^{jl}}{\omega - \bar{\omega}} - \cos \alpha \left[(k^j k^k - \mathbf{k}^2 \delta^{jk}) (\Sigma^{-1})^{kl}(\bar{\omega}, \mathbf{k}) - \omega \bar{\omega} \varepsilon^{jk}(\bar{\omega}, \mathbf{k}) (\Sigma^{-1})^{kl}(\bar{\omega}, \mathbf{k}) \right] \right\}. \end{aligned} \quad (3.3.7)$$

This result, which reduces to the formula (3.3.1) when $\cos \alpha = 0$, will be further studied in the subsequent sections for two different unstable plasma systems.

3.4 Self-interactions

As already discussed in detail in the context of the equilibrium result (3.2.9), the energy loss formulae include the effect of self-interaction – also called the vacuum effect – which needs to be subtracted if it is non-zero. In this section we calculate the self-interaction contribution to the energy loss given by Eq. (3.3.1) and (3.3.7). We follow the same method as in Sec. 3.2. We evaluate the formulae (3.3.1) and (3.3.7) with the propagator $\Sigma^{-1}(\omega, \mathbf{k})$ in the form (3.2.7) with the vacuum dielectric functions (3.2.10). However, the calculation is not the same as the one done in Sec. 3.2. The equilibrium result (3.2.9) only has a contribution from the pole $\omega = \bar{\omega}$, but the energy loss formulae (3.3.1) and (3.3.7) with a vacuum propagator also include contributions from the poles $\omega = 0$ and $\omega = \pm|\mathbf{k}|$, which make the effect of self-interaction time dependent. We discuss only the vacuum contribution to the energy loss formula for correlated initial conditions (3.3.7), because the corresponding result for uncorrelated initial conditions can be obtained by setting $\cos \alpha = 0$.

To compute the vacuum effect we substitute into the formula (3.3.7) the vacuum propagator (3.2.7) with $\varepsilon_L(\omega, \mathbf{k}) = \varepsilon_T(\omega, \mathbf{k}) = 1$. In this way one finds the longitudinal part

$$\left. \frac{d\bar{E}_L(t)}{dt} \right|_{\text{vacuum}} = ig^2 C_R \int \frac{d^3 k}{(2\pi)^3} \frac{\bar{\omega}}{k^2} \int_{-\infty+i\sigma}^{\infty+i\sigma} \frac{d\omega}{2\pi i} \frac{e^{-i(\omega-\bar{\omega})t}}{\omega} \left[\frac{\bar{\omega}}{\omega-\bar{\omega}} + \cos \alpha \right], \quad (3.4.1)$$

and the transverse one

$$\begin{aligned} \left. \frac{d\bar{E}_T(t)}{dt} \right|_{\text{vacuum}} &= ig^2 C_R \int \frac{d^3 k}{(2\pi)^3} \left(1 - \frac{\bar{\omega}^2}{k^2} \right) \int_{-\infty+i\sigma}^{\infty+i\sigma} \frac{d\omega}{2\pi i} \frac{e^{-i(\omega-\bar{\omega})t}}{\omega^2 - k^2} \\ &\quad \times \left[\frac{\omega}{\omega - \bar{\omega}} + \cos \alpha \frac{\omega \bar{\omega} + k^2}{\bar{\omega}^2 - k^2} \right], \end{aligned} \quad (3.4.2)$$

where $k \equiv |\mathbf{k}|$. Performing the integral over ω , which includes contributions from the poles at $\omega = \bar{\omega}$ and $\omega = 0$ in case of the longitudinal part (3.4.1) and the poles at $\omega = \bar{\omega}$ and $\omega = \pm k$ in case of the transverse one (3.4.2), we obtain

$$\left. \frac{d\bar{E}_L(t)}{dt} \right|_{\text{vacuum}} = -(1 - \cos \alpha) g^2 C_R \int \frac{d^3 k}{(2\pi)^3} \frac{\bar{\omega} \sin(\bar{\omega}t)}{k^2}, \quad (3.4.3)$$

$$\begin{aligned} \left. \frac{d\bar{E}_T(t)}{dt} \right|_{\text{vacuum}} &= -(1 - \cos \alpha) \frac{ig^2 C_R}{2} \int \frac{d^3 k}{(2\pi)^3} \left(1 - \frac{\bar{\omega}^2}{k^2} \right) \\ &\quad \times \left(\frac{e^{-i(k-\bar{\omega})t}}{k - \bar{\omega}} - \frac{e^{i(k+\bar{\omega})t}}{k + \bar{\omega}} \right). \end{aligned} \quad (3.4.4)$$

We note that the pole $\omega = \bar{\omega}$ does not actually contribute to the transverse part (3.4.4) because the integrand is odd as a function of \mathbf{k} and therefore it gives zero when integrated.

The integrals over \mathbf{k} are calculated in spherical coordinates using an upper cut-off k_{\max} . Summing the longitudinal and transverse parts, the complete vacuum contribution to the energy loss formula (3.3.7) equals

$$\begin{aligned} \left. \frac{d\bar{E}(t)}{dt} \right|_{\text{vacuum}} = & -\frac{(1 - \cos \alpha)g^2 C_R}{4\pi^2 t^2} \left[2(\text{Si}(k_{\max}t) - \sin(k_{\max}t)) \right. \\ & \left. + (2k_{\max}t - \text{Si}(2k_{\max}t)) \right], \end{aligned} \quad (3.4.5)$$

where $\text{Si}(z)$ is the sine integral defined as

$$\text{Si}(z) \equiv \int_0^z dx \frac{\sin(x)}{x}. \quad (3.4.6)$$

The first term in the expression (3.4.5) is the longitudinal part and the second term represents the transverse piece which linearly diverges with increasing k_{\max} . Both the longitudinal and transverse contributions go to zero when $t \rightarrow 0$. The vacuum contribution to the energy loss formula with uncorrelated initial conditions (3.3.1) is given by Eq. (3.4.5) with $\cos \alpha = 0$. From Eq. (3.4.5) it is clear that the vacuum contribution is not zero unless we choose maximally correlated initial conditions (for which $\cos \alpha = 1$), and therefore the self-interaction effect must be subtracted from the energy loss formula in all other cases.

3.5 Unstable plasmas

The energy loss in isotropic plasmas has been calculated from the general formula (3.1.23) in section 3.2. In this section we develop our formalism to apply it to a general class of anisotropic momentum distributions of plasma constituents which was introduced in Sec. 2.4.1. The dispersion relations of the collective modes, which are needed to compute the energy loss, are derived in Chapter 2 for all possible degrees of deformation from the extremely prolate case, when the momentum distribution is infinitely elongated in one direction, to the extremely oblate distribution, which is infinitely squeezed in one direction.

To compute the energy loss using the formula (3.1.23) we have to invert the matrix Σ defined by Eq. (2.1.2) or (2.1.11), which is the inverse gluon propagator in the temporal axial gauge. In isotropic plasmas the matrix depends on only one vector \mathbf{k} . It can be decomposed into transverse and longitudinal components and is therefore easily inverted giving Eq. (3.2.7). We will now consider momentum distributions of the plasma constituents of the form (2.4.1). In this case the matrix Σ depends on two vectors \mathbf{k} and \mathbf{n} , and it is symmetric $\Sigma^{ij} = \Sigma^{ji}$. The procedure of the inversion of a matrix is introduced in the Sec. 2.1.2

In our derivation of the energy loss formula and our calculation of energy loss for isotropic systems, we have mostly used the terminology of classical electrodynamics of continuous media, with the dielectric tensor playing a key role. From now on we will switch to the language of quantum field theory and make use of the polarisation tensor and gluon propagator which were already introduced in Eqs. (2.1.5) and (2.1.11). The two languages are equivalent as QCD in the hard-loop approximation is essentially classical but the terminology of quantum field theory is more commonly used when working with the distribution (2.4.1). Then, one refers to Σ^{-1} as to the gluon propagator in the temporal axial gauge. In Appendix A.4 we show that this gauge is particularly convenient in the energy loss calculations.

In order to simplify the notation, in the rest of this section we omit the arguments which denote dependence on the wave vector. For example, we write $\alpha(\omega, \mathbf{k})$ as $\alpha(\omega)$, $\Delta^{ij}(\omega, \mathbf{k})$ as $\Delta^{ij}(\omega)$, *etc.*

3.5.1 Integrand

Substituting the propagator (2.1.17) into the energy loss formula (3.3.7) and contracting all indices, we obtain an expression that we will use to do calculations for the extremely prolate and extremely oblate momentum distributions presented in Sec. 3.6. We use a spherical coordinate system with the z -axis along the anisotropy vector \mathbf{n} . The angles θ and ϕ are the zenithal and azimuthal angles of the vector \mathbf{k} , and Θ is the angle between the velocity of the test parton \mathbf{v} and the anisotropy vector \mathbf{n} . In our coordinate system the vectors \mathbf{n} , \mathbf{v} and \mathbf{k} are

$$\begin{aligned}\mathbf{n} &= (0, 0, 1), \\ \mathbf{v} &= (\sin \Theta, 0, \cos \Theta), \\ \mathbf{k} &= k(\sin \theta \cos \phi, \sin \theta \sin \phi, \cos \theta).\end{aligned}\tag{3.5.1}$$

The energy loss formula (3.3.7) is written as

$$\frac{d\overline{E}(t)}{dt} = g^2 C_R \int \frac{d^3 k}{(2\pi)^3} \int_{-\infty+i\sigma}^{\infty+i\sigma} \frac{d\omega}{2\pi i} e^{-it(\omega-\bar{\omega})} \text{Integrand},\tag{3.5.2}$$

where the integrand is divided into several different pieces by writing it as

$$\text{Integrand} = A_j + G_j + \cos \alpha (A_{\text{ic}} + G_{\text{ic}} + [AA]_{\text{ic}} + [GG]_{\text{ic}}).\tag{3.5.3}$$

The two terms A_j and G_j are the contributions from the first term in the square bracket in (3.1.23) which comes from the parton current (3.1.14). When the initial fields are set to zero, or when we have uncorrelated initial conditions, these are the only terms that survive. They are proportional to $\Delta_A^{-1}(\omega)$ and $\Delta_G^{-1}(\omega)$. The terms A_{ic} , G_{ic} , $[AA]_{\text{ic}}$, $[GG]_{\text{ic}}$ are the contributions from the second two terms in the square bracket in Eq. (3.1.23) and come from the initial fields. They are proportional to $\Delta_A(\omega)$, $\Delta_G(\omega)$, $\Delta_A(\omega) \Delta_A(\bar{\omega})$ and $\Delta_G(\omega) \Delta_G(\bar{\omega})$. In the future we will refer to the first two terms in the formula (3.5.2) as ‘current contributions’, and the last four terms will be called ‘field contributions’. After performing all contractions we obtain

$$\begin{aligned}A_j &\equiv \frac{\hat{\omega} [\tilde{\omega}^2(x^2 - 1) - x^2 - Y^2 + 1]}{(1 - x^2)(\hat{\omega} - \tilde{\omega})\Delta_A^{-1}(\omega)}, \\ G_j &\equiv \hat{\omega} \frac{Y^2 \beta'(\omega) - \tilde{\omega}(x^2 - 1) \{ \tilde{\omega} [k^2(\hat{\omega}^2 - 1) - \alpha(\omega) - \gamma(\omega)] + 2kY\delta(\omega) \}}{(1 - x^2)(\hat{\omega} - \tilde{\omega})\Delta_G^{-1}(\omega)}, \\ A_{\text{ic}} &\equiv \left(\frac{\hat{\omega}}{\tilde{\omega}} - 1 \right) A_j,\end{aligned}$$

$$\mathbf{G}_{\text{ic}} \equiv \left(\frac{\hat{\omega}}{\tilde{\omega}} - 1 \right) \mathbf{G}_j,$$

$$[AA]_{\text{ic}} \equiv \frac{k^2(\hat{\omega}-\tilde{\omega})(\hat{\omega}+\tilde{\omega})}{\hat{\omega}\tilde{\omega}\Delta_A^{-1}(\tilde{\omega})} A_j,$$

$$[GG]_{\text{ic}} \equiv \frac{k^2(\hat{\omega}+\tilde{\omega})1}{\tilde{\omega}(1-x^2)\Delta_G^{-1}(\omega)\Delta_G^{-1}(\tilde{\omega})} (kY\tilde{\omega}(1-x^2) [\beta'(\tilde{\omega})\delta(\omega) + \beta'(\omega)\delta(\tilde{\omega})] \\ + Y^2\beta'(\omega)\beta'(\tilde{\omega}) + k^2\tilde{\omega}^2(1-x^2)^2\delta(\omega)\delta(\tilde{\omega})),$$

where we have used the symbols

$$x \equiv \cos \theta, \quad \hat{\omega} \equiv \omega/k, \quad \tilde{\omega} \equiv \bar{\omega}/k, \quad Y \equiv \cos \Theta - x\tilde{\omega},$$

and defined the function $\beta'(\omega) \equiv \omega^2 - \beta(\omega)$.

3.6 Extremely prolate and oblate plasmas

In the early stages of a heavy ion collision, when partons are initially released from the incoming nucleons, the momentum distribution is strongly elongated along the beam - it has a prolate shape. Due to free streaming the distribution evolves in the local rest frame to a form which is squeezed along the beam - it has oblate shape. In this section we consider the extremely prolate and extremely oblate distributions which are defined by the Eq. (2.4.9) and (2.4.8), respectively, with the normalisation condition (2.4.10).

The spectrum of the collective modes of the extremely prolate and extremely oblate plasmas is analysed in detail in Sec. 2.7 and 2.8, respectively. Here we use the obtained results to calculate the energy loss separately in Sec. 3.6.1 and 3.6.2 for extremely prolate and oblate system.

As discussed in Sec. 3.1, we calculate the frequency integral of the energy loss formula (3.5.2) with a contour in the lower half plane that encloses all singularities of the integral. The significance of the imaginary modes can be seen immediately. Denoting the real part of an imaginary mode generically as γ , it is clear that the residue of a pure imaginary mode contains a factor $e^{\gamma t}$ which grows exponentially with time. However, the magnitude of the unstable mode is small (in mass units) and the region of phase space for which the unstable mode exists is quite limited. Since there is also an oscillatory factor $e^{-i\omega t}$ under the integral (3.1.23), it is not clear whether the energy loss will increase exponentially as a function of time.

The integral over the wave vector \mathbf{k} is taken numerically in spherical coordinates with the z -axis along the anisotropy vector \mathbf{n} . Since the integral is ultraviolet divergent, we regulate it by introducing an upper cut-off at some finite momentum k_{\max} . For both oblate and prolate plasmas, there is a potential divergence when an imaginary mode goes to zero, as the wave vector approaches its threshold value. However, these divergences cancel exactly (sometimes in combination with the residue from the pole at $\omega = 0$). There are divergences that depend on the azimuthal angle when $\bar{\omega} = 0$ and $\bar{\omega} = \pm\omega_-$ but they are odd and can be regulated using a principal part prescription.

The current contribution to the energy loss, or the energy loss with the uncorrelated initial condition, is very oscillatory and hard to calculate, but we have checked that it is of the order of the equilibrium energy loss discussed in Sec. 3.2 and its magnitude is much smaller than the field contribution. In Sec. 2.7 we show the current contribution for one example.

In the two subsequent sections we present our numerical results on the energy loss in the extremely prolate and extremely oblate plasmas. In all our numerical calculations

$C_R = 3$, which corresponds to a gluon and our results are expressed in the units of m . As in Sec. 3.2, the energy loss is divided by $g^2 m^2$ and therefore the value of the coupling constant g is not specified.

3.6.1 Extremely prolate plasma

In Fig. 3.2 we present the integrand of the energy loss in prolate plasma as a function of k and $\cos\theta$ for $\Theta = \pi/12$. The integral over azimuthal angle ϕ has been done and the small spikes at the top of the figure are produced by numerical issues. The meaning of the angles θ , ϕ , Θ is explained by Eq. (3.5.1). Comparing this plot to that shown in Fig. 2.19, one clearly sees the influence of the unstable mode - the integrand is large in the domain of k and $\cos\theta$ where the mode ω_- exists.

Fig. 3.3 shows the current contribution to the energy loss (or the energy loss with $\cos\alpha = 0$) as a function of time for $\Theta = 0^\circ$. Since $d\bar{E}/dt$ is negative, the parton loses energy. The two curves represent two values of $k_{\max} = 3m$ and $k_{\max} = 5m$, one sees that the magnitude of the energy loss increases with k_{\max} . The result is time dependent but it is approximately the same magnitude as the equilibrium energy loss at a given k_{\max} . As seen in Fig. 3.1, the equilibrium energy loss equals $-0.12 g^2 m^2$ for $k_{\max} = 3m$ and $-0.18 g^2 m^2$ for $k_{\max} = 5m$.

In Fig. 3.4 we show the field contribution to the energy loss (with $\cos\alpha = 1$) as a function of time for $k_{\max} = 5m$ and four angles Θ between the parton velocity and the anisotropy vector \mathbf{n} . The energy loss $d\bar{E}/dt$ is positive and it increases exponentially with time, showing the effect of the unstable modes. The parton thus gains the energy and the magnitude of $d\bar{E}/dt$ at later times is much bigger than in equilibrium plasmas (see Fig. 3.1). The sign of the field contribution to the energy loss is determined by the sign of the phase factor $\cos\alpha$ and therefore if we change the initial condition from $\cos\alpha = 1$ to $\cos\alpha = -1$ we will get exponentially growing energy loss instead of exponentially growing energy gain. Since the field contribution to the energy loss is much bigger than the current contribution, the sign of $d\bar{E}/dt$ is actually controlled by the sign of $\cos\alpha$. Therefore, the energy loss crucially depends on the initial condition.

One observes in Fig. 3.4 a strong directional dependence of the energy loss. For a prolate system, the most important wave vectors are those for which $\mathbf{k} \perp \mathbf{n}$ where the threshold wave vector (2.7.9) goes to infinity, see also Fig. 2.19. When $\mathbf{k} \perp \mathbf{n}$ the unstable mode has an associated electric field that is parallel to the vector \mathbf{n} . This point is explained in Sec. 3.7. The energy transfer is most efficient when the electric field is parallel to the velocity of the test parton ($\mathbf{v} \parallel \mathbf{E}$). Therefore, one expects the largest energy transfer when $\mathbf{v} \parallel \mathbf{n}$.

This argument is shown schematically in Fig. 3.10a and verified by the results presented in Fig. 3.4 which demonstrates that the magnitude of the energy loss is maximal at $\Theta = 0^\circ$ and rapidly decays when the angle Θ grows.

In Fig. 3.5 we show the energy loss as a function of k_{\max} for $\Theta = 0^\circ$ and two times $t = 5/m$ and $t = 8/m$. The energy loss oscillates slightly, but the k_{\max} dependence can be roughly approximated as $\log k_{\max}$, as in the equilibrium case. As discussed in Sec. 3.2, the k_{\max} divergence indicates a breakdown of the classical theory.

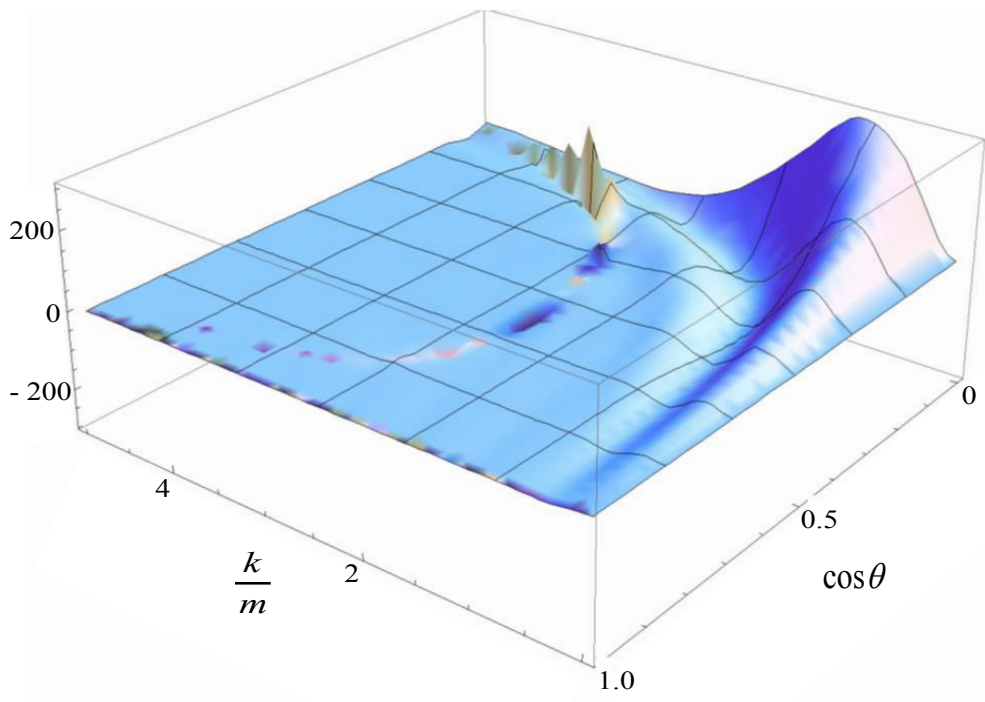


FIGURE 3.2: The integrand of the energy loss with $\cos\alpha = 1$ in extremely prolate plasma as a function of k and $\cos\theta$ for $\Theta = \pi/12$ and $t = 8/m$. The integral over azimuthal angle ϕ is performed.

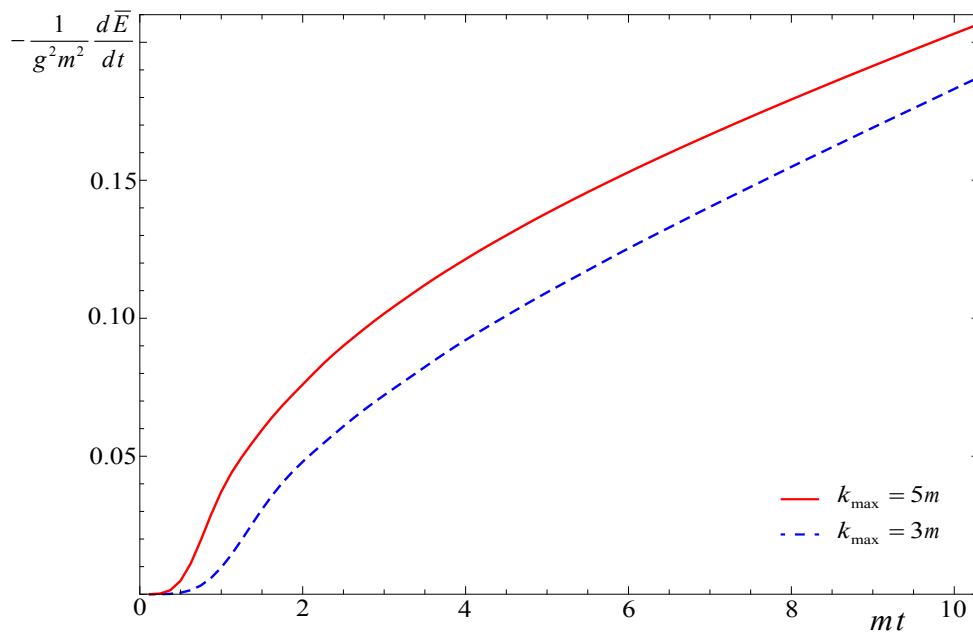


FIGURE 3.3: Current contribution to the energy loss as a function of t for $\Theta = 0^\circ$, for two different choices of the k_{\max} . The red (solid) curve is for $k_{\max} = 5m$, and blue dashed for $k_{\max} = 3m$.

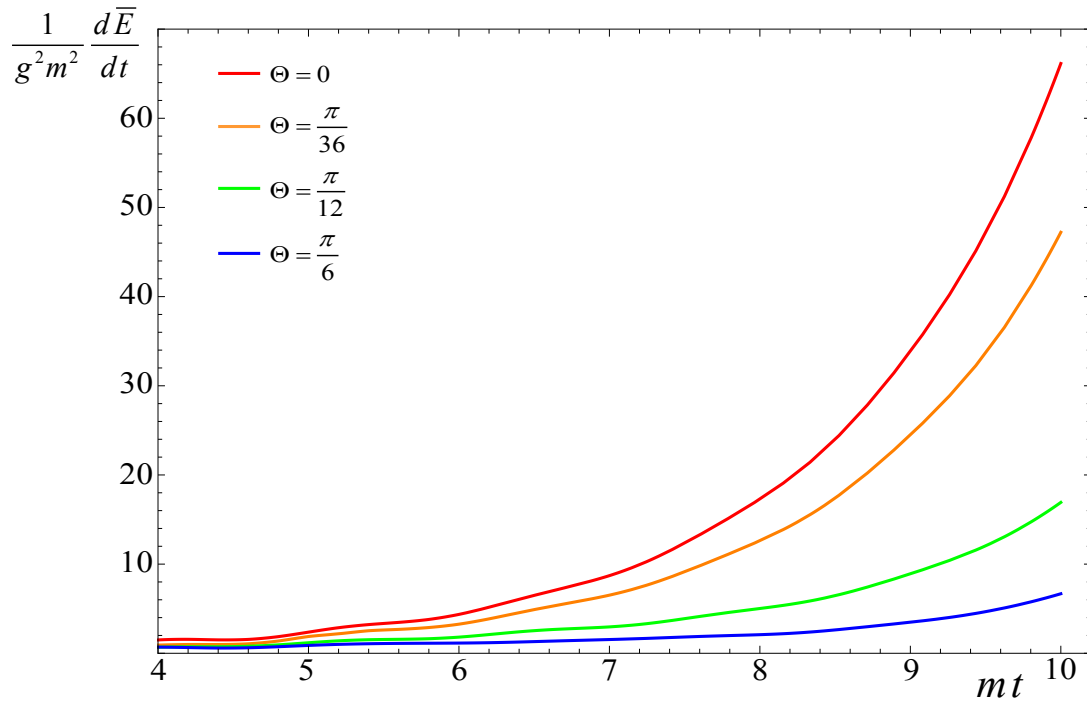


FIGURE 3.4: The field contribution to the energy loss in prolate plasma as a function of time for four angles Θ between the parton velocity and the anisotropy direction: $\Theta = 0$ (red), $\Theta = \pi/36$ (orange), $\Theta = \pi/12$ (green), and $\Theta = \pi/6$ (blue). The cut-off parameter $k_{\max} = 5m$.

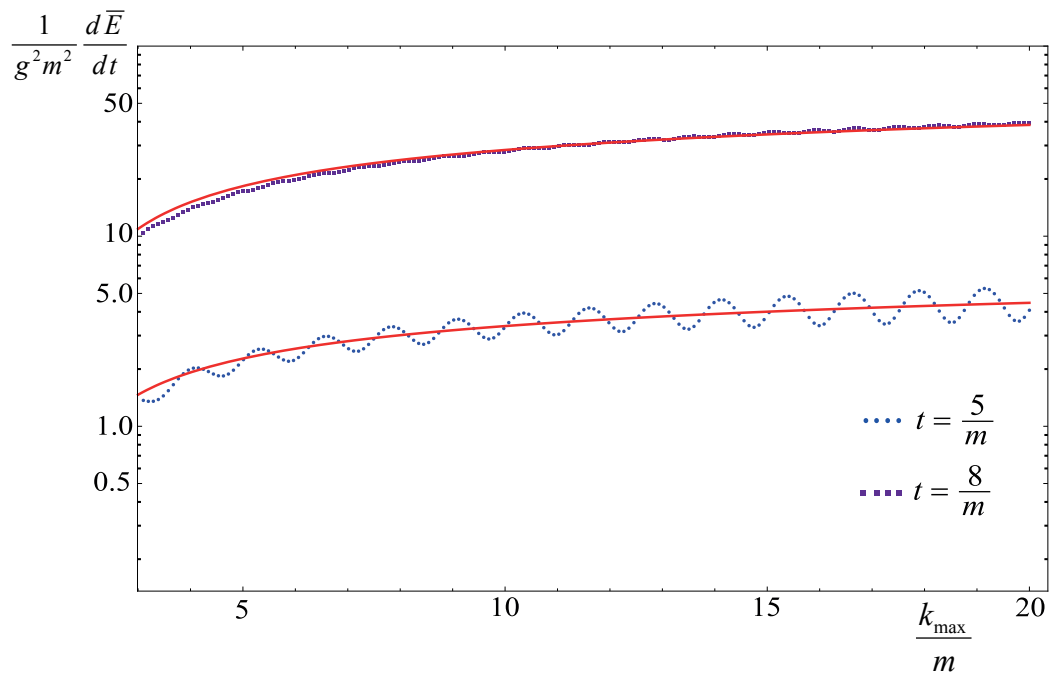


FIGURE 3.5: The field contribution to the energy loss in prolate plasma at $\Theta = 0$ as a function of k_{\max} for $t = 5/m$ (circles) and $t = 8/m$ (squares). The red solid curves are a logarithmic fit.

3.6.2 Extremely oblate plasma

Calculations in oblate plasma are much more difficult than those in prolate plasma because the components of the polarisation tensor defined by Eq. (2.1.12) have a more complicated structure. They contain square roots that are not defined along the section of the real axis where the arguments of the roots are negative. There are therefore contributions to the frequency integral from the discontinuities between the upper and lower sides of the cuts that are difficult to calculate. We have checked for several cases that they are small when compared to the pole contributions and we therefore neglect them. One consequence of this more complicated structure is that the spectrum of collective modes is richer - there two unstable modes instead of one as in the case of prolate plasma. It is impossible to solve the dispersion equations analytically and one can only obtain the dispersion relations numerically. Finally, there is a technical complication related to the fact that the dominant contribution to the energy loss in the oblate plasma comes from the domain of wave vectors \mathbf{k} which are almost parallel to the anisotropy vector \mathbf{n} . When $\mathbf{k} \parallel \mathbf{n}$ we have $\mathbf{n}_T = 0$ and the decomposition (2.1.8) is ill defined. This occurs because when $\mathbf{k} \parallel \mathbf{n}$ the matrix Σ does not depend on two independent vectors \mathbf{k} and \mathbf{n} but only on one vector \mathbf{k} or \mathbf{n} , for details see Sec. 2.8.1

In our calculation the domain where $\mathbf{k} \parallel \mathbf{n}$ was treated analytically and combined with the results of the numerical computation, as described below. Because of these technical difficulties, we give numerical results for the extremely oblate plasma only for a rather small value of $k_{\max} = 2m$. The equilibrium energy loss for this value of k_{\max} , which will be used as a reference point, equals $-0.079 g^2 m^2$, see Fig. 3.1.

As in the case of prolate plasma, the current contribution is significantly smaller than the field contribution. The latter is shown in Fig. 3.6 when the parton's momentum is perpendicular to the anisotropy vector \mathbf{n} ($\Theta = \pi/2$). The red points represent the contribution due to the A -modes, blue points represent the G -modes and black gives the sum. The black is not exactly the sum of the red and blue because in the calculation with all modes the points at $x = \pm 1$, which are obtained analytically, are combined and integrated together with the numerical data which is calculated over the range $-0.9996 < x < 0.9996$. One observes in Fig. 3.6 that the unstable A -mode is responsible for the largest effect. Since the field contribution to the energy loss is much bigger than the current contribution, the sign of the energy loss is determined by the sign of $\cos \alpha$ which expresses the dependence on the initial conditions. $d\bar{E}/dt$ is negative for $\cos \alpha < 0$ and it is positive when $\cos \alpha > 0$. As seen in Fig. 3.6, the energy loss in oblate plasma can be orders of magnitude bigger than in an equilibrium plasma with the same k_{\max} .

For an extremely oblate system, the most important wave vectors are those for which $\mathbf{k} \parallel \mathbf{n}$, since both of the thresholds k_{oA} and k_{oG} go to infinity in this limit, see Eq. (2.8.6)-(2.8.7). This behaviour is also shown in Figs. 2.24-2.25. As explained in Sec. 3.7, instead of two different pairs of imaginary modes A and G , we have two pairs of identical modes which are purely transverse when $\mathbf{k} \parallel \mathbf{n}$. The electric field associated with these modes is perpendicular to both \mathbf{k} and \mathbf{n} . Since the energy loss is maximal when the parton velocity is parallel to the electric field, such a situation occurs in the oblate system when \mathbf{v} is perpendicular to \mathbf{n} , or $\Theta = \pi/2$. This argument is shown schematically in Fig. 3.10b. The effect is seen explicitly in Figs. 3.7-3.9. Fig. 3.7 shows that for both A - and G -modes the energy loss is dominated by the region $x \approx 1$ and the right panel proves that when $x = 1$ the biggest effect is observed when $\Theta = \pi/2$. Fig. 3.9 presents the energy loss as a function of Θ for $t = 25/m$. The figure shows that $d\bar{E}/dt$ drops rapidly when Θ becomes smaller than $\pi/2$.

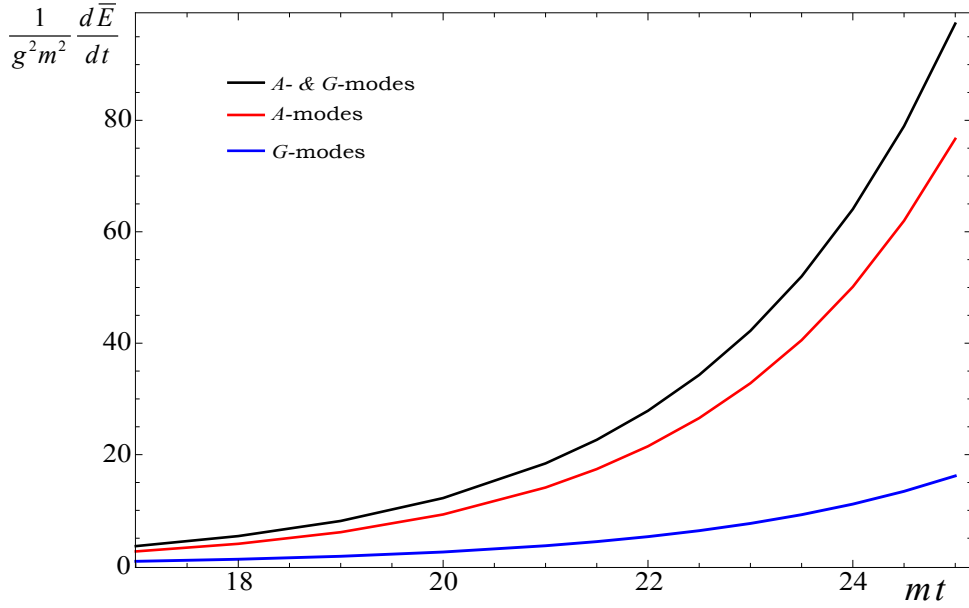


FIGURE 3.6: The field contribution to the energy loss in oblate plasma as a function of time for $\Theta = \pi/2$. The red lines corresponds to the effect of *A*-modes, blue the *G*-modes, and the black line represents the sum.

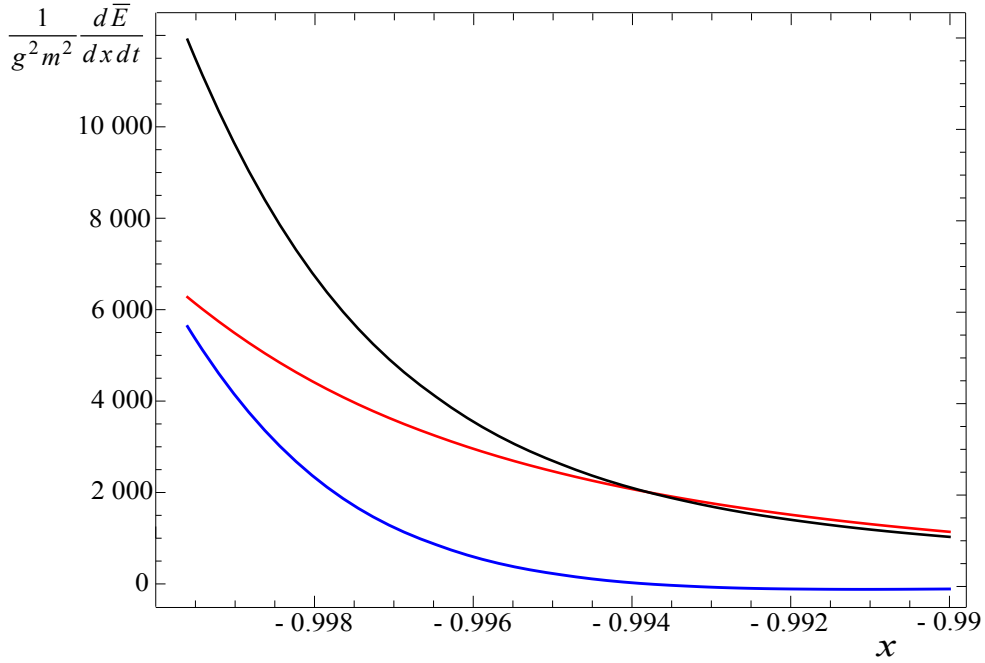


FIGURE 3.7: The integrand of the field contribution to oblate energy loss after integrating it over ϕ and k for $t = 25/m$. The integrand is shown as a function of $x \equiv \cos \theta$ for $\Theta = \pi/2$. The red, blue and black lines represent the effect of, respectively, *A*-modes, *G*-modes and the sum of *A* plus *G*-modes.

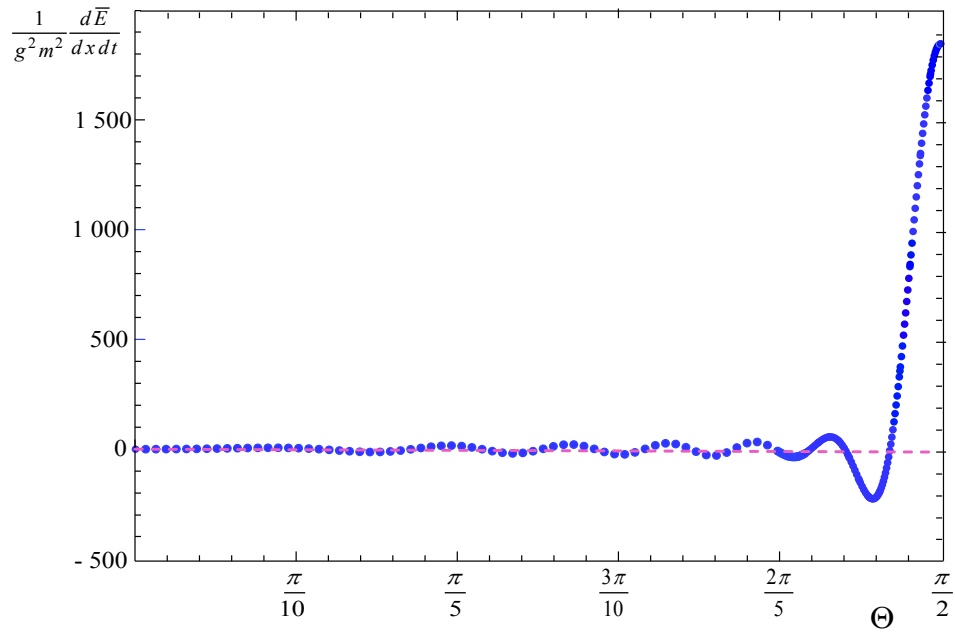


FIGURE 3.8: The integrand of the field contribution to oblate energy loss after integrating it over ϕ and k for $t = 25/m$. The integrand is shown as a function of Θ for $x = 1$.

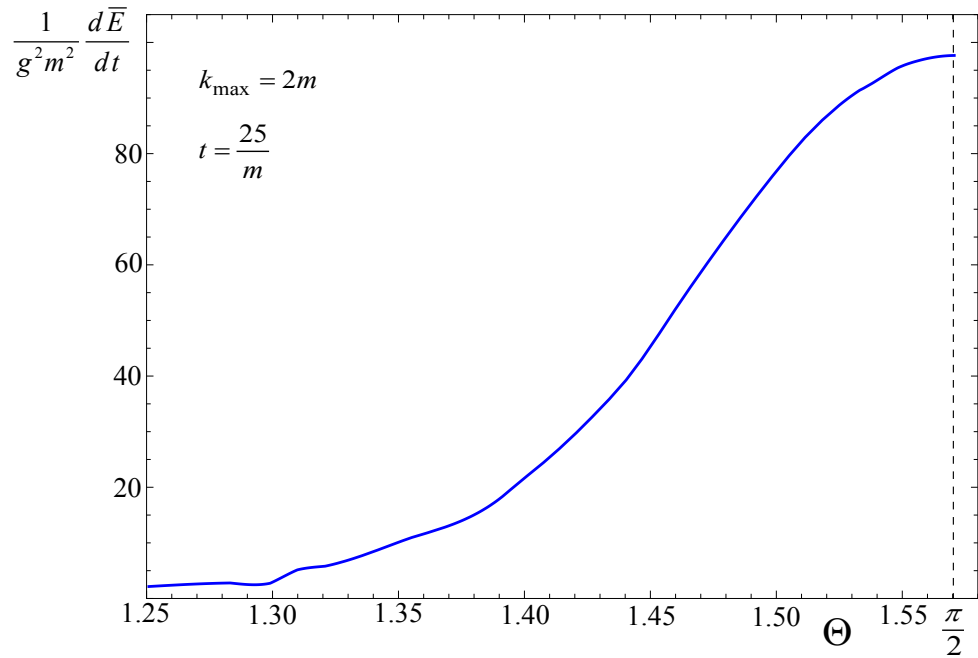


FIGURE 3.9: The field contribution to the energy loss in oblate plasma as a function of the angle Θ for $t = 25/m$.

3.7 Important configurations

In this section we look at the prolate system in the special case that the wave vector of the unstable mode is perpendicular to the direction of anisotropy ($\mathbf{k} \perp \mathbf{n}$) and the oblate system when these two vectors are parallel ($\mathbf{k} \parallel \mathbf{n}$). These regions of \mathbf{k} are important because they are the part of the domain of \mathbf{k} for which the unstable modes exist up to infinite k , see Eqs. (2.7.9), (2.8.6), (2.8.7) and Figs. 2.19 and 2.24-2.25. We will further show that the energy loss is maximal when the velocity of the test parton \mathbf{v} is parallel to \mathbf{n} in the prolate plasma and when $\mathbf{v} \perp \mathbf{n}$ in the oblate one. The arguments discussed in this section are illustrated in Fig. 3.10.

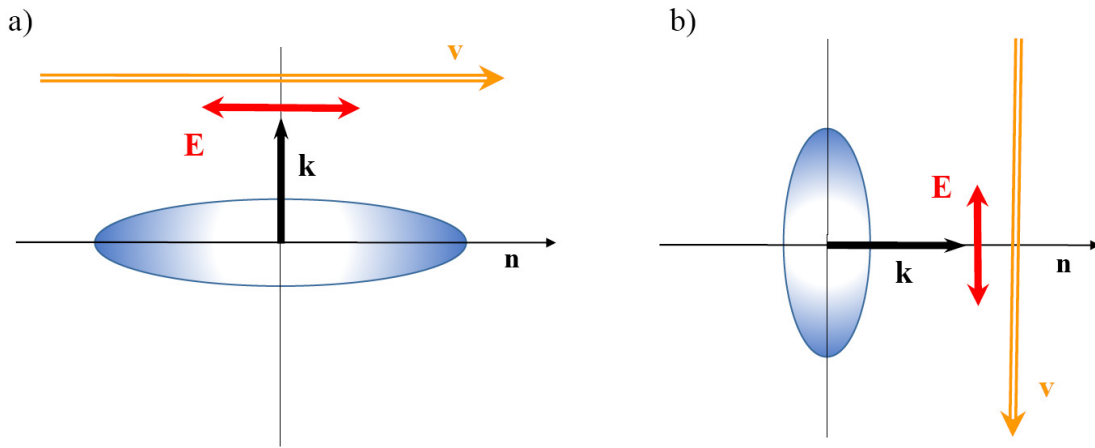


FIGURE 3.10: The largest wave vectors of unstable modes at different orientations. In the prolate plasma (left panel) there is one unstable G -mode, which exists for $0^\circ < \theta \leq 90^\circ$, and in oblate plasma (right panel) there are two unstable A - and G -modes which exist for $0^\circ \leq \theta < 90^\circ$ and $0^\circ \leq \theta < 45^\circ$, respectively.

We start with the prolate system. The linearized Yang-Mills or Maxwell equations of electric field $\mathbf{E}(\omega, \mathbf{k})$ can be written as:

$$\Sigma^{ij}(\omega, \mathbf{k})E^j(\omega, \mathbf{k}) = 0, \quad (3.7.1)$$

with the matrix Σ defined by Eq. (2.1.2). Since the equation (3.7.1) is homogeneous, there are solutions if the determinant of the matrix Σ vanishes - this is the general dispersion equation (2.1.1). When $\mathbf{n} = (0, 0, 1)$ and $\mathbf{k} = (k, 0, 0)$, Eq. (3.7.1) is

$$\begin{bmatrix} \omega^2 - \beta(\omega) & 0 & 0 \\ 0 & \omega^2 - k^2 - \alpha(\omega) & 0 \\ 0 & 0 & \omega^2 - k^2 - \alpha(\omega) - \gamma(\omega) \end{bmatrix} \begin{bmatrix} E_x(\omega, \mathbf{k}) \\ E_y(\omega, \mathbf{k}) \\ E_z(\omega, \mathbf{k}) \end{bmatrix} = 0, \quad (3.7.2)$$

where

$$\alpha(\omega) = \beta(\omega) = \frac{m^2}{2}, \quad \gamma(\omega) = \frac{m^2(k^2 - \omega^2)}{2\omega^2}. \quad (3.7.3)$$

The imaginary modes appear as solutions of the equation $\omega^2 - k^2 - \alpha(\omega) - \gamma(\omega) = 0$ which controls the z -component of the electric field. Therefore, the exponentially growing component of \mathbf{E} is parallel to \mathbf{n} . Since the maximal energy loss occurs when $\mathbf{v} \parallel \mathbf{E}$, the maximal effect requires $\mathbf{v} \parallel \mathbf{n}$.

Let us now consider the oblate plasma. When $\mathbf{n} = (0, 0, 1)$ and $\mathbf{k} = (0, 0, k)$, Eq. (3.7.1) is

$$\begin{bmatrix} \omega^2 - k^2 - \alpha(\omega) & 0 & 0 \\ 0 & \omega^2 - k^2 - \alpha(\omega) & 0 \\ 0 & 0 & \omega^2 - \beta(\omega) \end{bmatrix} \begin{bmatrix} E_x(\omega, \mathbf{k}) \\ E_y(\omega, \mathbf{k}) \\ E_z(\omega, \mathbf{k}) \end{bmatrix} = 0, \quad (3.7.4)$$

where the coefficients $\alpha(\omega)$ and $\beta(\omega)$ are given by Eq. (2.8.10). The imaginary modes appear as solutions of the equation $(\omega^2 - k^2 - \alpha(\omega))^2 = 0$ which controls the x - and y -components of the electric field. Therefore, the exponentially growing component of \mathbf{E} is perpendicular to \mathbf{n} and the maximal energy loss occurs when $\mathbf{v} \perp \mathbf{n}$.

The prolate plasma system produces the strongest instability when the wave vector \mathbf{k} is exactly transverse to the anisotropy vector \mathbf{n} . For the oblate system the situation is exactly reversed and the strongest instability occurs when the wave vector and anisotropy vector are parallel to each other.

The orientation of the largest wave vectors of unstable modes is schematically shown in Fig. 3.10. Since the A -modes are transverse, the chromoelectric field of the maximally unstable A -mode in oblate plasma is perpendicular to \mathbf{n} . The G -modes are, in general, neither transverse nor longitudinal. However, the maximally unstable G -modes (with $\mathbf{k} \parallel \mathbf{n}$ in oblate plasma and $\mathbf{k} \perp \mathbf{n}$ in prolate plasma) are transverse. Therefore, for G -modes in prolate systems and both A -modes and G -modes in oblate plasmas, the chromoelectric field of the maximally unstable modes is aligned with the direction where the momentum of plasma particles is maximal. This observation is important because the dynamics of unstable systems are dominated by the fastest growing unstable modes.

Chapter 4

Conclusions and Outlook

In first part of the thesis, we have performed a systematic analysis of plasmons - gluon collective modes - in quark-gluon plasma in case when the momentum distribution of plasma constituent is anisotropic. We have considered two-stream system and the system with distribution function which is obtained by either squeezing or stretching the isotropic distribution. We have analysed the distributions with all degrees of deformation along the beam axis from the extremely prolate distribution, which is infinitely elongated along the beam, to the extremely oblate distribution, which is infinitely squeezed with respect to the beam axis. In every case we have calculated the dispersion curves of complete spectrum, in some cases numerically and when it has been possible analytically.

All obtained solutions of dispersion equations are either pure real or pure imaginary and they always appear as pairs of partners with opposite sign. In all systems under consideration, except the isotropic plasma, there are unstable modes (positive pure imaginary solutions). Imaginary solutions exist only for certain wave vectors.

We have checked that even for arbitrarily small anisotropy unstable modes are present - there is no threshold value of the anisotropy parameter for which instabilities develop. However, the growth rate of instability decreases and the domain of wave vectors for which unstable modes exist shrinks, as the anisotropy parameter decreases. However, our work does not take into account inter-parton collisions which reduce the growth rates and domains of wave vectors of the unstable modes and effectively stabilize systems of sufficiently small anisotropy.

The analysis of collective modes in anisotropic plasmas is an important part of our study because the results obtained in Chapter 2 have been used extensively in the analysis of parton energy loss in unstable QGP presented in Chapter 3.

In the second part of the thesis we have first derived the energy loss formula for a high-energy parton flying across an unstable plasma which experiences a rapid temporal evolution due to exponentially growing collective modes. Except special cases, the energy loss formula includes an effect of self-interaction which must be subtracted to get a physically meaningful result. Since the formula is found as the solution of an initial value problem, initial values of the chromodynamic fields present in the plasma must be chosen. In case of equilibrium plasmas, the initial conditions are ‘forgotten,’ and the well-known formula of collisional energy loss is reproduced. When the initial conditions are chosen in such a way that the initial fields are not correlated with the current generated by the test parton, the parton typically loses energy and the magnitude of the energy loss is comparable to that in an equilibrium plasma of the same mass parameter m (2.4.10). When the initial chromodynamic field is induced by the parton, it can be either accelerated or decelerated depending on the relative phase factor. With correlated initial conditions, the magnitude of the energy loss grows exponentially in time and can much exceed the absolute value of the energy loss in an equilibrium plasma.

We have derived an expression for the energy loss for arbitrarily prolate or oblate plasmas and performed numerical calculations for the specific examples of the extremely prolate and extremely oblate systems. The energy loss is not only time dependent but it appears to be also strongly directionally dependent. The configurations when the energy loss is maximal in the prolate and oblate plasmas are illustrated in Fig. 3.10. In these special configurations, the magnitude of the energy loss can be much bigger than that in an equilibrium plasma. Beyond a narrow cone which is centered around the optimal direction, the magnitude of energy loss rapidly drops.

One wonders what are possible consequences of our findings for the jet suppression observed in relativistic heavy-ion collisions. Since a high-energy parton can be either accelerated or decelerated in an unstable plasma, we expect that the energy loss strongly fluctuates and that the fluctuations are particularly large in the configurations depicted in Fig. 3.10.

Quark-gluon plasma at an early stage of a relativistic heavy-ion collision has initially a prolate momentum distribution which evolves fast due to free streaming to an oblate momentum distribution. During the process of equilibration the plasma is oblate and it remains oblate in the subsequent evolution because of viscosity effects. Jet quenching is observed at both RHIC and LHC at almost vanishing rapidity in the center of mass of colliding nuclei. This configuration is just as shown in Fig. 3.10b where the jet momentum is transverse to the vector \mathbf{n} . We suspect that the jet quenching pattern can be changed when the jet axis is tilted in such a way that the near-side jet has a small but positive (negative) rapidity while the away-side jet has a small but negative (positive)

rapidity. The effect of unstable modes is then reduced and the energy-loss fluctuations are expected to be much smaller.

One should remember that we have discussed in this work only collisional energy loss. There are simple arguments that indicate that radiative energy loss behaves very differently. Radiative energy loss is controlled by the parameter \hat{q} which measures the momentum broadening of a parton. This parameter is by definition positive and grows exponentially in an unstable plasma, and so does the radiative energy loss, which is always negative. Therefore, before we draw a conclusion about a possible role of unstable plasma in jet suppression phenomenology, the effects of both collisional and radiative energy loss must be combined.

Our results rely on initial conditions chosen in a very specific way. In future studies a method of averaging over initial conditions to mimic the situation in relativistic heavy-ion collisions should be proposed.

Our approach to the energy loss in unstable QGP is fully classical and thus it is limited to small momentum transfers. A quantum approach needs to be developed but it is certainly a very complex initial value problem.

Appendix A

A.1 Classical dispersion equation

For the completeness of our discussion, we show here how the dispersion equation of plasma waves is derived in classical electrodynamics. One starts with sourceless Maxwell equations in a medium. After Fourier transformation to the space of frequencies ω and wave vectors \mathbf{k} , they give

$$k^i D^i(\omega, \mathbf{k}) = 0, \quad \epsilon^{ijk} k^j E^k(\omega, \mathbf{k}) = \omega B^i(\omega, \mathbf{k}), \quad (\text{A.1.1})$$

$$k^i B^i(\omega, \mathbf{k}) = 0, \quad \epsilon^{ijk} k^j B^k(\omega, \mathbf{k}) = -\omega D^i(\omega, \mathbf{k}), \quad (\text{A.1.2})$$

where $\mathbf{E}(\omega, \mathbf{k})$, $\mathbf{D}(\omega, \mathbf{k})$, $\mathbf{B}(\omega, \mathbf{k})$ are the electric field, electric induction and magnetic field, and ϵ^{ijk} is the completely antisymmetric tensor. The electric induction is expressed through the electric field by means of the electric permeability tensor $\epsilon^{ij}(\omega, \mathbf{k})$ as

$$D^i(\omega, \mathbf{k}) = \epsilon^{ij}(\omega, \mathbf{k}) E^j(\omega, \mathbf{k}). \quad (\text{A.1.3})$$

Substituting the dielectric induction in the form (A.1.3) into Maxwell equations, one finds the following equation of motion of the electric field

$$[-\mathbf{k}^2 \delta^{ij} + k^i k^j + \omega^2 \epsilon^{ij}(\omega, \mathbf{k})] E^j(\omega, \mathbf{k}) = 0. \quad (\text{A.1.4})$$

Solutions of the homogeneous equation (A.1.4) exist, provided the determinant of the matrix (2.1.2) vanishes. This is the dispersion equation (2.1.1).

A.2 Components of polarization tensor

We present here the components α , β , γ , δ of the polarization tensor computed with the ξ -distribution (2.4.1) and σ -distribution (2.4.6). The azimuthal and polar integrals in the formulas (2.4.11)-(2.4.14) can be evaluated analytically, but the results are lengthy, and not very enlightening. We give here only the expressions with the polar integral unevaluated using the following notation: $\hat{\omega} \equiv \omega/k$, $x \equiv \cos \theta$ and $y \equiv \cos \theta'$. We also define

$$R_{\pm} \equiv \sqrt{\hat{\omega} + i0^+ - xy \pm \sqrt{1-x^2}\sqrt{1-y^2}}. \quad (\text{A.2.1})$$

The results for the ξ -distribution (2.4.1), which appeared previously in [43] with the normalization constant $C_{\xi} = 1$, are

$$\frac{\alpha_{\xi}(\omega, \mathbf{k})}{C_{\xi} m^2} = \int_{-1}^1 \frac{dy(\xi xy + \hat{\omega})}{(x^2 - 1)(\xi y^2 + 1)^2} \left[\frac{x^2 - 2xy\hat{\omega} + y^2 + \hat{\omega}^2 - 1}{R_+ R_-} + xy - \hat{\omega} \right], \quad (\text{A.2.2})$$

$$\frac{\beta_{\xi}(\omega, \mathbf{k})}{C_{\xi} m^2} = \int_{-1}^1 \frac{dy \hat{\omega}}{(\xi y^2 + 1)^2} \left[\frac{\hat{\omega}(\xi xy + \hat{\omega})}{R_+ R_-} + (\xi + 1)(-x)y - \hat{\omega} \right], \quad (\text{A.2.3})$$

$$\begin{aligned} \frac{\gamma_{\xi}(\omega, \mathbf{k})}{C_{\xi} m^2} = \int_{-1}^1 \frac{dy}{(x^2 - 1)(\xi y^2 + 1)^2} & \left[- \frac{((x^2 + 1)\hat{\omega}^2 + x^2 - 4xy\hat{\omega} + 2y^2 - 1)(\xi xy + \hat{\omega})}{R_+ R_-} \right. \\ & \left. + \xi(x^2 + 1)y(x\hat{\omega} - y) + \hat{\omega}(x(x^2 - 3)y + (x^2 + 1)\hat{\omega}) \right], \end{aligned} \quad (\text{A.2.4})$$

$$\begin{aligned} \frac{k \delta_{\xi}(\omega, \mathbf{k})}{C_{\xi} m^2} = \int_{-1}^1 \frac{dy}{(x^2 - 1)(\xi y^2 + 1)^2} & \left[\frac{\hat{\omega}(x\hat{\omega} - y)(\xi xy + \hat{\omega})}{R_+ R_-} \right. \\ & \left. - \hat{\omega}(y((\xi + 1)x^2 - 1) + x\hat{\omega}) \right]. \end{aligned} \quad (\text{A.2.5})$$

For the σ -distribution (2.4.6) we obtain

$$\frac{\alpha_\sigma(\omega, \mathbf{k})}{C_\sigma m^2} = \int_{-1}^1 \frac{dy((\sigma+1)\hat{\omega} - \sigma xy)}{(x^2-1)(\sigma(y^2-1)-1)^2} \left[\frac{x^2 - 2xy\hat{\omega} + y^2 + \hat{\omega}^2 - 1}{R_+ R_-} + xy - \hat{\omega} \right], \quad (\text{A.2.6})$$

$$\frac{\beta_\sigma(\omega, \mathbf{k})}{C_\sigma m^2} = \int_{-1}^1 \frac{dy \hat{\omega}}{(\sigma(y^2-1)-1)^2} \left[\frac{\hat{\omega}((\sigma+1)\hat{\omega} - \sigma xy)}{R_+ R_-} - (\sigma+1)\hat{\omega} - xy \right], \quad (\text{A.2.7})$$

$$\begin{aligned} \frac{\gamma_\sigma(\omega, \mathbf{k})}{C_\sigma m^2} = & \int_{-1}^1 \frac{dy}{(x^2-1)(\sigma(y^2-1)-1)^2} \quad (\text{A.2.8}) \\ & \left[\frac{((x^2+1)\hat{\omega}^2 + x^2 - 4xy\hat{\omega} + 2y^2 - 1)(\sigma xy - (\sigma+1)\hat{\omega})}{R_+ R_-} \right. \\ & \left. + ((\sigma+1)(x^2+1)\hat{\omega}^2 + \sigma(x^2+1)y^2 + x\hat{\omega}y(-4\sigma + x^2 - 3)) \right], \end{aligned}$$

$$\begin{aligned} \frac{k \delta_\sigma(\omega, \mathbf{k})}{C_\sigma m^2} = & \int_{-1}^1 \frac{dy \hat{\omega}}{(x^2-1)(\sigma(y^2-1)-1)^2} \left[\frac{(x\hat{\omega} - y)((\sigma+1)\hat{\omega} - \sigma xy)}{R_+ R_-} \quad (\text{A.2.9}) \right. \\ & \left. - y(-\sigma + x^2 - 1) - (\sigma+1)x\hat{\omega} \right]. \end{aligned}$$

As explained in Sec. 2.4.2 and summarized in Eq. (2.4.18), all four coefficients are real when ω is real and $\omega^2 > k^2$. When ω is real but $\omega^2 < k^2$, the coefficients become complex. For imaginary valued ω , all four coefficients are real. In Fig. A.1-A.4 we show the components of the polarization tensor α_σ , β_σ , γ_σ , $k \delta_\sigma$ as functions of ω/k for $\sigma = 10$ and $\theta = 40^\circ$. In each part of the figure, we show the real and imaginary parts of the component for real ω and the pure real components for imaginary ω . For reference, the curves for α and β in isotropic plasma are also shown. The blue (dotted) line is the real part with real ω , the green (dashed) line is the imaginary part with real ω , and the red (solid) line is the pure real result when ω is imaginary. The lighter lines in the panels presenting the coefficients α_σ and β_σ correspond to the isotropic distribution.

The polarization tensors of the ξ - and σ -distribution exhibit a kind of symmetrical structure when they are plotted as functions of $x \equiv \cos\theta$. One finds the following pattern. The real part of X_ξ , where X is either α , β or γ , has a maximum when the real part of X_σ has a minimum and *vice versa*. The imaginary parts of X_ξ and X_σ are maximal and minimal, respectively, for the same values of x . In case of δ , the positions of the maxima of real parts coincide and the maximum of the imaginary part of δ_ξ coincides with the minimum of the imaginary part of δ_σ and *vice versa*. These results are shown in Fig. A.5-A.10 for the coefficients α and β .

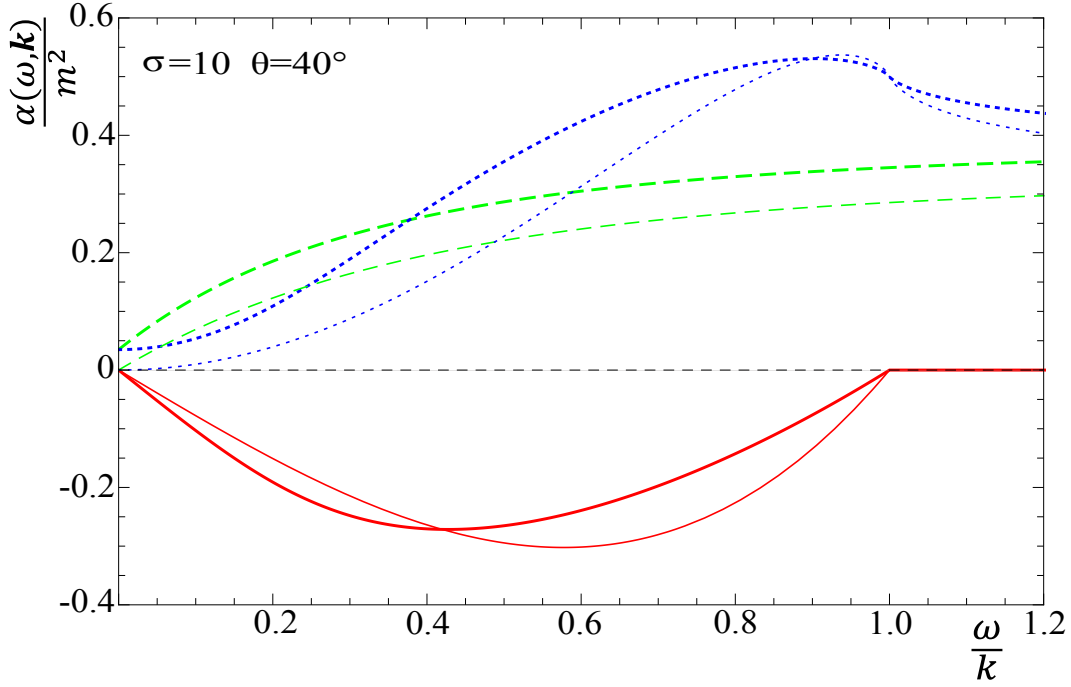


FIGURE A.1: The component α_σ of the polarization tensor obtained from the σ -distribution with $\sigma = 10$ and $\theta = 40^\circ$.

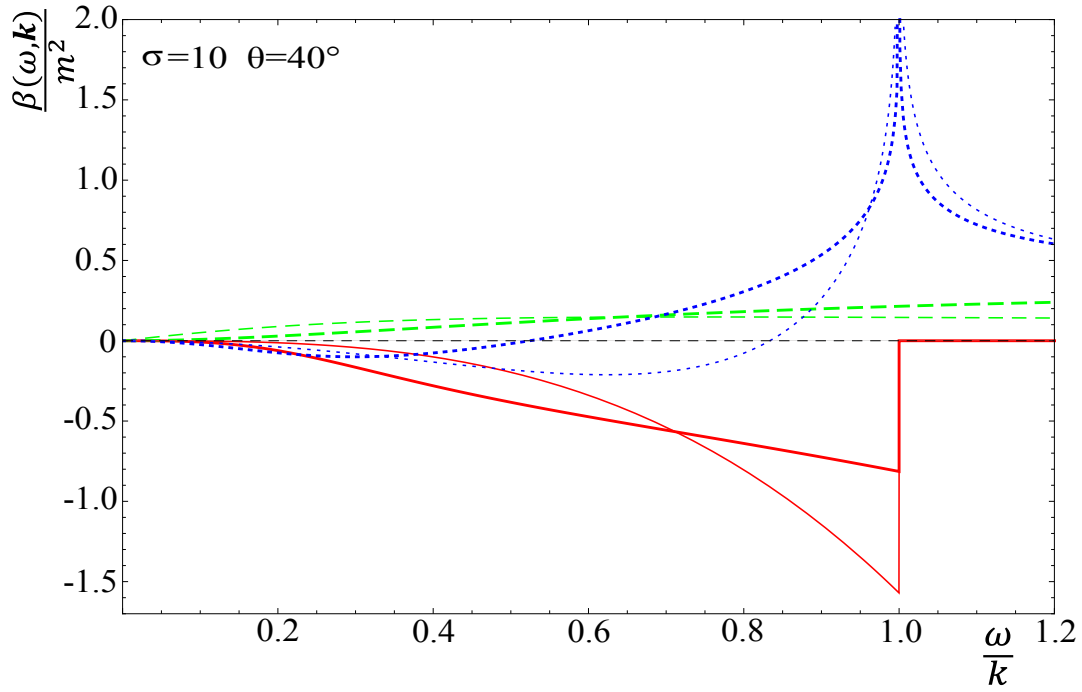


FIGURE A.2: The component β_σ of the polarization tensor obtained from the σ -distribution with $\sigma = 10$ and $\theta = 40^\circ$.

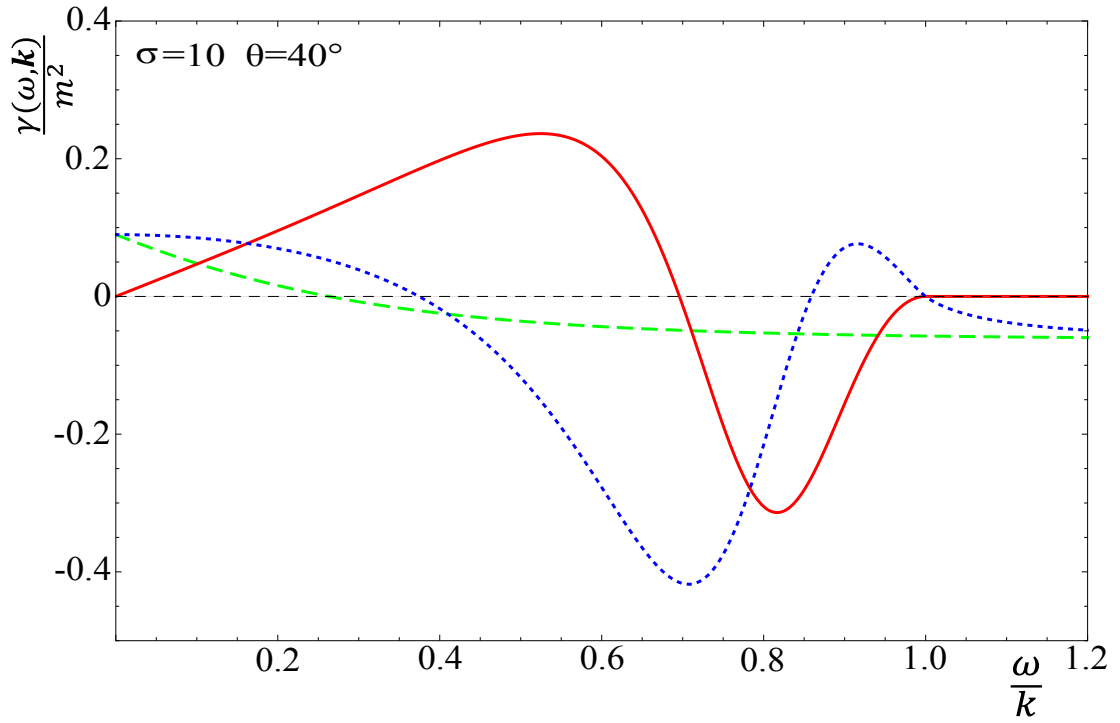


FIGURE A.3: The component γ_σ of the polarization tensor obtained from the σ -distribution with $\sigma = 10$ and $\theta = 40^\circ$.

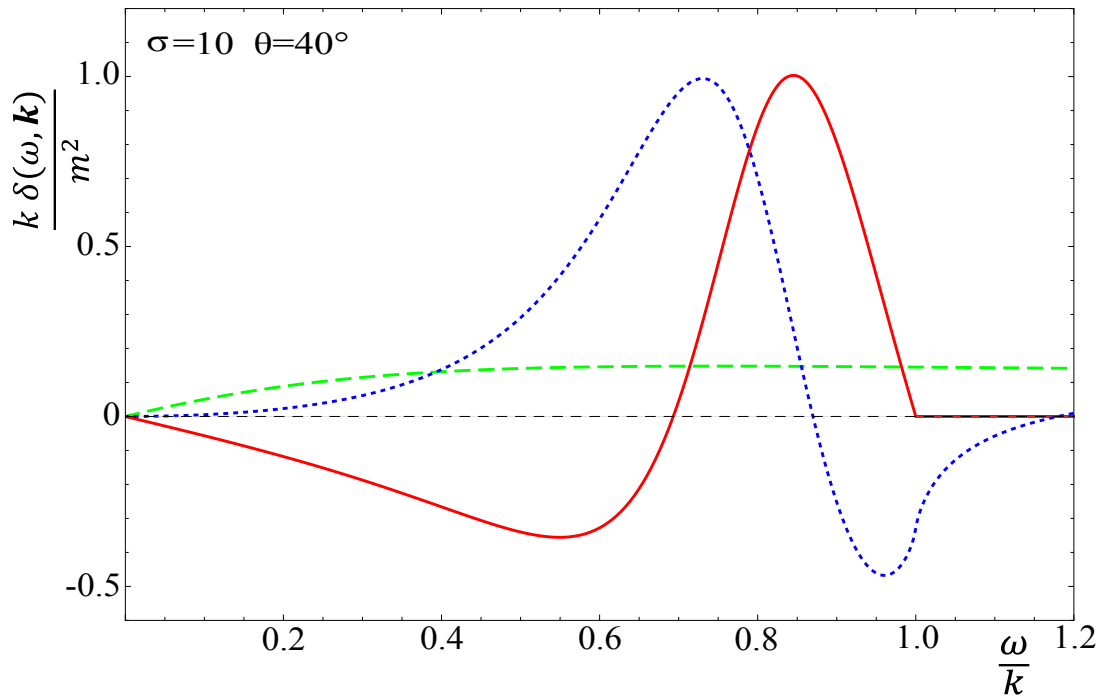


FIGURE A.4: The component $k \delta_\sigma$ of the polarization tensor obtained from the σ -distribution with $\sigma = 10$ and $\theta = 40^\circ$.

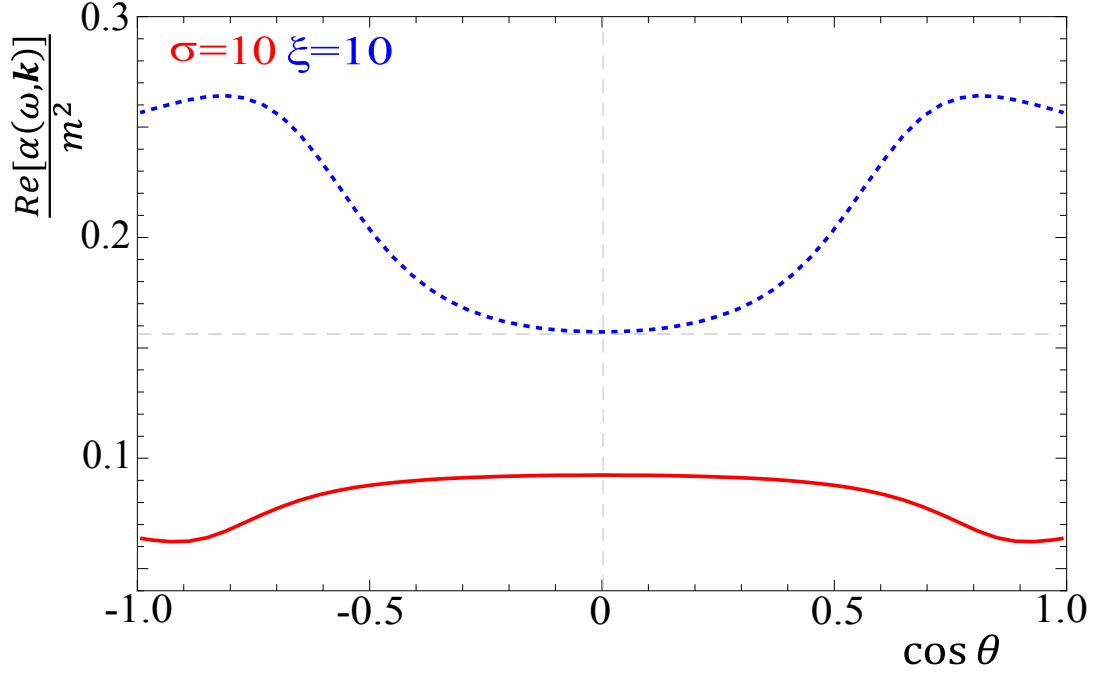


FIGURE A.5: The real component α of the polarization tensor with $\sigma = 10$ (red (solid) line) and $\xi = 10$ (blue (dotted) line) versus $x \equiv \cos \theta$ with $\omega/k = 0.8$ or $\omega/k = 0.8i$.

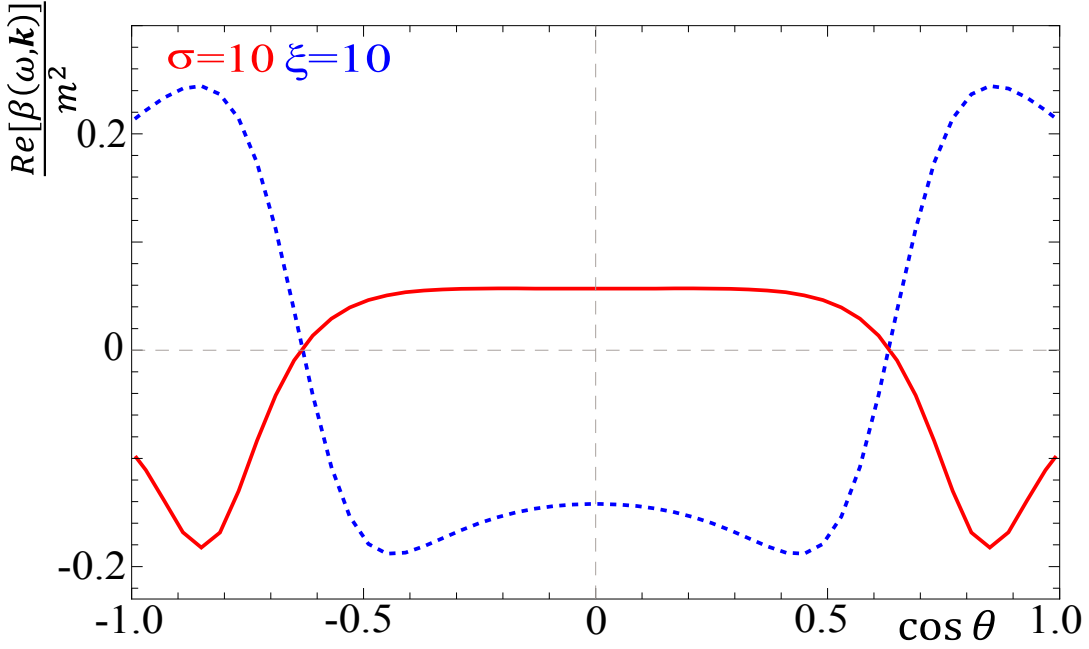


FIGURE A.6: The real component β of the polarization tensor with $\sigma = 10$ (red (solid) line) and $\xi = 10$ (blue (dotted) line) versus $x \equiv \cos \theta$ with $\omega/k = 0.8$ or $\omega/k = 0.8i$.

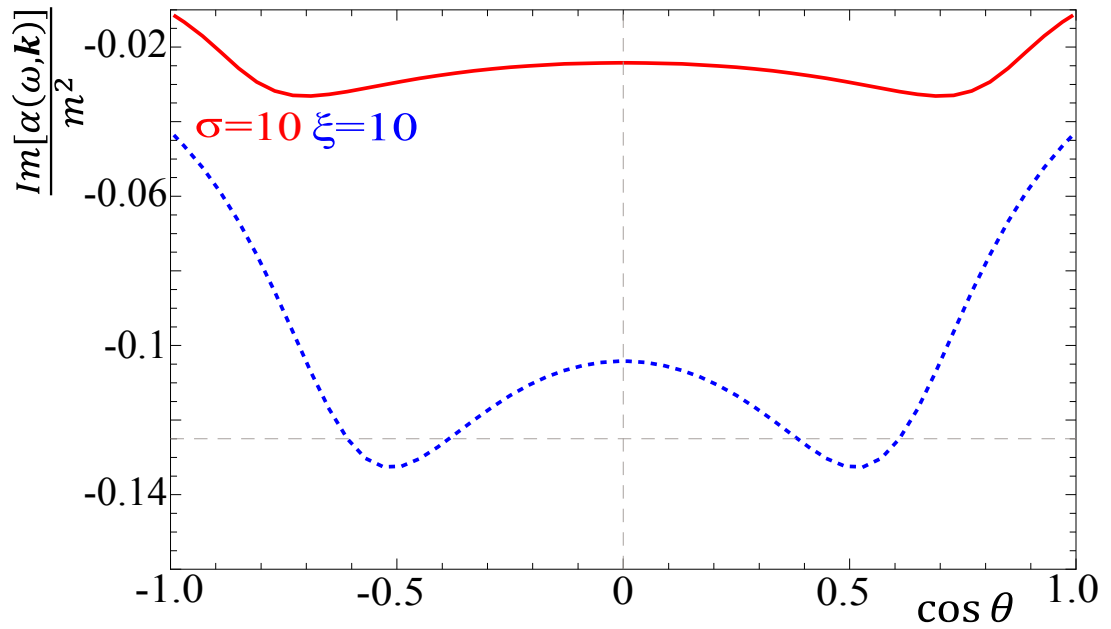


FIGURE A.7: The imaginary component α of the polarization tensor with $\sigma = 10$ (red (solid) line) and $\xi=10$ (blue (dotted) line) versus $x \equiv \cos \theta$ with $\omega/k = 0.8$ or $\omega/k = 0.8i$.

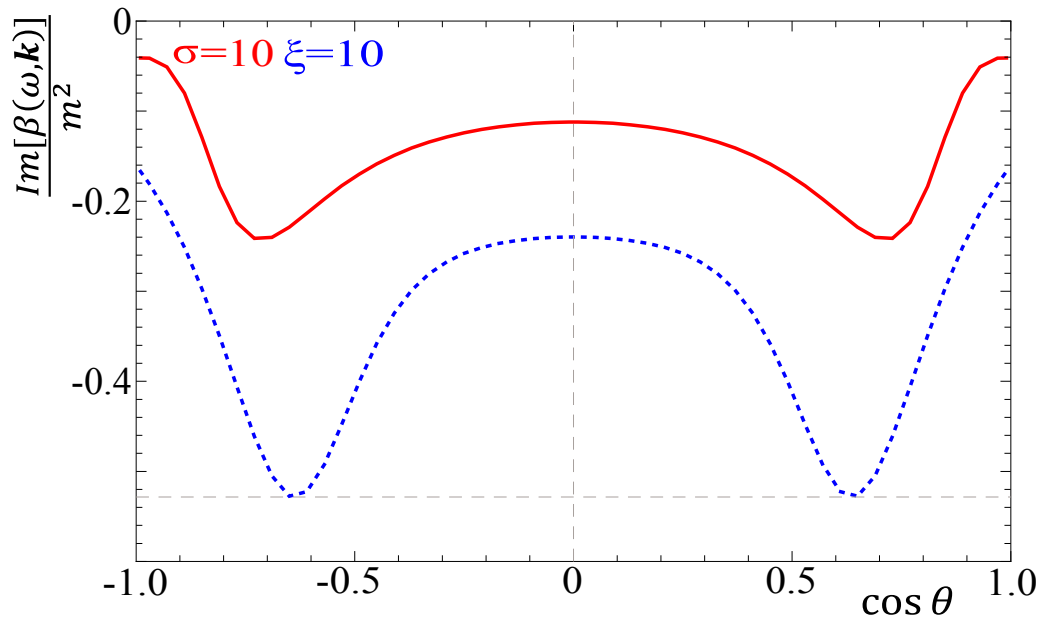


FIGURE A.8: The imaginary component β of the polarization tensor with $\sigma = 10$ (red (solid) line) and $\xi=10$ (blue (dotted) line) versus $x \equiv \cos \theta$ with $\omega/k = 0.8$ or $\omega/k = 0.8i$.

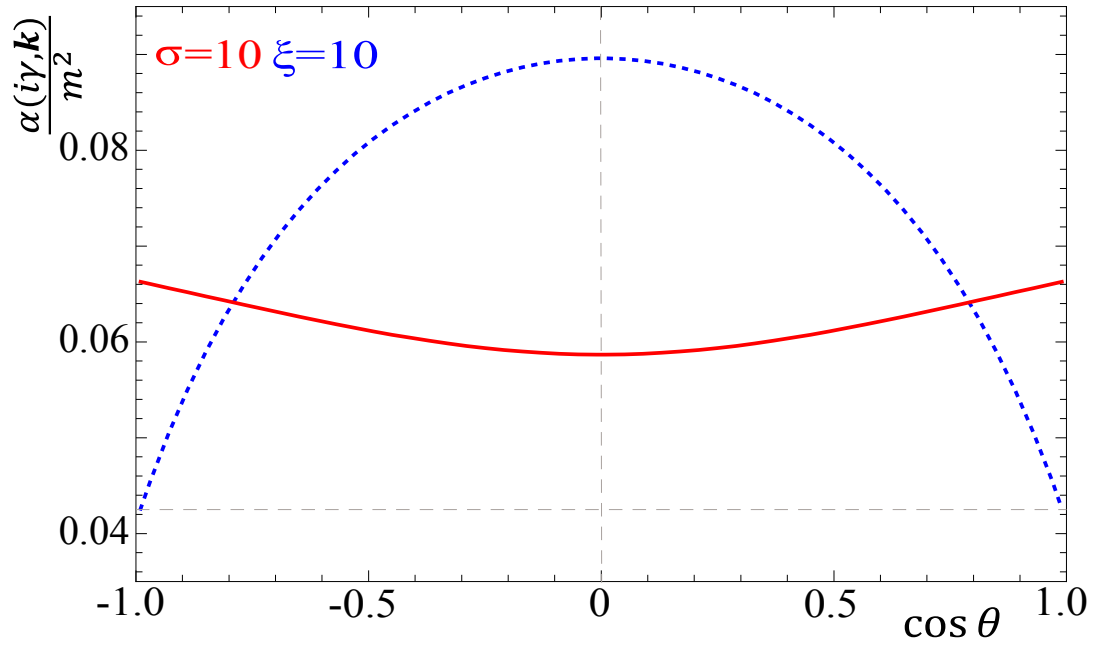


FIGURE A.9: The component α of the polarization tensor obtained with σ - and ξ -distribution for $\sigma = \xi = 10$ and for imaginary ω .

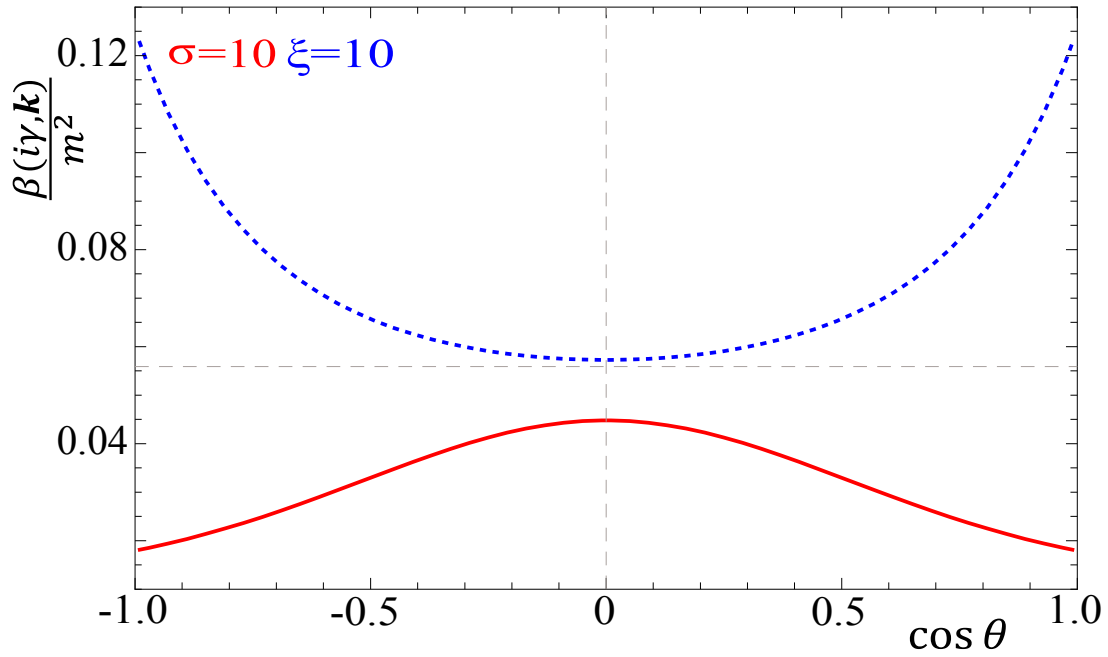


FIGURE A.10: The component β of the polarization tensor obtained with σ - and ξ -distribution for $\sigma = \xi = 10$ and for imaginary ω .

A.3 Reality of energy loss

We prove here that the energy loss (3.1.23) is real for any momentum distribution that satisfies the mirror symmetry $f(\mathbf{p}) = f(-\mathbf{p})$. For this purpose we take the complex conjugate of the formula (3.1.23) and obtain

$$\begin{aligned} \frac{dE^*(t)}{dt} = & -gQ^a v^i \int \frac{d^3k}{(2\pi)^3} \int_{-\infty-i\sigma}^{\infty-i\sigma} \frac{d\omega}{2\pi i} e^{i(\omega-\bar{\omega})t} \Delta^{*ij}(\omega, \mathbf{k}) \\ & \times \left[-\frac{i\omega g Q^a v^j}{\omega - \bar{\omega}} + \epsilon^{jkl} k^k B_{0a}^{*l}(\mathbf{k}) - \omega D_{0a}^{*j}(\mathbf{k}) \right], \end{aligned} \quad (\text{A.3.1})$$

where the inverse matrix Σ^{-1} is replaced by the retarded propagator Δ . Now we change the integration variables $\omega \rightarrow -\omega$ and $\mathbf{k} \rightarrow -\mathbf{k}$ which gives

$$\begin{aligned} \frac{dE^*(t)}{dt} = & -gQ^a v^i \int \frac{d^3k}{(2\pi)^3} \int_{-\infty+i\sigma}^{\infty+i\sigma} \frac{d\omega}{2\pi i} e^{-i(\omega-\bar{\omega})t} \Delta^{*ij}(-\omega, -\mathbf{k}) \\ & \times \left[-\frac{i\omega g Q^a v^j}{\omega - \bar{\omega}} - \epsilon^{jkl} k^k B_{0a}^{*l}(-\mathbf{k}) + \omega D_{0a}^{*j}(-\mathbf{k}) \right], \end{aligned} \quad (\text{A.3.2})$$

Since the initial fields $\mathbf{B}_{0a}(\mathbf{r})$ and $\mathbf{D}_{0a}(\mathbf{r})$ are pure real in coordinate space, we have

$$\mathbf{B}_{0a}(\mathbf{k}) = \mathbf{B}_{0a}^*(-\mathbf{k}), \quad \mathbf{D}_{0a}(\mathbf{k}) = \mathbf{D}_{0a}^*(-\mathbf{k}). \quad (\text{A.3.3})$$

In Sec. 2.1.2 we have proved that for mirror-symmetric momentum distributions, the retarded propagator defined by Eq. (2.1.11) satisfies the relations

$$\Re \Delta^{ij}(-\omega, -\mathbf{k}) = \Re \Delta^{ij}(\omega, \mathbf{k}), \quad \Im \Delta^{ij}(-\omega, -\mathbf{k}) = -\Im \Delta^{ij}(\omega, \mathbf{k}),$$

which give

$$\Delta^{*ij}(-\omega, -\mathbf{k}) = \Delta^{ij}(\omega, \mathbf{k}). \quad (\text{A.3.4})$$

Using the relations (A.3.3) and (A.3.4), the right side of Eq. (A.3.2) is identical to the right side of Eq. (3.1.23), which completes the proof that the energy loss given by the formula (3.1.23) is real.

A.4 Temporal axial and Feynman-Lorentz gauges

In this appendix we show that the temporal axial gauge is particularly convenient for the energy loss calculation because it naturally provides gauge independent results. In contrast, we show that in Feynman-Lorentz gauge current conservation must be explicitly enforced to remove gauge dependence. To simplify the problem, we consider an electromagnetic plasma.

The electromagnetic analog of the energy loss formula (3.1.23) is clearly gauge invariant, as the derivation of the formula is gauge invariant at every step. The gauge dependent potential A^μ is not used at all and the energy loss is written in a form that depends only on the dielectric tensor and electric and magnetic fields which are physical quantities. However, when we switch to the terminology of quantum field theory and the inverse dielectric tensor is replaced by the photon propagator in the temporal axial gauge, the gauge independence of the formula (3.1.23) is not evident any more. In this appendix we will show that although the energy loss formula looks different in the Feynman-Lorentz gauge, it is still gauge invariant. We also explain why temporal axial gauge is much more convenient for the energy loss calculation. In this appendix we use the usual (two-sided) Fourier transformation and not the one-sided transformation which was used in Sec. 3.1.

To further simplify the problem we will consider not the whole energy loss formula but only the electric field generated by the test particle in vacuum. We will solve the Maxwell equation

$$\partial_\mu F^{\mu\nu}(x) = j^\nu(x), \quad (\text{A.4.1})$$

where $x = (t, \mathbf{r})$, $F^{\mu\nu} \equiv \partial^\mu A^\nu - \partial^\nu A^\mu$ and j^μ is the particle's current. The electric field, which is the physical quantity of interest, is expressed through the four-potential as

$$\mathbf{E}(x) = -\nabla A^0(x) - \dot{\mathbf{A}}(x), \quad (\text{A.4.2})$$

which in the momentum space is

$$\mathbf{E}(k) = -i\mathbf{k}A^0(k) + i\omega\mathbf{A}(k). \quad (\text{A.4.3})$$

We note that $k = (\omega, \mathbf{k})$ denotes here the four-vector and not $|\mathbf{k}|$.

In order to solve equation (A.4.1) for the potential, one must choose a gauge. The resulting solution has the form $A = \text{propagator} \times \text{current}$. Both the propagator and the vector potential are gauge dependent. However, if we calculate the electric field from the potential using Eq. (A.4.2) or (A.4.3), the result must be gauge independent. This is true when current conservation is imposed.

We start by considering Feynman-Lorentz gauge ($\partial_\mu A^\mu = 0$) in which the Maxwell equation (A.4.1) is

$$\square A^\mu(x) = j^\nu(x), \quad (\text{A.4.4})$$

and the (two-sided) Fourier transformed solution reads

$$A^\mu(k) = \Delta_{\text{FLG}}^{\mu\nu}(k) j_\nu(k), \quad (\text{A.4.5})$$

where

$$\Delta_{\text{FLG}}^{\mu\nu}(k) = -\frac{g^{\mu\nu}}{k^2 + i\text{sgn}(\omega)0^+} = g^{\mu\nu} D_{\text{FLG}}(k) \quad (\text{A.4.6})$$

is the retarded photon propagator in the Feynman-Lorentz gauge. From equations (A.4.3), (A.4.5) and (A.4.6) we obtain the electric field generated by the current $j^\nu(k)$

$$E^i(k) = -iD_{\text{FLG}}(k)(k^i j^0(k) - \omega j^i(k)). \quad (\text{A.4.7})$$

Now we consider the temporal axial gauge ($A^0 = 0$). The (two-sided) Fourier transformed field equation (A.4.1) splits into two equations

$$-\omega k^i A^i(k) = j^0(k), \quad (\text{A.4.8})$$

$$[(-\omega^2 + \mathbf{k}^2)\delta^{ij} - k^i k^j] A^j(k) = j^i(k). \quad (\text{A.4.9})$$

The solution of the second equation (A.4.9) is

$$A^i(k) = -\Delta_{\text{TAG}}^{ij}(k) j^j(k), \quad (\text{A.4.10})$$

where

$$\Delta_{\text{TAG}}^{ij}(k) = \frac{1}{\omega^2 + i\text{sgn}(\omega)0^+} \frac{k^i k^j}{\mathbf{k}^2} + \frac{1}{\omega^2 - \mathbf{k}^2 + i\text{sgn}(\omega)0^+} \left(\delta^{ij} - \frac{k^i k^j}{\mathbf{k}^2} \right) \quad (\text{A.4.11})$$

is the retarded photon propagator in the temporal axial gauge. Substituting the solution (A.4.10) into Eq. (A.4.3) and using ($A^0 = 0$) we obtain

$$E^i(k) = -i\omega \Delta_{\text{TAG}}^{ij}(k) j^j(k). \quad (\text{A.4.12})$$

We have found that in Feynman-Lorentz gauge the electric field is given by Eq. (A.4.7) and in temporal axial gauge it is given by Eq. (A.4.12) with the additional constraint (A.4.8). The two equations for the electric field look different, but if current conservation is imposed they are in fact the same. Current conservation gives the relation

$$\omega j^0(k) = \mathbf{k} \cdot \mathbf{j}(k). \quad (\text{A.4.13})$$

Using (A.4.13) the electric field obtained from the Feynman-Lorentz gauge (A.4.7) can be written in the form

$$E^i(k) = -\frac{i}{\omega} D_{\text{FLG}}(k) (k^i k^j - \omega^2 \delta^{ij}) j^j(k). \quad (\text{A.4.14})$$

Equations (A.4.6) and (A.4.11) give the equality

$$\Delta_{\text{TAG}}^{ij}(k) = \frac{1}{\omega^2} D_{\text{FLG}}(k) (k^i k^j - \omega^2 \delta^{ij}). \quad (\text{A.4.15})$$

Using Eq. (A.4.15) it is easy to see that the expressions (A.4.12) and (A.4.14) are equivalent.

When working in the temporal axial gauge, current conservation merely tells us that the solution (A.4.10) satisfies Eq. (A.4.8) automatically and the electric field is naturally gauge independent. Equivalently, the electric field in (A.4.12) can be derived from the Maxwell equations (3.1.4) and (3.1.5) without any reference to the four-potential A^μ . In contrast, if Feynman-Lorentz gauge is used, current conservation must be explicitly enforced. The authors of [86] resolved this problem by modifying somewhat artificially the parton's current.

Bibliography

- [1] M. Gell-Mann, Phys. Lett. **8**, 214 (1964).
- [2] G. Zweig, Developments in the Quark Theory of Hadrons, Volume 1. pp. 22–101 (1964).
- [3] O. Greenberg, Phys. Rev. Lett. **13**, 598 (1964).
- [4] J. Bjorken and S. Glashow, Phys. Lett. **11**, 255 (1964).
- [5] R. P. Feynman, Phys. Rev. Lett. **23**, 1415 (1969).
- [6] J. Bjorken, Phys. Rev. **179**, 1547 (1969).
- [7] M. Breidenbach, J. I. Friedman, H. W. Kendall, E. D. Bloom, D. Coward, et al., Phys. Rev. Lett. **23**, 935 (1969).
- [8] C. N. Yang and R. L. Mills, Phys. Rev. **96**, 191 (1954).
- [9] D. J. Gross and F. Wilczek, Phys. Rev. Lett. **30**, 1343 (1973).
- [10] H. D. Politzer, Phys. Rev. Lett. **30**, 1346 (1973).
- [11] J. C. Collins and M. Perry, Phys. Rev. Lett. **34**, 1353 (1975).
- [12] E. V. Shuryak, Sov. Phys. JETP **47**, 212 (1978).
- [13] G. Chapline, M. Johnson, E. Teller, and M. Weiss, Phys. Rev. **D8**, 4302 (1973).
- [14] T. Lee and G. Wick, Phys. Rev. **D9**, 2291 (1974).
- [15] U. W. Heinz and M. Jacob (2000), nucl-th/0002042.
- [16] E. W. Kolb and M. S. Turner, in *High energy physics in the 1990's: proceedings* (1988), pp. 37–43.
- [17] M. A. Stephanov, PoS **LAT2006**, 024 (2006).
- [18] S. Bethke, Nucl. Phys. Proc. Suppl. **234**, 229 (2013).

- [19] I. Arsene et al. (BRAHMS), Nucl. Phys. **A757**, 1 (2005).
- [20] B. Back, M. Baker, M. Ballintijn, D. Barton, B. Becker, et al., Nucl. Phys. **A757**, 28 (2005).
- [21] J. Adams et al. (STAR), Nucl. Phys. **A757**, 102 (2005).
- [22] K. Adcox et al. (PHENIX), Nucl. Phys. **A757**, 184 (2005).
- [23] M. Gagliardi, Nuovo Cim. **C037**, 187 (2014).
- [24] T. Ženiš (ATLAS), in *Proceedings, 20th International Conference on Particles and Nuclei (PANIC 14)* (2014), pp. 469–472.
- [25] R. Schöffbeck (CMS), EPJ Web Conf. **95**, 03032 (2015).
- [26] R. Snellings, J. Phys. **G41**, 124007 (2014).
- [27] T. Schörner-Sadenius, ed., *The Large Hadron Collider* (Springer, Berlin, 2015).
- [28] T. Ludlam and L. McLerran, Phys. Today **56N10**, 48 (2003).
- [29] G. Martinez (2013), 1304.1452.
- [30] U. W. Heinz, AIP Conf. Proc. **739**, 163 (2005).
- [31] J. D. Bjorken, FERMILAB-PUB-82-059-THY (1982).
- [32] J. Adams et al. (STAR), Phys. Rev. Lett. **91**, 072304 (2003).
- [33] Y. Lee (CMS), J. Phys. **G38**, 124015 (2011).
- [34] W. Florkowski, *Phenomenology of Ultra-Relativistic Heavy-Ion Collisions* (World Scientific Publishing Company, Singapore, 2010).
- [35] W. Jas and S. Mrowczynski, Phys. Rev. **C76**, 044905 (2007).
- [36] W. Florkowski, R. Ryblewski, and M. Strickland, Phys. Rev. **C88**, 024903 (2013).
- [37] W. Florkowski, M. Martinez, R. Ryblewski, and M. Strickland, PoS **ConfinementX**, 221 (2012).
- [38] S. Mrowczynski and M. H. Thoma, Ann. Rev. Nucl. Part. Sci. **57**, 61 (2007).
- [39] E. S. Weibel, Phys. Rev. Lett. **2**, 83 (1959).
- [40] S. Mrowczynski, Phys. Rev. **C49**, 2191 (1994).
- [41] P. B. Arnold, J. Lenaghan, G. D. Moore, and L. G. Yaffe, Phys. Rev. Lett. **94**, 072302 (2005).

- [42] J. Randrup and S. Mrowczynski, Phys. Rev. **C68**, 034909 (2003).
- [43] P. Romatschke and M. Strickland, Phys. Rev. **D68**, 036004 (2003).
- [44] P. B. Arnold, J. Lenaghan, and G. D. Moore, JHEP **0308**, 002 (2003).
- [45] A. Rebhan, P. Romatschke, and M. Strickland, Phys. Rev. Lett. **94**, 102303 (2005).
- [46] P. B. Arnold, D. T. Son, and L. G. Yaffe, Phys. Rev. **D59**, 105020 (1999).
- [47] E. Shuryak, J. Phys. **G30**, S1221 (2004).
- [48] Z. Xu and C. Greiner, Eur. Phys. J. **C49**, 187 (2007).
- [49] R. Baier, A. H. Mueller, D. Schiff, and D. Son, Phys. Lett. **B502**, 51 (2001).
- [50] R. Baier, A. H. Mueller, D. Schiff, and D. Son, Phys. Lett. **B539**, 46 (2002).
- [51] M. E. Carrington, K. Deja, and S. Mrowczynski, Phys. Rev. **C90**, 034913 (2014).
- [52] K. Deja and S. Mrowczynski (2015), 1503.08861.
- [53] M. Bellac, *Thermal Field Theory* (Cambridge University Press, Cambridge, 2000).
- [54] P. Romatschke and M. Strickland, Phys. Rev. **D70**, 116006 (2004).
- [55] M. Attems, A. Rebhan, and M. Strickland, Phys. Rev. **D87**, 025010 (2013).
- [56] W. Florkowski, R. Maj, R. Ryblewski, and M. Strickland, Phys. Rev. **C87**, 034914 (2013).
- [57] A. Dumitru, Y. Guo, and M. Strickland, Phys. Lett. **B662**, 37 (2008).
- [58] M. Martinez and M. Strickland, Phys. Rev. **C78**, 034917 (2008).
- [59] B. Schenke and M. Strickland, Phys. Rev. **D76**, 025023 (2007).
- [60] J.-P. Blaizot and E. Iancu, Phys. Rept. **359**, 355 (2002).
- [61] D. F. Litim and C. Manuel, Phys. Rept. **364**, 451 (2002).
- [62] S. Mrowczynski and M. H. Thoma, Phys. Rev. **D62**, 036011 (2000).
- [63] S. Mrowczynski, A. Rebhan, and M. Strickland, Phys. Rev. **D70**, 025004 (2004).
- [64] R. Kobes, G. Kunstatter, and A. Rebhan, Nucl. Phys. **B355**, 1 (1991).
- [65] E. M. Lifshitz and L. P. Pitaevskii, *Physical Kinetics* (Pergamon, Oxford, 1981).
- [66] I. N. Bronshtein and K. A. Semendyayev, *Handbook of Mathematics* (Van Nostrand Reinhold, New York, 1985).

- [67] B. Schenke, M. Strickland, C. Greiner, and M. H. Thoma, *Phys. Rev.* **D73**, 125004 (2006).
- [68] M. E. Carrington, K. Deja, and S. Mrowczynski (2015), 1506.09082.
- [69] S. Peigne and A. V. Smilga, *Phys. Usp.* **52**, 659 (2009).
- [70] A. Majumder and M. Van Leeuwen, *Prog. Part. Nucl. Phys.* **A66**, 41 (2011).
- [71] M. H. Thoma and M. Gyulassy, *Nucl. Phys.* **B351**, 491 (1991).
- [72] S. Mrowczynski, *Phys. Lett.* **B269**, 383 (1991).
- [73] E. Braaten and M. H. Thoma, *Phys. Rev.* **D44**, 1298 (1991).
- [74] E. Braaten and M. H. Thoma, *Phys. Rev.* **D44**, 2625 (1991).
- [75] A. Peshier, *Phys. Rev. Lett.* **97**, 212301 (2006).
- [76] B. G. Zakharov, *JETP Lett.* **86**, 444 (2007).
- [77] M. Gyulassy and M. Plumer, *Phys. Lett.* **B243**, 432 (1990).
- [78] X.-N. Wang and M. Gyulassy, *Phys. Rev. Lett.* **68**, 1480 (1992).
- [79] R. Baier, D. Schiff, and B. G. Zakharov, *Ann. Rev. Nucl. Part. Sci.* **50**, 37 (2000).
- [80] M. Gyulassy, P. Levai, and I. Vitev, *Nucl. Phys.* **B594**, 371 (2001).
- [81] U. A. Wiedemann, *Nucl. Phys.* **B588**, 303 (2000).
- [82] Y. L. Dokshitzer and D. E. Kharzeev, *Phys. Lett.* **B519**, 199 (2001).
- [83] P. Romatschke and M. Strickland, *Phys. Rev.* **D71**, 125008 (2005).
- [84] S. K. Wong, *Nuovo Cim.* **A65**, 689 (1970).
- [85] S. Peigne, P.-B. Gossiaux, and T. Gousset, *JHEP* **04**, 011 (2006).
- [86] A. Adil, M. Gyulassy, W. A. Horowitz, and S. Wicks, *Phys. Rev.* **C75**, 044906 (2007).
- [87] P. M. Chesler, M. Lekaveckas, and K. Rajagopal, *JHEP* **1310**, 013 (2013).
- [88] T. Tajima and J. M. Dawson, *IEEE Trans. Nucl. Sci.* **26**, 4188 (1979).
- [89] W. B. Mori, T. Katsouleas, J. M. Dawson, J. M. Kindel, and D. W. Forslu, *Nature* **311**, 525 (1984).
- [90] W. P. Leemans, B. Nagler, A. J. Gonsalves, C. Toth, K. Nakamura, C. G. R. Geddes, E. Esarey, C. B. Schroeder, and S. M. Hooker, *Nature Phys.* **2**, 696 (2006).